

Fuel Cell and Battery Hybrid System Optimization

Increased Range and Endurance

J. Hoogendoorn



Technische Universiteit Delft



Fuel Cell and Battery Hybrid System Optimization

Increased Range and Endurance

by

J. Hoogendoorn

to obtain the degree of Master of Science in Aerospace Engineering
ter verkrijging van de graad van Master of Science in Aerospace Engineering

at the Delft University of Technology,
aan de Technische Universiteit Delft,

to be defended publicly on Thursday March 29, 2018 at 13:00 PM.
in het openbaar te verdedigen op donderdag 29 maart om 13:00 uur.

Student number:	4231155	
Thesis Committee:	Prof. Dr. Ir. L.L.M. Veldhuis,	TU Delft, Chair Committee
	Dr. Ir. M. Voskuijl,	TU Delft, Supervisor
	Ir. P.C. Roling,	TU Delft, External Group
	Ir. A. de Boer,	NLR, Supervisor
Thesis Supervisor:	Ir. R. van Benthem,	NLR, Supervisor

Abstract

Aircraft manufacturers are increasingly exploring emission-free flight or emission reduction for larger passenger aircraft. The low energy density of state-of-the-art battery technology limits the application to small, electric, fixed wing aircraft up to a flight time of approximately one hour. To overcome these limits, a combination of fuel cells and batteries to exploit the benefits of battery power density and hydrogen energy density was studied. Current Lithium-Ion battery cells reach approximately 1.6 kW/kg of maximum power density, much higher than fuel cell systems. On the other hand, the energy storage capacity of suitable hydrogen storage methods is much larger than battery cells, the latter have an energy density of 240 Wh/kg.

Because most demonstrated applications are for fixed wing aircraft, the unmanned GeoCopter GC-201 helicopter was used for performance requirements, weight and volume analysis. The study focuses on the preliminary sizing of the powertrain and the optimization of fuel cell and mission profile variables for this vehicle. Helicopter performance modelling, fuel cell static behavior as well as a battery discharge simulation are combined with lower fidelity models for other components.

The study results in a comparison of battery-only and fuel cell-battery configurations through payload-range diagrams, allowing for a quick evaluation of application areas. These mainly show that batteries excel at high payload, low range applications whereas a fuel cell-battery combination shows clear advantages at low payload, longer range applications. Liquid hydrogen will be shown to be comparable to the current micro gas turbine powered rotorcraft, with 400 and 500 km range capabilities respectively. Range capabilities for 300 bar and 700 bar compressed gas tank storage options show 140 and 180 km, with battery-only reaching a maximum range of 80 km.

Acknowledgements

This thesis report is an important last step towards my degree in Aerospace Engineering. This thesis has been supervised from within Delft University of Technology and NLR (Netherlands Aerospace Centre). My years at Delft University of Technology have helped me to be where I am today and helped me grow on a personal level besides the fact that I have been able to extend my knowledge in many ways. I am grateful for my opportunity to perform this thesis under direct supervision at the Netherlands Aerospace Centre in Amsterdam.

I would like to thank my principal supervisors, Dr. Ir. Mark Voskuil of Delft University of Technology and my supervisors Ir. Alte de Boer and Ir. Roel van Benthem of the Netherlands Aerospace Centre. I have consistently been given the freedom to pursue the topics I deemed relevant within this thesis and have been allowed to turn this thesis into my own work, while being steered in the right direction when needed. I would also like to acknowledge the other committee members for their time to go through this thesis.

Finally, I must express my gratitude to my parents, my girlfriend, friends and fellow students and colleagues for providing me with unfailing support and continuous encouragement throughout my years of study at Delft University of Technology and during the research and writing of this thesis.

Joey Hoogendoorn
March 2018

Contents

1	Introduction	1
I	Background	6
2	Demonstrated Applications	7
2.1	Fuel Cells in UAVs	7
2.2	Small Manned Aircraft	8
2.3	Larger Passenger Aircraft	9
3	Battery Technology	11
3.1	Overview of Battery Technology.	11
3.1.1	Market Forecast	11
3.1.2	System Performance Indicators	12
3.1.3	Lithium-Ion	14
3.1.4	Lithium-Sulfur	15
3.1.5	Lithium-Air	15
3.2	Battery Discharge Characteristics	16
3.3	Battery Modelling Options	17
3.3.1	Battery Model Simulations	17
4	Fuel Cell Technology	18
4.1	Working Mechanism of Fuel Cells	18
4.2	Fuel Cell Technologies	18
4.2.1	Comparison of Fuel Cells	19
4.2.2	Market Forecast	22
4.2.3	System Performance Indicators	22
4.2.4	Proton Exchange Membrane and Solid Oxide Fuel Cells	23
4.2.5	High Temperature Fuel Cells	24
4.2.6	Low Temperature (LT) and High Temperature (HT) PEMFC	25
4.3	Balance of Plant (BoP) Components	26
4.3.1	Humidifier	26
4.3.2	Compressor	26
4.3.3	Cooling System	27
4.4	Fuel Cell Stack Design Characteristics.	28
4.4.1	Nernst Equation and Limitations	28
4.4.2	I-V Characteristics: Polarization Curve.	29
4.4.3	Fuel Utilisation and Efficiency	30
4.4.4	Stoichiometry Effects	31
4.4.5	Pressure Effects	31
4.4.6	Dynamic Behaviour: Transient Response	32
4.5	Hydrogen Storage	32
4.5.1	Hydrogen Storage Overview	32
4.5.2	Liquid Hydrogen Storage.	33
4.5.3	Metal Hydrides.	34
4.6	Fuel Cell Modelling	35
4.6.1	Static Modelling	35
4.6.2	Modelling of Dynamic Behaviour	35

5	Powertrain Configurations	36
5.1	Powertrain Overview and Efficiencies	36
5.2	Battery and Fuel Cell Mix	37
5.3	Series Powertrain	37
5.4	Parallel Powertrain	37
5.5	Active and Passive Hybrid Systems	38
5.5.1	Active Hybrid System	38
5.5.2	Passive Hybrid System	38
5.5.3	Recommendations	39
5.6	Test Setup	39
6	Interim Summary and Modelling Overview	41
II	Modelling	43
7	Test Environment: Reference Helicopter and Mission Profiles	44
7.1	Helicopter Applications	44
7.2	Weight and Volume Overview: Geocopter GC-201	45
7.3	P-V Curves OGE and IGE and Mass Change	45
7.4	Mission Profiles: Test Environment	47
7.4.1	Assumptions	47
7.4.2	Mass Change	48
7.4.3	Strategy	48
7.4.4	Symbol Definition	48
7.4.5	Best Endurance and Best Range Mission Profiles	48
7.4.6	Advanced Helicopter Mission: Best Range with with a Drop-Off	50
7.4.7	Top-Level Power Analysis	53
7.4.8	Power Overview	55
8	Helicopter Performance Requirements	56
8.1	Assumptions	56
8.2	Theory: P-V curve	56
8.3	Helicopter Background Equations	56
8.3.1	Hover Power	56
8.3.2	Vertical Climb and Descent	58
8.3.3	Download in Hover	58
8.3.4	Forward Flight: Glauert Momentum Theory	58
8.3.5	Forward Flight: BEM Theory	58
8.3.6	Fuselage Flat Plate / Parasitic Drag Power	59
8.3.7	Total Power in Forward Flight (BEM)	59
8.4	EMPRESS Inputs	59
8.5	Resulting P-V Curve	62
8.6	MGT (Conventional) Performance Analysis	63
8.6.1	Hover Ceiling	63
8.6.2	Forward Speed Ceiling and Flight Envelope	63
8.7	Segment Analysis: Conventional	66
8.7.1	Best Endurance	66
8.7.2	Best Range	66
8.7.3	Payload-Range	69
9	Fuel Cell Sizing	70
9.1	Assumptions	70
9.2	I-V Curve Modelling	70
9.2.1	Reference Stacks, Parameters and Hypothesis Test	71
9.2.2	Pressure Modelling Approach	71
9.2.3	Least Squares MatLab: Algorithm and Application	72
9.2.4	Mass Flow and Efficiency	73

9.3 Fuel Cell Stack Sizing	74
9.3.1 Understanding Voltage Requirements	74
9.3.2 Cell to Stack	75
9.3.3 Cell Weight and Volume	75
9.3.4 Stack Weight	76
9.3.5 Volume.	76
9.3.6 Miscellaneous Weight and Chapter Remarks.	76
10 Compressor Sizing and Effects	78
10.1 Assumptions	78
10.2 Air Properties	78
10.3 Compressor Sizing	79
10.3.1 Compressor Conditions	79
10.3.2 Mass Flow and Power Requirement	79
10.4 Reference Compressors	80
10.4.1 Compressor Types	80
10.4.2 Compressor Efficiencies	81
11 Balance of Plant: Additional Components	83
11.1 Battery Overhead	83
11.2 Storage Options	84
11.3 Pressure Regulators	86
11.4 Inverter	86
11.5 Electric Motor.	86
11.6 Power System Controller	87
11.7 Fuel Cell System: Overhead	87
12 Battery Modelling	88
12.1 Method Verification.	89
12.2 SoC and DoD	90
12.3 Modelling Approach: Curve Fitting	90
12.3.1 Data Extraction	90
12.3.2 Multiple Regression: MatLab.	91
12.3.3 Data Preparation.	91
12.3.4 Objective Function and Tolerances	92
12.3.5 Initial Values	92
12.4 Modelling Results: Discharge Curves	92
12.5 Modelling in SimScape	92
12.6 Simulation of LG-HG2 According to Curve Fit Results.	94
12.6.1 Methodology.	94
12.6.2 Conditions	95
12.6.3 Simulation Test	95
12.6.4 Charging Modelling: Future Improvement Consideration	99
12.7 Voltage Range and Aviation Standards	99
12.8 Battery Sizing for Battery-Only Configuration.	99
12.8.1 Volume: Cylinder Packing	100
12.8.2 Battery Limits	101
12.8.3 Range and Endurance Calculations through Simulation	101
12.9 Battery Sizing for the FC-B Configuration	101
13 Sizing Procedure and Optimization	103
13.1 Sizing Steps	103
13.1.1 Battery-Only Configuration	103
13.1.2 FC-B Configuration	104
13.2 Definition of Optimization	104
13.2.1 Design Objective	105
13.2.2 Normalizing Variables	106
13.2.3 Optimizer Settings	106

III Results, Conclusions and Recommendations	107
14 Results: Battery-Only and FC-B Configurations	108
14.1 P-V Curves Helicopter	108
14.2 Battery-Only Configuration	109
14.2.1 Fixed Parameters.	109
14.2.2 Variables for Optimization: Battery-Only.	109
14.2.3 Initial Points	110
14.2.4 Payload-Range: 500m, 1500m (Unoptimized)	110
14.2.5 Payload-Range: Optimized Battery.	112
14.2.6 Sensitivity of Nominal Energy Density	114
14.2.7 Maximum Endurance: 500 m	114
14.3 Fuel Cell + Battery Configuration	115
14.3.1 Storage Options	115
14.3.2 Discrete and Semi-Discrete Battery Sizing and Notation	116
14.3.3 Fixed Parameters.	116
14.3.4 Variable Choice and Initial Points	116
14.3.5 Payload-Range: 500m and 1500m (Unoptimized)	117
14.3.6 Payload-Range: Optimized with i,p,h,RoC,RoD	121
14.3.7 Sensitivity of FC,sys Overhead and Stack Weight	128
14.3.8 Comparison B-Only an FC-B Configurations to Conventional MGT Powered GC-201	128
14.3.9 Sensitivity to Vertical RoC	129
14.4 Forecast 2030	130
14.5 Piloted/Manned Helicopter	132
14.6 Energy Density and Power Density	132
15 Conclusions	137
Bibliography	139
A Appendix A: Battery-Only 500 and 1500m Simulations	143
B Appendix B: FC-B Configuration Battery Simulations	146
C Appendix C: FC-B Configuration Vertical RoC Investigation	149
D Appendix D: FC Fitting Parameters	156

Nomenclature

List of Abbreviations

AC	Alternating Current
AFC	Alkaline Fuel Cell
APU	Auxiliary Power Unit
B-Only	Battery Only Configuration
BoP	Balance of Plant
C-E	Compressor-Expander
DBFC	Direct Borohydride Fuel Cell
DC	Direct Current
DFAFC	Direct Formic Acid Fuel Cell
DMFC	Direct Methanol Fuel Cell
DoE	U.S. Department of Energy
ECS	Environmental Control System
EMF	Electro Motive Force (See OCV)
EV	Electric Vehicle
FC-B	Fuel Cell - Battery Configuration
FC	Fuel Cell
ISA	International Standard Atmosphere
LCO	Lithium Cobalt Oxide (battery type)
LFP	Lithium Iron Phosphate(battery type)
LH2	Liquid Hydrogen
LMO	Lithium Manganese Oxide (battery type)
LPA	Large Passenger Aircraft
LTO	Lithium Titanium Oxide (battery type)
MCFC	Molten Carbonate Fuel Cell
MGT	Micro Gas Turbine
NCA	Lithium Nickel Cobalt Aluminium Oxide (battery type)
NCM	Lithium Nickel Cobalt Manganese Oxide (battery type)
NLR	Nederlands Lucht- en Ruimtevaart Laboratorium
OCV	Open Circuit Voltage
PAFC	Phosphoric Acid Fuel Cell
PEMFC	Proton Exchange Membrane Fuel Cell
SAT	Small Air Transport (4-19 passengers)
SOFC	Solid Oxide Fuel Cell
UAV	Unmanned Aerial Vehicle

List of Symbols

$\bar{C}_{D,p}$	Mean rotor profile drag coefficient	[-]
δ	Pressure Ratio	[-]
\dot{M}	Molar Flow	[mol/s]
\dot{m}	Mass Flow	[kg/s]
η	Efficiency	[-]
$\eta_{H_2,tank}$	Hydrogen Storage Efficiency	[kg/kg]
$\eta_{vol,tank}$	Hydrogen Volumetric Storage Efficiency	[kg/L]
λ_T	Lapse Rate	[K/m]
μ_{H_2}	Hydrogen Utilization	[-]
Ω	Rotational Speed	[RPM]
ρ	Density	[kg/m ³]
σ	Rotor Solidity Factor	[-]
θ	Temperature Ratio	[-]
A	Area	[m ²]
A_c, A_{new}	Fuel Cell Active Area	[cm ²]
A_m, A_b	Area of main rotor, blades	[m ²]
B	Fuel Cell Activation Loss Parameter	[V ln(A/cm ²) ⁻¹]
C, C-Rate	Battery Discharge Rate	[h ⁻¹]
D_m	Diameter of Main Rotor	[m]
DoD	Depth of Discharge	[-]
E_0	Open Circuit Voltage	[V]
F	Faraday Constant	[C/mol]
$f_{overhead}$	Fuel Cell System Overhead Factor	[-]
GTOW	Gross Take-Off Weight	[kg]
h	Altitude	[m]
i	Fuel Cell Current Density	[A/cm ²]
I, I _b	Current	[A]
k	Induced Power Coefficient	[-]
LHV	Lower Heating Value	[MJ/kg]
M	Molar Weight	[kg/mol]
m	Fuel Cell Concentration Loss Parameter	[V]
MTOW	Maximum Take-Off Weight	[kg]
n	Fuel Cell Exponential Concentration Loss Parameter	[cm ² /A]
N_c, n_c	Number of cells	[-]
N_m	Number of Rotor Blades	[-]
N_s, N_p	Number of cells in Series and Parallel	[-]
P	Power	[W]
p	pressure	[N/m ²]
pc	Peukert Coefficient	[-]
Q	Heat	[W]
Q, Q _{bat} , Q _{Rat}	Actual and Rated Battery Capacity	[Ah]
R	Universal Gas Constant	[J kg ⁻¹ K ⁻¹]
R, r	Ohmic Resistance	[Ω]
R_{H_2}	Hydrogen Gas Constant	[J kg ⁻¹ K ⁻¹]

RoC, RoD	Rate of Climb / Descent	[m/s]
SFC	Specific Fuel Consumption	[kg kW ⁻¹ hr ⁻¹]
SoC	State of Charge	[-]
T	Temperature	[K]
T	Thrust (Helicopter)	[N]
t, t*	Time, Surrogate Time	[s]
V	Voltage	[V]
V	Volume	[dm ³]
V _{BE} , V _{BR}	Best Endurance/Range Velocity	[m/s]
v _i	Induced Velocity	[m/s]
W	Component Mass	[kg]

Introduction

Aircraft manufacturers are increasingly exploring emission-free flight and emission reduction for larger passenger aircraft. The low energy density of battery technology limits electric aircraft for longer range flight profiles and batteries are therefore generally only used in small aerial vehicles, mostly for demonstrating the technology as seen in e.g. the Airbus E-fan. The Pipistrel Alpha Electro 2-seat trainer aircraft is fully electric and already in production while reducing flying cost significantly. However, endurance is still limited to approximately an hour of flight.

These limitations call for hybrid systems in which the battery technology is combined with other energy and power sources. This thesis focuses on the possibilities to exploit the benefits of fuel cell technology in combination with batteries (FC-B configuration) towards an increase in range and endurance. This is done for an unmanned reference helicopter with a MTOW of 100 kg, the Geocopter GC-201. This test case used throughout this thesis is shown in Figure 1.1. The reason for a helicopter UAV test case of 100 kg is that helicopters show a much smaller power difference between nominal cruise power and the peak power when compared to fixed wing aircraft. Also, the power level at cruise is high compared to fixed wing aircraft, making the fuel cell system larger. Furthermore, most demonstrated applications are fixed wing aerial vehicles. The benefit of the UAV application is that no volume is lost in the cabin. Volume is, however, considered throughout this study.



Figure 1.1: PH-1XA Geocopter (NLR / Dutch Aerospace Center). The same GC-201 can be found under registration PH-1AA

The power system of a combined fuel cell and battery configuration is shown in Figure 1.2, with the helicopter shown at the top right. It shows the main components needed in such a fuel cell system, which requires a number of additional components such as air compressors, storage tanks, pressure regulators, cooling and humidification (sometimes included in the fuel cell stack), an inverter and a motor. These components will therefore also be sized in this study.

The reason for a combination of fuel cells and batteries is shown in Figures 1.3 and 1.4, where energy and power densities are shown on a system level. A battery-only system has a very low energy density as a result of the low energy density of battery cells and the required overhead forming a large fraction of the weight. Small battery packs delivering peak power (FC-B) are even more likely to show reduced energy density as a result of series and parallel discretization. Fuel cell systems however, show much higher energy density as a result of the energy content of hydrogen at 33.3 kWh/kg. The power density of batteries on the other hand is approximately 1.5-2 kW/kg for cells, with a possible reduction to under 1 kW/kg due to overhead and series/parallel discretization. Compared to state-of-the-art fuel cell systems, this a factor two higher and

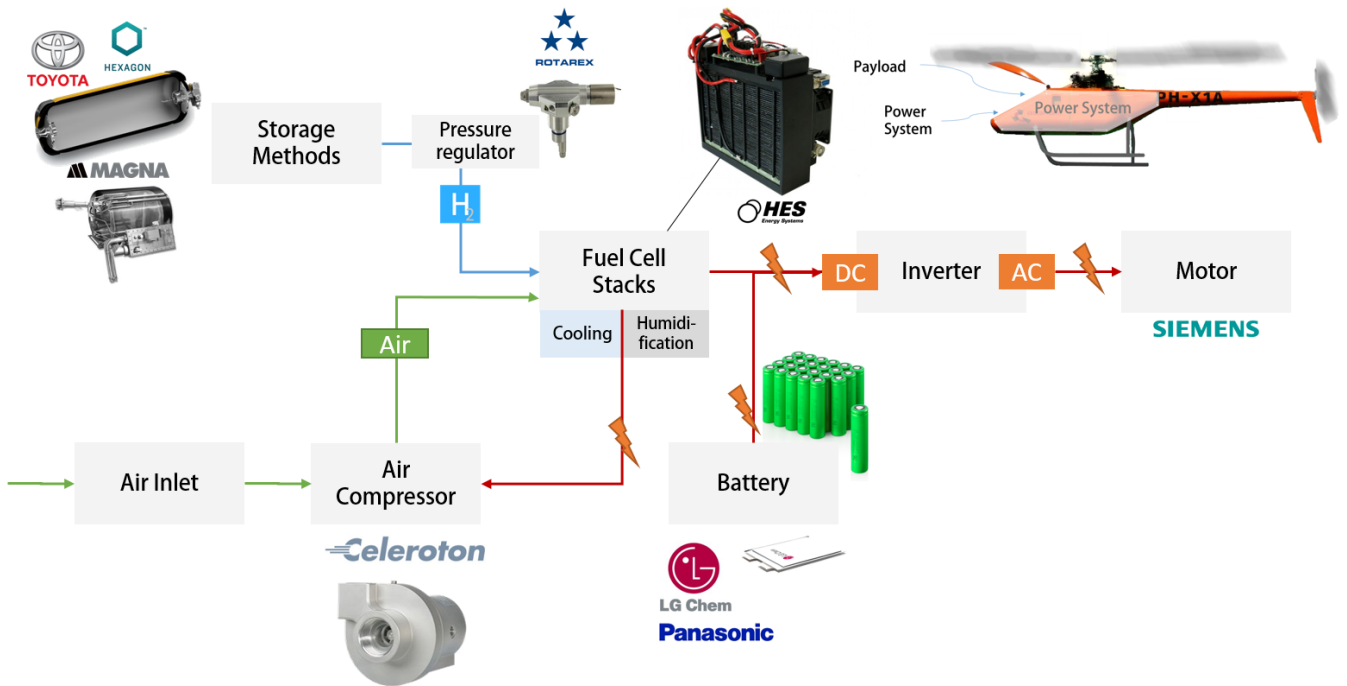


Figure 1.2: FC-B system overview with main components and a number of manufacturers of shown components such as Hexagon Lincoln, Toyota and Magna Steyr/BMW (storage options), Rotarex (700 bar pressure regulator), Horizon Energy Systems (fuel cell), LG and Panasonic (Li-Ion batteries), Celeroton (compressor) and Siemens (electric motor)

therefore batteries are very useful for short duration peak power phases. The resulting powertrains will be analyzed at the end of the results section, showing these results for both volumetric and gravimetric power and energy density.

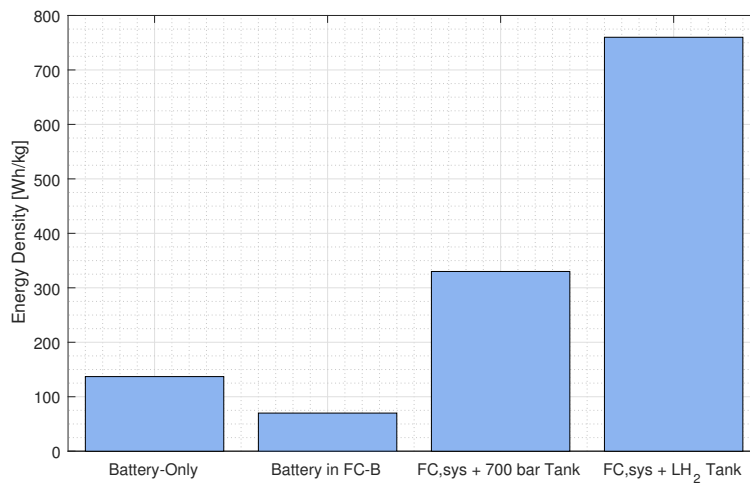


Figure 1.3: Actual system energy densities further elaborated on in the results section of this study. Battery cell energy density is normally close to 250 Wh/kg [6], 33.3kWh/kg for H_2 and 1.7kWh/kg for hydrogen plus a 700 bar storage tank. For the two right bars, the fuel cell system weight (stack + cooling + compressor + controller + pressure regulator) was included. Batteries include overhead.

Research Objective

The research objective is to make recommendations on focus areas for further electric hybrid powertrain improvements with the main goal of extending the range of electrically powered aerial vehicles that show a clear difference between long-duration nominal and a short-duration peak power levels. The goal is to understand which components inside a fuel cell system require the largest improvements based on their relative weight and what flight profile is most suitable for a FC-B configuration. The main goal is to have an improved understanding of possible application areas for a variety of payloads.

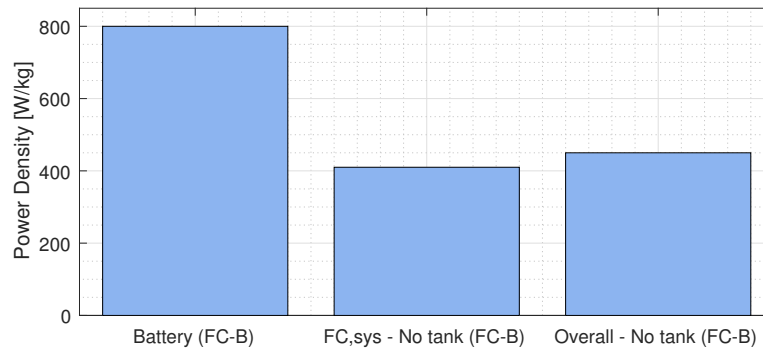


Figure 1.4: Actual power density in the FC-B configurations. Battery cell power density goes up to 1.8kW/kg, but when including overhead and series/parallel discretization, this could drop below 1kW/kg. The FC stacks alone reach approximately 500-700W/kg, but when including overhead the fuel cell system (without the tank) goes down to ~400 W/kg. The FC-B configuration in totality reaches 450 W/kg, excluding hydrogen storage

The objective of improved range and endurance is achieved by a variable optimization of the fuel cell, battery and mission profile, including a battery discharge simulation for sizing purposes and a better understanding of battery performance. Variables such as fuel cell current density and stack pressure as well as variable mission profile parameters are included, which affect peak power and its duration, but also the fuel cell performance. Furthermore, experimental data from literature will be used to set up the fuel cell model, whereas the battery is modelled based on experimental data and a custom discharge simulation is verified using the MatLab SimScape Power Systems tool. The helicopter performance is modelled through validated NLR software EMPRESS. The modelling approach is summarized as follows:

- Create a **higher fidelity** analysis and model of fuel cell and battery performance for the most significant variables that impact system level performance. Also, helicopter power curves will provide accurate helicopter power and speed data.
- Create **medium to low fidelity** models for Balance of Plant (BoP) components to be used in the optimization, where power requirements and weight are key outputs. Balance of Plant is terminology within the fuel cell industry for fuel cell system additional components on top of the fuel cell stack itself.

The results will contribute a sizing and optimization method for an electric hybrid powertrain using fuel cells and batteries, with state-of-the-art parameters and characteristics for balance of plant components which form the overhead of the respective systems. As a result of this analysis, the most suitable applications and main areas of improvement will become clearer. Also, the competitiveness of a FC-B system to a Battery-only system will be important for understanding in what situations the different configurations may thrive. This results in the following research question and a few subquestions, in which hybrid refers to an all-electric powertrain with different power sources.

How can the range and/or endurance of an electrically powered helicopter UAV be optimized by using a hybrid fuel cell-battery powertrain?

- What are the most suitable fuel cell and battery technologies for a hybrid powertrain in aerial vehicles?
- What are the trade-offs, main parameters, variables and modelling options for powertrain components?
- How do the mission profile parameters influence helicopter power levels?
- How can the powertrain be sized and its performance optimized?
- What are the application areas for the Battery-Only and FC-B configurations?

Chapter Structure

The first 6 chapters form **Part I** in this study and provide mostly a literature review, consisting of an analysis of the majority of components and important parameters of fuel cells and batteries. Chapter 2 gives an overview of demonstrated applications, which are generally not rotorcraft such as in this study. Again, this study focuses on the unmanned GeoCopter GC-201 of 100 kg MTOW. Chapter 3 provides a battery technology review,

with a strong focus on state-of-the-art Li-Ion technology, performance characteristics and future technology such as Lithium-Sulfur and Lithium-Air.

This is followed by a larger chapter of the main focus area of this research, the fuel cell technology and its Balance of Plant (which are basically the additionally required components) in Chapter 4. This component overview was also shown in Figure 1.2. The fuel cell working principle for the most common fuel cell (PEMFC) in vehicular applications is shown in Figure 1.5. This figure directly explains the need for hydrogen on one side and air or oxygen on the other side as seen in the powertrain overview (Figure 1.2). At the anode of the fuel cell the hydrogen enters and is broken up into hydrogen protons and electrons at the membrane. The release of electrons directly results in electrical current. On the cathode side, the hydrogen proton reacts with oxygen to form water and heat, which are the only products in a PEMFC. These two reactions within a fuel cell are summarized by the following two reactions.

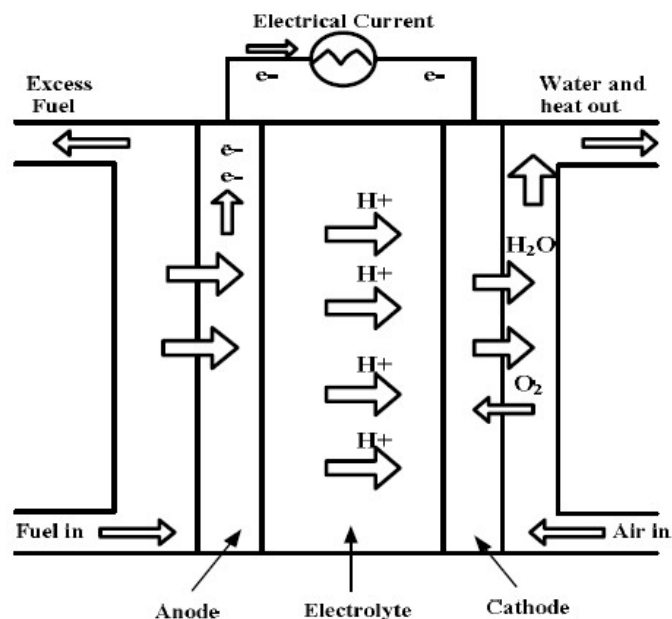
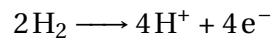


Figure 1.5: Schematic of a Proton Exchange Membrane fuel cell (PEMFC) commonly used in vehicular applications [15]

Chapter 5 then gives an overview of different powertrain lay-outs and test setups that can be used in future studies, of which a parallel powertrain was shown in Figure 1.2. Chapter 6 will provide an interim summary / conclusion with focus areas for the next chapters.

Part I is followed by the modelling chapters in **Part II**. The reference helicopter is first elaborated on in Chapter 7, which provides an overview of all weights and volumes available in the Geocopter GC-201 and gives a good idea of the respective budgets inside this UAV. This is followed by an overview of mission profiles. These are best range and best endurance mission profiles that consist of realistic flight sections to model both peak power and cruise power phases, by combining hover, climb, cruise and descent phases. The helicopter performance model is then elaborated on in Chapter 8. This is required to get an understanding of power requirements in all flight sections of the mission profiles considered.

The next step is modelling the power system, which starts with the modelling of the fuel cell. This is elaborated on in Chapter 9. This is followed by the compressor sizing (Chapter 10) as it needs to be powered by the fuel cell as air is needed to operate the fuel cell. This is followed by a chapter on other additional components (also called Balance of Plant for fuel cells), see Chapter 11. This includes the battery overhead, fuel cell system overhead, inverter, motor, controller and pressure regulator modelling. The more elaborate modelling and simulation of battery discharge curves is elaborated on in Chapter 12.

Finally, the modelling part is concluded with Chapter 13 which elaborates more on the sizing and optimization procedure using flow diagrams and optimization settings. This gives an overview of the procedure followed using the tools and parameters from all previous chapters. This is summarized in Figure 1.6 and will be further elaborated on in that final modelling chapter for both the battery-only and fuel cell-battery configuration. It shows that the optimizer sends a number of variables to the analysis, in which fuel cell and

BoP sizing is performed and analysed for off-design conditions. It shows that the power of the compressor will be included in the fuel cell design power. Helicopter performance requirements are used to determine peak power levels for the battery sizing and simulation, after which the hydrogen storage weight can be determined. Chapter 13 will further elaborate on this.

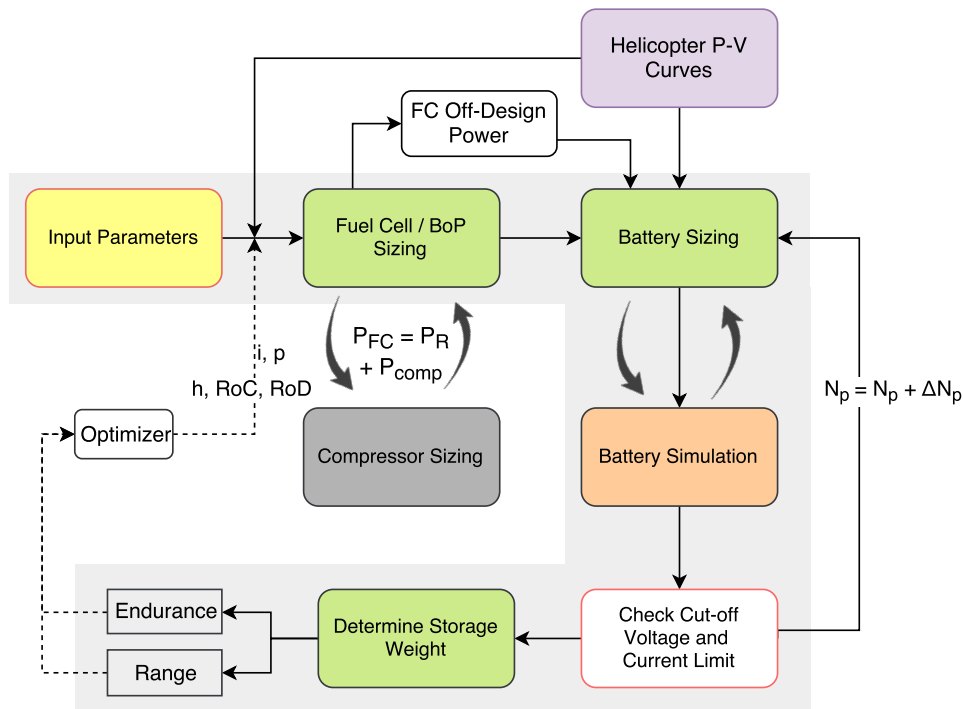


Figure 1.6: Sizing procedure for the FC-B configuration

Finally, the results for battery-only and FC-B configurations are shown for unoptimized and optimized cases in Chapter 14. These results mainly compare payload-range diagrams of the different power system configurations. This is inside **Part III** of this thesis which elaborates on results and conclusions.

I

Background

Demonstrated Applications

This chapter discusses previous applications of electric powertrains. This includes some all-electric battery only applications but will show a timeline for fuel cell usage in UAVs and small aircraft as well. Fuel cells that have been demonstrated as a replacement for APUs in larger aircraft will also be included. Note that the overview provided here will not include all applications but rather an indication of fuel cell usage in previous years. It should be noted that most of these applications are not rotorcraft.

The first fuel cell powered manned aircraft was the Boeing Fuel Cell Demonstrator aircraft which took off in 2008. Similar to this study, it uses battery technology to aid the fuel cell during take-off and climb. The first manned aircraft capable to take off using solely fuel cell power - and therefore no aid from other power sources - was the DLR-H2 Antares, based on the power glider Antares 20E. This was then used as a flying testbed for testing fuel cells in aviation operating conditions.

2.1. Fuel Cells in UAVs

Fuel cells have been tested in a significant number of UAVs. Given the fact that fuel cell systems are less complex at lower power requirements as they can potentially be air cooled, this is still an application that is often explored [32]. Furthermore, UAVs that previously ran on small gas turbines reap the benefit from a more significant efficiency increase. Also, given weight and volume restrictions, unmanned aerial vehicles bring limitations of fuel cell applications down to a more acceptable level. UAVs demonstrated in the period of 2003-2009 are given by Table 2.1 [55]. Most of the UAVs considered by Spencer and Martin (2013) [55] were below a take-off weight of 50kg. The majority of these UAVs are, however, fixed wing aircraft which benefit from higher aerodynamic efficiency and therefore also lower power requirements when compared to rotorcraft with a similar MTOW.

Organization (date)	Fuel Cell Type	Reactant Storage Type	Endurance	Vehicle Type
AeroVironment (2003)	PEMFC	H2 Sodium Borohydride	0.2 hr	Fixed Wing
AeroVironment (2005)	PEMFC	H2 Cryogenic	24 hr	Fixed Wing
Naval Research Lab (2006)	PEMFC	H2 Gaseous	3.3 hr	Fixed Wing
Adaptive Materials Inc. (2006)	SOFC	Propane	4 hr	Fixed Wing
Georgia Inst. of Tech. (2006)	PEMFC	H2 Gaseous	0.75 hr	Fixed Wing
CSU Los Angeles (2006)	PEMFC	H2 Gaseous	0.75 hr	Fixed Wing
DLR/HyFish (2006)	PEMFC	H2 Gaseous	0.25 hr	Fixed Wing
CSULA/OSU (2007)	PEMFC	H2 Gaseous	12 hr	Fixed Wing
KAIST (2007)	PEMFC	H2 Sodium Borohydride	10 hr	Fixed Wing
AeroVironment (2007)	PEMFC	H2 Sodium Borohydride	9 hr	Fixed Wing

Table 2.1: Fuel Cell Powered UAVs from 2003 to 2009 [55]

The Ion Tiger programme by the Naval Research Laboratory started in 2007 with a 300W system which at the end of the programme resulted in the same weight (1kg) fuel cell delivering 550W. In 2009 the UAV as part of this programme flew 26 hours carrying a 5 kg payload. Hydrogen was compressed up to 5000 psi (345 bar) in a carbon/aluminium compressed gas tank. In May 2013 the UAV was flown for 48 hours and 1 minute using a liquid, cryogenic hydrogen fuel storage tank and delivery system. Due to a much lower energy density of Li-ion batteries, the same (fixed wing) UAV would only be able to fly 4 hours using battery technology. In the case of even longer flight times, the advantage of hydrogen energy density becomes more pronounced as the storage will be a larger part of the overall system weight. Hence, for long endurance or long range missions, high storage efficiency is most likely to be one of the most significant factors to consider [62]. The

goal of the Ion Tiger programme was a weight reduction mostly through the improvement of a few of the main components. Within the aim of only allocating 38-40 wt% to the power source and fuel system, it was recognized that the sizing is determined largely by the interrelated properties of the stack, compressor and heat exchanger. A schematic of the Ion Tiger Fuel Cell System is shown in Figure 2.1, showing a typical system for small UAVs. The Ion Tiger has a MTOW of just over 15 kg and a cruise power of only 267W, of which 67W is used by avionics, flight controls, payload and conversion losses (7W).

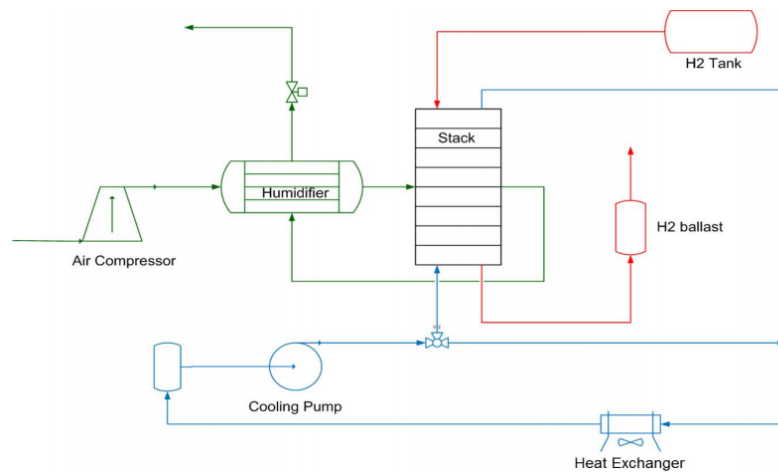


Figure 2.1: Schematic of the Ion Tiger Fuel Cell System, showing the Fuel Cell stack and Balance of Plant (BoP) components such as the air compressor, pumps, humidifier and heat exchanger. [62]

Improvements were made through a new humidifier design, new air blowers, higher stack power, integrated control electronics and a 99% hydrogen utilization. Some fuel cell designs for small UAVs are self-humidified and do not require an extra humidification system [1]. Increasing the operating temperature and a more robust humidification of the fuel cells made the heat exchange less critical (more efficient operation) and allowed for a heat exchanger weight reduction. The heat exchanger - using ambient air as the coolant - design was also improved.

Another Ion Tiger improvement was in the storage efficiency. Where a 350 bar compressed gas tank was used previously, a cryogenic tank for liquid hydrogen was used to support a longer flight time, from 1 to 3 days. The advantage of liquid hydrogen is a three times higher energy density than the 350 bar tank and results in 0.5kg of hydrogen storage in a 3.6 kg tank, making it more storage efficient than most compressed gas tanks.

Boeing subsidiary Insitu first completed a prototype flight with the ScanEagle UAV in 2011. In 2017, a successful test flight was performed using a Protonex fuel cell propulsion system, a Ballard Power Systems subsidiary. The 22kg UAV uses a PEMFC in combination with a high pressure hydrogen tank. The original UAV ran a piston engine on JP-8 military fuel at 1.12kW, but both configurations have an endurance of over 24 hours. Hydrogen production is made possible on-the-ground by reforming accessible military fuels. The ScanEagle has a service ceiling of almost 6000 meters and a cruise speed of 30.8 m/s.

2.2. Small Manned Aircraft

In the small manned aircraft category, electrically powered vehicles have been demonstrated mostly for a single seater or two-seat aircraft. However, most aircraft tend to have glider characteristics with relatively low peak powers. The first demonstrator was the Boeing Fuel Cell Demonstrator vehicle operated in 2008 and uses both a battery and a fuel cell. The airplane completed four test flights in which it took off and climbed at a velocity of 100km/h to 1067 meters altitude (3500ft). The platform chosen for this aircraft is the Diamond HK36 Superdimona glider with a MTOW of 770kg and a Lift-to-Drag (L/D) ratio of 27. The reason for choosing this aircraft was due to this high L/D and high useful load capacity (210kg). The fuel cell was sized for a 24kW gross output and the battery was designed for an additional 50-75kW. The rate of climb was 1.5-2m/s and take-off and climb lasted about 5 minutes. Aircraft ground speed during cruise was approximately 100-110km/h, at a brake power of about 15kW (and input power 17kW) [31]. A clear difference between peak and cruise power can be recognized, where the advantages of the different power sources can potentially be exploited the most.

The DLR Antares-H2 had its maiden flight in 2009, in which an altitude of 2.6km was reached and showed that the fuel cell could still function above 2km, although at reduced power. The aircraft was based on the Antares 20E. In 2012, DLR incorporated a higher performance, more compact fuel cell system by Hydrogenics.

DLR expects that coupling the fuel cell system with a Li-ion battery pack will further enhance the performance and increase the range. Currently it is exclusively powered by a fuel cell system.

The ENFICA-FC had its maiden flight in 2010, powered by a 20kW PEMFC and 20kW of batteries. The aircraft, the Rapid 200FC was designed for a 144km/h flight. This project by the Politecnico di Torino has shown good results in a demonstrated flight. The results of this research can be compared to the results obtained in the ENFICA-FC project. A performance analysis and power requirements were estimated by Romeo and Borello [50].

Another fuel cell aircraft was developed in a combined effort by DLR (Institute of Engineering Thermodynamics) with partners Hydrogenics, Pipistrel, H2FLY, Ulm University and Stuttgart Airport and is the 4-seater called HY4. This uses a combination of fuel cells and batteries and had its first flight in 2016. The motor output delivers 80kW, has a maximum speed of 200km/h and a cruise speed of 145 km/h. It can achieve a range of 750 to 1500 kilometers and has a MTOW of 1500kg. The goal of the HY4 is to further develop fuel cell technology for usage in regional aircraft for up to 19 passengers, corresponding to the goal set by the Clean Sky programme for Small Air Transport (SAT).

Aircraft that run on batteries only have also been demonstrated, the Airbus E-fan being a prominent example. However, these aircraft are very restricted in energy density. The E-fan performed a channel crossing in 37 minutes time of 74km, showing its endurance and range limitations. It flew at 1000m altitude and weighs only 600kg. The maximum power output is 60kW, resulting in a maximum speed of 220km/h. However, more recently the Pipistrel Alpha Electric (2-seater) has been taken to production and has an endurance of approximately 1 hour.

When comparing the aircraft cruise power in the previous examples to the cruise power of a Robinson R-22 type helicopter (around 70 kW for a MTOW of ~635 kg) [8], it can be seen that the power levels are relatively low compared to that of the helicopter. This means that the fuel cell is likely to require a larger part of the weight budget and there will be less room for hydrogen storage.

2.3. Larger Passenger Aircraft

Because of the limitations of battery and fuel cell technology, it is difficult to use these technologies for the propulsion of larger aircraft and other aerial vehicles. Most of the research therefore focuses on replacing power systems such as APUs and the ECS towards 'more electrically aircraft'. A clear advantage here is a major increase of the system efficiency. The focus of the majority of research in this area is in the high temperature Solid Oxide Fuel Cells (SOFC) as the operating temperature of the stack is up to 1000°C. Due to this high temperature, the exhaust heat can be used for the fuel reforming process, fuel pre-heating for usage in the gas turbine or expansion in a turbine. This can increase efficiency up to 70%.

Boeing already considered a hypothetical 440kW SOFC APU as it would be close to 75% efficient during flight, compared to 40-45% of a conventional APU. A major drawback is the 40 minute start-up time of the SOFC and therefore it was suggested to never turn off the fuel cell. For larger applications where aircraft have a quick turnaround time between flights, this seems feasible given the much higher potential efficiency.

DLR investigated a 90kW PEMFC for different applications for usage in an Airbus A320 [26]. These applications can be found in Figure 2.2 and they are quite varied. Tests were performed on high altitude performance of the fuel cell, showing quite dramatic losses at lower stack pressures. This can be seen in Figure 2.3 and shows difficulty reaching high power in high altitude applications to 12km (200 mbar). An increase of stack pressure from the nominal generally shows the opposite effect. In a real scenario, it is expected that the fuel cell system would run on cabin air for larger passenger aircraft or requires a dedicated compressor system using part of the fuel cell output power and reducing the fuel cell efficiency.

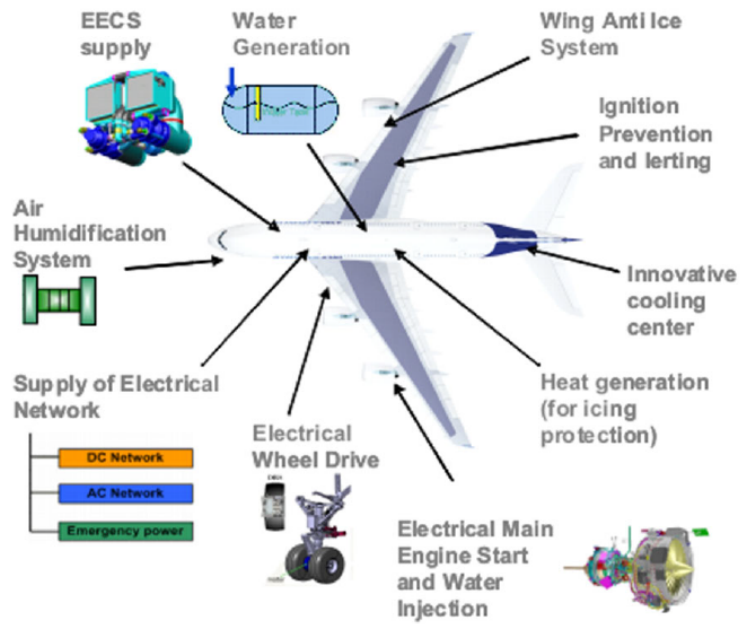


Figure 2.2: Applications of fuel cells for large passenger aircraft [26]

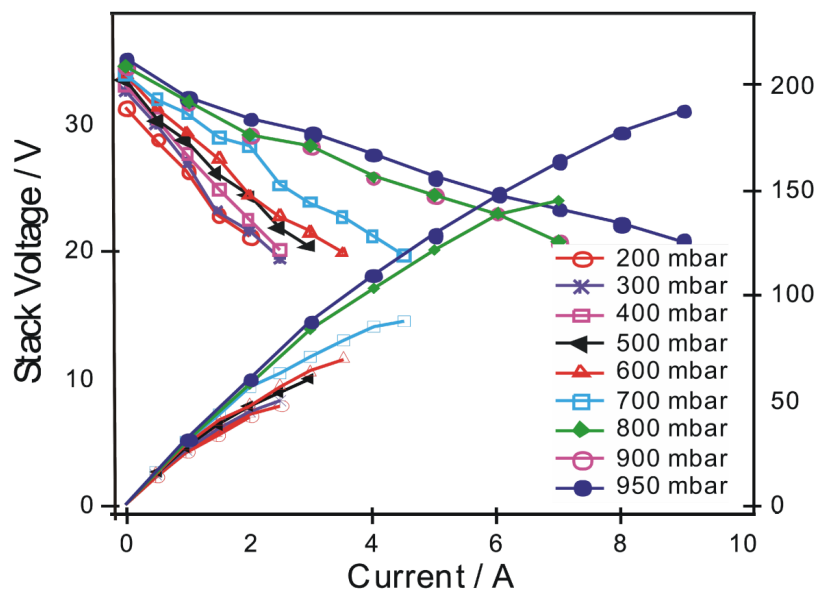


Figure 2.3: High altitude test of a PEMFC [26]

Battery Technology

Battery technology has found its way into the automotive industry but not to the same extent in the aircraft industry. The major difference is that although mass is important for on-the-ground vehicles, it is even more important for aircraft as it directly affects the feasibility. This chapter will provide an overview of battery technologies available and researched. Furthermore, it discusses important characteristics of batteries, a market forecast, power and energy density as well as available modelling opportunities (more detail in Part II of this thesis).

3.1. Overview of Battery Technology

Battery technology can be found in different configurations. The current and most promising battery technologies use lithium anodes for two main reasons. Lithium is the third lightest element and it has a high oxidation (reduction) potential [40, 66]. Hence it is clear why most current batteries are based on a lithium anode and why the most promising future battery technology such as Lithium-Sulfur (Li-S) and Lithium-Air (or Li-O_2) also share this anode.

An overview of the considered battery technology is shown in 3.1. Lithium-Ion (Li-Ion) batteries, possibly near-future Lithium-Sulfur (Li-S) and very promising high energy density - but experimental - Lithium-Air (Li-O_2) are shown. Lithium-Ion has many variations as can also be seen in Figure 3.1, each with their respective advantages and disadvantages. Advanced Li-Ion means improvements of Li-Ion over the current state-of-the-art cells through incremental improvements according to Lux Research [33]. Solid-state Li-Ion uses a solid electrolyte and has increased safety for this reason. Lux research and major manufacturers are also expecting major cost reductions when adopting this technology.

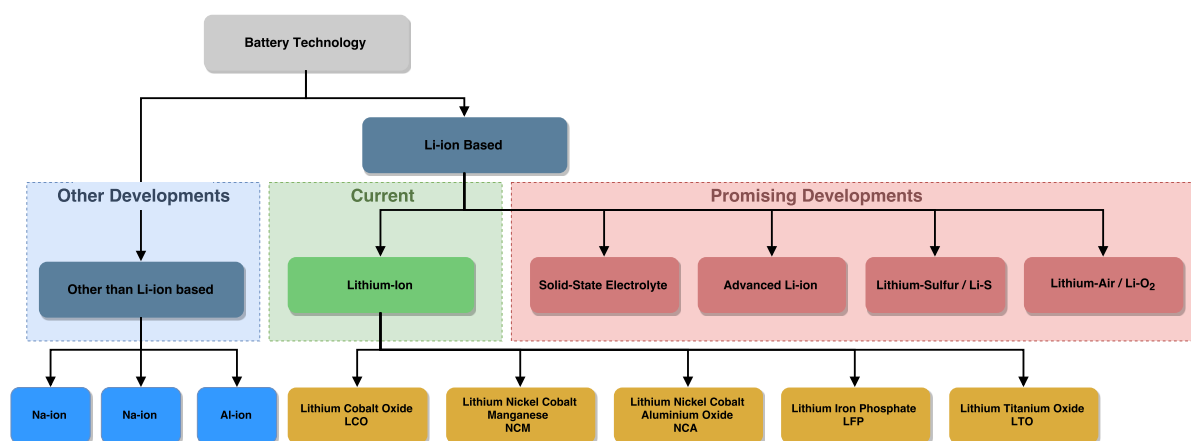


Figure 3.1: Battery technology: both mass-produced and in development. Partially adjusted from [33]

3.1.1. Market Forecast

An important consideration, also for strategic planning, is a market forecast and roadmap. Figure 3.2 shows a forecast until 2035, showing mostly advanced Li-Ion to emerge, followed by Lithium-Sulfur around 2025 and Li-Ion with a solid electrolyte towards 2030. Solid-state Li-Ion batteries are then expected to obtain market share quicker than Lithium-Sulfur according to Lux Research [33]. Initially Lithium-Sulfur benefits from simpler manufacturing and lower cost.

Big manufacturers are already investing in the promising technologies. Bosch bought Seeo, which develops polymer (electrolyte) solid-state batteries. Dyson bought Sakti3, also developing solid-state batteries. Toyota Motors is running one of the largest solid-state battery research laboratories. The large producer of chemicals, BASF, invested heavily into Lithium-Sulfur developer Sion Power. Lux Research indicates that early adopter markets will be key and suggest a focus on e.g. military. Military UAVs can be a good application for early adoption.

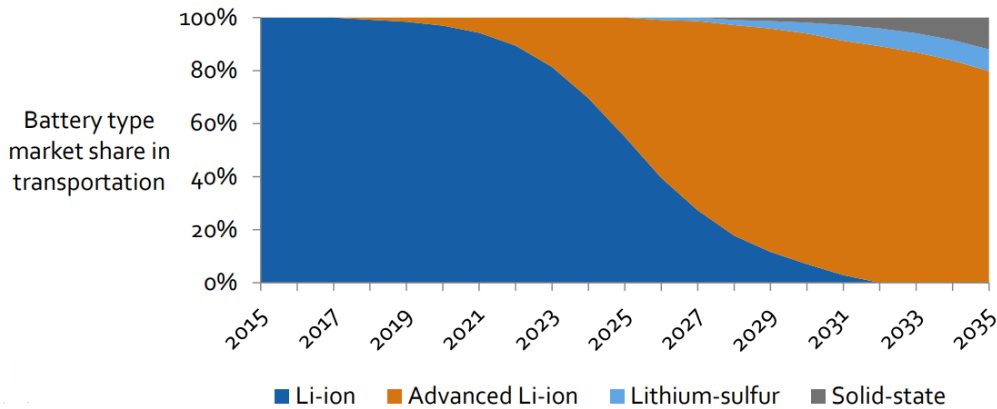


Figure 3.2: Battery roadmap to 2035 by Lux Research [33]

3.1.2. System Performance Indicators

This subsection indicates the performance characteristics of the battery types. On a system level, weight and volume are important constraints and therefore the gravi- and volumetric power and energy densities will be provided and estimated in this subsection. This will be an important comparison with fuel cell technology to understand the merits of using batteries and fuel cells. Figure 3.3 shows an overview of energy densities reached [17]. The practical values are most important in this. the Li-Air is an estimated battery-to-wheels efficiency (hence for cars, at about 90% efficiency) and the theoretical value is based purely on thermodynamics. Li-S energy density at 370 Wh/kg corresponds well to other literature and current progress [14, 46], whereas the Li-Ion energy density is a bit low, although credible, after taking into account the fact that the energy cells require a support structure and other subsystems such as cooling. It should be noted that the practical values include the powertrain efficiencies. The actual theoretical gasoline energy density is around 13 kWh/kg, but an internal combustion engine has low thermal efficiency when compared to an electric motor. Girishkumar et al. [17] used a 12.6% tank-to-wheel efficiency for gasoline, based on a U.S. fleet average of 2008. Therefore, the current practical gasoline energy density is most likely higher than shown in Figure 3.3.

It can be seen that the most promising configuration is Lithium-Air, reaching a practical energy density closer to that of gasoline (fuel tank to wheel). Li-S has reached a higher readiness level compared to Lithium-Air cells. It should be noted that the Lithium-Air energy density is not fair when provided at this value. First of all, Li-Air energy density is often inflated as the battery mass is often based on anode mass and oxygen, ignoring the cathode, electrolyte and other cell components, say Rahman et al. [47]. The maximum practical value according to Rahman et al. is closer to 1,300-1,400 Wh/kg. Furthermore, the mass of the battery system increases as the oxygen reduction reaction takes place in the system.

Solid-state Li-Ion batteries are expected to increase the energy density of current Li-Ion by up to three times. Advanced Li-Ion can eventually yield energy densities of 300-350 Wh/kg [33]. It should be noted that the improvements in lithium battery cell technology may eventually be able to compete with fuel cell system energy densities. Combinations of different battery cell technologies could then be used to have a mixture of high power density and high energy density cells, without the increased complexity of fuel cells and their balance of plant (BoP) requirements.

Power Density

In terms of power density, Li-Air shows very low values according to Girishkumar et al. [17] for experimental cells, not even remotely approaching the power density of state-of-the-art Li-Ion cell technology. Lithium-Ion batteries have a ranging power density depending on the exact cathode configuration, also discussed in Section 3.1.3, but can generally be discharged at high current rates and easily reach 1.5 kW/kg and higher.

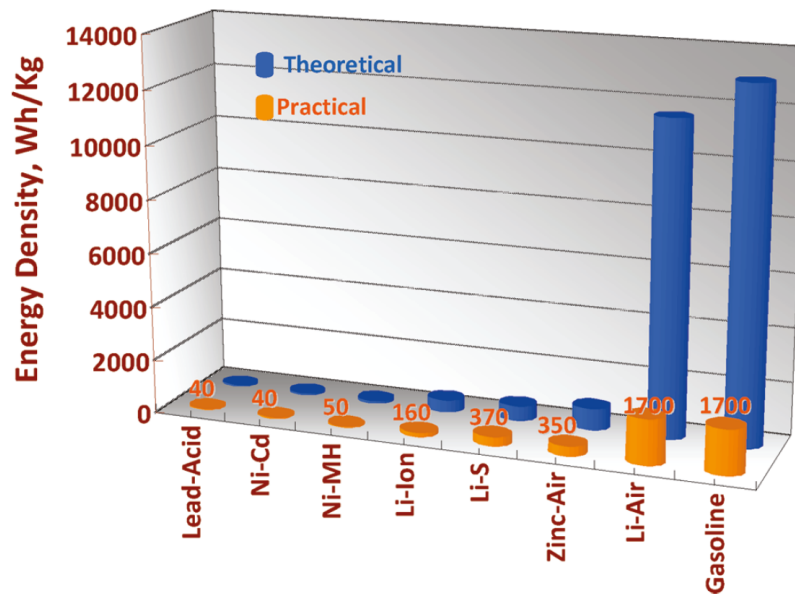


Figure 3.3: Energy density overview of battery technology [17]

The power density of the Oxis Energy (Li-S) cells is estimated at around 600 W/kg and 170 W/L based on their UltraLight Pouch Cell specifications [14], which is due to the relatively low maximum discharge rate of 2C. Li-Ion cells are generally capable of reaching much higher discharge rates and these Li-S cells are often tested at discharge rates below 1C. Li-Ion cells show that capacity is generally highest at low discharge rates. These characteristics will also be discussed in Section 3.2.

Volumetric Energy Density

The volumetric energy density is mainly important for volumetric constraints. According to Rahman et al. the Lithium-Ion volumetric energy density is approximately 650 Wh/L for state-of-the-art cells, whereas Li-Air has a volumetric energy density that is realistically much closer to 1,520-1,680 Wh/L [47]. For Li-S cells, this energy density is similar to Li-Ion cells at 600-800 Wh/L according to Sion Power and demonstrated around 200 Wh/L by Oxis Energy [14, 46]. Figure 3.4 shows the comparison between different cell types. For applications where volume is more limiting than weight, Li-S may not be the best solution.

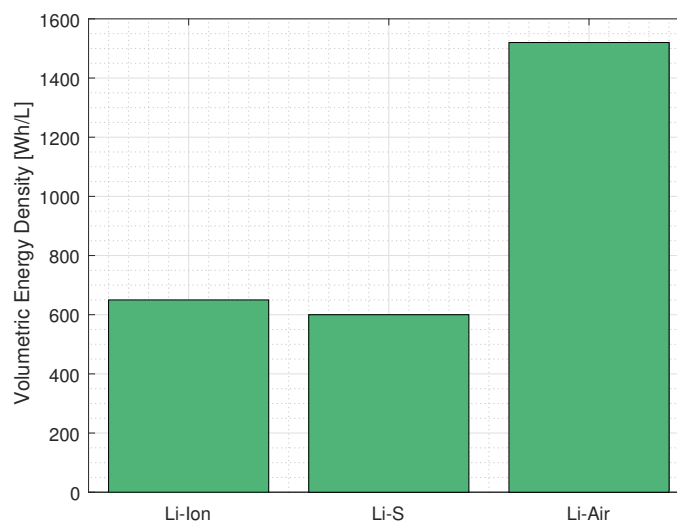


Figure 3.4: Volumetric energy density of Li-Ion, Li-S and Li-Air battery cells according to Rahman et al. (2014) [47]

Crystal Structure	Cathode Compound	Abbr.	Industry Code	Advantages	Disadvantages
Layered	LiCoO ₂	LCO	ICR	<ul style="list-style-type: none"> • High specific capacity • High nominal voltage • High volumetric capacity • Low self discharge 	<ul style="list-style-type: none"> • Thermal runaway risk • High Co cost • Low discharge rate • Capacity fade (high C/deep cycle)
Layered	LiNiMnCoO ₂	NMC	INR	<ul style="list-style-type: none"> • Good cycling performance • Lower cost (reduced Co) • High discharge voltage 	
Layered	LiNiCoAlO ₂	NCA	-	<ul style="list-style-type: none"> • Low self discharge • Lower cost of Ni (vs. Co) • High discharge voltage 	<ul style="list-style-type: none"> • High temp. capacity fade • Thermal runaway risk
Spinel	LiMn ₂ O ₄	LMO	IMR	<ul style="list-style-type: none"> • Mn cheaper than Co or Ni • Mn less toxic than Co or Ni • High discharge voltage 	<ul style="list-style-type: none"> • Poor cycle performance
Olivine	LiFePO ₄	LFP	IFR	<ul style="list-style-type: none"> • High thermal stability • High discharge capability • Flat voltage discharge curve • High cycle life 	<ul style="list-style-type: none"> • Lower average potential • Limited energy density
Spinel	Li ₄ Ti ₅ O ₁₂	LTO		<ul style="list-style-type: none"> • Superior thermal stability • High discharge rate • High volumetric capacity • High cycle life 	<ul style="list-style-type: none"> • High cost of Ti • Low energy density • Low nominal voltage

Table 3.1: Overview of Li-Ion naming and qualitative list of advantages/disadvantages. The table contains summarized information from [40]

3.1.3. Lithium-Ion

Lithium-Ion batteries are well established and already widely used in the mobility industry. Very popular high energy density cells are 18650, indicating the dimensions of a cylindrical cell. It is important to recognize that there is a range of cathode configurations, which have also been industrialized. There are major differences between these cells and specific characteristics such as high power density - often the result of a high maximum discharge rate - can be advantageous in a hybrid powertrain where batteries are used for relatively short peak power phases.

Recent developments in Li-Ion technology are mainly in the development of commercial intercalation materials which dictate the cathode compound. These consist of Lithium Cobalt Oxide (LCO), Lithium Nickel Cobalt Manganese Oxide (NCM), Lithium Nickel Cobalt Aluminium Oxide (NCA), Lithium Iron Phosphate (LFP) and Lithium Titanium Oxide. Different intercalation cathodes will have an effect on the properties, but also the cost as for example manganese (Mn) is much cheaper than Cobalt (Co) or Nickel (Ni). The NCA cathode has been commercialized successfully by Panasonic and is widely used in Electric Vehicles by e.g. Tesla for its high discharge capacity [40], while still yielding a high gravimetric energy density. Table 3.1 shows a qualitative overview of the advantages and disadvantages of the different types.

In general the layered type of cathodes show a higher degree of thermal instability. Storage life of for example NCA is better than spinel type such as LMO. Layered cathodes (LCO, NCA and NMC) generally show relatively high energy and power densities. However, spinel crystal structures potentially possesses higher operating voltage and higher discharge rate capability as well as thermal stability. Battery cycle life is however a weakness for spinel crystal structures [7].

LCO batteries were one of the first commercially introduced but have some major disadvantages such as: High Co cost, high capacity fade at high current rates and mainly low thermal stability [40]. The latter makes it more dangerous to use, which is increasingly important for aerospace applications. The LCO battery type has the lowest thermal stability, which will result in thermal runaway when the cathode is heated above a certain point. This makes the battery more dangerous to use and the discharge rate is limited. In the aviation industry reliability is extremely important. Thermal runaway occurred in the Boeing Dreamliner 787 planes in 2013, grounding the aircraft for a long time [74]. The LCO type has reasonably good performance but will always be a high risk option due to thermal runaway in the electrolyte. However, it should be noted that the NCA type shows only minor improvements over LCO in terms of thermal runaway and is still commonly used

in the automotive industry, indicating improved battery management.

As can be seen in Table 3.1 the different battery types have its own characteristics. Trade-offs have to be made between cycle life, energy density, power density (maximum discharge rate or C-rating) and thermal stability. The latter means that LCO is not a recommended option for aviation considering its higher risk of thermal runaway. Another significant consideration is lifetime cost, which depends on both material - or cathode compound - and the cycle life. The main aim of electric vehicles (EVs) and the usage of alternative energy storage is a CO_2 reduction to reduce the global warming potential. The risk here is a lack of acknowledgment of the environmental intensity of EVs, resulting in a problem shift from the road to a finite number of facilities in the production chain but also a potential of pollution within production chain [21], e.g. lithium mining.

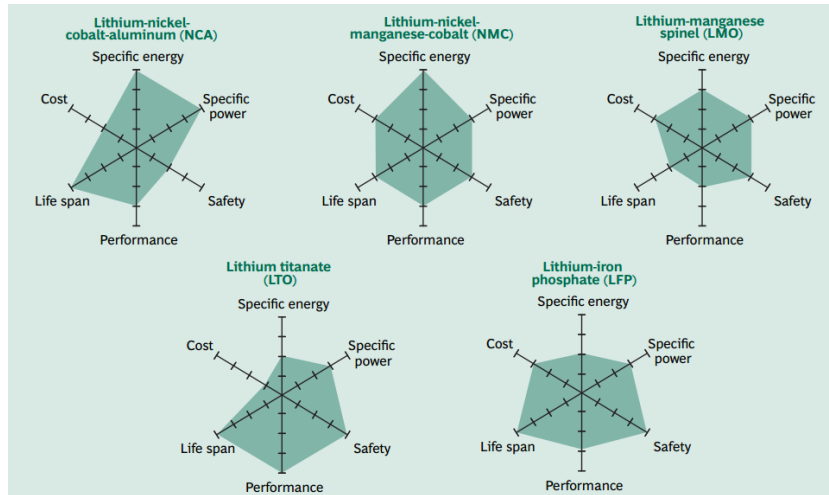


Figure 3.5: Battery Trade-off Overview [11].

A trade-off between batteries can be seen in Figure 3.5 [11]. Comparing this to the advantages and disadvantages shown in Table 3.1 the following remarks can be made. Both indeed show the low safety of NCA, which is similar to the original LCO Lithium-Ion battery, caused by a higher thermal instability. A higher Cobalt (Co) content also shows a generally higher price which is improved with the much cheaper Manganese (Mn), making LMO and NMC cheaper. The Titanium (Ti) in LTO results in a high cost of the battery, but high safety. LFP also performs well on high safety as they both have superior thermal stability. The layered variants with Co contents all show worse thermal stability performance. At the same time, the specific energy of the batteries with Co content do show high specific energy and power. The poorer thermal stability properties of the layered (LCO/NMC/NCA) cells result in relatively low discharge rates. The cycle life is especially positive for LFP and LTO, where this is generally worse for LMO.

3.1.4. Lithium-Sulfur

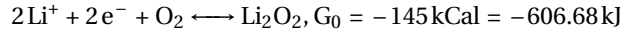
Main players in the Lithium-Sulfur (Li-S) battery technology are Fraunhofer-Gesellschaft, PolyPlus, Sion Power, Oxis Energy and Sony. Sion Power, as mentioned before has received major investments and has a partnership with Airbus. Their Li-S battery technology is used on the Zephyr 7, an Airbus project. Sion Power cells show gravimetric energy densities between 300 and 400 Wh/kg [46]. The exact characteristics of possible production cells are unknown. Limited discharge rates could potentially lead to reduced power densities and lower usefulness in combination with a fuel cell. However, the energy density of the cells will come closer to that of fuel cell systems.

3.1.5. Lithium-Air

Lithium-Air batteries are promising as they have a theoretical energy density of 5200 Wh/kg, taking into account the mass of the anode lithium and the cathode O_2 after discharging [47, 59]. Lithium-Air has a low Technology Readiness Level (TRL) as it is proven mostly in a laboratory setting, but has the most promising gravimetric energy density. Reports vary, with estimated specific energies of 1000-2000 Wh/kg, but generally a practical energy density of 1700Wh/kg is given. The specific power can range from 0.4-0.67kW/kg, which is lower than that of current state-of-the-art Lithium-Ion batteries [24, 68].

One aspect of Lithium-Air batteries is the mass gain that will occur while discharging the battery. The reason is that Lithium-Air batteries (or rather $Li - O_2$) require oxygen to collect on the cathode. For aircraft applications where mass is of significant importance, the degree of this mass gain should be understood as it

may impact performance and other aircraft design aspects. The mass increase can be based on [59], which in turn based its analysis on the research by Vegh et al. [68]. Here the Lithium-Air battery mass increase has been modelled according to the following reaction.



The reaction potential of Lithium- O_2 equals 3.1V [59]. The mass rate is given by Equation 3.1 and a change in mass over the entire period is given by Equation 3.3 [59, 68]. These equations are based on the electrons needed in the reaction.

$$\dot{m} = \frac{M_{\text{O}_2} \cdot P}{V_{0,\text{Li}_2\text{O}_2} \cdot F} = \frac{[\text{kg/mol}] \cdot [\text{W}]}{[\text{V}] \cdot [\text{C/mol}]} = \frac{[\text{kg}] \cdot [\text{A}]}{[\text{C}]} = \frac{[\text{kg}]}{[\text{s}]} \quad (3.1)$$

Here M_{O_2} is the molar weight of oxygen, P the power of the system, V_0 the reaction potential and F the Faraday constant in C/mol . Note that the charge can be represented by Equation 3.2.

$$Q[\text{C}] = I \cdot t \quad (3.2)$$

$$\Delta m[\text{kg/Wh}] = \frac{M[\text{kg/mol}] \cdot 3600}{V[\text{V}] \cdot F[\text{C/mol}]} \quad (3.3)$$

In this formula, M is the specific mass of oxygen and F is the Faraday constant which has the unit C/mol , representing the charge per mol electrons. V is equal to the reaction potential of Li_2O_2 . This allows for a mass increase estimate of the battery. Note that 3600 is to represent the energy over an hour, as the unit Coulomb for charge Q is Ampere-second (As).

The research done by Vegh et al. [68] investigated a gas turbine powered baseline aircraft with a payload of 114 passengers and a design range of 4400 km. The power system was then replaced by Li-Air batteries at 2000 Wh/kg. The gross take-off weight (GTOW) equals approximately 59.8 tonnes, whereas the maximum landing weight is 67.5 tonnes. The battery weight is 29.64% of the maximum landing weight, which is 20 tonnes. This shows that the battery weight increases from 12.3 to 20 tonnes during the flight, which is a 63% increase. The total aircraft weight therefore increases with 12.9% from take-off to landing, which is quite significant.

3.2. Battery Discharge Characteristics

This section will elaborate on some characteristics useful for sizing of the battery pack. This gives an overview of how batteries are generally evaluated. Figure 3.6 shows the discharge curves of a cylindrical battery cell [6]. It can be seen that the voltage drops as the cell is discharged. Due to the definition of the axes, the area under the curve is the energy content of the cell at a certain current. The axes can also be represented using State of Charge (SoC) or Depth of Discharge (DoD), which are normalized with the rated capacity. It can be seen that the capacity is reduced when discharge rate is increased. The discharge rate is often indicated by a C-rating, where the reciprocal of this rate indicates the time (hours) it takes to discharge the battery.

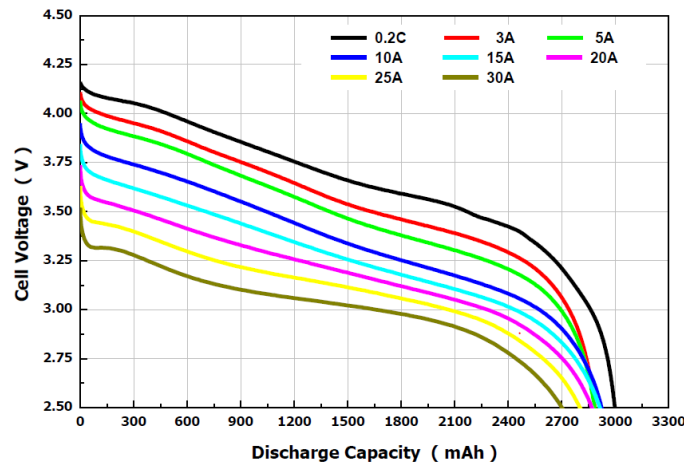


Figure 3.6: Constant current discharge curves of an LG-H2 18650 cell by LG Chem [6]

3.3. Battery Modelling Options

Batteries can be modelled with different levels of fidelity. A very low fidelity approach is using constant energy and power density for the sizing of the battery pack. When the battery is discharged, however, it was seen that the voltage drops and capacity reduces at higher discharge rates (Figure 3.6). This method could be slightly improved by using tabulated data, relating discharge rate to capacity and nominal voltage. For preliminary sizing and simulation purposes, empirical battery models are generally used.

Empirical Battery Models

Commonly, batteries are modelled through curve fitting of data obtained through experiments or from data sheets by the manufacturer. The latter is generally readily available for the majority of battery cells. Different models can be used for this purpose. One of them was used by Datta and Johnson and Vegh et al. [8, 68] and can be summarized by the following method.

For this method, two coefficients, the Peukert coefficient and the internal resistance need to be determined so that the model matches the battery considered. The Peukert coefficient is generally close to 1 (1.0-1.05) for Lithium-Ion batteries [8]. Peukert's law can be used to approximate the reduction in battery capacity with increasing current. Equation 3.4 shows parameter f which is a function of depth of discharge (DoD), which in turn is indicated by x . This is then used to determine the resistance of the battery as seen in Equation 3.5, where r_0 is a constant resistance and C is the C-rate, so the current as a fraction of the rated capacity. Equation 3.6 shows the discharge power of the cell at a certain DoD as the resistance r depends on the DoD.

$$f = 1 - \exp(-20x) - \exp(-20(1-x)) \quad (3.4)$$

$$r = r_0 \cdot (1 + C \cdot f) \quad (3.5)$$

$$P_{disc} = I^2 \cdot r \quad (3.6)$$

A more commonly used fitting model is Shepherd's model, which will be further elaborated on in the chapter on battery modelling, Chapter 12. The modified Shepherd's model will also be shown and is used by multi-physics simulations in SimScape Power Systems [64]. Verstraete et al. [70] proposed an addition to the original Shepherd's model, allowing the curve fit to be done for different discharge curves simultaneously. This should improve the simulation results for a larger range of discharge rates. This is the model chosen to be used for the modelling and simulation procedure and further elaborated on in Chapter 12.

3.3.1. Battery Model Simulations

The Shepherd's models are generally used for the curve fitting procedures. These are subsequently used for simulations. As mentioned before, the generic battery model in one of the multi-physics applications (SimScape Power Systems) uses Shepherd's modified model for curve fitting for a single discharge rate [64]. Other multi-physics software allowing for batteries and also fuel cells to be modelled and simulated are COMSOL or ANSYS. Because of access to SimScape Power Systems, as well as relatively top level simulation requirements, it was chosen to investigate the performance and usefulness of this model. Effects such as temperature dependence and aging are out of the scope of this study.

It will be shown that custom simulations are also possible and show improved results when a multiple regression curve fit based on the extension of Shepherd's original model by Verstraete et al. [70] is applied. It will also be shown that the fit of Shepherd's modified model within SimScape shows poor results, but that the simulation can verify the custom simulation code.

Chapter Conclusion

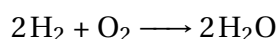
It was shown that Li-Ion cells are available in a wide variety of chemical configurations with different properties. Generally, the layered (crystal structure) Li-Ion cells are used for vehicular applications as a result of high energy density and relatively high discharge capabilities. For the modelling, the LG-HG2 cell will be used as it possesses these advantageous characteristics and discharge curves are widely available for Li-Ion cells. It was shown that energy density is quite limiting, while recognizing some potential towards and beyond 2030 with Li-S and Li-Air technology. Li-Air technology can change aircraft design procedures due to an increasing mass during discharge. As a result of high energy density, Li-Air is most promising for larger passenger aircraft. The main characteristics for the battery modelling are the capacity loss and reduced voltage at higher discharge rates. Chapter 12 will elaborate on the modelling procedure.

Fuel Cell Technology

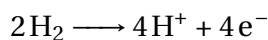
Fuel cell technology is a key part of this research. This goal of this chapter is to provide an overview of fuel cell system characteristics, Balance of Plant (BoP) and an overview of the technologies that could potentially be used for small aerial vehicle applications. Balance of Plant is a commonly used term for the additional components required in a fuel cell system.

4.1. Working Mechanism of Fuel Cells

This section provides a basic explanation of how fuel cells work. The details are different for the different types of fuel cells, but are in principle the same. An important part of the principle of fuel cells is that instead of combusting the fuel - often hydrogen - directly, the reaction is split up into two parts. The combustion reaction is shown in the following reaction.



By splitting up this reaction, it allows for creating useful electrical energy instead of heat. At the anode, hydrogen gas is fed and splits up into hydrogen protons, and electrons. On the other side of the electrolyte or proton membrane, the hydrogen proton reacts with the oxygen fed at the cathode to form water. This is shown with the following reactions. Different fuel cells will have alternative reactions at the anode and cathode but all have the same purpose. Figure 1.5 already showed a schematic of a proton exchange membrane fuel cell.



In fuel cells the above reactions take place in a single cell, consisting of the anode, cathode and electrolyte. Because the cells provide low voltage, they are generally connected in series through a bipolar plate. This is shown in Figure 4.1. This plate functions as a connection but also to feed fuel to the anode and oxygen to the cathode, making sure these flows are split up.

Fuel cells are far from 100% efficient and hence cooling is required, especially for low temperature fuel cell stacks such as low temperature proton exchange membrane fuel cells which are commonly used. Heat is released at the cathode where water is formed. This could be solved by running excess air through the cathode side. Liquid cooling is also a possibility and is especially preferred for power systems at higher power.

4.2. Fuel Cell Technologies

There is a wide range of fuel cell technologies available. They are mainly distinguished by their electrolyte material and operating temperatures [35], but also by the fuels used. For example, a direct methanol fuel cell (DMFC) directly uses the fuel without reforming processes. Also, some fuel cells allow a wider range of fuels to be used in the system as a result of their operating temperature and hence internal reforming capability. The main fuel cell systems are shown in Figure 4.2, but not necessarily limited to the types shown.

Other differences between the fuel cell types are the balance of plant (BoP) components needed to create a full system, efficiencies, typical system power range and application type. The fuel type is limited for fuel cells such as the PEMFC, where only hydrogen can be used. Variations of the PEMFC are DMFC and DFAFCs, which directly use methanol (CH_3OH) and formic acid (HCOOH) as fuels respectively.

The fact that some fuel cells, such as PEMFC, are limited to hydrogen only with very low or no carbon monoxide (CO) allowed, does not mean that no other hydrocarbon fuels can be used. Another option that is considered in the literature study is the option for reforming hydrocarbon fuels into hydrogen (and CO) which

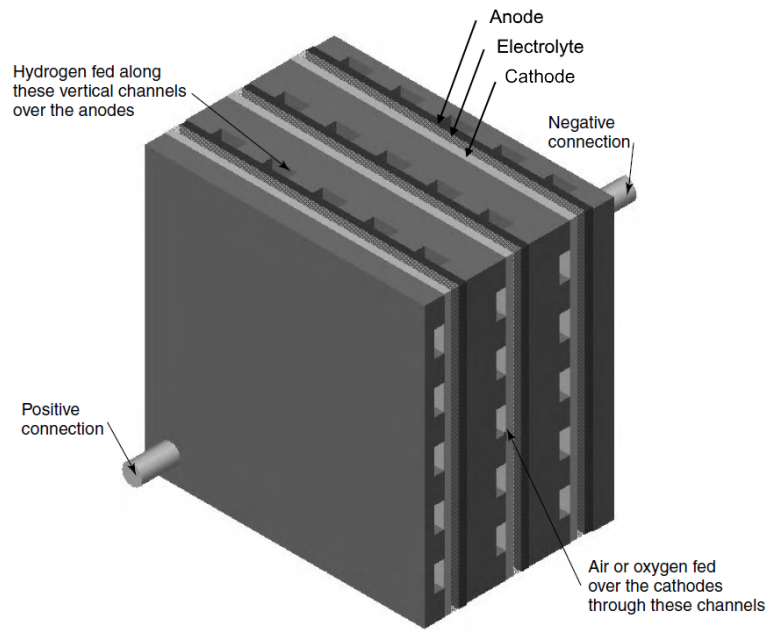


Figure 4.1: Fuel cell with anode, cathode, electrolyte and bipolar plates. Adjusted from [32]

can then be fed into the fuel cell system directly. Methane and methanol are popular fuels for this specific purpose, but other options could even be formic acid or fuels normally used in the combustion engine. An important consideration would be the cleaning of the fuel and added balance of plant (BoP) components and complexity. However, reforming options will be discussed in a later section. This means that instead of using DMFC or DFAFC, PEMFC could still be used with the same fuels, but adding a reformer.

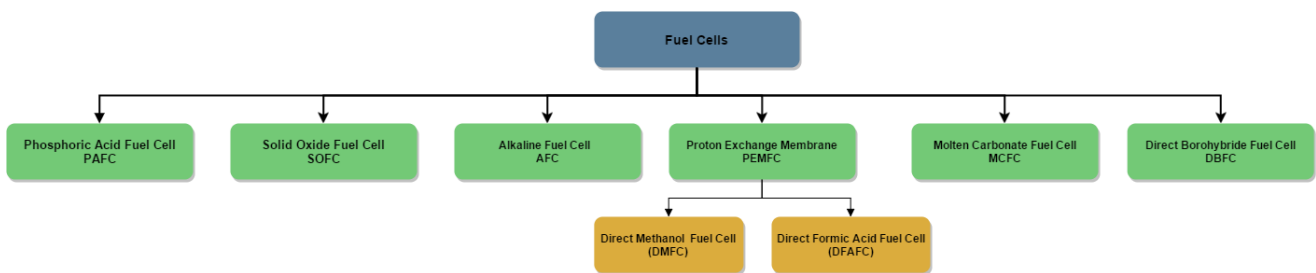


Figure 4.2: Overview of Fuel Cell types

4.2.1. Comparison of Fuel Cells

A direct comparison has been made for both a qualitative and quantitative overview of the state-of-the-art and applications of fuel cells. An overview of the main specifications is shown in Table 4.1. The main application areas as well as advantages and disadvantages are shown separately in Table 4.2.

Table 4.1 covers a number of specifications for each of the fuel cell types. These are fuel used, the mobile ions through the membrane/electrolyte, the operating temperature, power density on a cell and electrical efficiency. The latter is without using the exhaust heat for useful purposes, which can increase system efficiency. Also, additional systems will be needed to support the fuel cell stack, which take away useful power and hence reduce the fuel cell efficiency. Finally, the power range is indicated for the different fuel cells, so that the application options are known. Table 4.2 includes common application areas, advantages and disadvantages of the fuel cell types.

Type	Fuel	Mobile Ion	T[°C]	p [W/cm^2]	Electrical efficiency [%] [35]	Power Range
PEMFC	H_2	H^+	30-100 [32]	0.7+ [38]	40-50	0.05-100kW (LT PEMFC) [35]
			40-80 [20]			< 200kW (HT PEMFC) [35]
DMFC (sub-PEMFC)	Methanol (CH_3OH)	H^+	20-90 [32] 50-130	0.25 [38]	20-30	< 5kW [35]
DFAFC (sub-PEMFC)	Formic Acid ($HCOOH$)	H^+	Range of PEM/DM	0.1-0.375 [77]		Very low
SOFC	H_2 , CO and CH_4	O^{2-}	500-1000 [32] 600-1000 [20]	0.15-0.7 [38]	45-60	2kW-MW [32] 2.5-250kW, up to 100 MW [35]
			600-1000			
AFC	H_2	OH^-	50-200 [32] 65-220 [20] 65-220	0.1-0.3 [38]	45-60	1-100kW [35]
MCFC	H_2 , CO	CO_3^{2-}	~ 650 [32] 650 [20]	0.1-0.12 [38]	45-55	Up to MW [32] 100-2000kW [35]
			600-700			
PAFC	H_2	H^+	~ 220 [32] 205 [20] 150-220	0.14 [38]	40-45	5-200 MW [35]
DBFC	$NaBH_4$	Anionic (OH^-) or Cationic (Na^+)	20-85	-	30-40	10^{-3} - 0.5 kW [35]

Table 4.1: Specification overview of different fuel cell stack types

Type	Applications	Advantages	Disadvantage
PEMFC	Transport applications Quick start-up times HT PEMFC stationary [35] LT PEMFC vehicular / stationary [35] Fast load-following dynamics	Most researched low temperature fuel cell Quick start-up times because of low temperature Fast load-following dynamics [38] Robust	External reformer and water shift/purification to remove CO [20] External reforming requires heat and water input [20] Fuel limited to hydrogen if the aim is low BoP complexity [20] Narrow temperature range [20] Hard to use rejected heat for cogeneration [20]
DMFC	Portable [35]	Can use methanol directly, no steam reforming such as for PEMFC Reduced fuel (storage) weight compared to a gaseous hydrogen fuel Methanol has an energy density of 4900Wh/L [77]	Reduced electrical efficiency due to methanol crossover [60] No larger systems (<5kW)
DFAFC	Portable systems [77]	High electromotive force (EMF) / open circuit voltage of 1.48V [77] Limited crossover membrane compared to DMFC [77]	Volumetric energy density limited at 2104Wh/L [77] Low power density [77]
SOFC	Stationary [20, 35] Mobile Power [20] Auxiliary Power (APUs) [20]	CO useable in fuel No CO ₂ requirement cathode as with MCFC [20] Potentially high system efficiency of ca. 70 % [20]	Costly materials at high temperatures [20] Corrosion of stack components [20] Limited power density due to disadvantages / reduced thermal cycling and stack life [20]
AFC	Space [35] Naval [35]	Proven in space applications Excellent performance on hydrogen fuels [20]	Air and fuel supply must be free from CO ₂ [32] Requires external reformer and purification to remove CO and CO ₂ trace [20] External reforming requires heat and water input
MCFC	Stationary [35]	High efficiency with hydrocarbon fuels [20] Rejected heat can be used for reforming and cogeneration [20] (Partial) Internal reforming [20] CO directly useable as fuel [20]	Demonstrated most extensively in stationary applications [20] Corrosive nature of electrolyte [20] High temperature limits material choices [20] CO ₂ requirement cathode for ion requires extra BoP [20]
PAFC	Stationary [35]	Easy water management [20] Less sensitive to CO than PEMFC and AFC, reformate allowed with up to 1-2 % CO [20, 38] Waste heat can be used for cogeneration [20]	Mostly used for stationary applications [20] High corrosive nature of PA requires expensive materials [20]
DBFC	Portable [35]	High OCV Non-precious metals (no need for Pt catalysts) [35]	Relatively low efficiency and low power applications [35]

Table 4.2: Fuel cell types, their applications and strength and weaknesses

4.2.2. Market Forecast

It is important to have an estimate of the market forecast to consider if it makes sense pursuing a certain technology. Figure 4.3 shows a market forecast [49] for some major fuel cell types, where PEMFC and SOFC deserve the most interest due to a relatively high TRL of PEMFC and potential of SOFC in LPA. A large increase in the fuel cell market can be seen until 2025 for both PEMFC and SOFC and it is therefore likely that R&D for these types is large too.

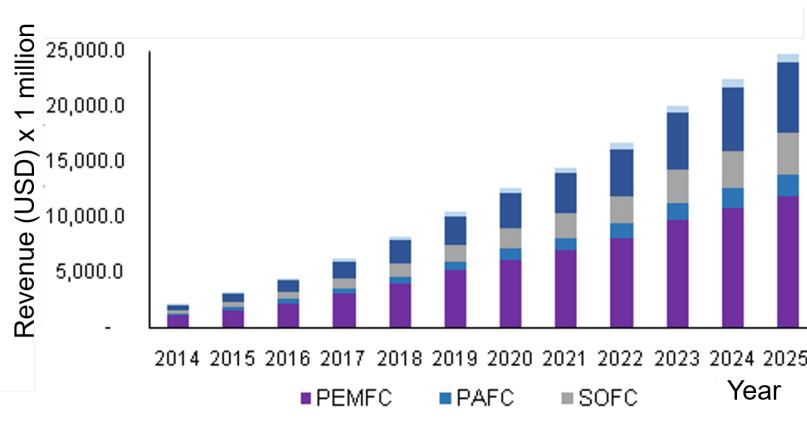


Figure 4.3: Global fuel cell market revenue by product, 2014 - 2025 (USD Million). Adjusted from [49]

4.2.3. System Performance Indicators

This subsection indicates the performance characteristics of fuel cell systems with a focus on low temperature PEMFC as these are the most researched and used in vehicular applications. Hence these systems deal with the largest mass and volume constraints and relatively lightweight, high energy density systems are available. Other fuel cell types are generally used in large stationary applications or only available at a very low power output.

Good system performance indicators are, just as discussed for batteries, gravi- and volumetric energy density (Wh/kg and Wh/L) and power density (W/kg and W/L). In terms of energy density the LHV indicates a theoretical maximum energy density of hydrogen of about 33kWh/kg, compared to 12.8kWh/kg of kerosene. However, the actual fuel cell system energy density is much lower. The main reason is that the only energy containing subsystem is the storage mechanism, which is for compressed gas at 350 or 700 bar about 15-20 times heavier than the hydrogen itself, also see Section 4.5. This already reduces the theoretical maximum energy density to about 2kWh/kg. Depending on the power needed from the fuel cell stack, of which the power density can potentially reach about 2kW/kg, the energy density is further reduced as weight is added. Other components to run the fuel cell called the balance of plant components (BoP), such as compressors, pumps, valves, humidifiers, pressure regulators and cooling system will further increase mass and reduce the energy density. This therefore depends on the system maximum power output and the percentage of weight going to the hydrogen storage subsystem.

Literature hence shows different values for the energy densities as it is fully application specific, but an example is provided by Guida and Minutillo [18]. This design was aimed for a solution where 24kW of power was needed for 6 hours, with a weight of less than 400kg at 3km altitude. The final solution weighed 282kg with an energy density of 0.51kWh/kg. It should be noted that NLR has lightweight compressor designs that are lighter than the ones considered here. Also, because of the 6-hour duration at 24kW, the storage tank weight is relatively high. The fuel cell used for this analysis has a specific power of 0.4kW/kg, already including air cooling elements, whereas an extra cooling unit is included. Other commercial fuel cells show up to 2kW/kg for the fuel cell stack alone and hence there is potential to be gained here. Furthermore, it may not be optimal to fly at a 3km altitude for fuel cell powered aircraft, possibly reducing compressor power. Another critical point is that extra small components have not been considered, even though they may weigh more than the hydrogen or batteries.

Figure 4.5 shows the specific energy of the system at different runtimes, clearly showing that energy density goes more towards storage energy density as the tank grows. For very short flights, current state-of-the-art lithium batteries will be competitive in terms of energy density. In the case of Guida and Minutillo [18], the calculations were made for a power requirement of 24kW. Batteries will be less competitive if the power requirement is reduced as the size of components not containing energy will be reduced. It also, however, shows that future advanced Li-ion or Li-S batteries can be very competitive as the blue line in Figure 4.5 will move up beyond 300Wh/kg. Power density of the system is also always lower than the power density of the

fuel cell stack, because the balance of plant components do add weight and reduce output power. Considering the 24% mass contribution of the fuel cell stack in this example, the power density is about 0.1kW/kg and is therefore very low when compared to batteries.

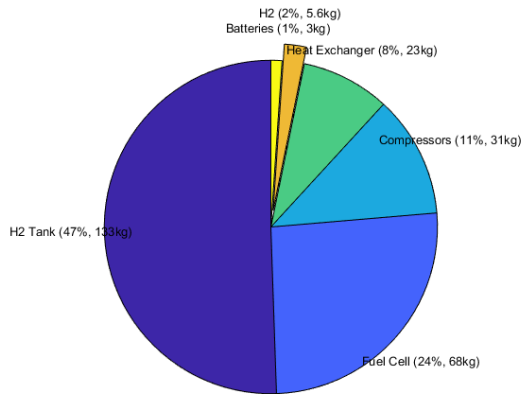


Figure 4.4: Weight percentage with respect to the system weight. Pie diagram based on tabulated data from [18]

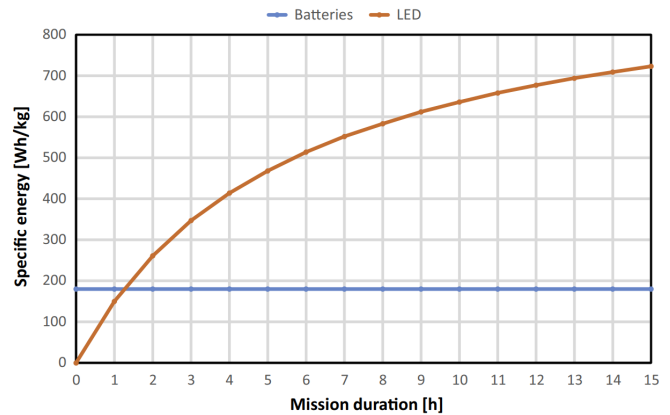


Figure 4.5: Specific energy vs. mission duration: comparison between the Long Endurance Demonstrator (LED) and a LiPo battery system [18]

4.2.4. Proton Exchange Membrane and Solid Oxide Fuel Cells

The two fuel cells with relatively high maturity level are PEMFC and SOFC. PEMFCs are low temperature fuel cells and SOFC high temperature fuel cells [12]. PEMFC runs on pure hydrogen and SOFC is capable of running on hydrocarbon fuels with the need for pre-reforming and reforming to ensure H_2 and CO at the anode. System components will be quite different due to the different balance of plant requirements and the operation of SOFC on other fuels. In a PEMFC the outlet gas can hardly be used effectively to increase system efficiency, whereas the SOFC with its high temperature operation can use the excess heat to increase system efficiency. The SOFC shows large advantages when used in combination with gas turbine components as it has many advantages when used with hydrocarbon fuels. Because the SOFC heat can be used for external (pre-)reforming but also to drive a turbine, this is generally the preferred fuel cell type for gas turbine hybrid systems when the fuel cell is used for non-propulsive purposes.

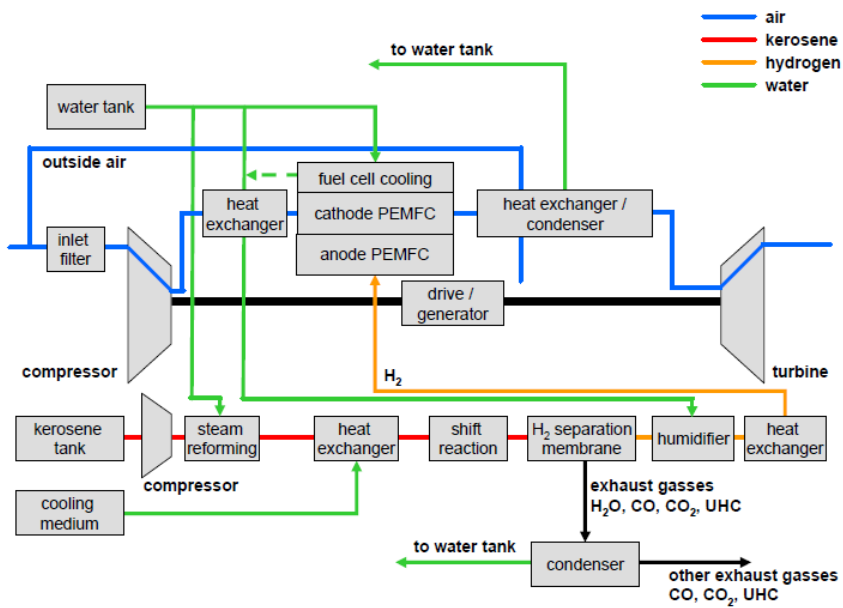


Figure 4.6: Kerosene based PEMFC hybrid (gas turbine) schematic [12]

Balance of Plant components would be much less extensive in case of the SOFC as can be seen in Figures

4.6 and 4.7 [12]. According to Eelman et al. efficiencies in such hybrid systems (although for APUs) can yield >75% for SOFC-based systems and >40% for PEMFCs. SOFCs are best applied where slow dynamics and start-up times are not critical and if the usage of hydrocarbon fuels is preferred [38].

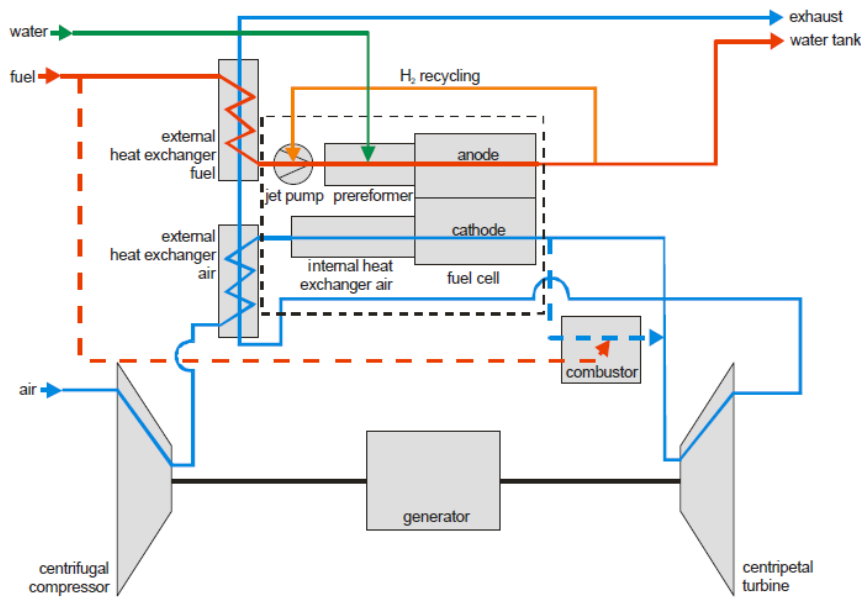


Figure 4.7: Kerosene based SOFC hybrid (gas turbine) schematic [12]

4.2.5. High Temperature Fuel Cells

The advantage of high temperature fuel cells, such as SOFC and MCFC, is that they can do internal reforming of hydrocarbon fuels at the operating temperature. SOFC uses a combination of H_2 and CO as the fuel at the anode. Figure 4.8 shows the cell voltage as a function of temperature of different fuel cell types. High temperature fuel cell systems have in essence a lower reversible cell voltage at their operating temperature, indicating that the fuel cells have lower efficiency. The main reason is that if the reactants inflow (so fuel and air) remains the same, the flow of electrons and current does not change and hence the power output (and thus work) reduces at higher temperature. An important consideration here is, however, that the actual voltage is determined based on losses (polarization) once a load is applied and there is no more open circuit potential. When current is applied, resistance inside the fuel cell will reduce the practical voltage. The resistance usually goes down as temperature goes down, meaning that ohmic losses in the fuel cell are lower for high temperature fuel cells. This means that even though the potential is lower, the actual practical cell voltage is similar for low and high temperature fuel cells. Cell voltage is highly dependent on temperature for the different fuel cells, see Figure 4.8. Activation losses are almost negligible or at least very low for SOFC, as these losses are due to reaction rates.

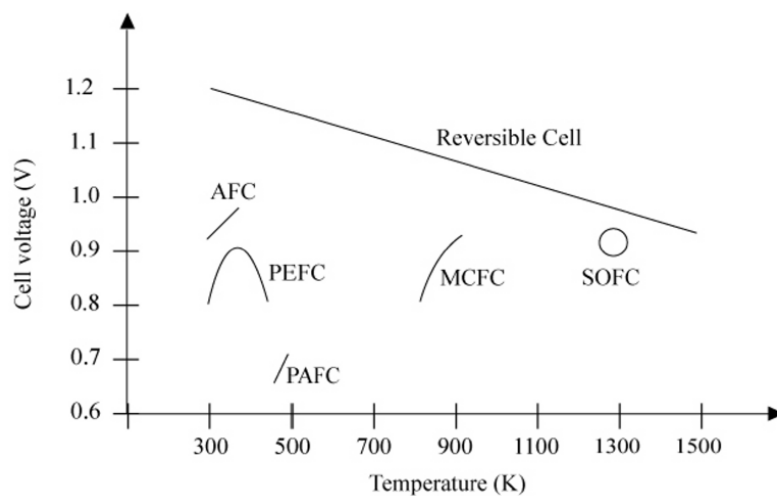


Figure 4.8: Comparison of reversible and practical cell voltage for different fuel cell types within their operating temperature range [45]

Because of the high temperature of the SOFC, a promising concept for larger power systems is a hybrid of SOFC fuel cells and a gas turbine [48]. The main focus here is the usage of this combination for operating the APUs. The high temperature exhaust can be used to drive the turbine which in turn drives the necessary compressors to supply compressed air to the fuel cell system. Furthermore, the exhaust heat can be used for endothermic reforming processes depending on the fuel type used for the fuel cell.

4.2.6. Low Temperature (LT) and High Temperature (HT) PEMFC

In the recent years, there has been a lot of research on a membrane that can replace the Nafion membrane used in current commercial PEMFC. Even though the most researched fuel cell is the low temperature PEMFC (LT-PEMFC), the increasingly researched option is a high temperature PEMFC (HT-PEMFC) which uses this new membrane. Where LT-PEMFC generally operate below 100°C, HT-PEMFC operate at temperatures that range from 120-200°C. Rosli et al. reviewed the HT-PEMFC based on vehicular system requirements [51], as reliable power production, high durability and steady-state and transient operation are important for this exact purpose.

One advantage is that no humidification is necessary for the HT-PEMFC compared to its LT version. LT-PEMFC generally uses a Nafion membrane with a hydrophobic base and water is needed as a transport carrier of the proton. Humidification of the membrane is therefore always needed to reach optimal performance. This adds complexity and weight to the system in the form of a humidifier. Some systems have self-humidification, as the water that is formed in at the cathode can be used for this. Too little water will reduce conductivity and increase cell resistance. The Nafion membrane restricts the temperature to the range of LT-PEMFC as it is very sensitive to moisture levels, say Rosli et al. [51]. Heat is needed for the reaction speeds, but a higher temperature will dry up the membrane. Some obstacles of LT-PEMFC are humidification and the production cost of high purity H_2 - which is needed to prevent anode catalyst poisoning. Rosli et al. (2017) mention that HT-PEMFC is still in early development.

One major aspect is the increased CO tolerance of HT-PEMFC, allowing for hydrogen production to be much simpler using for example steam reforming of methane. Where tolerance to CO is in the parts per million range for LT-PEMFC, HT-PEMFC allow for operation on hydrogen with a much higher percentage of CO. This can be seen in Figure 4.9. This higher tolerance reduces production cost of hydrogen but this does not conform to a zero-emission approach. However, it is then possible to use this HT-PEMFC system in hybrid aerial vehicles in which hydrogen is produced within the vehicle (from the already available hydrocarbon fuel) and the excess heat from the HT-PEMFC can be used to increase overall system efficiency.

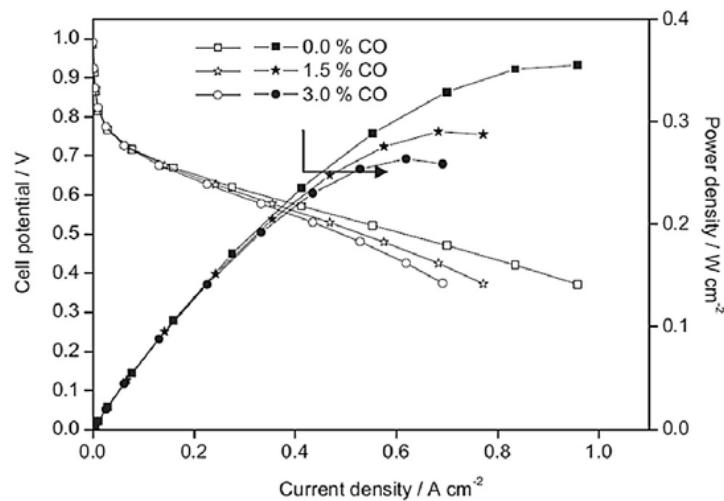


Figure 4.9: CO tolerance of a HT-PEMFC at 160°C [51]

Taking into account the electrical efficiency of PEMFC, which is similar for HT-PEMFC at ~50%, a cooling system is needed. Given the higher operating temperature, the difference in temperature between the stack and the ambient should be much larger and therefore easier to cool. LT-PEMFC may also require heating elements for effective operation as exhaust heat is hard to use effectively for maintaining stack temperature. Furthermore, at high compression ratios the air temperature at the compressor outlet may be closer to the operating range of HT-PEMFC, reducing the need for cooling of this air inflow. The exhaust heat of a HT-PEMFC is also more useful for other purposes in a combined heat and power system. It is expected that the start-up time and transient response of the HT-PEMFC will be slower, encouraging FC systems with batteries for start-up and fast response peak powers.

4.3. Balance of Plant (BoP) Components

Balance of Plant (BoP) is used as terminology for the fuel cell system hardware required on top of the hydrogen storage and the fuel cell stack itself. This balance of plant consists of multiple elements which either increase system mass or the power requirements and therefore reduce efficiency, energy density and power density. BoP is needed for smooth and proper operation of the fuel cell and hence consists of systems that support the fuel cell stack. The pressure of the reactant gases for example influences the fuel cell performance and hence an air compressor is often included to improve the performance. The next sections discuss some of the larger components, such as humidifiers, compressors and the cooling system. However, other components seen are, but not limited to, pumps, blowers, pressure regulators and reformers. The fuel storage tank - often for gaseous hydrogen - can also be included in the BoP. It is important to understand the system requirements, although some fuel cell stacks in industry include cooling and self-humidification.

4.3.1. Humidifier

In the case of a PEM fuel cell the polymer electrolyte membrane works better if it is kept humid. Hence humidifiers are a necessity for better operation. It was shown before that HT-PEMFC may not require a humidifier. The humidification process can consist of water or steam injection. In some cases self-humidifying stacks are also found for LT-PEMFC. According to Barbir [1] the reactant gases are required to be saturated at the cell operating temperature, requiring both water and heat. The United States Department of Energy (DoE) provides a list with the status and 2020 targets of air compression and humidifier membrane targets, including their weight and volumes [43]. This is based on the automotive fuel cell system status in 2015 and the expected status of 2020. Table 4.3 shows humidifier specifications according to the U.S. DoE [43]. These values can be used for conceptual and preliminary sizing when the stack used in the sizing is not self-humidifying.

Characteristic (80kW System)	2015 Status	2020 Targets	Units
Maximum operating temperature	110–125	> 95	[°C]
Maximum pressure differential between wet and dry sides	0.75	0.75	[bar]
Maximum pressure drop at full flow (each side)	< 0.03	0.035	bar
Water transfer at full flow	7.4	5	[g/s]
Maximum air leakage at full flow	0.5	0.5	
Volume	4.3	5	[L]
Weight	2.7	5	[kg]
Humidifier membrane water transfer flux at full flow	> 0.03	0.025	[g·min ⁻¹ ·cm ²]

Table 4.3: DoE humidifier status and forecast for 2020 [43]

4.3.2. Compressor

The compressor is an important component for the fuel cell stack. Fuel cell stacks can operate under atmospheric properties but at elevated altitude the performance will decrease. The performance of a fuel cell stack can be improved by having elevated stack pressure. A solution is the usage of a compressor, which is driven by a motor requiring power. Also, a compressor adds weight to the system. Generally, stacks are compressed up to 2-3 bar [1, 32], but its usefulness depends on the system parameters. An expander can be used [8] to offset some of the power requirements for some compressor configurations.

Table 4.4 summarizes the status of compressors used in fuel cell systems according to the U.S. DoE [43]. These values can be used in any sizing process, although decisive factors for exact compressor sizing will be stack operating pressure, stoichiometry and the needed deviation from stoichiometric conditions for continuous and efficient operation - which is generally 2 for air. Compressor efficiency is an important indication for component selection in terms of power and weight requirements. The overall efficiency can be split up into a multiplication of motor and controller efficiency and isentropic efficiency as seen in Equation 4.1.

$$\eta_{comp} = \eta_{m+c} \cdot \eta_{isentropic} \quad (4.1)$$

It is important to keep these efficiencies separate. The motor will heat up depending on its efficiency, but the isentropic efficiency has a direct effect on the temperature change of the air through the compressor.

80kW (stack) Compressor with Motor and Motor Controller Characteristic	Without Expander		With Expander		Units
	2015 Status	2020 Target	2015 Status	2020 Target	
Input power at 100% flow	17.3	14	11	8	[kW]
Combined motor/motor controller η	80	90	80	90	[%]
C-E η 100% flow	73	80	71	75	[%]
Input power at 25% flow	3.3	2	2.3	1	[kW]
Combined motor/motor controller η 25%	57	80	57	80	[%]
C-E η 25% flow	64	70	62	65	[%]
System Volume	15	15	15	15	[L]
System Weight	22	15	22	15	[kg]

Table 4.4: Compressor-Expander Department of Energy (DoE) technology status and targets for 2020 for a 80kW PEMFC equivalent system [43]

4.3.3. Cooling System

The cooling system inside the powertrain is necessary for cooling different elements in the powertrain. Detailed cooling design is out of the scope of this study, therefore this section gives an overview of common cooling schemes. The biggest system that requires cooling is the fuel cell system, as its electrical efficiency is at about 50%. Depending on ambient temperature and the pressure ratio of the compressor, air may have to be cooled in a LT-PEMFC as it may be at a higher temperature than the stack pressure. The compressor motor also requires heat to be removed and requires cooling. Batteries and power electronics also require some degree of temperature management. Often applied cooling schemes for the fuel cell stack are given by Figure 4.10 [1]. For larger systems, liquid cooling is generally a preferred approach [32].

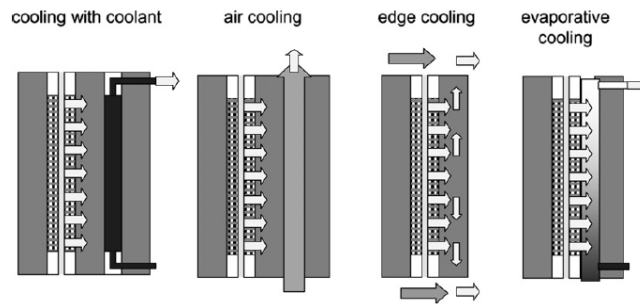


Figure 4.10: Cooling schemes of fuel cell [1]

The generated heat in a PEMFC can be approximated using Equation 4.2, where c is 1.482 when water leaves the stack as pure water at 25° and 1.254 when it leaves the stack as vapor. An energy balance is needed for further analysis, as part of the heat can be dissipated through natural convection. When a cooling design method is added in future studied, it should be noted that the pumps needed for the active cooling require power from the fuel cell. The following sections briefly explain the schemes of Figure 4.10.

$$Q_{gen} = (c - V_{cell}) \cdot I \cdot n_{cell} \quad (4.2)$$

Natural Convection

Some heat is dissipated through natural convection, largely dependent on the fuel cell stack outside surface area. Barbir [1] notes that for small stacks, the surface area ratio A_s/A_{act} (external over active cell area) results in more dissipation than heat generation at high ratios, making it difficult to even reach the fuel cell stack optimal operating temperature.

Air Cooling

Air cooling is generally performed at applications with low power output. An approach that could theoretically easily be performed in this case is increasing the mass flow over stoichiometry so that unused air molecules can transport the heat away from the system. Barbir shows that stoichiometry ratios of approximately 20 would be needed as compared to 2 for smooth operation of the fuel cell. This causes drying of the anode and its relative humidity can be calculated at the outlet of the fuel cell. For a normal operating range, Barbir shows [1] that relative humidity is about 10% making air cooling not feasible in this way.

Evaporative Cooling

Another option Barbir [1] specifies is evaporative cooling. Barbir notes that it is possible to calculate the exact amount of water and air flow rate needed to achieve saturation conditions at the outlet. This could then provide enough cooling for the stack.

Edge Cooling

Where most cooling methods have out-of-plane conduction at the bipolar plates, edge cooling uses in-plane conduction to the sides. The conduction of bipolar plates is critical for this cooling method. Typically this is only used for low power applications because heat transfer is limited. Barbir specifies that this may only be possible if the fuel cell flow field is made narrow enough [1]. A combination of dissipation through natural convection, air and liquid cooling (which requires separate channels) but also evaporative cooling may be applied.

4.4. Fuel Cell Stack Design Characteristics

One of the most important aspects of the fuel cell stack is the polarization curve, which relates the current to the voltage for steady-state behaviour. It is important to make a distinction between static and dynamic behaviour, especially in a hybrid powertrain configuration when the fuel cell is combined with batteries. Fuel cells have a relatively slow response to large changes in required electric load, whereas batteries are almost instantaneous. Batteries can therefore also be used to overcome the slow transient response of the fuel cell.

4.4.1. Nernst Equation and Limitations

The ideal performance of a fuel cell can be represented in different ways. A common way to define the ideal performance is based on the Nernst potential, which is represented as the cell voltage. The ideal performance can be modelled for a range of pressures and temperatures when the ideal potential is known for standard conditions. Fuel cell performance is generally improved with increasing temperature or pressure. The Nernst Equation can also be used when hydrocarbon fuels are used and therefore the ideal performance of different fuel cell types can be obtained. The influence of temperature is more pronounced for high temperature fuel cells than it is for low temperature fuel cells such as PEMFC. Equation 4.3 is the nernst equation, providing a theoretical basis for the open circuit voltage and an indication of fuel cell performance for a number of variables. Here P is the system pressure and α , β and δ indicate partial pressures of hydrogen, oxygen and water.

$$E(V) = E_0 + \frac{RT}{2F} \ln \left(\frac{\alpha \cdot \beta^{\frac{1}{2}}}{\delta} \right) + \frac{RT}{4F} \ln(P) \quad (4.3)$$

Fuel cells however deviate from this theoretical EMF or ideal voltage with increasing current potential. Electrical energy can only be output from the fuel cell when a current is drawn, but the cell potential is lowered from the equilibrium potential due to irreversible processes. These losses are called polarization or over potential and can be split up into the four loss mechanisms below. The current loss is not always considered [45], but is considered in the analysis by Haji [19].

- **Loss Mechanism 1:** Activation Losses in the low current region,
- **Loss Mechanism 2:** Ohmic Losses
- **Loss Mechanism 3:** Concentration losses which become more prominent at large current densities as gas reactant flow finds it hard to reach reaction sites
- **Loss Mechanism 4:** Loss due to internal current leakage, hydrogen crossover and unwanted side reactions (current loss) [19]

These losses can be approximated using relevant equations and are all proportional to the current (density). This proportionality ($\propto I$) and the estimation relations can be used to fit a curve with the theoretical relationships based on experimental results. These experimental results can often be found on data sheets and the fitted curve can be used for analytical purposes, for example in an optimization process. The activation loss is calculated using the Butler-Volmer equation and can be reduced to the Tafel equation for larger overpotentials (or large activation losses). Equation 4.4 indicates the Tafel equation for the activation losses at low current density. The activation losses are less prominent or not visible for high temperature fuel cells, such as Solid Oxide Fuel Cells (SOFCs).

$$\Delta V_{act} = \frac{RT}{\alpha \cdot n \cdot F} \cdot \ln \left(\frac{i}{i_0} \right) \quad (4.4)$$

In this equation, R is the universal gas constant, T the temperature, α the charge transfer coefficient and n the number of electrons involved. Furthermore, F is the Faraday constant, i the current density (A/cm^2) and i_0 the exchange current density. The second loss mechanism are the ohmic losses and follow Ohm's law. The voltage loss is hence due to the resistance of current flow (mainly limited to ion flow through electrolyte) and can therefore be represented by Equation 4.5, where R_{ohmic} is the total cell resistance (Ωcm^2) and i the current density (A/cm^2). This part of the losses hence shows a linear relationship.

$$\Delta V_{ohmic} = i \cdot R_{ohmic} \quad (4.5)$$

The third of the main loss mechanisms is the concentration loss. These occur over the full range of current densities but become more prominent and visible at the upper end of the current density, close to the limiting current density i_L . Equation 4.6 is generally the representation of these concentration losses, but is often replaced by an empirical, exponential term. This semi-empirical model will be shown in Section 4.6.1.

$$\Delta V_{con} = \left(\frac{RT}{nF} \right) \cdot \ln \left(1 - \frac{i}{i_L} \right) \quad (4.6)$$

The fourth loss was modelled by Haji [19] and indicated as a so-called current loss, causing a shift in current density. This is generally not taken into account in the modelling of steady-state behaviour.

4.4.2. I-V Characteristics: Polarization Curve

The polarization as discussed is the potential of the fuel cell after considering activation, ohmic and concentration losses. A fourth loss - the current loss - consisting of internal current leakage, hydrogen crossover and unwanted side reactions was considered by Haji [19].

The polarization curve is part of the static behaviour of a fuel cell and is often used for the sizing of the powertrain for its applications. The dynamic behaviour is especially important when large variations in power are present as the fuel cell transient response is relatively slow [39, 69, 70]. However, when the fuel cell is designed to operate at a nearly constant power level, the dynamic behaviour is less significant for PEMFCs. PEM fuel cells have a transient of approximately half a minute.

Figure 4.11 shows an example polarization curve with constant cathode gas temperature. This was obtained from testing a fuel cell stack (FC-42 by Schunk) and slowly increasing the current by adjusting the hydrogen flow [39]. It shows the maximum power at point I occurs at a relatively high current. Note that the hydrogen mass flow will be proportional to the current (or $I \propto \dot{m}_{H_2}$) as the fuel cell requires the electrons that are freed when the hydrogen reacts at the anode side. More on the effects of stoichiometry and efficiency will be discussed in the following sections.

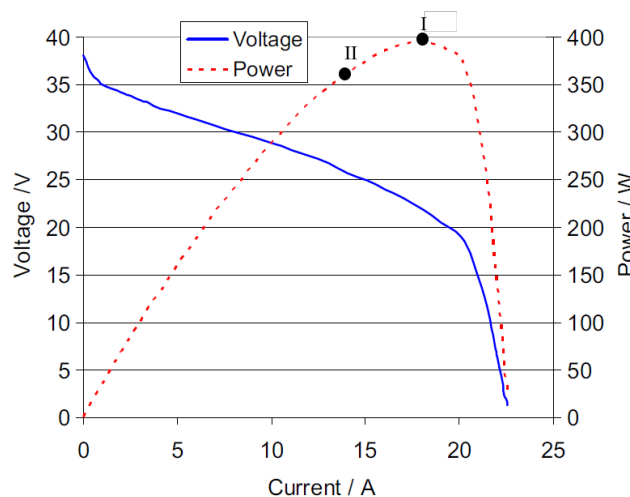


Figure 4.11: Polarization Curve of a fuel cell system. Modified based on [39]

It is important to recognize that for a given required power output, the stack weight itself is minimized by the combination of current and voltage that yields the maximum cell and therefore stack output power. This means the power density of the stack is maximized. If, however, the current is reduced to a lower value such as indicated by II in Figure 4.11, this means the power output is lower and the power density will be reduced. Although this affects the power density of the system, the reduction in current lowers the hydrogen feed and hence can potentially reduce the storage mass or increase the endurance with the same hydrogen mass. Also,

electrical efficiency is higher as it is directly related to the increased voltage. Operation at higher voltages is favourable in terms of stack efficiency.

The power deficit in high power modes will have to be corrected with either a higher power operation than the design point, an increased battery mass or operation of the battery at higher currents where possible. In the modelling phase of this study, the fuel cell power is not increased for peak power phases.

4.4.3. Fuel Utilisation and Efficiency

Efficiency is a key aspect of fuel cell performance as it dictates the weight and power requirements of its surrounding subsystems. When the voltage drops, the efficiency of the fuel cell stack decreases. Efficiencies can be defined in multiple ways. Verstraete et al. [69] chose to split up the electrical efficiency (Equation 4.7) into the voltage, faradaic and thermal efficiency, as well as fuel utilization. This is summarized by Equation 4.8. They show that low electrical efficiency at low power outputs is especially due to low faradaic efficiency and fuel utilization when performing experimental tests. When not considering the fuel utilization, the electrical efficiency follows the voltage efficiency and efficiency graph has the same shape as the I-V curve. The voltage efficiency drops as the operational current increases. Faradaic losses occur when some of the electrons from the hydrogen molecules leak through the membrane. These electrons reach the cathode directly instead of passing through the load and performing useful work. This means the electrolyte membrane is not a perfect insulator. Fuel utilization is defined as in Equation 4.9. For the reasons of fuel utilization and faradaic losses.

$$\eta_{el} = \frac{I \cdot V}{\dot{m}_{H_2} \cdot LHV} \quad (4.7)$$

$$\eta_{el} = \eta_F \cdot \eta_V \cdot \eta_{th} \cdot \mu_{H_2} \quad (4.8)$$

$$\mu_{H_2} = \frac{\dot{m}_{H_2,util}}{\dot{m}_{H_2,in}} \quad (4.9)$$

The electrical efficiency as shown in Equation 4.7 was used in combination with data from a commercial PEMFC by Horizon Energy Systems [63]. For this purpose, data from available graphs was obtained and fitted to be able to further analyze the electrical efficiency of the stacks and the estimation methods for mass flow. The equation for estimating the hydrogen flow rate is given by Equation 4.10, where F is the Faraday constant and M_{H_2} the molar mass of a hydrogen (H_2) molecule. This equation assumes stoichiometry and that the current is directly proportional by the release of electrons from the hydrogen. It shows reasonably good results, given that this assumes 100% fuel utilization. The conversion from slpm to kg/s was done according to Equation 4.11. Note that slpm is defined at 273.15 K (T_{STP}) and 1 atm (p_{STP}) pressure and that the division by 60 and 1000 is to account for time and volume definitions.

$$\dot{m}_{H_2} = \frac{n_c \cdot I}{2F} \cdot M_{H_2} \approx 1.045 \cdot 10^{-8} \cdot I \quad (4.10)$$

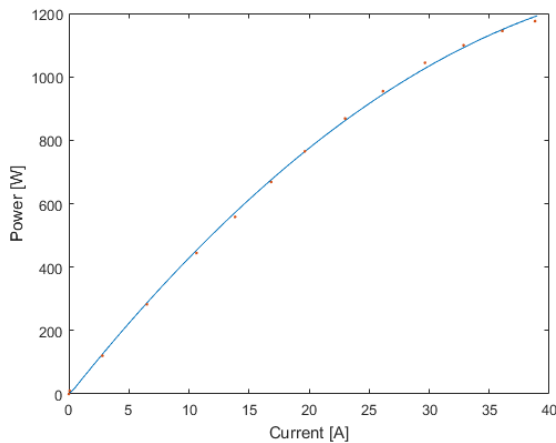


Figure 4.12: Fitted data to Power curve of Horizon H1000 1kW PEMFC stack [63]

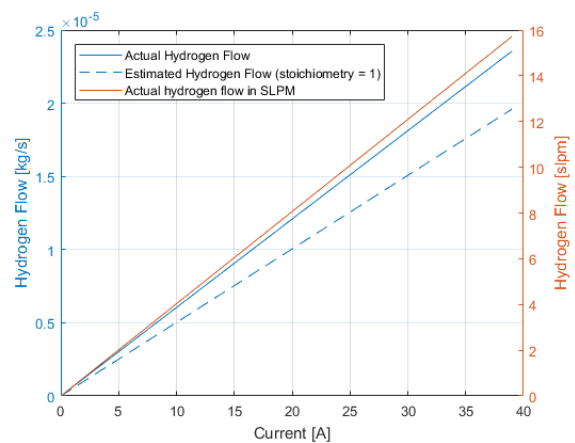


Figure 4.13: Fitted data to Hydrogen flow curve of Horizon H1000 1kW PEMFC stack and converted to mass flow from SLPM [63]

Verstraete et al. [69] show in a test of a similar fuel cell stack that beyond a certain power output (measured until 275W, nominal power output stack is 200W) the fuel utilisation is equal to 90% over 50W and close to

100% at power levels close to nominal. The fuel utilisation is given by Equation 4.9 and was measured by a moving average without the effect of purging, for which a mass flow meter was used. Other sources are according to Verstraete et. al consistent with the results, having a fuel utilisation of about 90-95%.

$$\dot{m}_{H_2} = \frac{slpm}{60 \cdot 1000} \cdot \frac{p_{STP}}{R_{H_2} \cdot T_{STP}} \quad (4.11)$$

4.4.4. Stoichiometry Effects

This section elaborates on the stoichiometry of the reaction and especially the approaches that can be used for the modelling of the required hydrogen flow. Generally based on stoichiometric reactions the hydrogen flow can be modelled based on the current through the system, as seen in the I-V curve. From the reaction, the oxygen and hence air mass flow can be determined. For hydrogen, operation at near-stoichiometry ratios around 1-1.2 is generally applied [1, 18, 32], whereas for air this ratio is generally closer to 2. Potentially, higher stoichiometry ratios can be used, partially for cooling or for improved performance as can be seen in Figure 4.14. However, increased mass flow will increase the blower requirements or if compression is used then compression power increases linearly with air mass flow. In many cases a stoichiometry of 2 is used and not further increased [8, 18]. However, it becomes clear that stoichiometry could be introduced as a variable for different purposes. This study will not introduce stoichiometry as a variable but it is recommended for future studies.

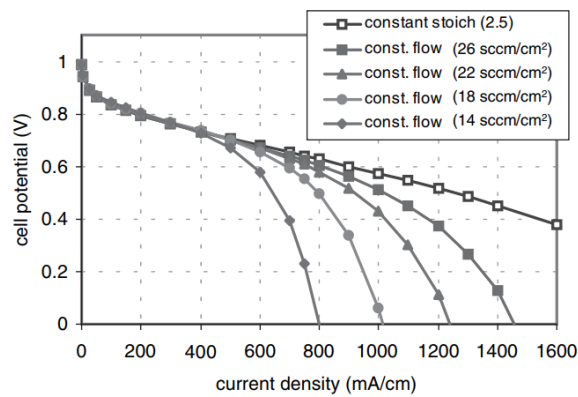


Figure 5-5 Fuel cell performance at different air-flow rates.

Figure 4.14: Effect of stoichiometry on fuel cell performance [1]

4.4.5. Pressure Effects

The effect of pressure and temperature on the system are important to understand. The operating pressure generally results in a cell voltage gain at the same current density and can be approximated in multiple ways. There is a trade-off between increased voltage and hence output pressure and the power needed to compress air to the right pressure. The pressure of the hydrogen inflow can be regulated through pressure regulators.

The influence of pressure on the I-V curve would create a shift upwards when neglecting the extra power needed for the compressor. This ΔV has a logarithmic dependence on the pressure ratio and hence the absolute values do not matter [1, 32]. This logarithmic dependence can be used as seen in Equation 4.12 where C needs to be found for a particular stack using experimental data [32]. Larminie and Dicks mention that this is generally 0.03-0.06 for most stacks.

$$\Delta V = C \cdot \ln\left(\frac{P_2}{P_1}\right) \quad (4.12)$$

Altitude Effect on Fuel Cell Operation

Batteries are mostly influenced by temperature, which can be regulated similar to a fuel cell using cooling and heating. However, batteries are not affected by the ambient pressure. The altitude influences fuel cell operation especially when a configuration is chosen where no compressor is used. As pressure is reduced with altitude, the fuel cell stack will have a negative ΔV . If a compressor is used, the pressure can be increased up to a certain point, either above, on or below the nominal stack pressure to ensure a certain performance and a well regulated mass flow. This is a trade-off considering compressor weight and power. It should be noted that if the compressor is designed for a certain stack pressure at a particular altitude, a performance reduction will be seen beyond this altitude unless the decision is made to size for a larger compressor.

4.4.6. Dynamic Behaviour: Transient Response

Compared to batteries, fuel cells have a slow transient response. The battery needs to be sized so that it can increase the power output up to the maximum power requirement, but also needs to have sufficient energy to deal with the transient of the fuel cell. PEMFC generally have an approximate transient from no load to rated power of 20-30 seconds [69, 70]. This can also be seen in Figure 4.15. Other fuel cell types, mostly the high temperature fuel cells such as SOFC, show poor dynamic behaviour [38]. The transient response is usually not considered for battery and fuel cell subsystem sizing due to designing for nominal conditions or near-constant power phases.

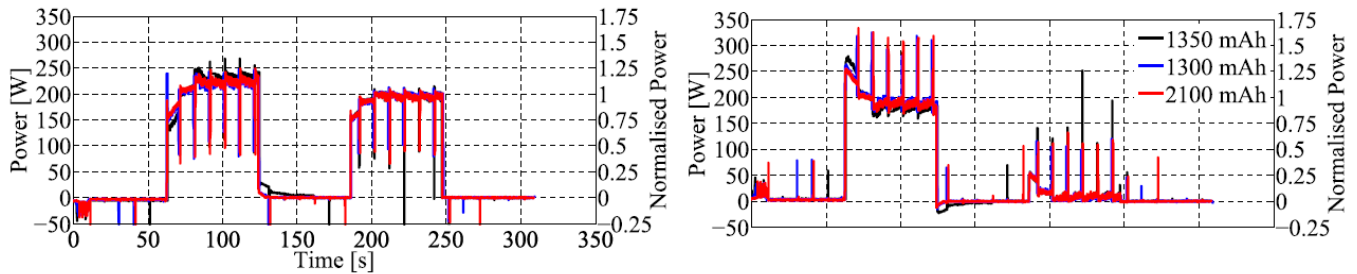


Figure 4.15: Transient behaviour of fuel cell (left) and batteries (right) in a hybrid parallel powertrain [70]

4.5. Hydrogen Storage

This section will discuss the majority of hydrogen storage options. Reforming of hydrocarbon fuels is also an option, but not considered further in the analysis. The options discussed here are either in pure hydrogen form (pressurized gas or cryogenic liquid) or held by a different fluid/solid in which hydrogen is absorbed and can be released. The main considerations are weight and volume, both important for aircraft applications and system limitations. An overview of different storage options is shown in Figure 4.16.

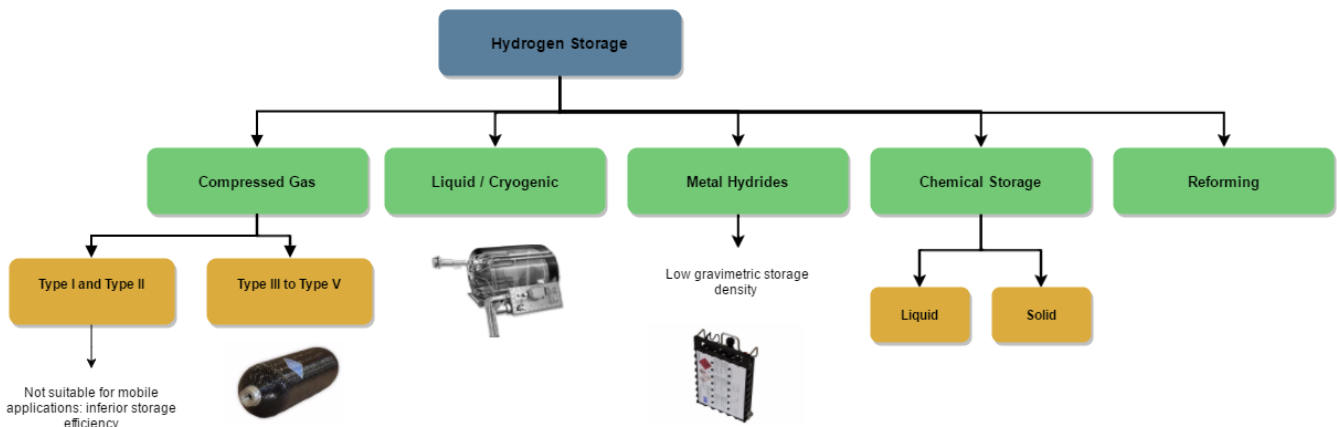


Figure 4.16: Hydrogen storage options which include hydrogen in gaseous, liquid, adsorbed (liquid/solid) and in the form of alternative fuels requiring reforming

4.5.1. Hydrogen Storage Overview

Hydrogen storage is an important part of the power system as compression of the gas or alternative methods are necessary to limit storage volume. Hydrogen is generally stored in 350 or 700 bar tanks, depending on the weight and volume requirements. There are five different compressed gas tank standards. Type I is an all-metal cylinder and Type II is a load-bearing metal liner hoop wrapped with continuous filament. These types are generally for lower pressure storage methods and therefore possess high volume. These are not suitable for vehicular applications Type III and Type IV are more advanced tanks where the former does use metal liners and the latter does not. Type V tanks are all-composite storage tanks.

Other options are liquid hydrogen which requires the liquefaction of hydrogen which needs to be stored at extremely low temperatures. Compact storage of hydrogen is possible in the form of metal hydrides, absorbing large amounts of hydrogen gas, at reduced pressures. Chemical hydrides or the usage of other liquid fuels in combination with a reformer stage can be considered too.

Data for tank options is acquired through available industrial hydrogen storage tanks and can be compared using gravimetric and volumetric efficiencies. The gravimetric efficiency (kg/kg) can be defined according to Equation 4.13 [18]. The same can be done in the same manner for volumetric hydrogen tank efficiency (kg/L) as seen in Equation 4.14.

$$\eta_{H_2,tank} = \frac{m_{H_2}}{m_{H_2} + m_{tank}} \quad (4.13)$$

$$\eta_{vol,tank} = \frac{m_{H_2}}{V_{tank}} \quad (4.14)$$

These storage efficiencies apply mainly to storage tanks but can also be translated to solid storage in the form of metal- or chemical hydrides. Comparisons to hydrocarbon fuels with the reformer stage can also be considered. An overview of hydrogen tanks is shown in Figure 4.17, with the corresponding DoE targets given in Table 4.5 [42].

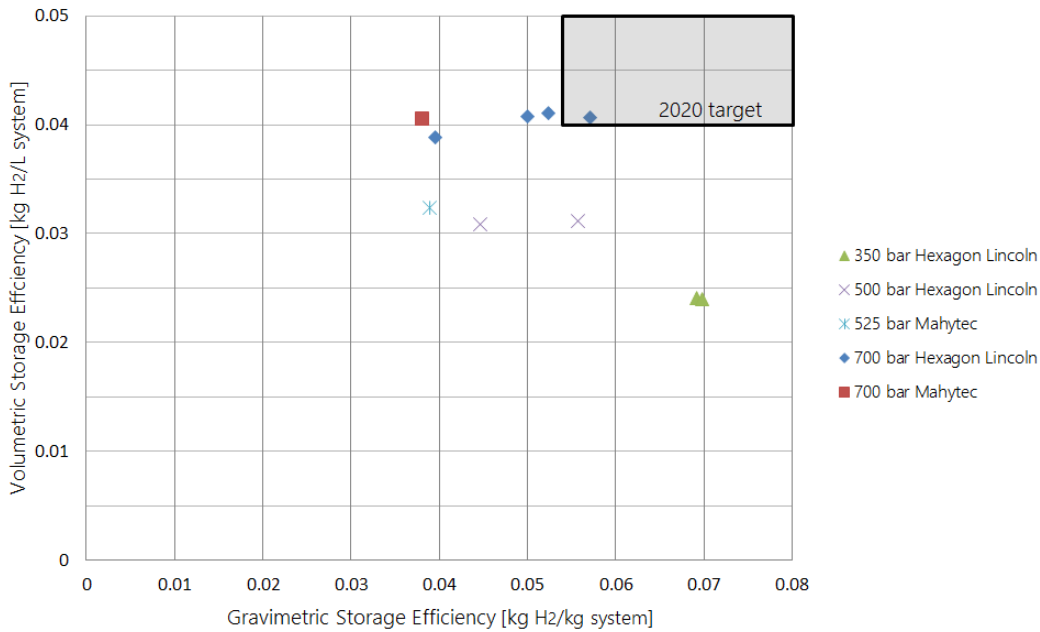


Figure 4.17: Compressed gas Type IV storage tank specifications and DoE targets [42]. Data from Hexagon Lincoln (Type IV) and Mahytec (Type IV)

Storage Parameter	Unit	2020 Goal	Ultimate Goal
Gravimetric storage capacity	kg H_2 / kg system	0.055	0.075
Volumetric storage capacity	kg H_2 / L system	0.04	0.07

Table 4.5: Department of Energy (DoE) targets for onboard hydrogen storage systems for light-duty vehicles [42]

4.5.2. Liquid Hydrogen Storage

Liquid hydrogen storage is a promising solution despite some of its shortcomings. Liquid hydrogen, or LH_2 , requires hydrogen to be kept in a cryogenic state at 20 K. This requires extensive insulation, generally through a vacuum flask or dewar. Some (design) considerations for liquid hydrogen storage are the following [58, 61]:

- The extensive insulation should keep the hydrogen in the cryogenic state for the duration of the mission
- Insulation must be designed based on liquid hydrogen evaporation to the gas phase
- Insulation is generally done through a vacuum and multi layer insulation (MLI) blankets. Another option is an inner and outer shell with a silica aerogel core, but the former is preferred
- Inner tank material considerations are generally aluminium, steel and composites
- Another design approach is a recooling system, which comes with a weight and volume penalty

- Boil-off rate due to heat loss must equate the fuel cell hydrogen consumption. Boil-off higher than fuel cell consumption means more unspent fuel. Boil-off lower than fuel cell consumption means a small amount of heating is needed.

The main benefits according Swider-Lyons et al. [61] are a higher energy storage per unit volume (Wh/L) and that the liquid hydrogen can be stored at a much lower pressure, around 3.5 bar compared to 300-700 bar for high pressure compressed gas tanks. In the case of the cryogenic tank of Swider-Lyons et al. the tank was designed for 3-day usage in a UAV, restricting the hydrogen boil off to the hydrogen gas usage by the fuel cell for three different flight phases (warm-up, climb-out, cruise and landing).

The Ion Tiger project resulted in a tank of 3.6kg storing 0.5kg of hydrogen, resulting in a hydrogen storage efficiency of 12wt%. It should be understood that storage efficiency will reduce when the design strategy is a boil off higher than the minimum hydrogen usage at the least demanding flight conditions. A possible solution is to work with multiple tanks to optimize the weight for boil off and to have a reduction of hydrogen waste as the tank would not have to be used in situations where hydrogen usage is lower than the boil off rate. The tank is shown in Figure 4.18. Swider-Lyons et al. also consider the liquid hydrogen systems and infrastructure and do not have a definite answer to whether it makes economical sense. Liquefaction of hydrogen also consumes about a third of the energy stored in the hydrogen. Considering boil off due to insulation quality further complicates the liquid hydrogen infrastructure. So despite the fact that it is promising for increased gravimetric storage efficiency, the underlying infrastructure requires major improvements.

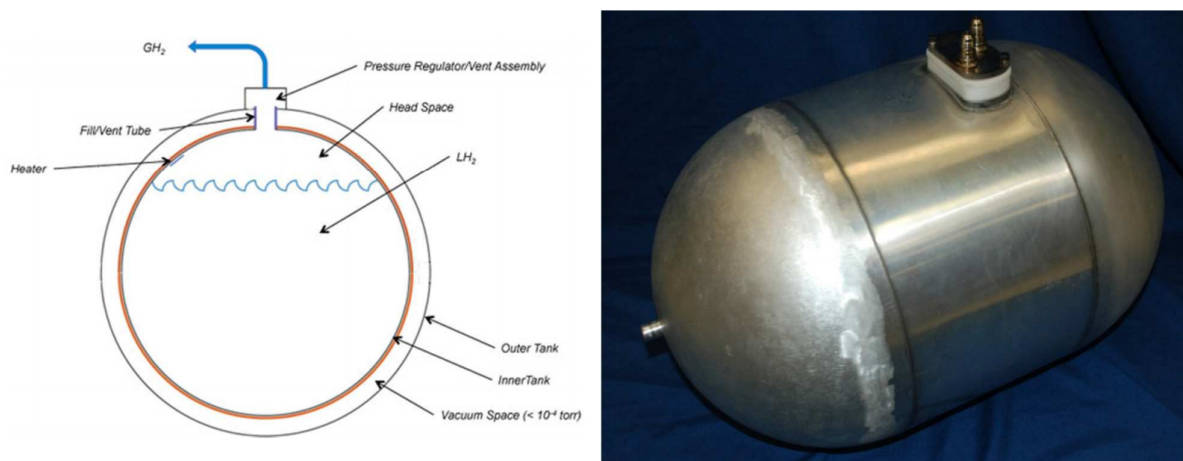


Figure 4.18: Liquid hydrogen flight dewar for the Ion Tiger. The schematic is shown (l) as well as the prototype (r) [61]

4.5.3. Metal Hydrides

One of the main issues with the usage of compressed hydrogen tanks and liquefied hydrogen is the volume of the storage system, reducing the available space for other subsystems and payload. Metal hydrides are a solid storage method with a reduction in volumetric requirements and are a safer way of hydrogen storage.

Metal hydrides, although lower in volume, do not show better gravimetric storage densities compared to compressed hydrogen tanks. Metal hydride gravimetric storage density or efficiency depends on the adsorption capability of hydrogen, which is for some solutions competitive with compressed gas hydrogen tanks. Two of these solutions are MgH_2 and $NaAlH_4$, which - as the release of hydrogen is endothermic - result in the need for heat addition for this release which is also called hydrogenation. The need for heating elements would further reduce the gravimetric storage density. A solution to this would be to use the heat of the fuel cell as long as this heat is approximately equal or higher than the hydrogenation enthalpy and should be seen as a condition to stay competitive as a lightweight storage option [35]. A second condition is that the hydrogen (plateau) pressure in the metal hydride is larger than the supply pressure to the fuel cell stack [35].

AB_2 and AB_5 hydrides are suitable for low- and moderately high temperature fuel cells, which means that they could be used in AFCs, low- and high-temperature PEMFCs and PAFCs. The downside as stated in the study is that the gravimetric hydrogen capacity is typically not more than 1.5-2% $kg H_2 / kg$ system (Rusman and Dahari [52] report a hydrogen storage capacity with low to moderate dehydrogenation temperatures of 1.5-3% kg/kg for common intermetallic metal hydrides) compared to overall storage weight, with the advantage that they require a relatively low energy input. This is low enough to require less than approximately half the heat loss of low temperature stacks.

Due to the high temperature operation of SOFC, they are suitable to be used in combination with MgH_2

metal hydrides, with a hydrogen storage density of approximately 7.6% kg/kg [9, 35, 52]. This limits the system to the usage of high temperature fuel cells, such as SOFC and MCFC. Another issue is that the 7.6wt% is fairly optimistic as the desorption of hydrogen requires the temperature to be maintained at 350°C and hence needs a system with sufficient thermal control. The thermal conductivity is relatively low for metal hydride powders, requiring a complex heat exchange system to reach adequate H_2 discharge rates [9]. Delhomme et al. (2012) built a system with a 6wt% of hydrogen in 10kg MgH₂ discs and a full system weight of 55kg, which makes it a complex 1wt% system. This excludes the added weight by increasing the heat exchanger complexity. The system is only 14L and would have been about 15L with the DoE 2020 goal for compressed hydrogen storage systems for 0.6kg of hydrogen. The low gravimetric storage efficiencies make metal hydrides at this stage not feasible for aerial applications.

4.6. Fuel Cell Modelling

Fuel cell modelling can be done at different levels, but it is important to first make the distinction between static and dynamic modelling. Different options for both will be provided in Sections 4.6.1 and 4.6.2. Static modelling is mainly used for system sizing and dynamic modelling for simulations.

4.6.1. Static Modelling

Static modelling means the modelling of polarization curves and variations to this curve depending on the variables such as pressure. This section will mainly discuss the approaches of modelling the curve itself, which means the voltage decrease with increasing load due to activation, ohmic and concentration losses.

In many cases, an empirical model is employed that is based on the physical losses. Empirical models are widely used in modelling of both batteries and fuel cells for system design. Verstraete et. al used a common empirical model [69], adopted from Larminie and Dicks [32]. Larminie and Dicks indicate that this simple equation provides an extremely good fit with existing fuel cells. The curve fits are performed using the expression of Equation 4.15. The first term is the open circuit voltage, the second an approximation of activation losses, followed by the ohmic resistance. The last term is an approximation of the concentration losses, which has been more widely used in the fuel cell community according to Larminie and Dicks [32]. The parameters to be fitted are open circuit voltage V_0 , B, R, m and n. Larminie and Dicks and Verstraete et al. show good fits with this modelling approach.

$$V = V_0 - B \cdot \ln(I) - R \cdot I - m \cdot \exp(n \cdot I) \quad (4.15)$$

The fuel cell can also be modelled using governing equations for the processes in a fuel cell, using mass, momentum and energy equations according to Barbir [1]. These processes include fluid flow, diffusion, phase change, and electrochemical reactions and is usually not applied for sizing but rather in the fuel cell design itself. Barbir provides an overview of 1D, 2D and 3D models used for fuel cell design.

4.6.2. Modelling of Dynamic Behaviour

The modelling of dynamic behaviour is important when power levels change rapidly, as this means the battery may have to be sized for larger peak powers. When the fuel cell power is designed for cruise and only small changes in the power level occur, dynamic behaviour is insignificant. Dynamic behaviour would only occur at start-up, when the fuel cell goes from no load to its design load. After a common start-up time of 30 s for PEMFC, this load is almost unchanged. Therefore, dynamic behaviour is not taken into account.

Dynamic/transient behaviour modelling would, however, be possible using multi-physics models that were also mentioned for the battery, such as ANSYS and COMSOL. These high fidelity models often consider electrochemical aspects, as well as fluid flow, diffusion and phase changes. These are more commonly used for the design of batteries or fuel cells. Dynamic behaviour modelling is also possible within SimScape Power Systems [65], offering a relatively simple, less physical approach but still requiring experimental results for the input parameters. The dynamic model in SimScape power systems is based on a voltage undershoot constant, response time and a modification to the Nernst voltage as a result of oxygen depletion due to a slower response. The model is not physics-based but rather an approximation of the real transient response through semi-empirical modelling.

Chapter Conclusion

The chapter showed that PEMFC is the most suitable fuel cell for mobile applications. The most suitable storage methods are compressed gas tanks and liquid hydrogen. Modelling of the dynamic behaviour is of small significance and static behaviour can be modelled through semi-empirical relations. Due to steady-state behaviour, no further simulations are needed. The working point on the polarization curve (to be modelled) is determined mostly by current, pressure and stoichiometry, of which the former two will be variables.

Powertrain Configurations

The powertrain is the configuration of components that provide power to the load. This chapter elaborates on efficiencies and configurations to understand the possibilities further. The focus will be on series and parallel configurations. The latter can be split up into active and passive hybrid systems. The chapter provides an overview of systems used in literature to define the configuration for the modelling part.

5.1. Powertrain Overview and Efficiencies

There are a number of components in the entire powertrain. These include but are not limited to the following main components. Preliminary sizing is possible for some of these components, others can be based on state-of-the-art electrical efficiencies and power densities.

- Fuel cell stack and components for cooling, compression, humidification, pressure regulation and storage
- Power electronics such as converters and inverters
- Batteries
- Electric Motor

This section shows two lay-outs, which will be further discussed in the following sections. These are series and parallel fuel cell and battery configurations, with slightly different roles.

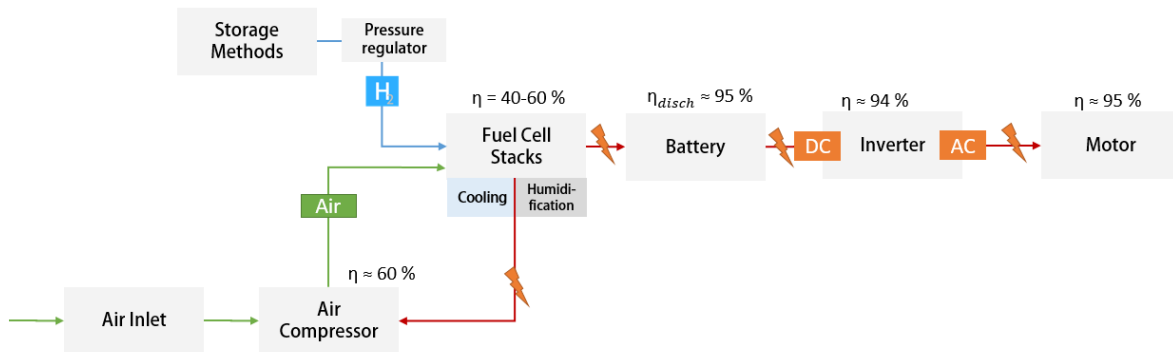


Figure 5.1: Powertrain lay-out with a fuel cell and battery in series

Figure 5.1 shows a powertrain lay-out with approximate efficiency values. The power delivered by the fuel cell stacks is used to charge the battery pack. Batteries generally have an efficiency of 95% although this can be taken into account by considering the discharge curves. This means, however, that the battery needs to be able to have a discharge rate high enough to deliver the full power requirement after the motor and inverter efficiency. Battery charging limits also have to be taken into account. The fuel cell would at least have to be designed to deliver power for the cruise phase, but battery content needs to be large enough to deal with initial peak power phases. The main disadvantage is the fact that the battery has to be oversized as it needs to deliver the peak power while staying within current limits. This can be overcome with a parallel powertrain as seen in Figure 5.2, where the battery only has to deliver the additional power required for peak power phases. Going back to efficiency figures, fuel cells themselves have an efficiency depending on the current density of the cells and is generally operated around 50% efficiency, but this will change when the operating voltage of the

stack is varied. Power electronics in general have a high efficiency around 95% [44]. Electric motors generally also operate at a high efficiency of 95% [54]. Compressor efficiency is generally between 70 and 75%, but further reduced when including motor efficiency.

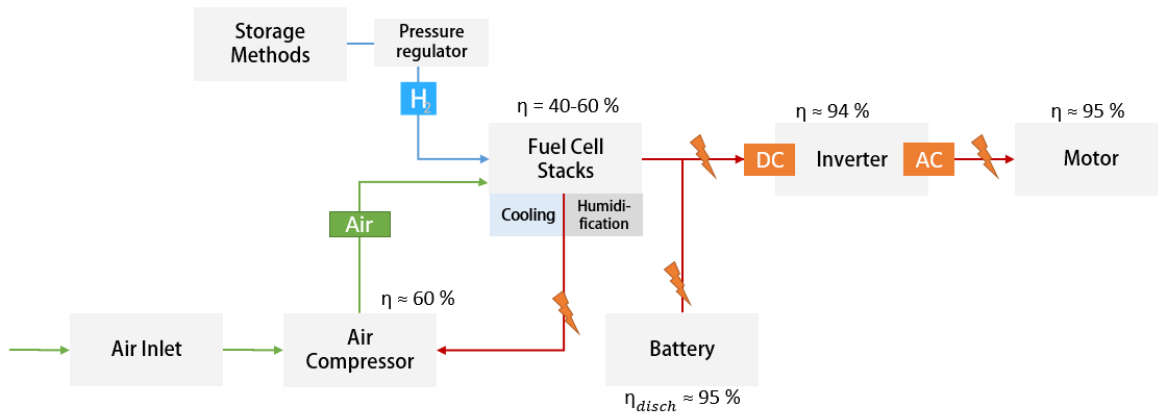


Figure 5.2: Powertrain lay-out with a fuel cell and battery in parallel. The inverter functions as a double inverter

5.2. Battery and Fuel Cell Mix

The optimal mix between the fuel cell and battery power systems can be defined in multiple ways. The ratio can be analyzed after performing the optimization. This ratio depends on a number of factors: the choice of powertrain configuration, the mission profile, how the mix is defined and the strategy used for the optimization. The following shows two definitions that can be used for defining the mix of the energy/power sources:

- Hybridization Factor: energy content of each power system
- Power Ratio: the ratio of maximum power delivered by the two sources

In the case of a series powertrain, the energy content of the battery is not so important as it can get all its energy from the fuel cell system that charges it. The power ratio is more important as the fuel cell can deliver a lower maximum power as long as the battery never depletes. When a parallel powertrain is chosen, both an energy content ratio and power ratio could be interesting results. In best range scenarios, it is always expected that hydrogen content is much larger and battery energy content is relatively low due to low energy density. The maximum power of the battery in a series configuration is higher than the fuel cell power, whereas in a parallel configuration the battery power will be the peak power minus the fuel cell available power.

5.3. Series Powertrain

A powertrain in series, as discussed and shown in Figure 5.1, uses a fuel cell to charge a battery and therefore the power to the load will only come from discharging the battery. With a good design, a near-constant voltage can be provided by the system, reducing the voltage range into the inverter. A limitation in the case of a series powertrain could be the charging rate of battery cells and should be taken into account when choosing a battery cell. The discharge rate of the battery should be low enough to allow for simultaneous charging. When choosing a cell where the charge rate is limited, the battery pack has to be sized according to this limitation. This results in a larger battery pack, which already has to be designed for the maximum power requirement.

The advantage of this system is that the inverter gets a single input from the battery, instead of an input from the fuel cell and battery. Basically, the battery is the power source and the fuel cell the energy source in this configuration. This powertrain is barely explored in literature, most likely because it does not allow for independent sizing as the battery needs to be sized for maximum power and charging, while fuel cell requirements are similar to a parallel powertrain. For a parallel powertrain, the battery can be sized for a lower power level.

5.4. Parallel Powertrain

A powertrain in parallel means that the battery and fuel cell can be sized independently. However, it does not necessarily mean that there is no dependence. If the system has passive power management, there is no

power converter and voltage of the two systems needs to match. Also, when using an inverter, having similar voltage of the two sources is beneficial. Recharging of the battery is still possible in a parallel powertrain, which could allow for a smaller battery depending on the mission profile and whether battery sizing is limited by energy content or current limits. The disadvantage compared to a series powertrain is that additional connections are needed and the inverter needs to deal with two separate inputs with different voltage levels.

The following section explains the difference between active and passive parallel (FC-B) systems in a parallel powertrain. It should be noted that the figures that will be used in the elaboration (Figures 5.3 and 5.4) assume a DC load, whereas most electric motors run on AC loads.

5.5. Active and Passive Hybrid Systems

A distinction needs to be made between active and passive hybrid power management systems. There are clear advantages and disadvantages for both types of power management systems. The difference between the both systems is the availability or lack of a power converter (DC/DC converter), meaning that the voltage has to be the same for the two power sources. Bernard et al. [2] investigated a passive hybrid system, using variable stack pressure to have better control over the polarization curve of the fuel cell stack. Nishizawa et al.[39] removed the DC/DC converter and used diodes to avoid unintentional recharging and reversal current. Verstraete et al. investigated the characteristics of an active hybrid system using an AeroStack setup by Horizon Energy Systems [69].

5.5.1. Active Hybrid System

An active hybrid system was explored by Nishizawa et al. [39] and uses a converter after the fuel cell stack, as seen in Figure 5.3. The advantage is that the battery pack and fuel cell can be individually sized. The disadvantage is that power electronics needs additional cooling, adds weight and volume and therefore also complexity. If this adds substantial weight a passive hybrid system could be investigated for the same purpose, but benefits may be gone as either the fuel cell stack or battery may not be optimally sized.

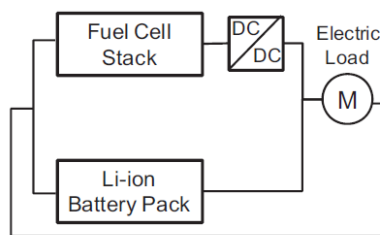


Figure 5.3: Conventional Hybrid with DC/DC converter [39]

5.5.2. Passive Hybrid System

The passive parallel hybrid system can be seen in Figure 5.4. This shows the setup by Nishizawa et al. who replaced the DC/DC by two diodes. The setup showed that it could potentially be applied in the Antares DLR-H2 electric aircraft test bed. The main aim of this setup was to prove the battery could compensate for the slower fuel cell output response.

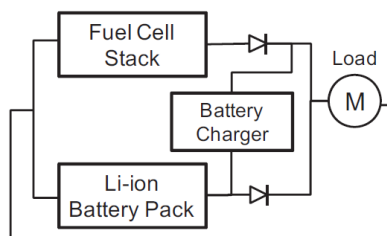


Figure 5.4: Direct(Active)Hybrid where the DC/DC has been replaced by two diodes [39]

For a direct hybrid system as proposed by Nishizawa et al. [39] the voltage operational range of the two power sources needs to be similar as there is no DC/DC converter in the powertrain, such as in a more conventional parallel hybrid system. This means no extra weight of the DC/DC converter and a lower complexity, but less optimization flexibility of the individual power sources.

Nishizawa et al. came up with design guidance on a direct hybrid system based on experimental results. Note that this method uses the graph as seen in Figure 5.5. Also it is exemplary of the limitations of the direct hybrid system, as voltage is automatically restricted depending on the fuel cell design. To conclude, a direct hybrid system offers reduced complexity and power losses. However, the reduced opportunity for optimization of individual systems may reduce power or energy density.

- Step 1: Determine the number of cells in the fuel cell stack based on required power
- Step 2: Define maximum acceptable voltage for the fuel cell stack ($U_{FC,0}$)
- Step 3: Define voltage at maximum power based on the polarization curve of the stack
- Step 4: Select the number of cells for the battery so that the open-circuit voltage of the battery is close to and higher than the voltage at maximum fuel cell power. It should remain below $U_{FC,0}$.

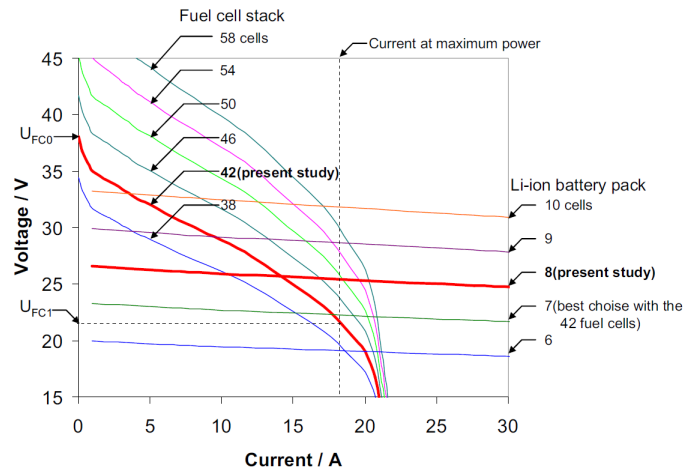


Figure 5.5: Design Method of Battery and Fuel Cell in Direct Hybrid[39]

5.5.3. Recommendations

The results of these different hybrid systems show that a variable optimization with range as the objective function will have more flexibility when a parallel active hybrid system (with DC/DC converter) is used. An active hybrid system requires an electronics box to (re-)direct and convert powers from/to the FC, battery and motor. Using a passive hybrid system would automatically impose a number of restrictions, such as equal voltage. This could mean that the battery could only be used in a limited voltage range, so only part of its capacity can be used. The specific weight and specific power differences of the two power sources - fuel cell and battery - can not be used to their full advantage. For specific applications the passive hybrid system can be a reasonable alternative. For the remainder of this study, an active parallel system will be considered due to flexibility reasons.

5.6. Test Setup

The goal of showing a number of test setups in this section is to understand possibilities for future analyses. The first reason for creating a test setup will be to increase the knowledge on fuel cell systems and the combination with batteries to create a hybrid electric powertrain. Overhead weight and volume will be easier to predict with more experience on a real system. The majority of test setups were made for a low power electric load. Verstraete et al. tested the dynamic behaviour [69] but also the characterization [70] of the powertrain elements and system. Testing can also be used as data for simplified models. Effects such as changing pressure and stoichiometry can be modelled using curve fits of the Nernst equation and losses.

This section shows a few examples of powertrain tests performed in literature. An example of a conventional parallel hybrid system as well as a direct hybrid system is provided. These were also discussed in the powertrain chapter.

Conventional Parallel Hybrid

Figure 5.6 shows a parallel hybrid experimental test setup. More examples are available in literature including component overviews. Examples from literature can be used in support of an experimental setup, also for an overview of measurement systems needed. Voltage, current, mass flow and pressure measurements need to

be done during the experiments. Furthermore, measurements are needed for input into the controllers for the compressor, cooling pumps, hydrogen flow and other components.

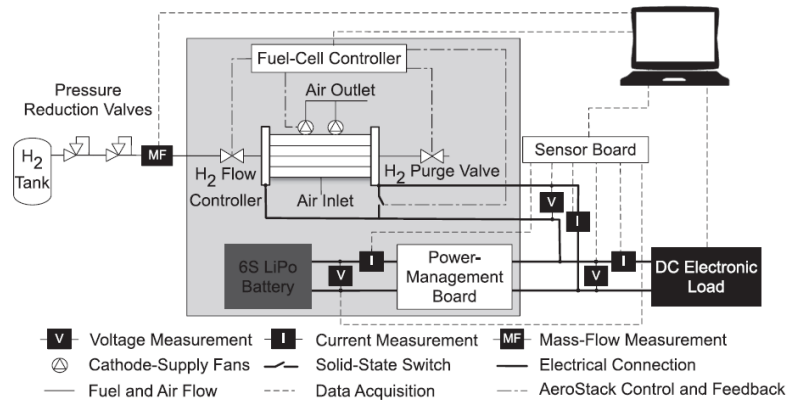


Figure 5.6: Conventional Parallel hybrid test setup [39]

Direct Hybrid

Nishizawa et al. have tested a direct hybrid system which does not include a DC/DC converter to either step up or step down the fuel cell voltage. Two diodes were used instead in this setup, in series with the two power sources. This test setup is shown in Figure 5.7. This also shows that a programmable electric load can be used for system testing.

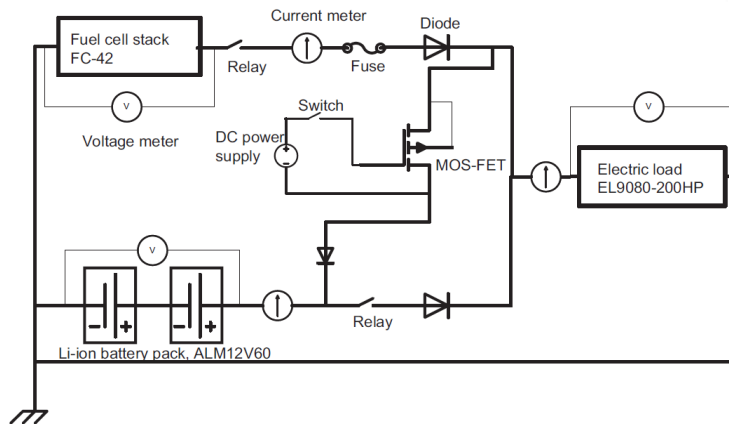


Figure 5.7: Direct hybrid test setup [39]

Interim Summary and Modelling Overview

The goal of the previous chapters has been to improve the understanding of using fuel cells for aviation applications. Conclusions can be made about the focus of previous research and existing research gaps that can be filled partially. The scope of this research can be defined further at this point, recognizing interesting research areas and a suitable approach for a FC-B configuration.

The aim of the research is to make recommendations on focus areas for further electric hybrid powertrain improvements, but also to have a clearer view on the range comparison of different power system configurations to increase clarity on application areas. After the previous chapters in which literature was reviewed, it is expected that the fuel cell stack will use a significant part of the weight budget for the power system with much lower power density compared to battery cells. However, because batteries can be discharged at high power for a short amount of time, they are very suitable for peak power phases in best endurance or best range applications. At the same time it is important to get a better overview of other components needed in a FC-B powertrain and their approximate weights and volumes. Only the 300 bar, 700 bar and liquid hydrogen storage methods seem to be of reasonable storage efficiency for usage in a FC-B configuration. Some balance of plant power requirements and weight will depend on operating conditions of the fuel cell stack and its size. In the upcoming analysis, the compressor power will be taken into account, but others neglected. Weights and volumes of battery overhead, storage tanks, pressure regulators, system controllers, electric motors and inverters will be determined.

Due to the advantages and disadvantage of the two power sources, an approach where the fuel cell stack is used for a low power cruise phase and the batteries for take-off, climb and hover phases is used. Hence maximum power needed by the two sources can be defined based on the mission profile variables. A certain battery size is required to deliver both the extra power and energy during the duration of the climb phase and thus highly dependent on aerial vehicle aerodynamic characteristics and mission profile parameters. The helicopter performance will be modelled using the validated NLR software tool EMPRESS.

The size range feasibility for solely relying on fuel cells and batteries is up to approximately 100kW as most PEMFC operate under this range. Low temperature PEMFC is also the fuel cell of choice for this study, but high temperature PEMFC will make system cooling easier. However, the technology readiness level of HT-PEMFC is low and therefore this is already a future recommendation.

In terms of modelling, both batteries and fuel cells are generally modelled using empirical models based on physical aspects of the technology. These show good correlations with experimental data. The same approach will be used in this study, with an additional battery discharge simulation. It will be shown that the standard battery model in SimScape Power Systems does not show good correlation with test data and therefore a custom simulation was created based on a multi-regressional fit of Li-Ion test data. The SimScape battery model will still be used for the verification of the custom simulation. Dynamic behaviour for the Li-Ion cells is not important (almost instantaneous) and is also not modelled for the fuel cells. The main reason is that the sizing approach results in a situation where fuel cell power is almost constant throughout the flight. The start-up time of 30 s of most PEMFC stacks is therefore neglected, but two OGE hover phases will be introduced at take-off and landing.

The end result will show a clear comparison between Battery-only and an FC-B configurations by an overview of payload-range diagrams for the helicopter UAV. This helicopter test case will be further elaborated on in the first chapter of Part II (modelling) of this thesis. The effect the storage method has on the range will be clarified. The role of the battery will also become clear through sizing with simulations. The effect of increased battery performance over the course of the next decade will be investigated as it could challenge fuel cell systems when the gravimetric energy density increases to solid-state or Li-S solutions.

Research Framework

Figure 6.1 shows the research framework considered in the remainder of this study. The study scope has been narrowed down to key components. For battery technology this means that the focus will be on the modelling of state-of-the-art Li-Ion batteries. However, since the main reason for using a fuel cell system additionally is increasing the energy density, the upcoming battery technologies will be compared to the energy density of the system in the different studied cases. For this reason, the final payload-range diagrams will include a lithium-sulfur (400Wh/kg) reference based on Li-Ion characteristics. For fuel cell technology the focus will be on PEMFC with the future recommendation of looking at HT-PEMFC cell data if available and comparable to LT-PEMFC data. The storage tank options to be considered are compressed gas tanks and liquid hydrogen. Typical range and endurance mission profiles with variable mission profile parameters will eventually be analyzed. High fidelity (semi-)empirical fuel cell and battery modelling and simulation of the latter will be performed, whereas lower fidelity sizing of all the additional components is applied. This includes weight, power and volume estimates based on state-of-the-art components.

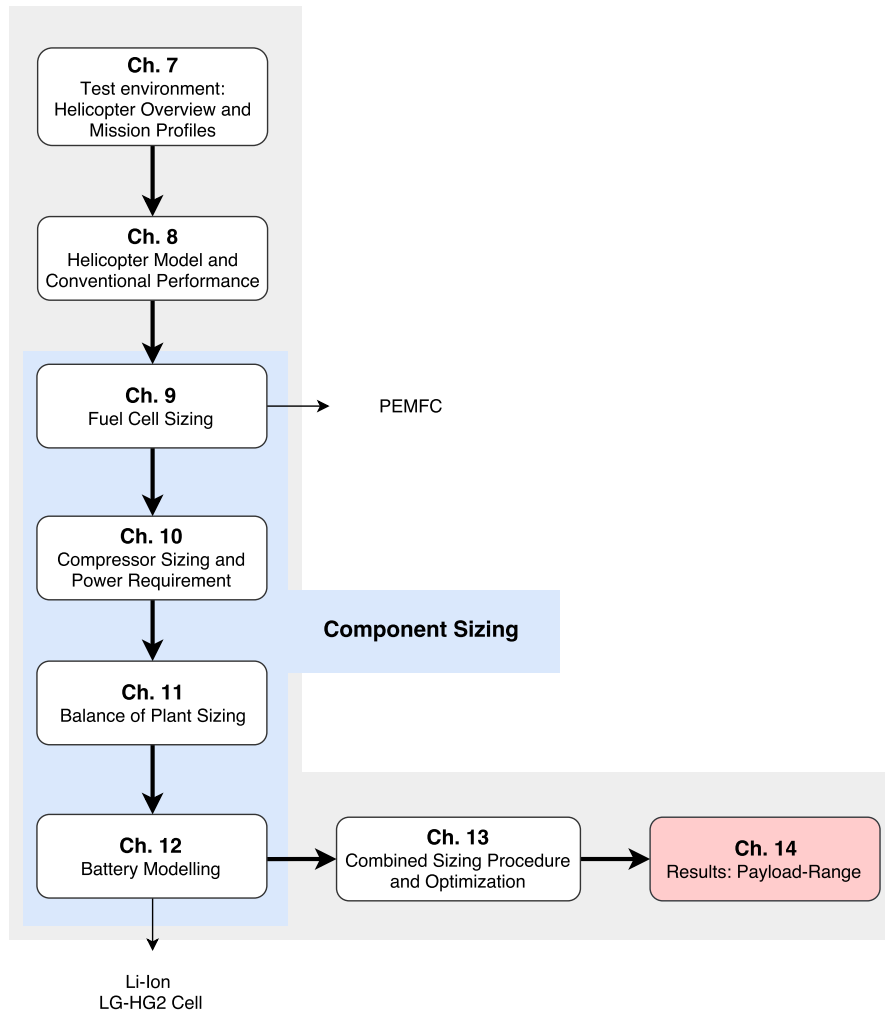


Figure 6.1: Structure and demarcation of following chapters: the modelling, sizing and optimization structure will be central points of the remainder of the study, followed by the results mainly in the form of payload-range diagrams

II

Modelling

Test Environment: Reference Helicopter and Mission Profiles

This chapter elaborates on the reference helicopter used in the analysis of both the battery-only and the fuel cell-battery (FC-B) implementation. This means dimensional, weight, volumetric and power data is gathered and analyzed. The result of this chapter should indicate the available weight, volume and provide an indication of power requirements. Furthermore, it will indicate how the current power system which includes the gas turbines and fuel tank will be replaced by their electric counterparts.

7.1. Helicopter Applications

Helicopters are used for applications in which a vertical take-off and landing are key components of a flight profile, either due to a difficult terrain or e.g. varying take-off and landing locations. The reference helicopter is a Geocopter GC-201 (UAV) with a MTOW of 100 kg and 16 kW of sea level available power, delivered by two micro gas turbines. This Geocopter at NLR can be seen in Figure 7.1. It has a maximum micro gas turbine output power of 16kW, which in reality turns out to be lower due to the the gas turbines not reaching their specified power.



Figure 7.1: PH-1XA Geocopter (NLR / Dutch Aerospace Center). The same GC-201 can be found under registration PH-1AA

In a research environment, helicopter UAVs may be applied for performing in-flight experiments of developed hardware, 'Beyond Visual Line of Sight' (BVLOS) flying but also for unmanned missions where the main requirement is endurance or range. A FC-B configuration is aimed at serving this exact requirement due to short peak power requirements and a long forward speed cruise phase.

A number of applications can be identified that require range and/or endurance, including terrain mapping, search and rescue operations, support to emergency services and security and defense operations. These are applications in which endurance and range play a larger role as opposed to e.g. wind turbine or oil rig inspection, where continuous peak power requirements due to longer hover, climb and descent phases are a key aspect.

These power requirements will be further elaborated on through the power (P-V) curves of the reference helicopter and will show that forward speed sections require lower system power.

7.2. Weight and Volume Overview: Geocopter GC-201

This section discusses the weight overview of the GeoCopter GC-201 reference helicopter. The main focus is to understand the available weight for the power system and hydrogen storage. This section will show the weight breakdown of the conventional GC-201 configuration and then show available weight at 100 kg MTOW. The current conventional helicopter is limited to 90 kg MTOW as a result of power limitations (controller-limited) from the installed micro gas turbines as they do not reach their specified power output. However, for the analysis in this study the MTOW of 100 kg and maximum output of 16 kW is considered.

Going from the weight breakdown in the conventional setup to the electric configuration can be summarized by the following points:

- The micro gas turbines (2x 8kW JetCat SPH5, 4.4 kg [23]) are replaced by an electric motor with state-of-the-art parameters of 7kW/kg as shown by some recent improvements [54]. This means the maximum power requirement will determine the sizing of the electric motors. Also, an inverter is needed that accepts both fuel cell and battery power and converts the electricity from DC to AC power. This is also taken as 7 kW/kg but also takes into account electric motor efficiency of 95%.
- The JetCat SPH5 peripherals (2x 0.65kg) are assumed to be replaced directly by electric motor peripherals of the same weight. This allows for installation and other excluded components as the electric motor power density only includes the electric motor itself.
- The payload volume will be calculated based on the available volume after taking into account all other component volumes.
- The current payload, which is the secondary autopilot, will be removed and is therefore available weight for the power system, hydrogen storage or another payload

Table 7.1 shows the weight breakdown in the original situation, which has 44.2 kg available for the fuel and a second payload, as the secondary autopilot is the current payload. Table 7.2 shows the same breakdown for the electrically powered helicopter. The electric motor replaces the current engine. Furthermore, an inverter will be needed between the power sources and the electric motor. This is approximately the same weight as the electric motor given the inverter power density of 7 kW/kg used in this study. This will be further elaborated on in Chapter 11, which gives an overview of smaller powertrain components.

The empty weight is about 40% of the full helicopter weight. Adding the electric motor and keeping the peripherals, this comes down to 43.6 kg. The inverter adds a similar weight as the electric motor. For the inverter and all other components as discussed in all previous sections, 56.4 kg is available. In the results section, the component weights were summed up manually and checked for consistency.

Weight Breakdown	Value	Unit	Source
Empty Weight + Blades - Engines	39.7	[kg]	NLR
Engines (2x JetCat SPH5 8kW)	4.4	[kg]	[23]
Engine Peripherals (2x)	1.3	[kg]	[23]
Secondary Autopilot Payload	6	[kg]	NLR
Minimum Fuel	4.4	[kg]	NLR
Total	55.8	[kg]	
MTOW	100	[kg]	NLR
Available (Fuel and Payload)	44.2	[kg]	Fuel Tank 40kg / 50L

Table 7.1: Weight Overview of the original GC-201 setup. Parts that are replaced by equivalent components are shown (orange), as well as parts kept (green) and parts removed (red). The available weight for fuel and payload is shown in gray.

A volume analysis was also made. It is known that the conventional kerosene fuel tank goes up to approximately 40 kg and therefore has a corresponding volume of 50 L. This volume can be used towards the power system. The volume breakdown is shown in Figure 7.3. It should be noted that the total available volume remains an estimate. Exact measurements may show a different number.

7.3. P-V Curves OGE and IGE and Mass Change

Figures 7.2 and 7.3 show the power curve for the Geocopter GC-201 out of the ground (OGE) effect and in the ground effect (IGE) respectively. These are standard helicopter performance curves and are shown at sea level. Both graphs show very similar results for a range of operating masses. In case of using batteries and fuel cells, there will be almost no mass change. Given the available mass of about 54.3 kg, it is expected based on

Weight Breakdown	Value	Unit	Comment / Source
Empty Weight + Blades (-Motor)	39.7	[kg]	
Electric Motor	~2.3	[kg]	~16 kW (7 kW/kg)
Inverter	~2.4	[kg]	~16 kW, 7 kW/kg and $\eta_m = 0.95$
Motor Peripherals	1.3	[kg]	
Total	45.7	[kg]	
MTOW	100	[kg]	Defined
Available Weight (Payload + Power System)	54.3	[kg]	

Table 7.2: Weight Overview of the new setup. Parts that are added by equivalent components are shown (orange), as well as parts kept (green) and parts removed (red). The available weight for the power system and payload is shown in gray.

Volume Breakdown	Value	Unit	Comments / Source
Fuel Tank Volume	50	[dm ³]	NLR
Internal Payload Bay	31.25	[dm ³]	IHS Jane's
Secondary Autopilot	10	[dm ³]	Assumed
Total Available Volume	91.25	[dm ³]	For Power System and H ₂

Table 7.3: Breakdown of available volume

preliminary analysis that approximately 0.5-2% of the vehicle mass can be used towards hydrogen storage, as a 700 bar compressed gas tank is about 17 times heavier than the hydrogen and liquid hydrogen estimated at about 8 times heavier. This means the mass change will be relatively low.

Figures 7.2 and 7.3 show performance curves from 70 kg to 100 kg MTOW. In the worst case, a 1 kg mass change at $V = 0$ m/s, will cause a difference of about 0.16 kW, when performing linear interpolation between the 90 and 100 kg lines. The effect of in-flight mass reduction will be considered negligible in the sizing. This simplifies the analysis for battery-only and FC-B configurations, as batteries also show no mass change. A mass change could, however, be seen in future battery applications if Lithium-Air technology finds its way out of the experimental phase into mass production.

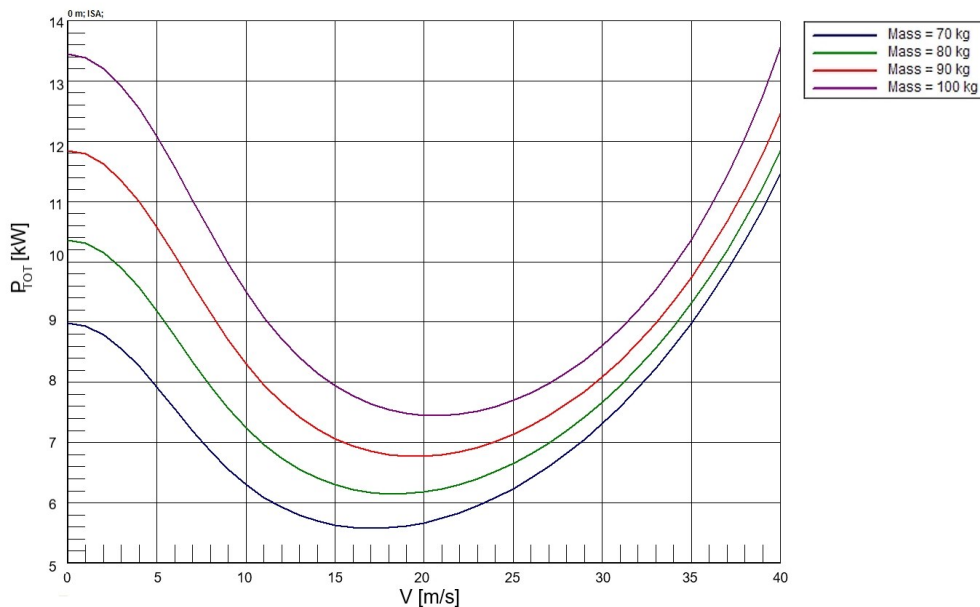


Figure 7.2: P-V curve: Out of Ground Effect (OGE)

The creation of these power curves will be elaborated the upcoming chapter. This was done through validated NLR software EMPRESS and again verified through basic helicopter theory.

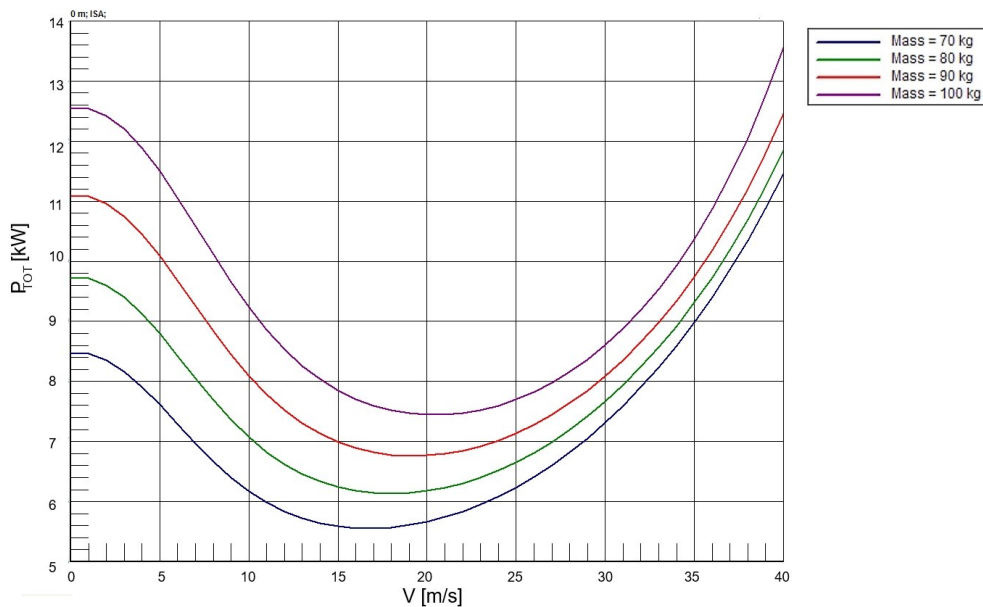


Figure 7.3: Power Curve: In Ground Effect (IGE)

7.4. Mission Profiles: Test Environment

This section elaborates on the best range and best endurance mission profiles in this study. The mission profiles are defined in this section so that the powertrain sizing is based on realistic performance requirements. The power requirements per phase are somewhat simplified as will be elaborated on in this section.

7.4.1. Assumptions

This section provides an overview of assumptions related to the mission profile, as well as the effect on the modelling and results.

- **Best endurance speed:** In case of a best endurance mission, the best endurance speed V_{BE} is used for all forward speed phases, which include the climb phase, cruise and descent. At this speed, the power requirement (P_{BE}) is lowest and therefore hydrogen mass flow is too.
- **Best range speed:** In case of a best range mission, the best range speed V_{BR} is used for all forward speed phases, which include the climb phase, cruise and descent. At this speed, the power requirement (P_{BR}) is higher than at the best endurance velocity. The velocity is also higher, but the combination yields the velocity at which the minimum P/V is found for each altitude and weight combination. This is generally done in helicopter theory [25], under the assumption that specific fuel consumption is independent of velocity. This is further explained in later sections.
- **Mass Change:** No mass change is considered in the entire flight. For the battery-only configuration using Lithium-Ion batteries this is obvious, but with future Li-Air technology this may change. For fuel cell operations this is still a valid assumption as preliminary analysis shows that no more than about 2 kg of the flight mass can be hydrogen content. The effect this has on power requirements is very low with a MTOW of 100 kg. This is further elaborated on in Section 7.4.2.
- **MTOW:** The aircraft is always flown at the MTOW of 100 kg and always filled up to this weight with hydrogen storage.
- **Power and Altitude Averaging:** For all flight sections, the power and altitude requirements will be averaged. The effect is not significant for the powertrain sizing, range and endurance.
- **Climb / Descent:** No climb efficiency is taken into account in one way or another. The performance requirements are a linear relationship between rate of climb and power.
- **Wind:** Wind is not taken into account in the analysis. The effect wind has on power requirements would be a consideration for future studies.
- **Constant Altitude Cruise:** The altitude in the cruise phase does not change, especially since there is barely any in-flight weight reduction.

- **Fuel Cell:** The fuel cell and balance of plant are designed at a specific current density and always operates on or under this current density and pressure ratio meaning compressor power remains constant. FC performance therefore goes up slightly when operated at lower altitudes than cruise.
- **Charging:** Although this chapter discusses charging options, no charging is considered in the sizing and final results. The results section will also show that battery energy content is not as limiting as the current limits of the battery. Only with multiple take-off and descent phases, this would most likely become a necessity.
- **Take-off and Landing Conditions:** Take-off and landing conditions are at sea level according to the ISA standard.

7.4.2. Mass Change

As was mentioned in the assumptions, no effect of mass change was considered in the performance analysis throughout the entire flight profile. This section further elaborates on this assumption.

A major difference between conventional and electrically powered vehicles is the mass change during the flight. A conventional aerial vehicle has a significant weight reduction as a result of fuel usage. For the reference helicopter, the maximum tank size is 40 kg, meaning 40% of the MTOW at 100 kg. The mass change for most battery types that are currently mass-produced (Li-Ion) is non-existent and the hydrogen mass flow is extremely low. The effect is therefore negligible, since the hydrogen itself will only be a small percentage of the MTOW. Most of the weight directly related to the hydrogen storage will be the storage method, where hydrogen has a low storage efficiency between 4 (300 bar) and 12 wt% (LH₂). For this reason, the hydrogen weight will generally only be approximately 0.5-2% of the MTOW, based on an early analysis that around 15 kg is available for storage at moderate payload weights. In conventional vehicles, the aircraft will be much lighter towards the end of the cruise phase, providing a major advantage in terms of range as a result of a reducing power requirement towards the end of the flight. For the cases studied in this research, the helicopter is always flown at the MTOW.

7.4.3. Strategy

The strategy for a battery-only configuration is simple. The battery is sized based on the available weight after accounting for the motor and inverter weights. This battery delivers both cruise and peak powers. For the FC-B configuration, the fuel cell is sized for the low power cruise phase and the battery is sized to fulfill the peak power requirements for the needed duration, this is summarized below:

- **Fuel Cell:** Due to the relatively low power density of the fuel cell stacks (with cooling) compared to battery cells, the design power of the fuel cell stacks is the cruise power, plus the power needed for the compressor
- **Battery:** Due to the high power density of battery cells and battery packs, they will be used for peak power phases as the duration of these segments is also relatively short. High battery discharge rates can therefore be used without depleting the entire battery to a SoC of 0%, even though the energy content of batteries is relatively low.

7.4.4. Symbol Definition

The symbols used in the profiles in this chapter are explained by Table 7.4. It should be noted that the fuel cell will be designed for cruise power. However, there is some potential when it turns out that the chosen, optimized current density is well below its maximum, because then the fuel cell is not operated at its maximum power during cruise. A bigger compressor could allow for an increased mass flow to allow for operation beyond the design point, so that the maximum fuel cell power is increased and the battery peak power is reduced.

For this study, the fuel cell will never be operated beyond P_{des} at cruise as indicated by the second symbol in Table 7.4, but either at P_{des} or slightly below P_{des} in the descent phase.

7.4.5. Best Endurance and Best Range Mission Profiles

Different mission profiles can be considered for the helicopter. The studied profiles will be best endurance and best range mission profiles. An extra third flight profile will be shown, which could be considered for further analysis.

- Best Endurance (Standard Mission)
- Best Range (Standard Mission)
- Best Range with Intermediate Stops (Advanced Mission)








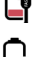


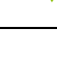
Symbol	Considers	Description
	Fuel Cell	Operation at P_{des}
	Fuel Cell	Operation between P_{des} and P_{max}
	Fuel Cell	Operation below P_{des}
	Battery	Discharging
	Battery	Charged to high SoC
	Battery	Partially Discharged
	Battery	Empty (~10% SoC)
	Battery	Charging
	Battery	Almost charged to required SoC
	Climb	Rate of Climb (Climb phase)
	Descent	Rate of Descent (Descent phase)

Table 7.4: Symbol description used in mission profiles

Best Endurance

Figure 7.4 shows a best endurance mission profile for e.g. observation purposes. Table 7.5 includes the description of the best endurance profile sections. Although the goal is best endurance, the profiles discussed in this chapter include some of the peak power phases to realistically model the power requirements of the helicopter.

The mission profile starts with a hover phase, which will be set at 30 s for both take-off and landing. This is followed by a vertical climb which will be set at 4 m/s to approximately reach the 16 kW peak power requirement. The main reason for incorporating a vertical climb phase is that helicopters are applied in vertical take-off and landing scenarios. The hover phase (1-1) and vertical climb phase (1-2) are both high power phases. This is followed by a climb phase to cruise altitude (2-3), which is performed at the best endurance forward velocity. Subsequently, a cruise phase with a to be determined length is followed by a descent procedure. A forward speed descent at V_{BE} (4-5) is followed by a vertical descent (5-1) and a hover phase (1-1). All vertical sections as well as the climb has peak power requirements from the battery.

It should be noted that in real life scenarios, a decision can be made to replace some of the hydrogen storage tanks needed for the long endurance phase by batteries, to allow for other maneuvers and longer peak power phases. If peak power phases are dominant, a battery-only configuration might be beneficial with the status of current technologies.

Section	Description
1-1	Hover (OGE) for a specified time
1-2	Vertical climb ($V_{FORWARD}=0$) at a defined RoC
2-3	Climb with a forward speed V_{ROC} at a defined RoC
3-4-3	Cruise at best endurance velocity V_{BE} for undefined time
3-4-3	...
...	...
3-4	Cruise at best endurance velocity V_{BE} for undefined time
4-5	Descent with a forward speed V_{ROC} at a defined RoD
5-1	Vertical descent ($V_{FORWARD}=0$) at a defined RoD
1-1	Hover (OGE) for a specified time

Table 7.5: Section explanation for a best endurance standard mission profile as shown in Figure 7.4

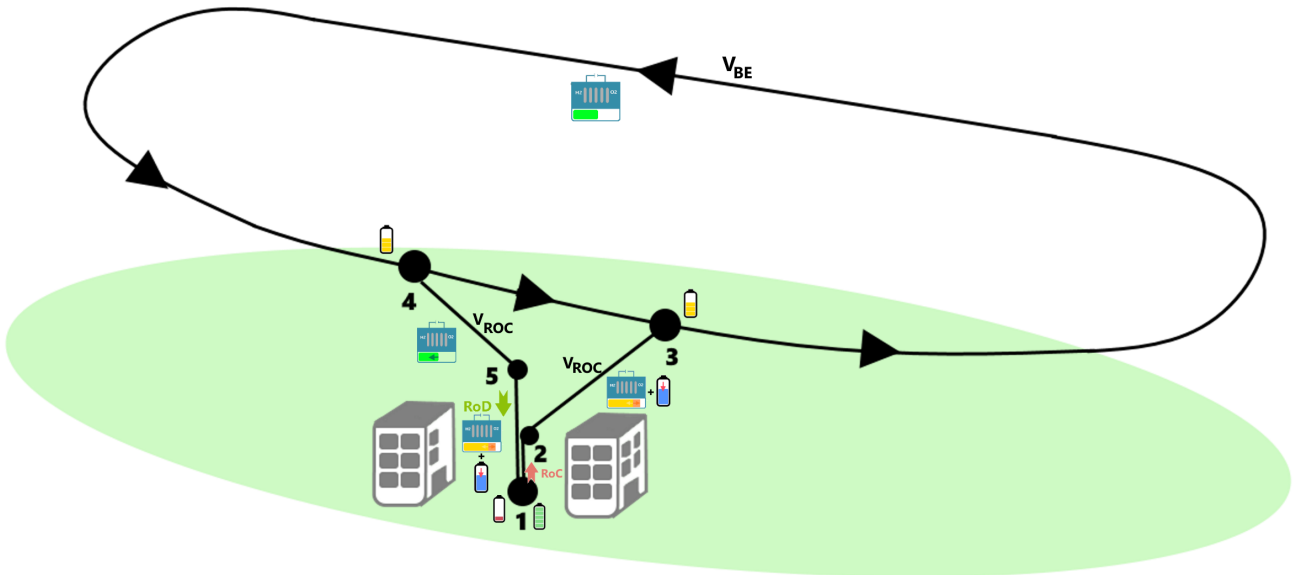


Figure 7.4: Endurance Mission Helicopter for Observation Purposes

Best Range

Figure 7.5 shows a best range mission profile for applications where large distances have to be travelled, while requiring a vertical take-off and landing. Table 7.6 shows the description of the sections shown in Figure 7.5. In the best range condition, the velocity and corresponding power are both higher than in the best endurance mission profile, due to the fact that best range is achieved at minimum P/V .

The best range profile is very similar to the endurance profile, but fuel cell design power will be higher as a result of a higher cruise power for the same altitude and weight. In both the endurance and range profiles, the forward speed descent allows the fuel cell to operate at a lower power and therefore lower current and hydrogen mass flow.

Figure 7.5: Standard mission profile for maximized range (hence V_{br}) with no intermediate stops.

7.4.6. Advanced Helicopter Mission: Best Range with with a Drop-Off

Finally, a more advanced best range profile is considered to show what effects this may have on fuel cell or battery sizing. This is a profile where battery charging could be considered when energy content is not sufficient after designing the battery for peak power. In this case, it can also be decided to bring a bigger battery, increase fuel cell design power or allow for charging during the cruise and descent phases.

Figure 7.6 shows the advanced mission profile for the helicopter. The individual sections are explained by Table 7.7. In this profile, the distances $d_1 + d_2 + d_3 = d_4 + d_5 + d_6$ as the vehicle returns to the original base with

Section	Description
1-2	Hover (OGE) for a specified time
2-3	Vertical climb ($V_{\text{FORWARD}}=0$) at a defined RoC
3-4	Climb with a forward speed V_{ROC} at a defined RoC
4-5	Cruise at best range velocity V_{BR} for undefined distance (max. range objective)
5-6	Descent with a forward speed V_{ROC} at a defined RoD
7-8	Vertical descent ($V_{\text{FORWARD}}=0$) at a defined RoD
8-9	Hover (OGE) for a specified time

Table 7.6: Section explanation for a best range standard mission profile as shown in Figure 7.5

a lower weight. Basically the objective is therefore to maximize $d_1 + d_2 + d_3$. When charging is not considered, such as in this study, this mission profile mainly affects the battery size which could potentially be slightly larger. The standard range mission profile could therefore give a good indication of the possibilities of this application. As the FC would be designed for the first cruise phase at the MTOW (4-5), the fuel cell power will be able to provide some of the peak power in the second phase of the mission profile (8-14) as the vehicle weight reduces due to a payload drop-off. This is only substantial with larger payloads. However, it will be shown in the results chapter that a FC-B configuration is less likely to be competitive at large payloads with widely available storage methods (300 and 700 bar storage tanks). This mission profile is a recommendation for future analysis but it will be shown that the battery has remaining capacity for the standard best range mission profile, meaning that this mission profile is most likely possible with the same configuration.

Section	Description
1-2	Hover (OGE)
2-3	Vertical climb (OGE, $V_{\text{FORWARD}}=0$) at defined RoC
3-4	Climb with a forward speed V_{ROC} at a defined RoC
4-5	Cruise at best range velocity V_{BR} for defined distance
5-6	Descent with a forward speed V_{ROC} at a defined RoD
6-7	Vertical descent (OGE, $V_{\text{FORWARD}}=0$) at defined RoD
7-8	Hover (OGE) at drop-off location and lose m_{payload} (8)
8-9	Vertical climb (OGE, $V_{\text{FORWARD}}=0$) at defined RoC
9-10	Climb with a forward speed V_{ROC} at a defined RoC
10-11	Cruise at best range velocity V_{BR} for defined distance
11-12	Descent with a forward speed V_{ROC} at a defined RoD
12-13	Vertical descent (OGE, $V_{\text{FORWARD}}=0$) at defined RoD
13-14	Hover (OGE)

Table 7.7: Section explanation of the mission profile in Figure 7.6

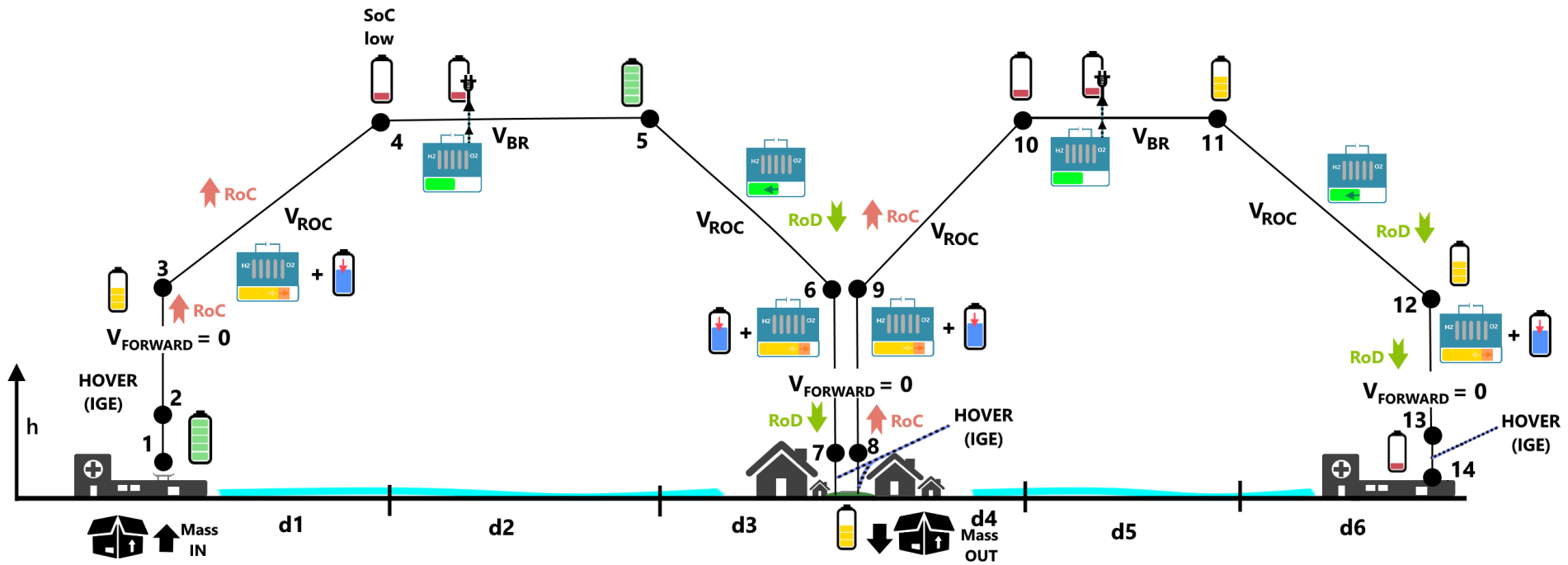


Figure 7.6: Advanced mission profile for the helicopter. This illustrates a mission profile that combines a large range (hence V_{br}) objective with a payload drop-off and return to origin. This means that the second phase $d_4 + d_5 + d_6$ is with a smaller weight and therefore more variables can be introduced.

7.4.7. Top-Level Power Analysis

This section elaborates on the top-level power requirements that can be based on the helicopter power curves that will be modelled in the following chapter. This section gives an overview of different power requirements throughout the mission profiles.

First of all, there are power losses in the engine and transmission that must be accounted for in the conventional system. These are gear train losses, but also include the power required for engine cooling and accessories such as a generator and oil pump. The approach for approximating these losses can be made more crude and is often done [25] because aerodynamic interference losses (the tail rotor works in the wake of the main rotor and fuselage) and tail rotor power (rather small fraction) have to be estimated as well. For this reason, a more approximate approach is often used. The combination of all these losses can be included into an efficiency factor expressed by η in Equation 7.1. The validated EMPRESS model is able to estimate these losses individually, which will be done in the next chapter. The required power by the rotor only consists of the power needed to perform the flight when excluding these losses and power requirement of e.g. the tail rotor.

$$P_{req,total} = \frac{1}{\eta} \cdot P_{req,rotor} \quad (7.1)$$

The power requirements below are all total power requirements needed during the mission profiles. This total power requirement can also be obtained from the NLR helicopter tool EMPRESS. The hover phases are in all cases calculated for the worst-case OGE condition.

- **P_{BR}**: Best range power at V_{BR}
- **P_{BE}**: Best endurance (or minimum power) at V_{BE}
- **P_{Climb,ROC}**: Climb power at the forward speed climb phase at specified velocity
- **P_{Climb,V_{FORWARD}=0}**: Climb power needed at the vertical climb phase
- **P_{Descent,ROC}**: Power requirement at the descent phase with specified rate of descent
- **P_{Descent,V_{FORWARD}=0}**: Vertical descent
- **P_{HOVER,IGE}**: Hover power in ground effect
- **P_{HOVER,OGE}**: Hover power out of ground effect

Best Range Power

The best range is determined through the integral in Equation 7.2, in which dR/dW_F is the specific range.

$$R = \int \frac{dR}{dW_F} dW_F \quad (7.2)$$

Generally the fraction (specific range) changes during the flight, but because hydrogen weight is so small, this is negligible. For the same weight, altitude and therefore also power, this is unchanged. Assuming that the specific fuel consumption is independent of velocity, this can be approximated.

Maximizing the specific range is maximizing Equation 7.3. The minimum fuel consumption per unit distance is technically the maximum range and achieved at the speed for minimum P/V when assuming the specific fuel consumption ($\text{kgH}_2/\text{kW}/\text{hr}$) is no function of velocity, but only a function of power. The fuel consumption is actually not independent of velocity due to the fact that power is velocity dependent and power directly affects hydrogen usage. The SFC is multiplied by the power, because SFC here is given by $\text{kg}/\text{kW}\cdot\text{hr}$, so normalized to kW. The maximum of this means that the aim is to look for the best distance per kg of fuel used.

$$\frac{dR}{dW_F} = \frac{V}{P \cdot SFC} \quad (7.3)$$

P/V minimization can be performed for the specific altitude and for the MTOW or the average weight during the cruise phase.

$$\min\left(\frac{P}{V}\right) \quad (7.4)$$

Best range power can therefore be approximated by minimizing P/V (Equation 7.4) according to Johnson [25]. For the GeoCopter GC-201 this is at approximately 30 m/s at sea level and 100 kg MTOW, above the best endurance velocity which is at approximately 20 m/s.

Best Endurance Power

The best endurance power is when the total power requirement is lowest. At sea level, this occurs at approximately 20 m/s (V_{BE}). This actually matches the velocity at which RoC is maximized. The best endurance power is the lowest power setting for level flight and is quite energy efficient compared to the hover power setting. The endurance is determined through specific endurance. Because this means minimum fuel usage, this occurs at the minimum power setting for a given altitude and weight. This can be clearly recognized in the power curves of the helicopter.

$$E = \int \frac{dE}{dW_F} dW_F \quad (7.5)$$

Best RoC/RoD Velocity

The velocity at which the maximum RoC can be obtained and at which descent power is lowest is the same as that for best endurance due to the lowest power requirement. The benefit is the highest excess power as the difference between available and required power is largest. Estimates for RoC can be determined using this information. For larger forward velocities the climb rate can be directly approximated through the excess power ΔP . This climb rate calculation is also seen in Equation 7.6 [25]. For lower velocities this is no longer valid due to the far-field freestream flow above the rotor is no longer 0.

$$V_{climb,ROC} = \frac{P_a - P_r}{W} = \frac{\Delta P}{W} \quad (7.6)$$

Power in Vertical Climb and Descent

A vertical climb phase is included for the reason of possible obstacles in the vicinity of the take-off and landing area. It is therefore important to have sufficient available power to perform a vertical climb (OGE) at moderate climbing speeds.

Momentum theory changes in the case of vertical climb or descent, because the freestream velocity above the rotor is suddenly increased by the climb rate. In combination with the induced velocity by the rotor, the power requirements vary. Equation 7.7 shows the relationship between climb rate and excess power for the vertical sections. This is under the assumption that the climb rate is small, but is often valid until the point where the climb rate is equal to the induced velocity in a hover condition, which can be approximated using Equation 7.8. If it is assumed that the thrust is approximately equal to the MTOW of the helicopter, this value is 6.5m/s. According to Johnson [25], the vertical climb rate of the vehicles is generally below this induced velocity and therefore the assumption valid. The maximum vertical climb rate considered in all analyses will be 4 m/s.

$$V_c \cong \frac{2\Delta P}{T} \quad (7.7)$$

$$v_i = \sqrt{\frac{T}{2\rho A}} \quad (7.8)$$

The induced velocity decrease due to the climb speed doubles the effectiveness of a given power change compared to a climb with a forward velocity. It is assumed that $T \approx W$ for small climb rates. In most analyses, the vertical sections are between 0 and 100 meters altitude with a climb rate of 4 m/s and descent rates of -2 m/s. In the optimization and final sensitivity analysis, these values will change.

7.4.8. Power Overview

Figure 7.7 shows the effect of climbing on the power requirement, taking previous considerations into account. For vertical rates, the excess power is double as effective compared to climbing at forward speeds. However, the power level of level hover flight is also higher.

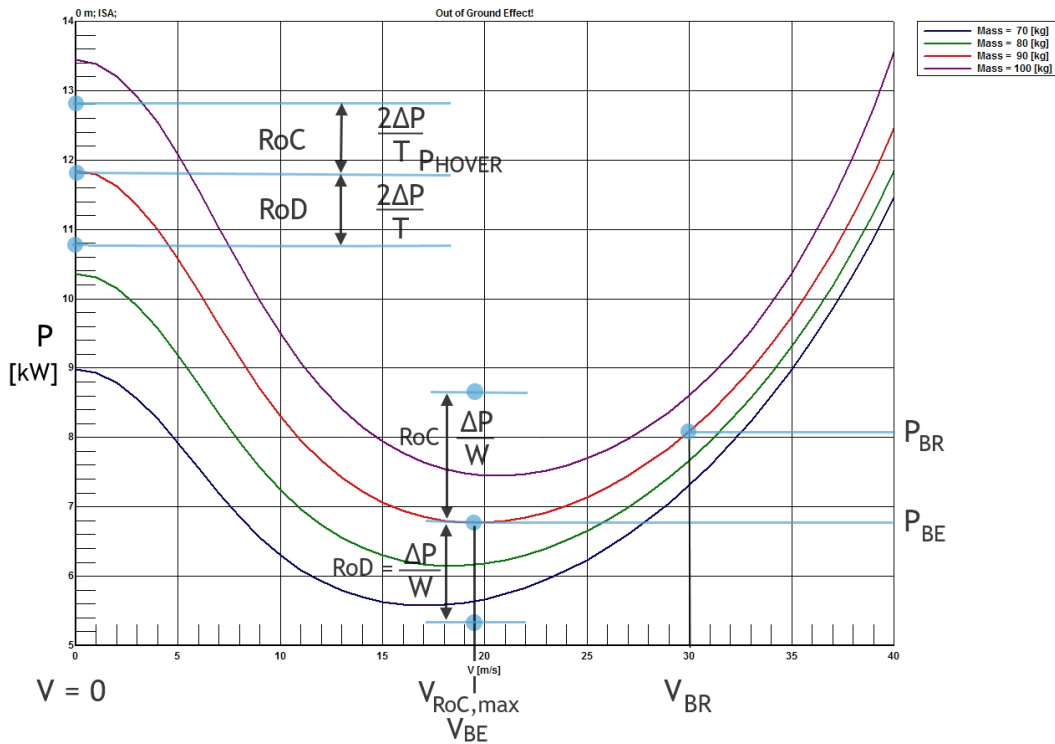


Figure 7.7: Power Levels in P-V curve drawn for 90 kg. An indication of the best endurance, best range and climb/descent rates is given

Chapter Conclusion

This chapter gave an overview of the unmanned GeoCopter GC-201, its weight and volume budget. An overview of power requirements and mission profiles was provided, which form the test environment of this thesis. Although the power curves (P-V curves) were shown in this chapter, it was not explained how these were obtained.

The next chapter explains more thoroughly how the P-V curves were constructed. This was mainly done through the validated tool EMPRESS within NLR. The results from this tool were again verified using helicopter theory. Validation with existing sea level data sets was performed, available for a number of maximum take-off weights. Chapter 8 will also give a performance overview of the micro gas turbine powered helicopter.

Helicopter Performance Requirements

This chapter elaborates on the helicopter performance and modelling. A discussion of the background of helicopter theory is performed for a better understanding of helicopter performance. Furthermore, it is used for verifying the EMPRESS model outputs but also directly used to derive inputs into the model. Also, some assumptions could be checked for validity using this background info. Furthermore, this chapter gives a performance overview of current micro gas turbine powered helicopter.

8.1. Assumptions

- **RoC:** $\Delta P/W$ is the estimate used for power levels in non-level flight
- **Vertical RoC:** $2\Delta P/T$ is valid for most helicopters in vertical climb/descent [25].
- **Thrust Equals Weight:** $T \approx W$ is used for the majority of the background equations that are used for estimating the parameters in the EMPRESS model, but the EMPRESS model does take into account the download from the main rotor onto the fuselage. However, for climb power requirements this assumption was still used for the top first two assumptions.

8.2. Theory: P-V curve

For horizontal flight in which the thrust is approximately equal to weight ($T \approx W$), power curves (or P-V curves) can be plotted for a specific helicopter at specific weight and altitude. These can then be used to determine power requirements for level flight as well as climb and descent phases. Figure 8.1 shows the power distribution, which consists of main rotor induced power (flow acceleration), blades profile power and helicopter parasitic power. Power also needs to be delivered to the tail rotor, miscellaneous hardware and payload. Tail rotor power generally decreases with forward motion.

8.3. Helicopter Background Equations

The helicopter tool EMPRESS (NLR) was used to obtain the power curves for different conditions. Because of confidentiality reasons, this report includes a generic model that has very similar performance to the actual helicopter, but not necessarily all inputs are correct. In order to understand helicopter performance and power requirements better, this section is dedicated to helicopter performance theory in order to understand the effects of the input parameters in EMPRESS. This helped getting first estimates on the parameters used in EMPRESS based on widely available helicopter data.

8.3.1. Hover Power

The hover power is determined through a relatively simple and straightforward analysis. Following momentum theory, the ideal power can be derived as Equation 8.1, given that $T \approx W$ and fuselage drag (D_f) is assumed ≈ 0 . The EMPRESS tool will also take into account this fuselage download through a download factor input.

$$P_{hover,id} = T \cdot v_i = T \sqrt{\frac{W}{2 \cdot \rho \cdot \pi \cdot R^2}} \approx \sqrt{\frac{W^3}{2 \cdot \rho \cdot \pi \cdot R^2}} \quad (8.1)$$

Deviations from the ideal power come from non-uniform induced velocity distribution on the rotor disc, rotational velocity in the wake and the blade rotor. The actual power requirement by the blade is increased because of the aforementioned effects, which result in the figure of merit (FM). This is seen in Equation 8.2. This value is generally between 0.6 and 0.8. A high FM means an (almost) ideal rotor with no blade drag nor

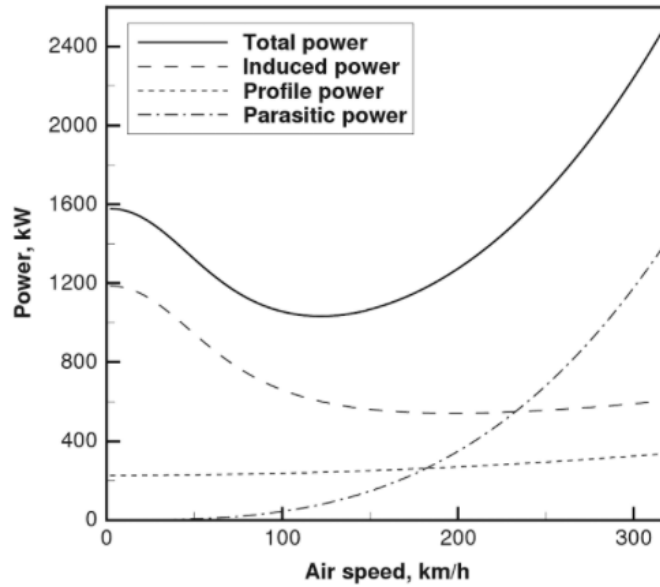


Figure 8.1: Helicopter power distribution in terms of profile, induced and parasitic drag [16]. The profile power is of the main rotor as a result of profile drag. Induced drag reduces with airspeed as a result of the air inflow angle into the rotor

other losses. A low FM (0.6) indicates a rotor design that most likely performs better at higher forward speeds. FM is an indication of hover efficiency for the main rotor only.

$$P_{hover,actual} = \frac{P_{hover,id}}{FM} \quad (8.2)$$

The FM can also be determined through blade element momentum (BEM) theory, which allows for a better understanding of hover at blade level. This is the method that the EMPRESS model also uses. This is seen in Equation 8.3. This also includes profile drag from the blades on top of the induced power from the induced velocity and normal force on the blade elements which form P_i . This does not yet include tail rotor power. The induced power is necessary to overcome the induced drag from the blades. The induced power is estimated in BEM through Equation 8.4 as the integral cannot be calculated analytically as v_i changes along the radius. To account for this non-uniform inflow, the correction factor k is used for the hover phase. This correction is in EMPRESS present in both the hover and forward speed phases, although it has a smaller effect on the forward speed phase due to lower induced power and higher parasitic power.

$$P_{hov} = P_i + P_{prof} \quad (8.3)$$

$$P_i = N \int_0^R dT \cdot v_i \approx k \cdot P_{id} \approx k \cdot T \cdot v_i \quad (8.4)$$

The profile power (Equation 8.5) is to overcome the blades profile drag and hence depends on the solidity factor σ . Another factor is the mean profile drag ($\bar{C}_{D,p}$) of the rotor blade. The solidity already includes the number of blades according to the definition. Solidity is normally low when rotor diameter is small. The Robinson R22 for example has a solidity under 0.05 for a rotor diameter that is about 5 meters. Equation 8.5 shows a power overview of the hover flight, including tail rotor power and power for other components.

$$P_{hov} = P_i + P_{prof} + P_{tail} + P_{misc} = k \cdot T \cdot v_i + \frac{\sigma \bar{C}_{D,p}}{8} \cdot \rho (\Omega R)^3 \cdot \pi R^2 + P_{tail} + P_{misc} \quad (8.5)$$

If tail and externals are not taken into account, then the \approx indication in Equation 8.6 holds true. However, performing tail rotor calculations will show that approximately 10% of the total power is required for the tail rotor. EMPRESS does take this into account and tail rotor power estimates were similar to the EMPRESS tool.

$$FM_{BEM} = \frac{P_{id}}{P_{hov}} = \frac{P_{id,hov}}{P_i + P_p + P_{tail} + P_{ext}} \approx \frac{P_i}{P_i + P_p} \quad (8.6)$$

8.3.2. Vertical Climb and Descent

The rate of climb is double of what would be estimated from the excess power in hovering flight due to additional air inflow from the upward movement [25]. Equation 8.7 shows the rate of climb in a vertical motion under the assumption that $T \approx W$.

$$C = \frac{2(P_d - P_{hov})}{W} \quad (8.7)$$

8.3.3. Download in Hover

Download in hover occurs due to fuselage drag from the downwards induced flow from the rotor. This means additional thrust is required and therefore thrust does not exactly equal weight. A download factor has to be considered in EMPRESS, which is embedded in the software. This is generally approximately 5%. The higher this value, the more the helicopter is pushed down by the main rotor and the more thrust/power the main rotor needs to deliver.

8.3.4. Forward Flight: Glauert Momentum Theory

Forward flight is another consideration in helicopter performance. Because there is a forward flight velocity component, the flow around the disc is asymmetric and even reversed flow is observed. The forward moving blade will be around drag divergence velocity and stall may occur on the aft-moving blade. Hence these are important parameters in forward moving flight.

Momentum theory in forward flight becomes quite different. Glauert proposed [25] a modified actuator disc, which bends down across the rotor disc. This can be seen in Equations 8.8 and 8.9.

$$V_R \approx \sqrt{V^2 + v_i^2} \quad (8.8)$$

$$v_i = \frac{T}{2\rho\pi R^2 V_R} \quad (8.9)$$

8.3.5. Forward Flight: BEM Theory

An important factor in forward flight is the non-dimensional advance ratio μ . One important consideration in forward flight is the fact that the drag that the rotor has to overcome is the difference between the advancing and retreating rotors. There is a difference between profile drag power (P_p) and total drag power P_d , in which the former only takes into account the frictional drag, but the latter has to consider the difference between advancing and retreating rotor blades. Equation 8.10 shows the advance ratio approximation used to non-dimensionalize the forward velocity.

$$\mu \cong \frac{V}{\Omega R} \quad (8.10)$$

The advance ratio μ is necessary for solving the integrals in solving for the profile drag P_p , resulting in Equation 8.11. The rotor drag power is calculated by Equation 8.12. This, again, is caused by the difference between advancing and retreating side.

$$P_p = \frac{\sigma \bar{C}_{Dp}}{8} \rho (\Omega R)^3 \pi R^2 (1 + \mu^2) = P_{p,hov} \cdot (1 + \mu^2) \quad (8.11)$$

$$P_d = \frac{\sigma \bar{C}_{Dp}}{4} \rho (\Omega R)^3 \pi R^2 \mu^2 \quad (8.12)$$

$$P_p + P_d = \frac{\sigma \bar{C}_{Dp}}{4} \rho (\Omega R)^3 \pi R^2 (1 + 3\mu^2) = P_{p,hov} \cdot (1 + 3\mu^2) \quad (8.13)$$

This expression is normally underestimated and a correction factor of 4.65 - according to the Bennett approximation - is used as in Equation 8.14 [25].

$$P_p + P_d = P_{p,hov} \cdot (1 + 4.65\mu^2) \quad (8.14)$$

The value \bar{C}_{Dp} can be approximated graphically as a function of lift coefficient and tip mach number. This can be done using Equations 8.15 and 8.16 and graphically determined based on mean lift coefficient and tip mach number [25]. Approximations using these equations show similar results to the EMPRESS model which bases these drag components on standard airfoils.

$$\tilde{C}_L = \frac{6.6C_T}{\sigma} \quad (8.15)$$

$$C_T \approx C_W = \frac{W}{\rho\pi R^2(\omega R)^2} \quad (8.16)$$

Also induced power $k \cdot T v_i$ reduces with increasing speed as a result of Glauert approximation in which the induced velocity reduces with increasing forward speed, as is also seen in Figure 8.1.

8.3.6. Fuselage Flat Plate / Parasitic Drag Power

This is the flat plate drag in forward flight, which, multiplied by velocity, results in the parasitic drag power from the fuselage. This is different from the download created by the rotor on the fuselage. Equation 8.17 shows the calculation of parasitic fuselage drag based on equivalent drag area. Due to the proportionality V^3 this effect is predominantly seen at higher velocities. The equivalent drag area is based on the drag divided by the dynamic pressure. This was estimated to be equal to 0.16 for the GC-201.

$$P_{par} = D_{par} \cdot V = \sum (C_D S)_S \cdot \frac{1}{2} \rho V^3 \quad (8.17)$$

8.3.7. Total Power in Forward Flight (BEM)

Equation 8.18 indicates the total power components in forward flight. Using previous results, this can also be written as Equation 8.19.

$$P = P_i + [P_p + P_d] + P_{par} + P_{tail} + P_{misc} \quad (8.18)$$

$$P = k \cdot T v_i + \left[\frac{\sigma \tilde{C}_{Dp}}{8} \rho (\Omega R)^3 (1 + 4.65 \mu^2) \right] + \sum (C_D S)_S \frac{1}{2} V^3 + P_{tail} + P_{misc} \quad (8.19)$$

8.4. EMPRESS Inputs

This section discusses the inputs provided to EMPRESS to create P-V curves corresponding to the available data for the GC-201. The end results showed a good correlation with this data for hover, medium speed and high speed in which stall and compressibility become more prominent. Some of the inputs were directly obtained from the helicopter itself, others were derived from literature resulting from the previous discussion [25]. An overview of inputs is provided in Table 8.1.

Main Rotor

Blade diameter and RPM were known parameters, as well as the number of blades. The chord of the blades was estimated to be 0.134 m, which was verified to be close to the actual dimension. Again, for confidentiality reasons, not all parameters are known but estimates are chosen to be not too far off or, within the suggested range by EMPRESS or derived from standard values in literature. Main rotor blade roughness was kept at the default value (1.0 in EMPRESS). This is not very sensitive to the input, a 10% increase causes an approximate 2% increase in hover power. The tip speed is determined for hover and therefore does not take into account the additional velocity due to forward flight. The solidity ratio is determined directly with Equation 8.20. The tip speed for the main rotor is relatively low at this RPM and equal to 129.6 m/s or Mach 0.38.

$$\sigma = \frac{N_m \cdot A_B}{A_m} = \frac{6 \cdot c_B}{\pi \cdot D_m} \quad (8.20)$$

The induced correction factor for the hover condition is set at 1.2 for hover and 1.26 for forward flight performance. The main rotor airfoil is the default airfoil in EMPRESS, slightly altered to resemble the GC-201 data better, especially the stall and compressibility behaviour. This was performed within suggested values.

Tail Rotor

The tail rotor has a much less significant effect on the total power, but at hover is still approximately 10% of the total power in the current configuration. The chord was set at 0.05 with a diameter of 0.53 [22]. Based on common values in literature, an RPM ratio between the tail and main rotor was set at 4.5. This results in a tail rotor RPM of 3375. The tip Mach number is then 0.275 in hover and will be slightly higher for advancing blades in forward flight. The blade drag coefficient is considered to be 0.01, similar to mean profile drag (\tilde{C}_{Dp}) values of the main rotor. The sensitivity of the results to this factor is insignificant. The induced factor of the tail rotor is considered to be 1.17 and also shows minimal effects to the power curve because the tail rotor

is a fraction of the total power. The blockage factor is set at 1.15 (hover) and 1.24 (regime), which accounts for tail rotor ineffectiveness from flow being blocked by the airframe. This blockage factor affects the thrust requirement directly from main rotor power, RPM and distance between the main and tail rotor [53], see Equation 8.21, where B_T is the blockage factor. This thrust requirement can then be used to calculate the induced velocity of the tail rotor and subsequently the induced power with the induced factor. This method showed very similar results to what was obtained with the EMPRESS tool. Profile drag is small for the tail rotor. The fin lift area has an insignificant effect on the power curves and was assumed at a lift coefficient of 0.

$$T_T = B_T \left(\frac{P_{MR}}{\Omega_{MR} \cdot l_{boom}} \right) \quad (8.21)$$

Engine Data

Two micro gas turbines of 8kW each are present in the helicopter. The SFC at maximum continuous power is equal to 1.32 kg/kW/hr [23]. The Jet-A1/oil mixture has an estimated density of 0.8kg/L. Installation losses in the model are taken as 5% and gearbox mechanical efficiency at 0.97. Because of lower maximum continuous power (MCP) than specified, the GC-201 currently operates at 90 kg MTOW because only 12 kW total can be reached. For this analysis, a 16 kW MCP is taken.

In order to complete the model, the turboshaft available power was scaled using ISA data for different altitudes [34] in Equation 8.22, resulting in the available power of Figure 8.2.

$$P_{av} = P_{MSL} \cdot \left(\frac{\delta}{\theta} \right) \quad (8.22)$$

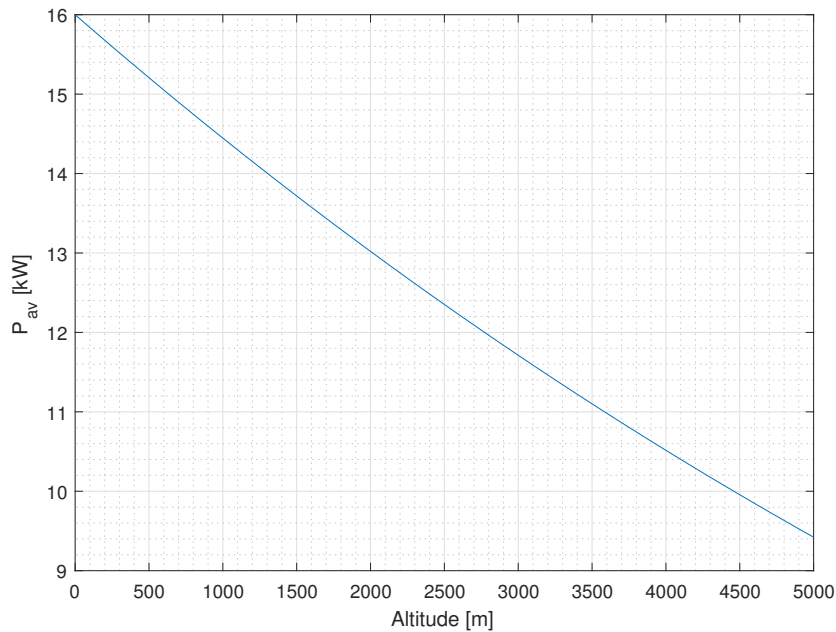


Figure 8.2: Engine available power corrections with altitude

Airframe

The most important part for the airframe is the horizontal drag area that determines parasitic drag. Besides that, the effect of the main rotor on the fuselage is taken into account by the download in hover. This effect increases the necessary thrust from the drag induced by the main rotor on the fuselage. Also, main-to-tail rotor spacing was estimated at 2.35 m. General data shows a MTOW of 100 kg, with an empty mass of 45.5 kg. When maximum fuel is in the helicopter, 14.5kg of payload can still be placed in the aircraft.

Parameter	Value	Unit	Description
Main Rotor			
N_{MR}	3	[-]	Number of Blades
c_{MR}	0.134	[m]	Blade Chord
D_{MR}	3.3	[m]	Main Rotor Diameter
σ	0.0776	[-]	Solidity
λ	1	[-]	Taper Ratio
Induced Factor (Hover)	1.2	[-]	Induced Factor (Hover)
Induced Factor (Regime)	1.26	[-]	Induced Factor (Regime)
RPM	750	[RPM]	Main Rotor
Tip Speed	129.59	[m/s]	Main rotor tip speed (hover)
Tail Rotor			
N_{TR}	2	[-]	Number of Tail Rotor Blades
c_{TR}	0.05	[-]	Tail Rotor Chord
D_{TR}	0.53	[-]	Tail Rotor Diameter
TR/MR ratio (RPM)	4.5	[-]	RPM Ratio
RPM_{TR}	3375	[RPM]	Tail Rotor RPM
Induced Factor (Hover)	1.17	[-]	Induced Factor (Hover)
Induced Factor (Regime)	1.17	[-]	Induced Factor (Regime)
Blockage Factor (Hover)	1.15	[-]	Blockage Factor (Hover)
Blockage Factor (Regime)	1.24	[-]	Blockage Factor (Regime)
Fin Lift Coefficient	0	[-]	Fin Lift Zero
Fin Area	0.2	[m ²]	Small
Engine / MGB			
Number of Engines	2	[-]	-
MCP per Engine	8	[kW]	Maximum Continuous Power
SFC at MCP	1.32	[kg/kW/hr]	Specific Fuel Consumption
Density Jet-A1	0.8	[kg/L]	-
Installation Loss	5	[%]	-
Gearbox η_{mech}	0.97	[-]	Mechanical Efficiency Gearbox
Airframe			
Horizontal Drag Area (C_dS)	0.16	[m ²]	-
Download in Hover	1.07	[-]	Download on Fuselage
Rotor Spacing	2.35	[m]	Main Rotor / Tail Rotor
General Mass Data			
MTOW	100	[kg]	Vehicle MTOW for 16kW rating
Empty Mass	45.5	[kg]	No Min. Fuel / Sec. Autopilot
Minimum Fuel	4.4	[kg]	Tank Size 40kg/50L
Available Fuel Mass	35.6	[kg]	Fuel Mass
Available Payload Mass (Max Fuel)	14.5	[kg]	At Maximum Fuel
General Data			
μ Regime	0.15	[-]	Advance Ratio
Main Rotor Height	1.0	[m]	Matching IGE/OGE Effects
Climb Efficiency	100	[%]	Assumed 100% Climb Efficiency

Table 8.1: Inputs and derived inputs for the EMPRESS model

8.5. Resulting P-V Curve

Figure 8.3 shows the P-V curves for different take-off masses resulting from the EMPRESS model with the previously discussed inputs. Figures 8.4 and 8.5 show the curves for a range of altitudes at 90 and 100 kg.

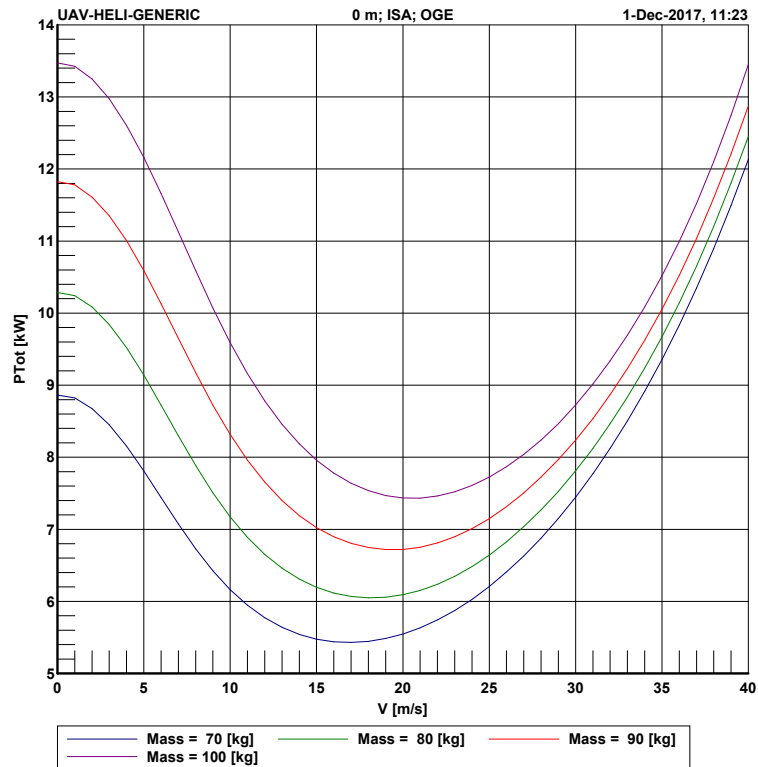


Figure 8.3: P-V curves at sea level (OGE) for 70 to 100 kg

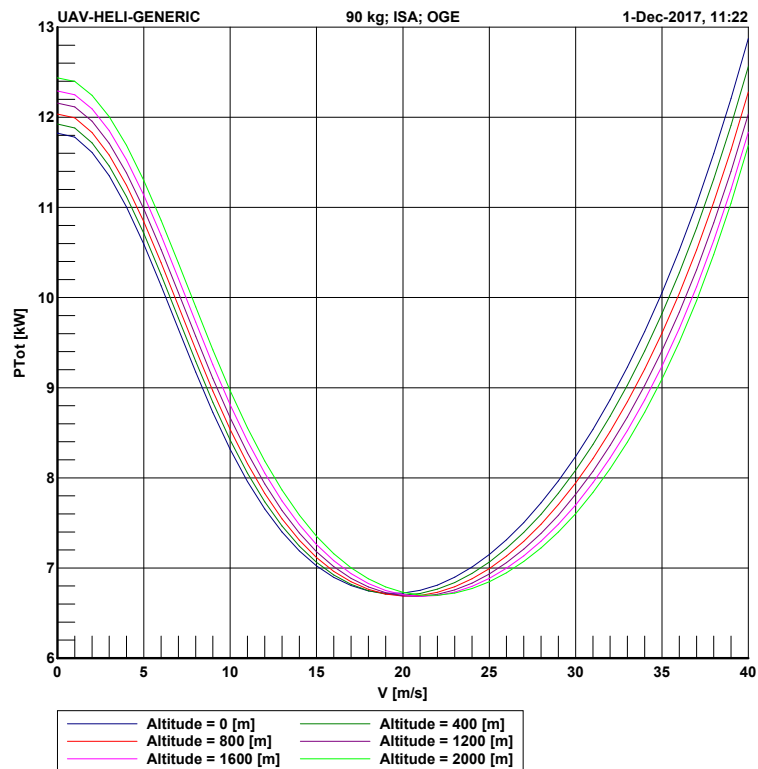


Figure 8.4: P-V curve at 90kg for an altitude range of 0-2000 m

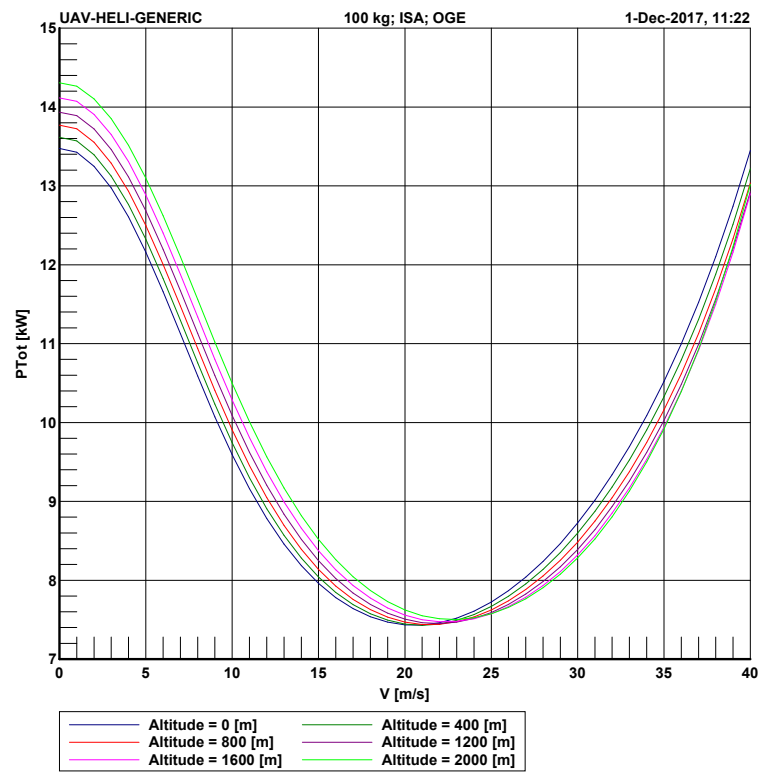


Figure 8.5: P-V curve at 100kg for an altitude range of 0-2000 m

8.6. MGT (Conventional) Performance Analysis

This section elaborates on the analysis of the conventional MGT powered Geocopter GC-201. The data in this section can be used as a reference regarding the performance of the helicopter.

8.6.1. Hover Ceiling

Jane's [22] indicates a service ceiling of 1800 meters for the Geocopter GC-201. A high power requirement can be observed at hover and the hover limit was determined for an altitude up to 2400 meters based on the power curves and the altitude derating of the engines. This is shown in 8.6. It can be seen that this results in a hover limit of approximately 2300-2400 meters for 90 kg and a reduced limit of approximately 1300 meters for 100 kg. Assuming Jane's indicates a hover ceiling, the values correlate quite well.

8.6.2. Forward Speed Ceiling and Flight Envelope

For different forward speeds, the power requirements vary significantly as can be seen in standard helicopter P-V curves. The EMPRESS model was used to determine total power requirements at different altitudes for the full range of forward velocities. Figure 8.7 and Figure 8.8 show the maximum altitude for the indicated forward speeds. Figure 8.9 shows the approximate flight envelope for the turboshaft powered GC-201, derived from the data of the previous figures. This was done for a weight of 100 kg. The envelope clearly shows that during hover, the maximum altitude is low as a result of the large power requirement. A maximum altitude of 4500 m could be reached at the best endurance velocity of around 20 m/s. However, it is expected that for the majority of applications this altitude is not needed.

It should be noted that a FC-B configuration has a large effect on this flight envelope. As a result of the sizing of the fuel cell for the cruise phase at best endurance or best range speed, the battery is used for all peak power phases. This means that higher altitudes - higher than what the FC is designed for - can be reached, but only for a short amount of time. The power requirements for cruise at different altitudes are very close together, which means only some additional power (few hundred Watts) from the battery may be necessary at higher altitudes. However, with the battery delivering peak powers up to 16 kW, the theoretical flight envelope is no worse than the one seen in this analysis as battery power is not lost at increased altitudes. Therefore, only the fuel cell power decreases slightly at elevated altitude.

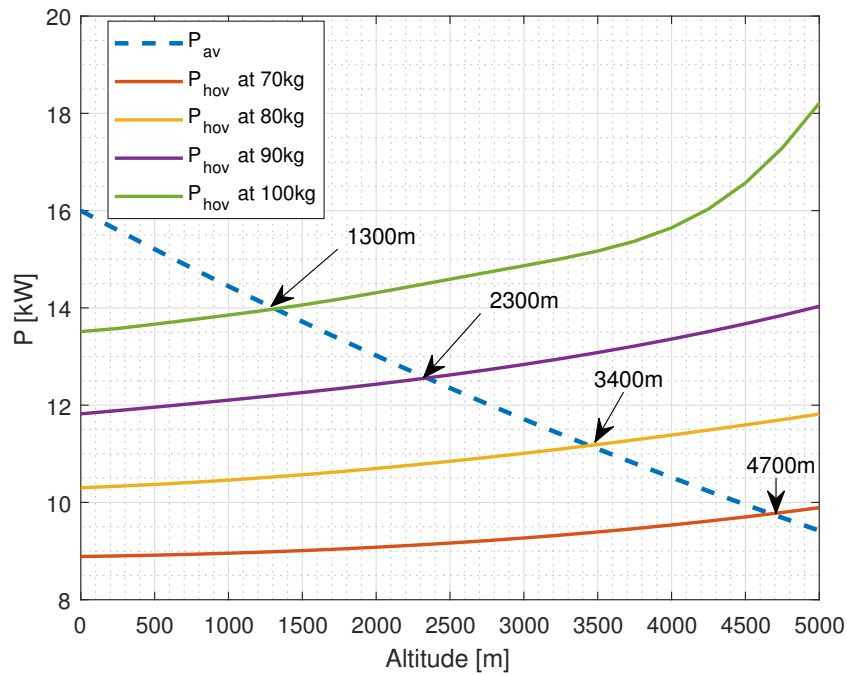


Figure 8.6: Hover altitude limit using the ISA standard

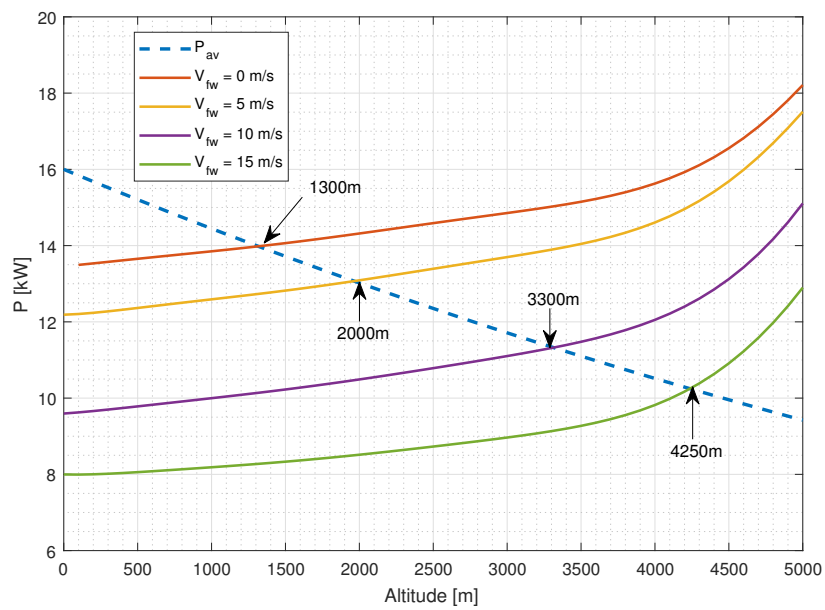


Figure 8.7: Altitude limit for level flight at forward speeds from 0 to 15 m/s using the ISA standard. The weight is 100 kg

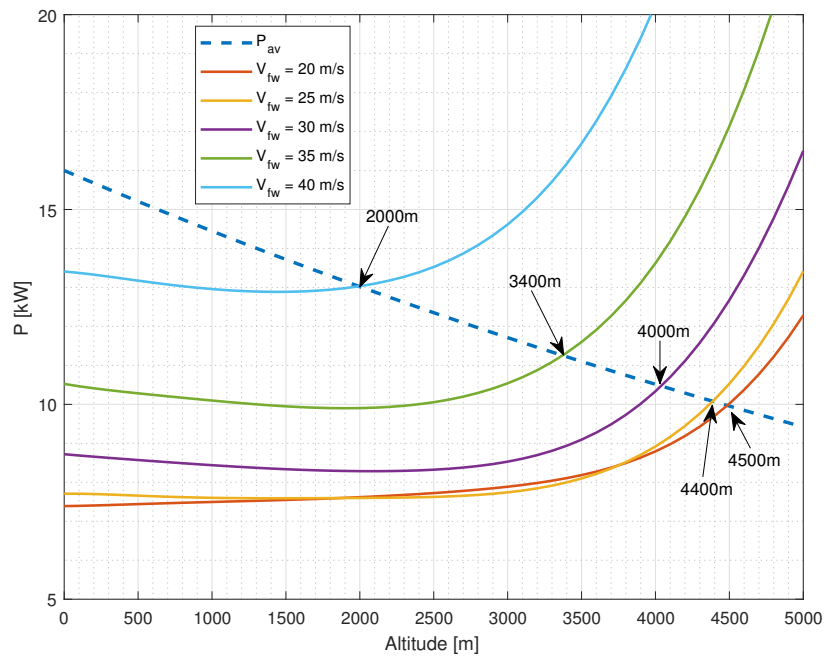


Figure 8.8: Altitude limit at altitude for level flight at forward speeds from 20 to 40 m/s using the ISA standard. and speeds from 0 to 15 m/s using the ISA standard. The weight is 100 kg

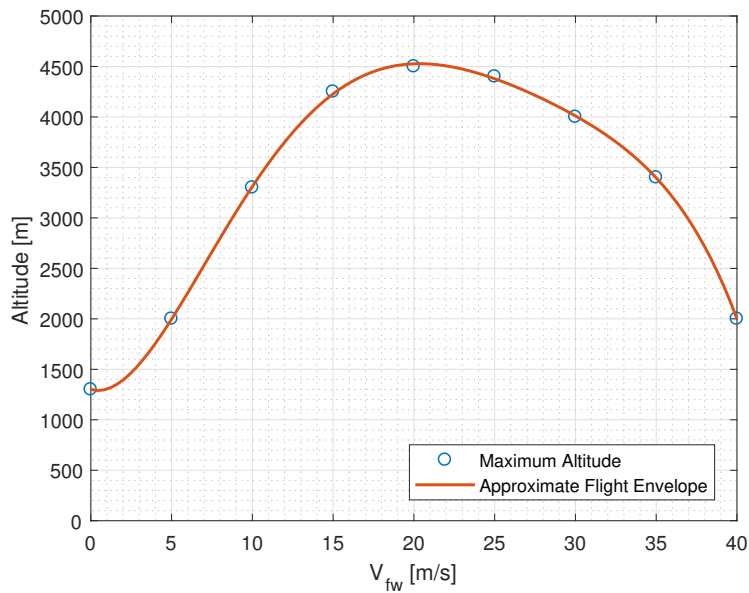


Figure 8.9: Approximate Flight Envelope of Gas Turbine Powered (Turboshaft) GC-201 at 100 kg weight. No data was retrieved beyond 40 m/s, but its maximum operating velocity near sea level is close to 45 m/s. This is because the power component due to the parasitic drag contribution scales with V^3

8.7. Segment Analysis: Conventional

It was chosen to have a maximum vertical rate of climb to 100 meters to ensure vertical clearance and to make sure the maximum power of 16kW at sea level is approximately reached. According to the climb theory and the 100 kg P-V curve, the maximum vertical rate of climb is approximately 4 m/s.

For the forward flight climb phase, the RoC is set at the maximum rate of climb possible at intermediate altitudes for this the conventional analysis, as the EMPRESS tool allows this to be done through a mission profile run.

For the best endurance case, the mission profile is quite simple, considering the fact that altitude has no effect on the power level and speed is not of any importance and the fuel usage in the segments that are not level flight only make up a very small portion of the fuel weight. Therefore, the range and endurance for the conventional MGT powered GC-201 are largely a function of the actual cruise phase and not so much the climb and descent phases. This will be seen in the fuel weight fractions during cruise in the following sections.

It should be noted that the mission profiles considered have level cruise, without an altitude change. Due to a mass reduction during the flight, there are further optimization options but that is out of the scope of this study - which has a focus on Battery-only and FC-B configurations.

8.7.1. Best Endurance

Table 8.2 shows the endurance mission for the MGT powered helicopter, with the maximum fuel tank size in the current configuration. That means 40 kg of fuel is available and 14.5 kg of payload is included when the MTOW is 100 kg. It can be shown that the helicopter can be flown for 219 minutes, with 96% of the fuel used during the cruise phase. When the entire payload is replaced with fuel in Table 8.3, the endurance is 312 minutes and a weight percentage of 97.2% in the cruise phase.

As a result of the helicopter weight reducing as fuel is burnt, a clear difference between power required in the initial hover and final hover phase can be seen, which is about halved. The impact weight has on the power requirement becomes very clear here and is a major advantage as average power requirements go down and a larger distance can be travelled. For battery or FC-B configurations, this is not the case and the entire flight is performed around the take-off weight, with only minor mass reductions as the hydrogen storage tank is depleted.

Segment	Description	Altitude [m]	Time [min]	Speed [m/s]	V_C [m/s]	P_r [kW]	Fuel Used [kg]
1	Hover OGE	0	0.5	0	0	13.45	0.2
2	Vert. Climb	0-100	0.42	0	4	15.88	0.2
3	Climb	100-500	0.98	20.6	6.8	15.15	0.3
4	Cruise	500	212	18.6	0	4.84	38.4
5	Descent	500-100	3.34	15.9	-2	3.56	0.5
6	Vert. Descent	100-0	1.67	0	-1	7.45	0.3
7	Hover OGE	0	0.5	0	0	7.56	0.1
			Total Time	219.4	[min]	Total	40
			Cruise Time	96.6	[%]	wt% Cruise	96.0
			Total Distance	241.0	[km]		

Table 8.2: Endurance profile for flight profile with a V_{BE} cruise phase at 500 m, 14.5 kg payload and 40 kg fuel.

8.7.2. Best Range

This section discusses the best range scenarios for the MGT powered GC-201. This means that the cruise phase uses a best range strategy. The average speed in the cruise phase is slightly higher than what will be seen in the battery-only or FC-B configurations that operate at 100 kg. This is a result of weight averaging in the sections, with a much lower average weight for the conventional power system.

500m

Table 8.4 shows the results for a best range mission profile at 500 m. The range with 40 kg fuel and 14.5 kg payload equals 345 km with almost 3 hours of flight time. If the payload is replaced by extra fuel, the range increases to 480 km and 4 flight hours. This can be seen in Table 8.5.

It should be noted that the fuel tank can clearly also be made smaller and more than 14.5 kg payload can be loaded onto the helicopter.

Segment	Description	Altitude [m]	Time [min]	Speed [m/s]	V_c [m/s]	P_r [kW]	Fuel Used [kg]
1	Hover OGE	0	0.5	0	0	13.45	0.2
2	Vert. Climb	0-100	0.42	0	4	15.88	0.2
3	Climb	100-500	0.98	20.6	6.8	15.16	0.3
4	Cruise	500	305	17.5	0	4.08	52.9
5	Descent	500-100	3.34	13.7	-2	3.14	0.4
6	Vert. Descent	100-0	1.67	0	-1	5.83	0.3
7	Hover OGE	0	0.5	0	0	5.9	0.1
Total Time			312.4	[min]	Total		54.4
Cruise Time			97.6	[%]	wt% Cruise		97.2
Total Distance			323.0	[km]			

Table 8.3: Endurance for flight profile with a V_{BE} cruise phase at 500 m, no payload and 54.5 kg fuel.

Segment	Description	Altitude [m]	Time [min]	Speed [m/s]	V_c [m/s]	P_r [kW]	Fuel Used [kg]
1	Hover OGE	0	0.5	0	0	13.45	0.2
2	Vertical Climb	0-100	0.42	0	4	15.88	0.2
3	Climb	100-500	0.98	20.6	6.8	15.16	0.3
4	Cruise	500	168	33.8	0	7.94	38.5
5	Descent	500-100	3.34	15.9	-2	3.56	0.5
6	Vert. Descent	100-0	1.67	0	-1	7.44	0.3
7	Hover OGE	0	0.5	0	0	7.55	0.1
Total Time			175.4	[min]	Total		40.1
Cruise Time			95.8	[%]	wt% Cruise		96.0
Tot. Distance			345.1	[km]			

Table 8.4: Range for flight profile with a V_{BR} cruise phase at 500 m, 14.5 kg payload and 40 kg fuel.

Segment	Description	Altitude [m]	Time [min]	Air Speed [m/s]	V_c [m/s]	P_r [kW]	Fuel Used [kg]
1	Hover OGE	0	0.5	0	0	13.45	0.2
2	Vert. Climb	0-100	0.42	0	4	15.88	0.2
3	Climb	100-500	0.98	20.6	6.8	15.16	0.3
4	Cruise	500	237	33.5	0	7.38	52.9
5	Descent	500-100	3.34	13.7	-2	3.14	0.5
6	Vert. Descent	100-0	1.67	0	-1	5.83	0.3
7	Hover OGE	0	0.5	0	0	5.9	0.1
Total Time			244.41	[min]	Total		54.5
Cruise Time			97.0	[%]	wt% Cruise		97.1
Total Distance			480.33	[km]			

Table 8.5: Range for flight profile with a V_{BR} cruise phase at 500 m, no payload and 54.5 kg fuel.

1500m

Table 8.6 shows the results for a best range mission profile at 1500 m. The range with 40 kg fuel and 14.5 kg payload equals 365.2 km with over 3 hours of flight time. If the payload is replaced by extra fuel, the range increases to 515 km and over 4 flight hours. This can be seen in Table 8.7. Some improvement can be observed over the 500 m altitude scenario.

Segment	Description	Altitude [m]	Time [min]	Speed [m/s]	V_c [m/s]	P_r [kW]	Fuel Used [kg]
1	Hover OGE	0	0.5	0	0	13.45	0.2
2	Vert. Climb	0-100	0.42	0	4	15.88	0.2
3	Climb	100-450	0.85	20.6	6.9	15.27	0.3
4	Climb	450-800	0.91	21	6.4	14.66	0.3
5	Climb	800-1150	0.97	21.4	6	14.16	0.3
6	Climb	1150-1500	1.04	21.7	5.6	13.68	0.3
7	Cruise	1500	172	33.8	0	6.8	36.4
8	Descent	1500-100	11.67	16.6	-2	3.14	1.5
9	Vert. Descent	100-0	1.67	0	-1	5.82	0.3
10	Hover OGE	0	0.5	0	0	5.89	0.1
Total Time			190.53	[min]	Total		39.9
Cruise Time			90.3	[%]	wt% Cruise		91.2
Tot. Distance			365.2	[km]			

Table 8.6: Range for flight profile with a V_{BR} cruise phase at 1500 m, 14.5 kg payload and 40 kg fuel.

Segment	Description	Altitude [m]	Time [min]	Speed [m/s]	V_c [m/s]	P_r [kW]	Fuel Used [kg]
1	Hover OGE	0	0.5	0	0	13.45	0.2
2	Vert. Climb	0-100	0.42	0	4	15.88	0.2
3	Climb	100-450	0.85	20.6	6.9	15.27	0.3
4	Climb	450-800	0.91	21	6.4	14.66	0.3
5	Climb	800-1150	0.97	21.4	6	14.16	0.3
6	Climb	1150-1500	1.04	21.7	5.6	13.68	0.3
7	Cruise	1500	249	33.5	0	6.8	51
8	Descent	1500-100	11.67	14.3	-2	3.14	1.5
9	Vert. Descent	100-0	1.67	0	-1	5.82	0.3
10	Hover OGE	0	0.5	0	0	5.89	0.1
Total Time			267.53	[min]	Total		54.5
Cruise Time			93.1	[%]	wt% Cruise		93.6
Total Distance			515.3	[km]			

Table 8.7: Range for flight profile with a V_{BR} cruise phase at 1500 m, no payload and 54.5 kg fuel.

8.7.3. Payload-Range

It could be seen that the endurance is approximately ranging from 267.5 to 312 minutes if the fuel tank was made bigger from 40 kg to 54.5 kg. This is the maximum endurance that can be obtained, considering altitude has a small effect on endurance. It can be seen that there is a clear distinction between a profile for range of endurance. Also, the weight fraction in cruise is always over 90% for the conventional power system, meaning the cruise power is dominant for the range or endurance. When the cruise phase is shorter - which is expected for battery-only or fuel cell systems - the cruise phase may not be as dominant anymore. Reaching higher altitudes may not be beneficial when too much power is needed to get there and the phase which is spent at that altitude gets shorter.

Note that these results are based on the V_{BR} that is picked by EMPRESS. This should be very similar to how it is picked (minimum P/V) in this study. Slight deviations might be possible as the code behind the EMPRESS tool is not visible. Also, EMPRESS supposedly does sectional averaging and weight plays a major role here.

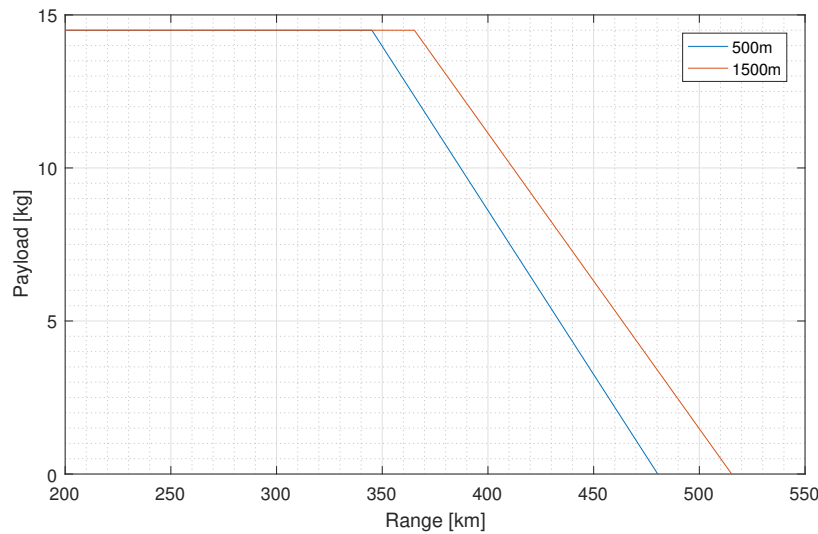


Figure 8.10: Payload-Range for a 100kg GC-201 at 500 meters and 1500 meters

Chapter Conclusion

This chapter worked towards the power curves of the helicopter used throughout this thesis. Both the endurance and range were estimated and show an endurance of approximately 4 hours and a range of up to 500 km for the conventional micro gas turbine powered helicopter. With a 14.5 kg payload, the range reduces to approximately 350 km. The payload can be further increased, but then the standard tank size for 40 kg Jet-A1 fuel has to be reduced. The next chapters will continue with the component sizing, starting with the fuel cell sizing. Best endurance and best range power levels are approximately 7.5 and 8.5 kW, which are the power requirements (at the rotor) for the fuel cell sizing. This does not yet include powertrain efficiencies. Additionally, the fuel cell needs to power the compressor.

Fuel Cell Sizing

This chapter focuses on the modelling of the fuel cell stack. First of all, the fuel cell performance strategy is laid out, after which the curve fitting of the polarization curve (I-V) is elaborated on through a curve fit parameter study and the least squares method applied. The reference stack and corresponding test data is then used for this curve fit at cell level, after which the full fuel cell stack sizing procedure is further elaborated on. The effect of increased or reduced stack pressure is also considered in the analysis. Finally, an overview of miscellaneous weight in a FC-B configuration is shown in the final section. It should be noted that the power density used for the reference stack already includes the cooling and humidification. The reference stack power density for this study will be shown to be approximately 550 W/kg and 500 W/L.

9.1. Assumptions

The assumptions for the fuel cell design are laid out below:

- The fuel cell stack is sized based on a reference stack that has integrated cooling features. The power and therefore power density of this stack hence contains both the fuel cells as well as the cooling components. The power density is relatively conservative at ~550 W/kg, considering other stacks without cooling or humidification components reach power densities between 1-2 kW/kg.
- The reference stack is self-humidifying, using water production to humidify the stack for better operation.
- Steady-state modelling is applied based on the polarization curve and the dynamic behaviour is not taken into account. The chosen strategy uses a nearly constant fuel cell power throughout the flight, with peak powers delivered by the battery pack.
- The pressure effect is modelled through a logarithmic approximation and the constant in this approximation is chosen to be a value within a common value range for different PEMFCs.

9.2. I-V Curve Modelling

There are different strategies possible for the modelling of the polarization curve (I-V). Furthermore, it should be noted that these curves can be modelled at stack level and cell level (i-V), where i is the current density (A/cm²). The starting point for steady-state modelling is generally by using available test data. In most cases, fuel cell manufacturers specify only the nominal curve, so limited data is available regarding the effect of pressure and other operating conditions.

Two options were considered: using an approximation of the pressure effect or using cell polarization curves at different pressure levels from experimental test data, such as in Figure 9.1. For the pressure effect, it has been shown by Larminie and Dicks [32] and Barbir [1] that reasonable results can be obtained by adding a term that uses the logarithmic scale of the pressure ratio. This is mostly valid in the ohmic range of the fuel cell polarization curve. The fuel cell model without the pressure correction is shown in Equation 9.1 with fitting parameters V_0 , B, R, m and n. The terms indicate the open circuit voltage, activation losses, ohmic losses and concentration losses respectively.

$$V = V_0 - B \cdot \ln(I) - R \cdot I - m \cdot e^{n \cdot I} \quad (9.1)$$

A parameter sensitivity was performed to understand the effects of the five parameters, V_0 (OCV in V), B (activation loss coefficient), R (ohmic resistance), m (coefficient in concentration loss) and n (exponential coefficient in concentration loss). The nominal fitting parameters were obtained from [69]. Figure D.1 to D.5 in Appendix D show the effect of these fitting parameters.

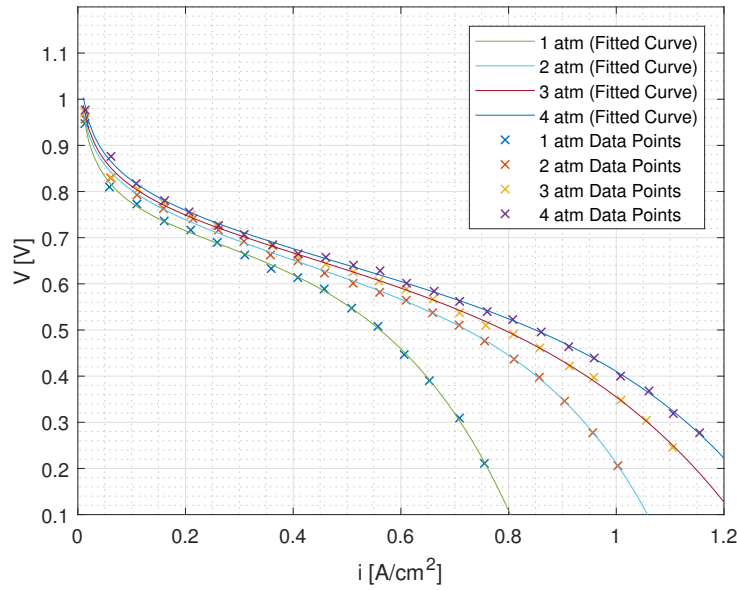


Figure 9.1: i-V curves used in the analysis by Datta and Johnson [8] showing the effect of changing stack pressure. Data sets from Datta and Johnson were refitted according to the described method in this chapter

9.2.1. Reference Stacks, Parameters and Hypothesis Test

The reference stack chosen for the analysis is a lightweight 200 W Aerostack, which was subsequently sized with the power density of the bigger 1 kW model, seen in Table 9.1. These stacks are self-humidifying and come with air cooling included. Similar power densities around 0.5 kW/kg are reached when considering the PowerCell stacks which use liquid cooling. The shown I-V curves in the data sheets are assumed to be net power outputs. Data sets for this stack were obtained from Verstraete et al. [69]. The data fit for the analysis in this thesis is performed at cell level. One of the advantages is that i-V curves can be easily compared, unlike full stack I-V curves.

Parameter	[W/kg]	Vol [L]	N_c	A [cm^2]	Pressure	Hum/Fan/Liq/Control
Aerostack 200	345	1.6	35	16.8	[1] amb.	Hum/Fan/Control
Aerostack 500	407	2				Hum/Fan/Control
Aerostack A1000	439 (2.5kg)	4.9				Hum/Fan/Control
Aerostack H1000	227					Hum/Fan/Control
PowerCell S2	360-724 at 5-25 kW	14.4-33.3				Hum/Liq
PowerCell S3 Prototype	2976					

Table 9.1: State-of-the-art commercial fuel cell stacks in the 200W to 25kW, showing power densities around 0.5kW/kg. The prototype PowerCell S3 shows increased power density and shows a future potential. The last column indicates the presence of a humidifier, fan, liquid cooling or control components

9.2.2. Pressure Modelling Approach

The pressure modeling approach is very straightforward, following the method as described by Larminie [32]. This is shown by ΔV_p - or the change in voltage - as a result of pressure in Equation 9.2. This means that the fuel cell model changes into Equation 9.3. This approach was shown to work well in the ohmic range of the fuel cell and was shown to be a value between 0.03 and 0.06 for a number of fuel cell stacks by Barbir and Larminie [1, 32]. Because there is no pressure data for the 200W Aerostack, this theory was checked in the ohmic range for two reference fuel cells. This is tabulated in Table 9.2, using data in the ohmic range from two sources [8, 71]. It shows that the range of constants indeed falls in the range indicated by Barbir and Larminie. A value of 0.06 was chosen for further analysis.

$$\Delta V_p = C \cdot \ln\left(\frac{P_{oper}}{P_{nom}}\right) \quad (9.2)$$

$$V = V_0 - B \cdot \ln(I) - R \cdot I - m \cdot e^{-n \cdot I} + C \cdot \ln\left(\frac{P_{oper}}{P_{nom}}\right) \quad (9.3)$$

Stack	Pressures [atm]	$\frac{P_2}{P_1}$	ΔV	C_1	$\frac{P_3}{P_2}$	ΔV	C_2	$\frac{P_{high}}{P_{low}}$	ΔV	C_3	C range
Datta & Johnson [8]	1-2-3-4	2	0.03	0.043	1.5	0.02	0.049	4	0.06	0.043	0.04-0.05
Wang et al. [71]	1-2.36-3.72	2.36	0.05	0.058	1.58	0.03	0.065	3.72	0.08	0.06	0.06

Table 9.2: Study on constant C in the pressure effect approximation showing that Larminie's [32] suggestion to use a value between 0.03-0.06 was quite correct on cell level

Figure 9.2 shows the least squares fit of the experimental data of Verstraete et al. [69]. The nominal pressure at which the fuel cell operates is approximately the ambient pressure. The final fit parameters are shown in Table 9.3 for the nominal pressure data set. The fit results are good with values for V_0 , B and R as expected. The effect of n is relatively small as a result of the small parameter m, expected due to very few data points for the concentration loss section.

Fitting Parameter	Value	Unit
V_0	0.83	[V]
B	0.014	[V/ln(A/cm ²)]
R	0.24	[Ω cm ²]
m	5.63E-06	[V]
n	11.42	[cm ² /A]

Table 9.3: HES Aerostack Ultralight 200W Single cell fitting parameters for nominal conditions, as seen in Figure 9.2

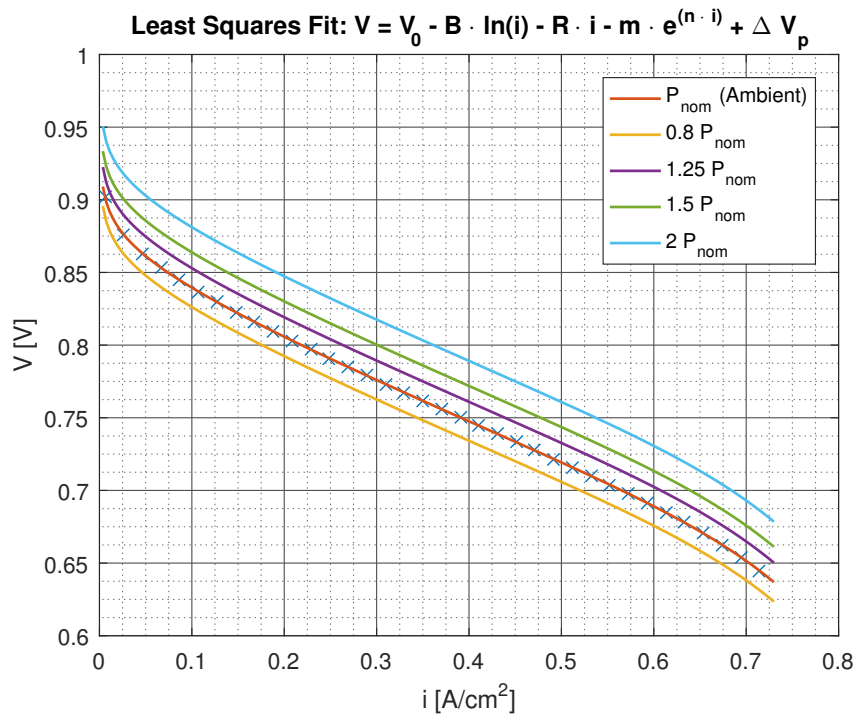


Figure 9.2: The Aerostack 200W fit for a single cell with $A = 16.8 \text{ cm}^2$ at the ambient temperature, with a pressure effect ΔV_p from 0.8 to 2 times the nominal ambient pressure

9.2.3. Least Squares MatLab: Algorithm and Application

This subsection describes the chosen fitting method in MatLab and includes its algorithm that was used to obtain the fit at nominal pressure in Figure 9.2. The empirical formula that requires fitting was described by Equation 9.1. This can be used for both the current (I) and current density (i) and it is just the coefficients and parameter values that will change when these are interchanged.

It can be seen that this is a non-linear formula with five parameters. This requires an optimization procedure for finding the right parameters. A least squares optimization was performed, using the *lsqcurvefit* Optimization Toolbox™ module in Matlab. The module is based on the *lsqnonlin*, but in the case of *lsqcurvefit* the empirical formula is required (and is in this case available).

$$\min_x \|F(x, xdata) - ydata\|_2^2 = \min_x \sum_i (F(x, xdata_i) - ydata_i)^2 \quad (9.4)$$

Equation 9.4 is the problem solved by the module in which the coefficients x are found. Vectors $xdata$ and $ydata$ come from the i and V data points of the i-V curve. The algorithm can be specified and is by default the trust-region-reflective algorithm. This can be changed and lower and upper bounds can be specified as well. Good results were obtained with the standard trust-region-reflective algorithm.

9.2.4. Mass Flow and Efficiency

This section elaborates on the mass flow analysis and the resulting efficiency of the considered cell for different stack pressures. Figure 9.3 shows the mass flow for the full 200 W HES Aerostack to confirm the approximation resembles the actual mass flow well. This linear approximation (following Equation 4.10) shows a direct relationship between mass flow of hydrogen and the current. This is already multiplied by the number of cells. The air flow is twice the stoichiometry mass flow and hydrogen flow is 1.2 times the mass flow needed for stoichiometry, based on commonly used factors [8, 32]. These are used throughout this study.

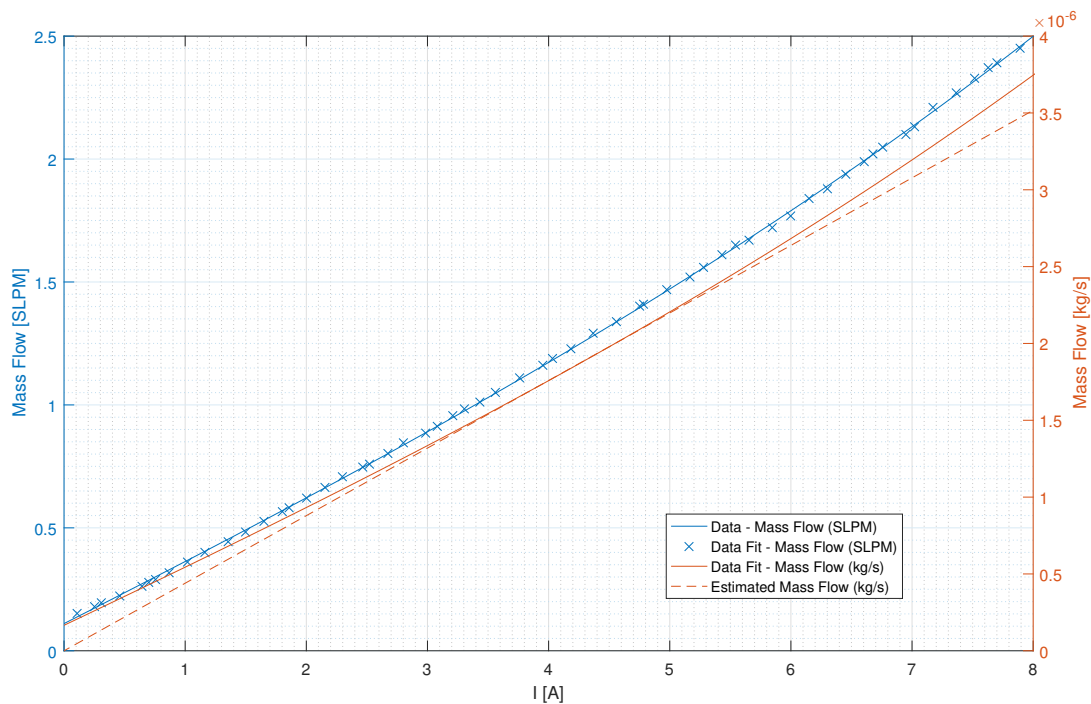


Figure 9.3: Mass flow of the 200W HES Aerostack (data from [69]) and an estimate that uses a commonly applied stoichiometry of 1.2 [8, 32] due to fuel crossover, purging etc.

Figure 9.4 shows the electrical efficiency for different stack pressures, evaluated according to Equation 4.7. This amounts to almost 5% when doubling the stack pressure. Extra compression will, however, require some of the fuel cell power to be used for that compression. Also, the compressor will occupy some of the weight budget. The benefit could be additional efficiency and possibly a small net power output increase for the same number of stacks. If only efficiency is the reason, flight times need to be large enough to have a sufficient reduction in weight. It is less likely this will happen with less efficient storage methods such as 300 or 700 bar storage tanks. The compressor will be further studied in the following chapter.

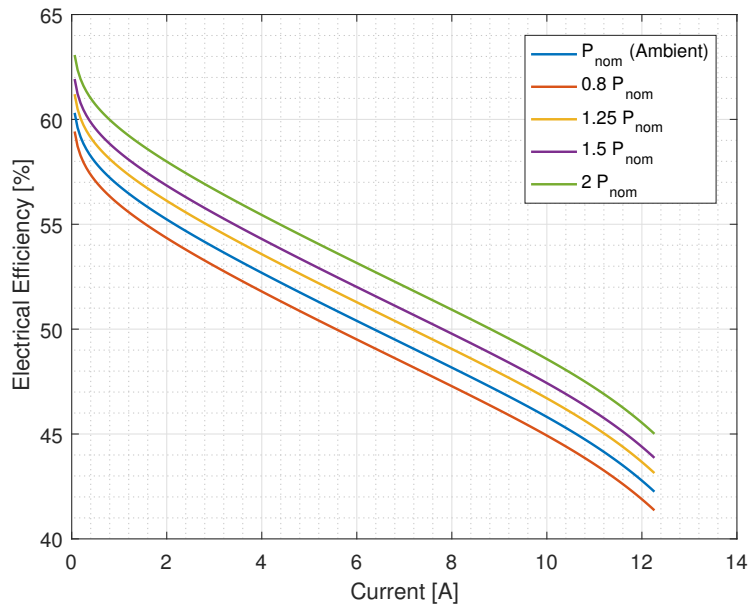


Figure 9.4: Electrical efficiency at different stack pressure levels to which the air mass flow will also have to be compressed

9.3. Fuel Cell Stack Sizing

The sizing of the fuel cell stack is derived from a number of inputs. The design or delivery power depends on the required cruise power, but also voltage requirements, stack pressure and compressor power. The weight of the fuel cell stack also depends on the chosen current density, where a lower current density means a reduction in cell power and an increased weight. The benefit is, however, improved efficiency. A simplified schematic is shown in Figure 9.5, which will be further elaborated on in the next sections. It shows that the I-V curve was used to perform a curve fit at cell level (i-V), see previous sections. The stack reference weight and volume are used to determine a cell density. Evaluation of voltage and power requirements yield the number of cells required, resulting in the total stack weight. P_{max} in this figure indicates the stack design power during cruise.

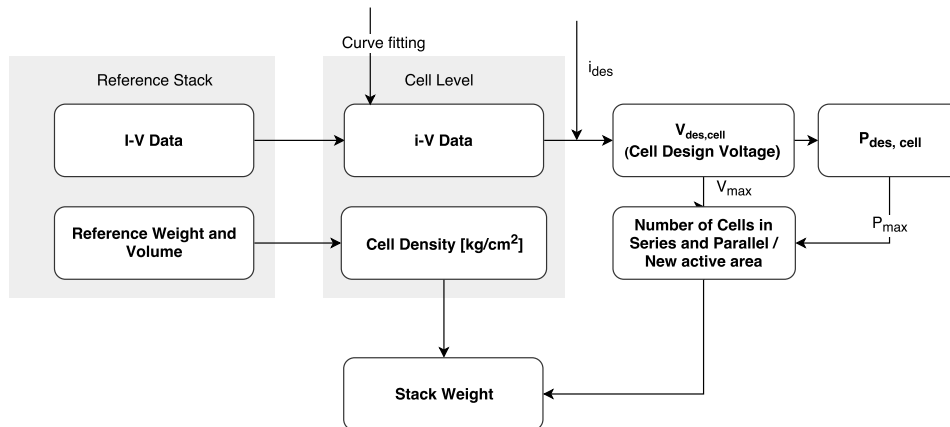


Figure 9.5: Schematic of fuel cell sizing

9.3.1. Understanding Voltage Requirements

The starting point is understanding the voltage requirement of the fuel cell system and the battery pack. These have to be as close as possible and therefore a maximum voltage of 270 Vdc (industry standard) needs to be achieved and maximum battery voltage needs to match this. This will be further elaborated on in the battery modelling chapter, where it will be shown that battery voltage drops during the discharge. Therefore a DC/AC inverter will be needed in the system due to non-matching voltages. The voltage of 270 Vdc is therefore one of the requirements in the fuel cell design. The other requirement is the power needed for the cruise phase. The fuel cell was fitted at cell level for an active area of 16.8 cm² and the following cell to

stack procedure allows for a slight reduction of this cell area to meet both voltage and power requirement. The reason is that uniformity and therefore the same performance cannot be guaranteed when enlarging the cells.

9.3.2. Cell to Stack

Given the low power density of the state-of-the-art fuel cell stacks, it is expected that the design current density is most likely at the upper end of the cell. For the stack pressure range, this means an approximate cell voltage window between 0.65 and 0.79. When operating at a best range velocity for altitudes between 500-2000m, the power requirement after taking into account the motor and inverter efficiency, is approximately 10 kW. A single cell at maximum power and 12.26 A will then have approximately 8 W of power for a nominal stack pressure of 1 atm. This would result in 1250 cells, resulting in over 800 V. Again, it is not possible to predict fuel cell performance when the active area is made larger due to non-uniformity. However, it is assumed that the active area can be reduced from 16.8 cm^2 to a slightly reduced size. For a 10 kW power requirement, putting 3 large fuel cell stacks in parallel will result in a voltage level around 270Vdc, with only a slight reduction in the active area.

Equation 9.5 shows that the cell design voltage is a function of current density and fuel cell stack pressure. These are two inputs for this calculation. Note that Equation 9.6 shows the number of cells that can be placed in series according to the maximum voltage requirement, which uses the result of the previous step. The number of cells needed to meet the power requirement is then calculated using Equation 9.7. It should be noted that the power requirement is the cruise power, which is iteratively determined as it also needs to deliver the power to run the compressor. Based on this it can be determined how many cells are put in parallel, which is the upper bound of the number of cells needed for the power requirement divided by the cells in series, see Equation 9.8. In this equation, that upper bound is multiplied by the number of cells in series to determine the total number of cells used. Because the upper bound was used, a new, smaller active area needs to be determined.

$$V_{c,des} = f(i_{des}, p_{FC}) \quad (9.5)$$

$$N_{c,V} = \frac{V_{max}}{V_{c,des}} \quad (9.6)$$

$$N_{c,P} = \frac{P_{des}}{P_{c,des,A=16.8cm^2}} \quad (9.7)$$

$$N_c = N_{c,V} \cdot \left\lceil \frac{N_{c,P}}{N_{c,V}} \right\rceil \quad (9.8)$$

The new active area is then determined through Equation 9.9, where A_c is the active area of the original cell. This takes into account the fact that more cells are present, but smaller. This assumes that the same uniformity is reached and there is no effect on weight. This is the advantage of doing a cell-level analysis before doing stack sizing. Also, although current changes, the number of cells also changes. Therefore, it has no effect on hydrogen and air mass flow. The new cell power is then determined through Equation 9.10, which is slightly lower than the original cell as surface area is smaller.

$$A_{new} = \left\lceil \frac{N_{c,P}}{N_{c,V}} \right\rceil \cdot \frac{N_{c,V}}{N_{c,P}} \cdot A_c \quad (9.9)$$

$$P_{c,des} = V_{c,des} \cdot i_{c,des} \cdot A_{new} \quad (9.10)$$

9.3.3. Cell Weight and Volume

It should be noted that cell weight can be derived from the overall stack weight. Given that the original HES Aerostack 200W has a weight of 0.5kg (note that the power density of the 1 kW stack was used) and is therefore rated at 400 W/kg. With a nominal pressure of 1 atm, the stack outputs in reality 275 W, resulting in 550W/kg. When the pressure is increased to 2 atm, this is approximately 290 W and 580 W/kg for the fuel cell stack, but it should be noted that the power density of the combination of fuel cell stack and compressor together may show different values. This is why it is important to perform a compressor sizing.

To mitigate a varying power density, each cell with an active area of 16.8 cm^2 gets an equivalent weight based on the entire fuel cell stack. The stack has 35 cells and a weight of 0.5kg. Equation 9.11 shows the cell density in terms of kg/cm^2 .

$$\rho_{cell} = \frac{W_{stack,ref}}{n_c \cdot A_c} \quad (9.11)$$

Considering the study allows the active area to be reduced, the real cell weight is determined by multiplying the cell density by the new active area. This means power density of the stack varies with usage and the power density can be controlled in sensitivity studies by reducing reference stack weight or on cell level directly using the cell density ρ_{cell} as long as overhead is considered. Comparing the figures used in this study to the weight of an experimental cell would most likely be unfair.

$$W_{cell} = \rho_{cell} \cdot A_{new} \quad (9.12)$$

9.3.4. Stack Weight

The stack weight can subsequently be determined as W_{stack} according to Equation 9.13. One consideration here is that stack weight is not directly a function of the original design power P_{des} , but needs to be determined through iteration with compressor design.

$$W_{stack} = N_c \cdot W_{cell} \quad (9.13)$$

9.3.5. Volume

In terms of volume, a similar analysis can be made. The volumetric power density can be derived from some reference stacks as seen in Table 9.4. The volumetric power density of the 200W Aerostack is low at 124W/L and likely to be higher when scaled up. The same is seen for different PowerCell S2 stacks, but performance in terms of gravimetric and volumetric power density is higher, reaching 526-682 W/kg and 530-700 W/L in the 10-20kW range. The Aerostack with the highest volumetric power density delivers 248W/L. The PowerCell stacks show that it would be reasonable to assume 500W/L for state-of-the-art stacks, meaning that the current 200 W reference stack will be reduced in volume from 1.6 to 0.55 L, a reduction of a factor 3. Some improvements in upscaling can already be seen going from the 200 W to the 500 W stack and also in the PowerCell stacks. This, combined with the fact the PowerCell stacks already show this performance should lead to a reasonable assumption.

Equation 9.14 calculates the stack volume, where n_c is the number of cells (35 for the 200W Aerostack) in the reference stack and N_c is the number of cells in the fuel cell stack design. The reference stack is considered to be 0.5 kg and 0.55 L according to the real gravimetric power density and the volumetric power density according to PowerCell fuel cell stacks.

$$V_{stack} = \frac{V_{stack,ref} \cdot N_c \cdot A_{new}}{n_c \cdot A_{ref}} \quad (9.14)$$

9.3.6. Miscellaneous Weight and Chapter Remarks

Now that the sizing of the fuel cell stack has been elaborated on, it is important to understand further sizing requirements. Overhead on top of the fuel cell stack and battery components can be quite significant due to other parts required for the fuel cell system. An overhead for both the battery and fuel cell can be considered to accommodate casings, cabling, and miscellaneous items, without considering possible power penalties these may have. Some of the major weight components are already considered due to the stack power density already including self-humidification and cooling, although this may not represent the final cooling setup necessary for the size of the system. Liquid cooled fuel cells, such as produced by PowerCell, provide similar power density, however.

It is important to determine a greater inventory and estimates of part weight and power density through further research. A sensitivity study on overhead needs to and will be performed to understand its impact. It is difficult to estimate the weight of many smaller parts. Therefore, only parts for which estimates can be made are included in this analysis, with an assumed overhead for the fuel cell system. This will be further elaborated on in Chapter 11. Equation 9.15 shows an overview of the power system weight, excluding motor and inverter components.

$$W_{total} = W_{stack} + W_{controller} + W_{comp} + W_{press,reg} + W_{batt} + W_{batt,overhead} + W_{storage} + W_{FC,sys-overhead} \quad (9.15)$$

Company	Product Name	Type	Power [W]	Stack Weight [kg]	Controller weight [kg]	P/W [W/kg]	Dimensions [mm]	Volume [L]	P/V [W/L]
HES Energy (Horizon)	Aerostak 200W Ultralight	PEMFC	200	0.5	0.08	345	107x126x120	1.6	124
HES Energy (Horizon)	Aerostak 500W Ultralight	PEMFC	500	1.15	0.08	407	126x116x138	2.0	248
HES Energy (Horizon)	Aerostak 1000W Ultralight	PEMFC	1000	2.2	0.08	439	266x156x118	4.9	204
HES Energy (Horizon)	Horizon H-100	PEMFC	100	1.29	0.4	59	118x104x94	1.2	87
HES Energy (Horizon)	Horizon H-200	PEMFC	200	2.23	0.4	76	118x183x94	2.0	99
HES Energy (Horizon)	Horizon H-300	PEMFC	300	2.79	0.4	94	118x262x94	2.9	103
HES Energy (Horizon)	Horizon H-500	PEMFC	500	2.52	0.4	171	268x130x122.5	4.3	117
HES Energy (Horizon)	Horizon H-1000	PEMFC	1000	4	0.4	227	268x219x122.5	7.2	139
HES Energy (Horizon)	Horizon H-2000	PEMFC	2000	10	2.5	160	350x183x303	19.4	103
HES Energy (Horizon)	Horizon H-3000	PEMFC	3000	15	2.5	171	350x183x418	26.8	112
HES Energy (Horizon)	Horizon H-5000	PEMFC	5000	30	2.5	154	350x212x650	48.2	104
Intelligent Energy	Heavy AC64 Stack (700-2700W Modular) - 24 cells	PEMFC	700	1.64		427	197x84x87	1.4	486
Intelligent Energy	Heavy AC64 Stack (700-2700W Modular) - 96 cells	PEMFC	2700	4.13		654	197x84x249	4.1	655
Intelligent Energy	Light AC64 Stack (700-2700W Modular) - 24 cells	PEMFC	700	0.62		1129	197x84x87	1.4	486
Intelligent Energy	Light AC64 Stack (700-2700W Modular) - 96 cells	PEMFC	2700	1.31		2061	197x84x249	4.1	655
Intelligent Energy	4kW Fuel Cell Power Unit / System (AC64 based)	PEMFC	4000	22	0	182	447x425x258	49.0	82
Intelligent Energy	AC10 stack standard - 12-320W	PEMFC	12	0.084		143	77x25x15	0.0	416
Intelligent Energy	AC10 stack standard - 12-320W	PEMFC	320	0.372		860	77x25x239	0.5	696
Intelligent Energy	AC10 stack lightweight - 12-320W	PEMFC	12	0.039		308	77x25x13	0.0	480
Intelligent Energy	AC10 stack lightweight - 12-320W	PEMFC	320	0.19		1684	77x25x189	0.4	880
Ballard Power Systems	FCgen-1020ACS (450W - 3kW)	PEMFC	2400	11		218	363x103x351	13.1	183
PowerCell	S2	PEMFC	5	13.9	-	360	148x199x480	14.1	354
PowerCell	S2	PEMFC	10	19	-	526	148x266x480	18.9	530
PowerCell	S2	PEMFC	20	29.3	-	682	148x400x480	28.4	700
PowerCell	S2	PEMFC	25	34.5	-	724	148x468x480	33.2	750
PowerCell	Prototype: PowerCell S3 (30-100kW)	PEMFC	98200	33		2976	444.0x420.0x156.0	29.1	3376

Table 9.4: Reference stacks considered in determining input parameters for state-of-the-art fuel cell stacks and reasonable values regarding gravimetric and volumetric power density

Compressor Sizing and Effects

This chapter discusses the component that plays a major role in the Balance of Plant (BoP) of the fuel cell system. The sizing method, integration and optimization variables will be discussed. The compressor power requirement will be considered and added to the fuel cell design power, as it runs the fuel cell directly. It also increases efficiency as previously mentioned, reducing hydrogen mass flows when compressor power is not too excessive.

10.1. Assumptions

This section discusses the assumptions made in the compressor and expander sizing.

- The power estimates follow isentropic relations, which means it is adiabatic and therefore no losses through the compressor walls.
- International Standard Atmosphere (ISA) is used to determine pressure and temperature at different altitudes.
- For compressor sizing, it is assumed pressure is not increased at the inlet and therefore fully by the compressor. Also drag penalties are not considered because of an air intake. It is assumed this is no worse than the micro gas turbines currently adding additional parasitic drag.
- Strategy follows a constant fuel cell operation in take-off, climb and cruise phase at which sizing is done for the longer cruise phase.

10.2. Air Properties

Air properties are a large part of compressor sizing. Variations of air properties and therefore pressure will play a large role in compressor sizing and compressor power requirement due to a lower ambient pressure. The power will also be shown linearly proportional to the compressor inlet temperature. First, the temperature and pressure will be given as a function of altitude, which is going to be a design variable. The altitude of most demonstrators of fuel cell and battery powered aircraft is generally 1000 meters. The stack pressure drop at higher altitudes will cause a power deficit due to either stack pressure losses or an available power reduction as a result of an increased pressure ratio and thus compressor power. The temperature as a function of altitude is given by Equation 10.1, in which T_{h_0} is the temperature at standard sea level conditions, λ_T the lapse rate and h the altitude above sea level. The lapse rate is the temperature reduction per meter altitude valid from 0-11km and equal to -0.0065K/m.

$$T(h) = T_{h_0} + \lambda_T \cdot h; \quad (10.1)$$

$$p(h) = P_{h_0} \cdot \left(\frac{T(h)}{T_{h_0}} \right)^{\frac{-g}{\lambda_T R}} \quad (10.2)$$

These properties need to be known at all altitudes the aerial vehicle operates at. These values are the ambient properties and assumed to be the intake pressure and therefore not considering any benefit from inlet compression. Drag penalties are also not considered as a result of requiring an air intake. The mass flow is relatively low and therefore the amount of air and the size of the compressor air intake is limited.

10.3. Compressor Sizing

Compressor sizing has a few different aspects on subsystem level. The first one is determining power levels with the effects of pressure ratio and mass flow. An important consideration is that air actually heats up when compressed, whereas the stack operates at approximately 80 degrees Celsius. Some degree of air cooling may be necessary to ensure the stack does not exceed the maximum operating temperature. The exact effect this has on the weight of the system is out of the scope of this study, but it is important to take this into account. The cooling of the compressor motor is also not taken into account, but would be a small fraction of the waste heat by the fuel cell stack. It is important to understand that higher stack pressures will also result in a higher compression ratio and therefore also air temperature.

10.3.1. Compressor Conditions

It is important to understand for what conditions the compressor is sized. Air mass flow and power requirements can be estimated at any given point for a certain pressure ratio and according to compressor properties.

Because stack pressure is introduced as a variable, the environmental conditions (ISA standard) at a certain variable altitude define the power needed to meet the stack pressure requirement. This compressor is driven by a motor which in turn has an efficiency, meaning that the actual power requirement is even larger. To show the order of magnitude of compressor power needed, a 15kW system was analyzed for different stack pressures at a range of altitudes. This can be seen in Figure 10.1. This would be the approximate power when the full power system is powered by fuel cells instead of a FC-B configuration. This proves the necessary iterative process because of a power derating of the fuel cell stack as a result of the compressor power requirement. At low altitudes and low stack pressures, the compressor power is moderate.

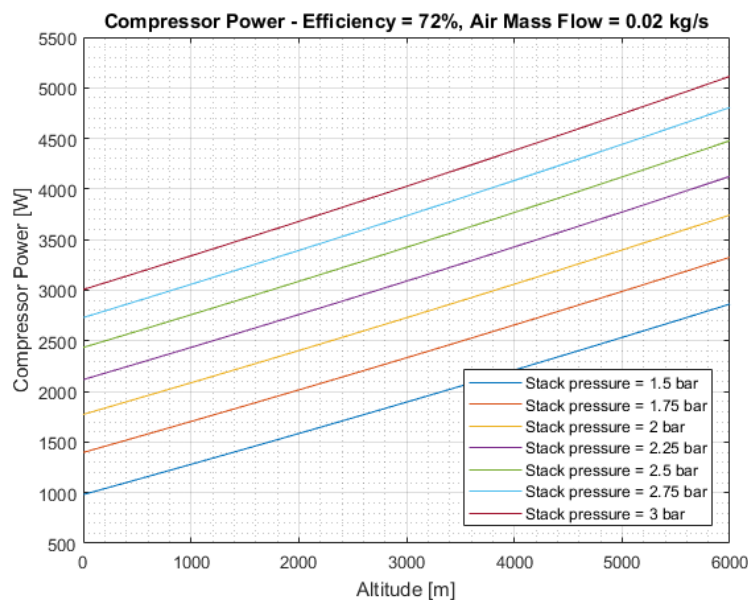


Figure 10.1: Compressor power requirements with an η_{isent} and air mass flow of a 1kW Horizon A1000 stack for a 15kW system

10.3.2. Mass Flow and Power Requirement

The mass flow and power requirements can be estimated for air, providing ample input requirements for the compressor sizing. An important consideration is that compressor sizing will be required for a given stack pressure at cruise altitude where ambient pressure is lowest. This yields the highest pressure ratio as could be seen in Figure 10.1. Although power level and thus mass flow remain the same in the climb phase according to the strategy, the pressure ratio decreases with reduced altitude. Equation 10.3 indicates the oxygen molar rate (mol/s) as can be derived according to the hydrogen needed for the current at the operating point, where only half the oxygen is needed compared to hydrogen. Where deviation from stoichiometry for hydrogen is generally slightly above 1, the stoichiometry for oxygen - and therefore air - is about 2 [1, 32], meaning that twice air needed for stoichiometry is delivered to the fuel cell stack. The equation for the air mass flow then depends on the mass flow of oxygen and the fact that oxygen is 21wt% of air. This can be seen in Equation 10.4

$$\dot{M}_{O_2} = \frac{n_c \cdot I}{4F} \quad (10.3)$$

$$\dot{m}_{air} = \frac{\dot{M}_{O_2} \cdot m_{M_{O_2}} \cdot \lambda}{0.21} \quad (10.4)$$

The mass flow of air needs to be estimated for Equation 10.5, which is a theoretical estimate for compressor power. It is important to understand that besides the isentropic compression efficiency, the motor and controller efficiency needs to be considered.

$$P_{comp,in} = \eta_{m+c} \cdot \dot{m}_{air} \cdot c_{p,air} \cdot \frac{T_1}{\eta_{is,comp}} \left(\left(\frac{P_2}{P_1} \right)^{\frac{\gamma-1}{\gamma}} - 1 \right) = \eta_{m+c} \cdot \frac{\dot{m}_{air} \cdot c_{p,air} \cdot T_1}{\eta_{is,comp}} \left(\Pi^{\frac{\gamma-1}{\gamma}} - 1 \right) \quad (10.5)$$

10.4. Reference Compressors

This section discusses the compressors considered in literature and gives an explanation of the chosen power density and limitations of the chosen compressor type. It will show that a turbo-compressor is very suitable for this application. The compressor weight is determined based on the power density factor PD_{comp} and the compressor input power $P_{comp,in}$ as seen in Equation 10.6

$$W_{comp} = PD_{comp} \cdot P_{comp,in} \quad (10.6)$$

10.4.1. Compressor Types

Most fuel cell systems can be operated with different compressor types: displacement compressor including scroll compressors, but also radial compressors such as produced by Celeroton [5]. Most displacement compressors are only applied in larger power systems. A scroll compressor was chosen by Guida and Minutillo [18], but miniaturisation is limited. Lightweight solutions are barely available, whereas the efficiency is reasonably high. Celeroton radial compressors have been used internally by NLR with good experience. One possible issue with these lightweight compressor solutions is reliability. These compressors perform at high RPM, high efficiencies and up to a pressure ratio of 1.7-1.7 for a single-stage compressor with typical fuel cell mass flows. The disadvantage is that the operating range of turbo compressors is limited as the combination of mass flow, RPM and pressure ratio cannot be chosen arbitrarily [5]. Celeroton claims that their turbo-compressors are significantly better in terms of overall performance compared to other well-established fuel cell compressors. This seems to be true in terms of weight, with similar efficiency levels. However, as noted, reliability is also of significant importance.


Comparison of Commercial Compressors

This section makes the comparison between a lightweight scroll compressor and radial compressors at the right mass flow for this fuel cell application. These are considered in the analysis:

- Scroll Compressors by Air Squared (Type of positive displacement compressor)
- Radial Compressors by Celeroton. It should be noted that Celeroton calls these radial compressors turbo-compressors and that these are used interchangeably here.

The Air Squared scroll compressor rotates at 4000 RPM whereas the Celeroton turbo-compressors rotate at up to 280,000 RPM. It is expected that about 10 kW of fuel cell power is needed. Early calculations based on Equation 10.3 for the used 200 W reference stack, shows that each cell gets a maximum current of 12.3A given the stack active area of 16.8 cm² and current density of 0.73 A/cm². Each of these stacks has 35 cells, totalling 280 W per stack or 8 W per cell. This equals about 1250 necessary cells for the power requirement. With the Faraday constant at 96,485.3 sAmol⁻¹, the current per cell at 12.3A, 1250 cells, a commonly used air stoichiometry of 2 and a molar mass of 32 g/mol, the air mass flow can be found as approximately 12 g/s. It is therefore expected that the final compressor air mass flow ranges between 8 g/s and 15 g/s depending on component efficiencies, the exact cruise power requirement and chosen compressor pressure ratio. This calculated mass flow falls in the range of the discussed compressors in Table 10.1. This means that approximately 600 LPM will be necessary, where the Air Squared compressor has an electric power requirement of approximately 600 W. Because of the high scroll compressor weight, the Celeroton turbo-compressor was chosen as the reference compressor.

The power density (kg/kW) of the compressor was determined through the rated power. Because the CT-17-1000.GB turbo-compressor works in the right operating conditions, the PD_{comp} of the compressor



Type	Turbo-compressor	Turbo-compressor	Scroll Compressor
Manufacturer	Celeroton	Celeroton	Air Squared
Product Name	CT-17-700.GB	CT-17-1000.GB	P24H056A-BLDC
P_2/P_1 at opt	1.1-1.6 (1.4)	1.1-1.6 (1.4)	1 bar _g
\dot{m} [g/s]	2-17	2-24	800LPM _v / 16g/s
\dot{m} at η_{opt} [g/s]	5-12 (8)	5-15 (12)	No data
η_{opt} (isent + m+c)	58%	59%	65%
Dimensions (est.) [mm]	~90x90x183	~90x90x183	~167x177x289
Volume [L]	1.5	1.5	8.5
Bearings	Air Bearings	Air Bearings	-
Weight [kg]	1.5	1.5	9.5
Rated Power [W_e]	700	1000	1.2
P_{in} at η_{opt} [W_e]	500	550	At 600LPM, around 600
PD_{comp} [kg/kW]	2.14	1.5	7.92
PD_{V,comp} [L/kW]	2.14	1.5	7

Table 10.1: Comparison of compressors suitable for fuel cell applications. Information and imagery acquired from [3, 4, 56, 57]. The mass flows and pressure ratios between brackets () show the mass flows at the optimum efficiency

was chosen to be 1.5 kg/kW. The power considered for this is the power needed from the fuel cell for the compressor, so after including the efficiencies. An isentropic efficiency of 72% and a motor plus controller efficiency of 85% were found based on this compressor. It should be noted that these compressors can be used in series to elevate the pressure.

10.4.2. Compressor Efficiencies

Compressor efficiencies are often split up in two parts as shown below. The isentropic efficiency considers all losses within the compression process, whereas the motor and controller efficiency consider losses in the components that drive and control the compressor.

- Isentropic efficiency
- Motor and controller efficiency

Air Squared notes that their isentropic efficiency is about 73% with a motor and controller efficiency of 90%, resulting in an overall efficiency of 65% [56]. The Celeroton efficiencies are approximately 72-73% and 85% respectively, resulting in a product line in which the average efficiency is about 60% [3].

Figure 10.2 shows the compressor map of the Celeroton CT-17-700.GB. Figure 10.3 shows a second version weighing in at the same 1.5 kg. The efficiency lines can be observed, but the values corresponding to those lines are left out of these data sheets.

Chapter Conclusion

This chapter showed the sizing procedure for the compressor, mainly consisting of atmospheric calculations, determining the power density for the compressor and the power requirement to be used in combination with that power density. A power density of 1.5 kg/kW and 1.5 L/kW will be used in further analyses. For low stack pressures and low altitudes, it was found that the compressor power will most likely be limited to around 10% of the fuel cell power. For real applications, the reliability should be tested of the chosen compressor. The next chapter elaborates on the other components found in the FC-B power system.

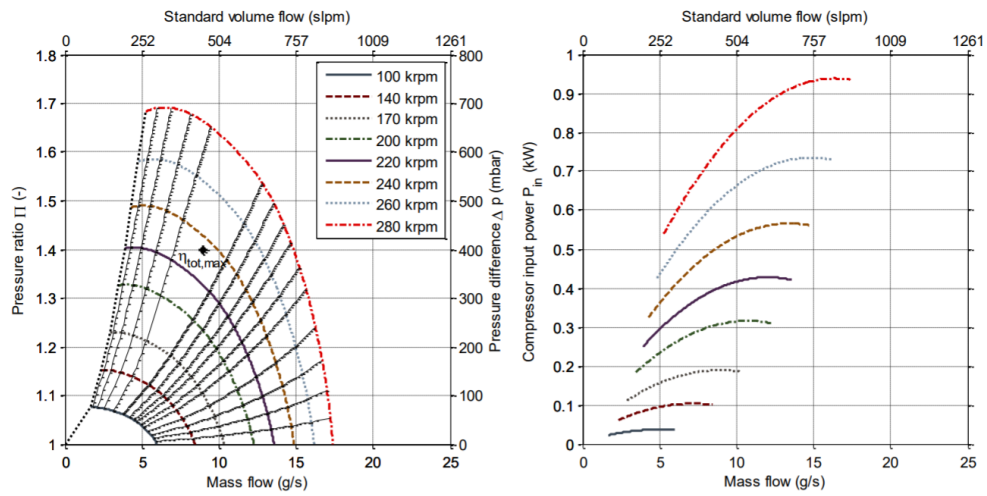


Figure 10.2: Celeroton compressor map example (CT-17-700.GB with Air Bearings) that weighs 1.5 kg [4]

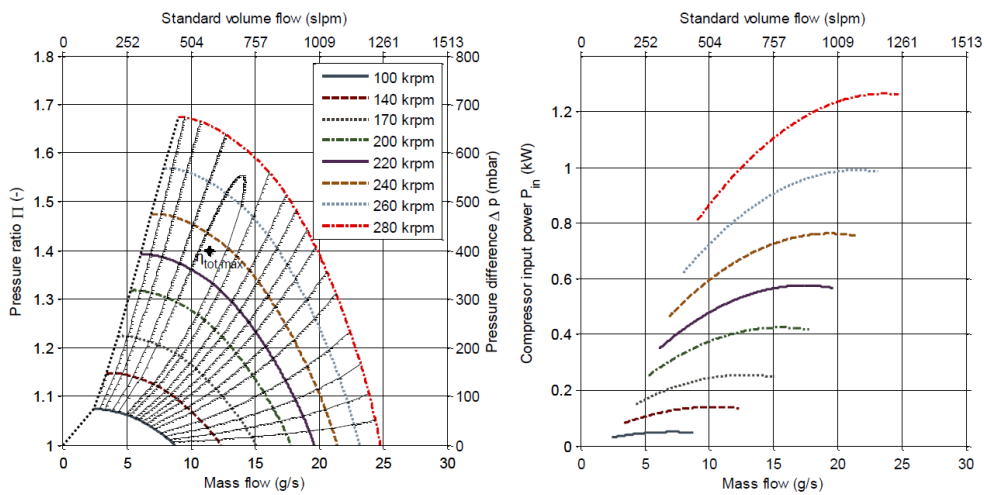


Figure 10.3: Celeroton compressor map example (CT-17-1000.GB with Air Bearings) that weighs 1.5 kg [3]

Balance of Plant: Additional Components

This chapter discusses the Balance of Plant or additional components of the fuel cell system and battery. The latter is encapsulated in a battery overhead factor or efficiency. Other components are the used storage values for further analysis, pressure regulators, the inverter, motor, controller and an assumption for fuel cell system overhead.

11.1. Battery Overhead

The battery overhead was determined based on different battery packs in the automotive industry. The overhead consists of all parts needed to obtain a fully functioning battery pack. Thermal management often plays a large role in battery packs due to their relatively low (maximum) operating temperature. Although the efficiency is generally set at approximately 95%, the temperature difference between the pack and atmosphere is low, meaning very effective cooling is necessary. The general overhead found in automotive battery packs will be discussed in this section.

Figure 11.1 shows what battery cells are used in current automotive applications. The 2016 Chevrolet Volt uses similar NMC-LMO pouch cells to the Renault Zoe. Considering most of these are already quite low, the actual pack energy density will be even lower.

Car company	Model	Cell producer	Cathode	Anode	Capacity (Ah)	Cell type	Cell energy density (Wh L^{-1})	Cell specific energy (Wh kg^{-1})
BMW	i3	Samsung	LMO + NMC	Gr	60	Prismatic	237	126
Bolloré	Bluecar	Batscap	LFP	Li		Prismatic	364	228
Coda	EV	Lishen	LFP	Gr	16	Prismatic	226	116
Daimler	Smart	LG Chem	NMC	Gr	50	Pouch	270	140
Fiat	500	Samsung	NMC-LMO	Gr	64	Prismatic	243	132
Honda	Fit	Toshiba	NMC	LTO	20	Prismatic	200	89
Mitsubishi	i-MEV	Li energy Japan	LMO-NMC	Gr	50	Prismatic	218	109
Nissan	Leaf	AESC	LMO-NCA	Gr	33	Pouch	309	155
Renault	Zoe	LG Chem	NMC-LMO	Gr	36	Pouch	275	157
Tesla	Model S	Panasonic	NCA	Gr	3.1	Cylindric	630	233

Figure 11.1: Energy density of cells used in the automotive industry [27]

Datta and Johnson [8] used a relatively old battery pack in their analysis as a reference. A single cell of the Nissan LEAF used in the analysis has a content of 125 Wh and weighs 0.8kg, meaning the energy content is approximately 156.25 Wh/kg. Based on the entire battery pack weight, each cell has an additional overhead of 0.6kg, reducing this energy density to 90 Wh/kg. This is a reduction of approximately 40%. The sheer size of the battery pack makes uniform cooling more difficult and this value could therefore be an overestimation for smaller battery packs.

The EPA (U.S. Environmental Protection Agency) document shows an energy density of the Tesla Model 3 battery pack of 150 Wh/kg [75]. The battery pack weighs 480 kg for the Model 3 Long Range (2017) version

Car	Cell Wh/kg	Pack Wh/kg	Overhead	Pack Wh/L	Voltage
Tesla Model 3 (2017)	~ 250	150 [75]	0.4	222 [75]	350 N 400 P
Nissan Leaf [8]	156.25	90	0.4	-	
Chevrolet Volt (2016) - 96S 3P Gen 1	155-190	87 [36]	0.43-0.54	118 [36]	
Chevrolet Volt (2016) - 96S 2P Gen 2	155-190	101 [36]	0.35-0.47	119 [36]	360 N 395 P
Renault Zoe 2013 [10]	160	-		300 (cell)	240-403
Renault Zoe 2017 [10]	240	136.7	0.43	500 (cell)	240-403
Assumed Value	240 (Nominal)		0.4		

Table 11.1: Overhead estimation based on Automotive battery pack reference values

that is rated at 74kWh, but has an actual energy content of 89kWh. This includes 4416 of the larger 2170 Li-ion cells. Limited information is available for these new cells, but assuming that energy density remains around 250 Wh/kg - which is very reasonable given the state-of-the-art cylindrical Li-ion cells - this again results in a 40% overhead. Other vehicles (Table 11.1) also show very similar overhead values for the battery pack. This means that of the entire battery pack weight, 40% is used by components other than the battery cells.

These reference values from the automotive industry provide a reasonable estimate for the overhead factor in the battery sizing. This also shows that weight reductions in the overhead will automatically result in improved battery pack energy density. For this thesis, the overhead is assumed 0.4 at all times. This is therefore for the Battery-only as well as the FC-B analyses. This overhead factor is also applied to the volume.

11.2. Storage Options

Three storage options will be modelled based on the performed literature study. Each of these show reasonable gravimetric storage efficiency, with the 300 bar tanks lacking in volumetric storage efficiency. All these methods have been demonstrated in industry.

- Compressed Gas Tanks: 300 bar
- Compressed Gas Tanks: 700 bar
- Liquid Hydrogen

The compressed gas tank is one of the most used methods of storage. Two parts are identified: the tank itself and the need for pressure regulation from 300 or 700 bar to the order of 0.5 to 4 bar depending on the exact fuel cell operating conditions. As a result of the literature study, the most feasible storage methods are 300 and 700 bar tanks, as well as liquid hydrogen (LH₂). Other options such as metal hydrides and other chemical storage methods are not considered in this analysis. However, based on the storage efficiency of other methods, the range and/or endurance can be easily approximated.

Table 11.3 shows an overview of reference storage methods ranging in size. Due to limited volume availability (80-100L) for the power system and storage method, the largest volume contribution comes from compressed gas tanks. For the 700 bar tank, the Hexagon Lincoln I, J and K are reasonable tank sizes. It is assumed that the characteristics of the Hexagon Lincoln I are valid for all 700 bar tanks. The state-of-the-art value of 0.057 (or 5.7wt%) can be reached with slightly larger tanks. For the 300/350 bar tanks within a reasonable volume (Luxfer L028/L034/L039), these values come down to 0.043kg/kg and 0.024kg/L. The chosen storage efficiencies are shown in Table 11.2. The liquid hydrogen storage efficiency comes from Swider-Lyons et al. [61], which also indicates that the Wh/L of LH₂ is three times higher than that of 350 bar. The power requirement for heating the liquid hydrogen is negligible.

Tank Type	kg/kg	kg/L
700 bar	0.052	0.041
300/350 bar	0.043	0.024
LH ₂	0.12	0.072*
*3x Wh/L of 5000 psi (345bar) storage tanks [61]		

Table 11.2: Chosen modelling parameters for the 300 and 700 bar tanks as well as liquid hydrogen storage method

Company	Name	Type (I/II/III/IV/V)	Pressure [MPa]	Pressure [bar]	Tank mass [kg]	H2 mass [kg]	Volume [L]	kg/kg	kg/L
Hexagon Lincoln	A	IV (Composite)	20	200	16	0.7	46	0.042	0.015
Hexagon Lincoln	B	IV (Composite)	25	250	164	8	450	0.047	0.018
Hexagon Lincoln	C	IV (Composite)	25	250	94	6	350	0.060	0.017
Hexagon Lincoln	D	IV (Composite)	30	300	112	7.2	350	0.060	0.021
Hexagon Lincoln	E	IV (Composite)	35	350	101	7.5	312	0.069	0.024
Hexagon Lincoln	F	IV (Composite)	35	350	112	8.4	350	0.070	0.024
Hexagon Lincoln	G	IV (Composite)	50	500	280	16.5	530	0.056	0.031
Hexagon Lincoln	H	IV (Composite)	50	500	229	10.7	347	0.045	0.031
Hexagon Lincoln	I	IV (Composite)	70	700	34	1.4	36	0.040	0.039
Hexagon Lincoln	J	IV (Composite)	70	700	29	1.6	39	0.052	0.041
Hexagon Lincoln	K	IV (Composite)	70	700	43	2.6	64	0.057	0.041
Hexagon Lincoln	L	IV (Composite)	70	700	59	3.1	76	0.050	0.041
Hexagon Lincoln	M	IV (Composite)	95	950	365	12.4	254	0.033	0.049
Mahytec	RGVBP	IV	4	40	130	3	850	0.023	0.004
Mahytec	RGVBP	IV	3	30	130	2.3	850	0.017	0.003
Mahytec	Tank H2 525 bar	IV	52.5	525	240	9.7	300	0.039	0.032
Mahytec	Tank H2 700 bar	IV	70	700	38	1.5	37	0.038	0.041
Luxfer	L028	III	35	350	17	0.7	29	0.040	0.024
Luxfer	L034	III	35	350	19	0.83	34	0.042	0.024
Luxfer	L039	III	35	350	21	0.94	39	0.043	0.024
Luxfer	Q095	III	35	350	48	2.28	94	0.045	0.024
Luxfer	V068	III	35	350	36	1.64	68	0.044	0.024
Luxfer	V068N	III	35	350	36.5	1.64	68	0.043	0.024
Luxfer	V074	III	35	350	37.5	1.78	74	0.045	0.024
Luxfer	V074N	III	35	350	39	1.78	74	0.044	0.024
Luxfer	W100	III	35	350	49	2.41	100	0.047	0.024
Luxfer	W100N	III	35	350	51.5	2.41	100	0.045	0.024
Luxfer	W150	III	35	350	69	3.61	150	0.050	0.024
Luxfer	W150N	III	35	350	71.5	3.61	150	0.048	0.024
Luxfer	W205	III	35	350	92.5	4.93	205	0.051	0.024
Luxfer	W205N	III	35	350	95	4.93	205	0.049	0.024
Luxfer	W322N	III	35	350	141	7.72	322	0.052	0.024

Table 11.3: Compressed gas tank overview of mostly 300/350 and 700 bar tanks

11.3. Pressure Regulators

Pressure regulators can be found below 1 kg for compressed gas tanks. This section describes how the weight of pressure regulators is taken into account for 300 and 700 bar tanks. Pressure regulators for 700 bar tanks are generally two to three times heavier than those for 300 bar. In the case of a 700 bar tank, a 2-step pressure regulator is required to reduce the pressure to the stack operating pressure, generally between 1 atmosphere and multiple atmospheres.

A patent by Boeing published in 2017 already indicates that state-of-the-art at that moment for 700 bar applications often require pressure regulators at approximately 2 kg [30]. It also indicates that this weight easily forms a large part of the weight budget of small UAVs from 5-15 kg. Also for a 100 kg helicopter with reasonable payload allowance, the pressure regulator takes away a significant fraction of the weight budget that is otherwise used by the storage tank. Table 11.4 shows the reference values used for the pressure regulators. For liquid hydrogen, there is no fixed value on top of the storage efficiency of the tank.

Application	Source / Manufacturer	Weight	Volume	Comments
~ 300 bar	TESCOM™ 20-1200 Series [13]	0.6	1.3	NGV 3.1 and TUV batch approved for onboard hydrogen fuel cell vehicles.
700 bar	Boeing Patent [30]	2	-	State-of-the-art

Table 11.4: Pressure regulators for 300 and 700 bar storage methods

11.4. Inverter

An inverter is sized based on a number of power densities found in literature. A more conservative estimate was made based on knowledge of the current industry standard, which show lower values than here estimated. The following assumptions are made:

- Inverter sizing is power density based
- Inverter is a double inverter, accepting power from the two parallel sources (fuel cell and battery). This means the inverter is sized for the maximum power through the inverter, so the sum of battery and fuel cell power delivered to the double inverter.
- The inverter accepts the power in any given combination of current and voltage (within the fuel cell and battery characteristics)
- The maximum voltage is used in the fuel cell and battery sizing and an input in the model. This means that the inverter sizing limits are known for further sizing as the battery voltage drop is known and the fuel cell remains at almost constant voltage

Table 11.5 shows some reference values found in literature. Eventually it was decided to use 7 kW/kg, 7 kW/L and an inverter efficiency of 94% towards the lower end of the demonstrated inverters. This is because the majority of commercial inverters still show lower power densities than seen in the table.

Case	kW/kg	kW/L	η_{inv}	P_{inv} [kW]	Type	Date Estimate	Date Article
Prototype [37]	6.49	-	97.7	50	Demonstrated	2017	2017
Design [76]	26.51	-	97.91	50			
Demonstrated [44]	17	15	N/A	-	Shown (Delphi)	2015	2014
U.S. DoE Target 2022 [28]	14.1	13.4	94%	-	Targets DoE 2022	2022	2015

Table 11.5: Inverter (DC/AC) power densities show a wide range of values in both demonstrated prototypes as well as targets

11.5. Electric Motor

The electric motor is also sized using state-of-the-art - and in this case also proven and applied - values for its power density. Siemens state-of-the-art electric motors for aviation purposes show power densities of up to 7 kW/kg and volumetric power densities of approximately 6.7 kW/L [54]. These maximum values were directly used for the electric motor sizing. Also, the electric motor efficiency was set at 95% based on the Siemens reference.

11.6. Power System Controller

The power system controller is considered to have a fixed weight. Experience within NLR resulted in a weight estimate of 0.3 kg for the controller. This therefore will not have a significant effect on the results in this study.

11.7. Fuel Cell System: Overhead

The overhead of the fuel cell system is based on a rough assumption. Also, it will be used in the sensitivity study to understand what occurs to the payload-range diagrams when the fuel cell system turns out to be heavier than anticipated. For all components other than the compressor, it is assumed that power inputs are negligible.

- Power cables
- Tubing for gas and liquid flows
- Casing and/or structural support
- Sensors
- Miscellaneous cooling equipment

$$W_{FC,sys-overhead} = f_{overhead} \cdot (W_{stack} + W_{controller} + W_{comp} + W_{press,reg}) \quad (11.1)$$

Equation 11.1 shows how the overhead weight is determined in this study. This $f_{overhead}$ is assumed to be 0.15 in all cases. A first estimate is that it will be close to 4 kg. A sensitivity will be performed by increasing this overhead factor to 0.3, which means approximately 8 kg is then available for miscellaneous components. Note that the storage system is not taken into account as this is one big component that just requires a few attachments. Taking the storage component into account for a volume overhead would also be unreasonable. The same $f_{overhead}$ is used for the volume estimates. The controller volume is most likely negligible and is set to 0. The weight and volume of turbo-compressors and pressure regulators is also small, meaning that these also have a small effect.

$$V_{FC,sys-overhead} = f_{overhead} \cdot (V_{stack} + V_{controller} + V_{comp} + V_{press,reg}) \quad (11.2)$$

Chapter Conclusion

This chapter provided an overview of parameters used for most of the components accounted for in the power system sizing. This was for the battery overhead, pressure regulators, storage method, fuel cell system overhead, inverter and motors. The fuel cell system overhead is the main assumption here, but will be used for a sensitivity study and the effect of a heavier overhead on the payload-range diagrams. The next chapter discusses the sizing and simulation of the batteries, the last component discussion in this study.

Battery Modelling

This chapter discusses the battery modelling procedure. Different models are used in literature for battery discharge curve fitting. The focus in this thesis is on the usage of existing semi-empirical models instead of physical electric circuits.

One of the common and most simple battery models is Shepherd's model, as seen in Equation 12.1 and usually written as in Equation 12.2 [41]. V_0 indicates the battery nominal voltage, R the ohmic resistance, i the current through the battery, SoC the state of charge and μ is a curve fitting parameter in Equation 12.1. The SoC is an important parameter which indicates the discharge or charge status of the battery.

$$V = V_0 - R \cdot i - \frac{\mu}{SoC} \quad (12.1)$$

Equation 12.2 is the more common way of writing the Shepherd's model. The symbol K is the polarization constant, in $1/Ah$. This is also a fitting parameter. Q is the maximum battery capacity in Ah , i the current and t the time in hours. A is the exponential voltage, in V , and also a fitting parameter. In the exponential, B is the exponential capacity in $1/Ah$ and is another fitting parameter. R is the ohmic resistance of the battery and can be treated as a fitting parameter. The same can be done with the voltage constant V_0 , which is generally around the nominal voltage.

$$V = V_0 - K \frac{Q}{Q - it} + A \cdot e^{-B \cdot it} - R \cdot i \quad (12.2)$$

The modified version of Shepherd's model also takes into account both charging and discharging and is used in various literature [67]. These consist of a discharge mode (Equation 12.3), but also a charge model.

$$V = V_0 - K \frac{Q}{Q - it} \cdot it - K \frac{Q}{Q - it} \cdot i + A \cdot e^{-B \cdot it} - R \cdot i \quad (12.3)$$

The charge model can be seen in Equation 12.4. This discharge and charge model are used by the generic battery model in SimScape Power Systems (MatLab-Simulink) [64]. For discharging the current is positive, while for charging the current is negative. These equations include an extra term that is called the polarization resistance. This allows for improving the model where a large reduction of voltage can be seen at high DoD or low SoC [41]. For cases where the resistance of the battery is in the order of $m\Omega$, this term is not very important. This is the case for the majority of cylindrical (18650) Li-Ion cells.

$$V = V_0 - K \frac{Q}{Q - it} \cdot it - K \frac{Q}{it - 0.1Q} \cdot i + A \cdot e^{-B \cdot it} - R \cdot i \quad (12.4)$$

The chosen model is Shepherd's original model because charging is not considered in this study. Also, the charging model considered in Shepherd's modified model does not represent a realistic charging method [64]. Instead, a multiple regression analysis is performed with an improvement in Shepherd's original model. This allows for the battery to be modelled realistically for the full range of discharge rates instead of a single discharge rate. The latter often results in very poor performance when the model is used for other discharge rates.

The method explained in the following sections therefore model discharge curves using the original Shepherd's model, but with an adjustment in the fitting parameter B [70]. This fitting parameter is split up into a cubic polynomial to account for variation in the exponential with different discharge rates, seen in Equation 12.5. The discharge rate is normalized with the rated capacity/current in Equation 12.6. Also, the standard Shepherd's model does not include Peukert's law [41], which has been introduced with Equation 12.7 (pc). This accounts for a capacity loss at higher discharge rates. Generally it can be observed that for Li-Ion the capacity loss is not significant and values between 1.0 (no effect) and 1.04 can be observed [6, 70]. However,

during the multiple regression analysis in the following sections, this Peukert coefficient proved to be of great value in improving the fit.

$$B = p_3 C^3 + p_2 C^2 + p_1 C + p_0 \quad (12.5)$$

$$C = \frac{I_b}{Q_{rat}} \quad (12.6)$$

$$Q_b = Q_{rat} \left(\frac{I_{rat}}{I_b} \right)^{pc-1} \quad (12.7)$$

12.1. Method Verification

The extended Shepherd's model was previously used by Verstraete et al. [70]. The first step in verifying this method was therefore to use the reference data from this source to see if these results are similar to what is obtained with the multiple regression code used in this study. Figure 12.1 shows the fit obtained by Verstraete et al. It can be seen that Equation 12.2 in combination with Equations 12.5 to 12.7 yield very reasonable results as the fit (dashed lines) is very similar to the experimental test data. The fit obtained with the multiple regression method in this study acquired very similar results to this fit and was therefore verified with the data of Verstraete et al. The following sections will apply this multiple regression on the LG-HG2 Li-Ion cell, which is different from the LiPo cells used by Verstraete et al.

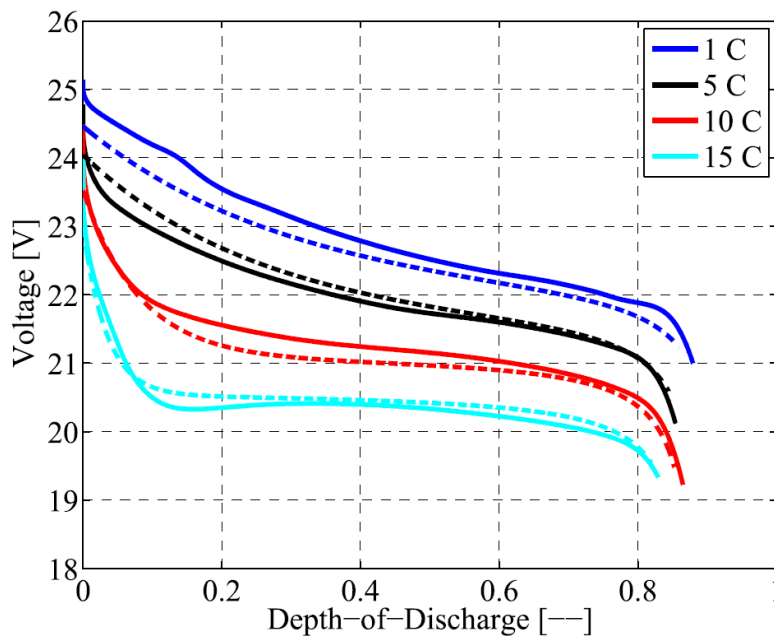


Figure 12.1: Li-Po battery multiple regression outcome using Shepherd's original model [70]. Very similar results were obtained when verifying the code with this fit. The dashed lines show the modelled discharge curves, the continuous graphs experimental data.

Table 12.1 shows the coefficients acquired in the non-linear fit by Verstraete et al. [70], which was performed on a 6-cell LiPo cell with a nominal voltage of 3.7 V (V_0). It should be noted that for this fit to be correct, it was found that instead of specifying the capacity and current in mAh and mA , Ah and A should be used. This means the coefficients as provided by Verstraete et al. should have different units. It is an important consideration, otherwise curve fitting will be difficult. This analysis concludes the verification of the multiple regression method which will be applied to a single 18650 cylindrical Li-Ion cell (LG-HG2).

Battery	K [V]	pc [-]	A [V]	R [Ω]	p_3 [mAh^2]	p_2 [mAh]	p_1 [mA]	p_0 [mAh^{-1}]	R^2
Nominal	0.08726	1.02	2.451	0.07712	$9.331e^{-5}$	0.1273	-0.6613	3.057	0.968
High-C	0.05832	1.019	2.702	0.04865	0.05308	-0.8332	3.511	-0.7699	0.983

Table 12.1: Battery model coefficients in the modelling approach by Verstraete et al. [70]

12.2. SoC and DoD

The definition of State of Charge (SoC) and Depth of Discharge (DoD) can be found in Equation 12.8. The SoC or DoD are normalized using the rated capacity Q_{rat} . SoC and/or DoD can be seen as how much of the capacity has been used and are values between 0 and 1.

$$SoC = 1 - DoD = 1 - \frac{\int I_b \cdot dt}{Q_{rat}} \quad (12.8)$$

When different discharge rates are needed for the application, vertical movements in the discharge curve occur. However, battery energy content will be reduced if one moves to a higher discharge rate as the voltage of the cell goes down. SoC, DoD or capacity (Ah) can each be used to indicate the battery status and perform further calculations. This is especially important when using the discharge curves for a power profile analysis. This will be discussed in the simulation procedure.

12.3. Modelling Approach: Curve Fitting

This section discusses the modelling approach, which will be applied to the the LG-HG2 cell at 3000 mAh and a nominal energy density of 240 Wh/kg. This cell performs well in terms of both energy density (low current) and power density (high current, ≈ 20 A). The specifications of this cell are summarized in Table 12.2.

The regression analysis is not a very straightforward procedure, as the Equation 12.2 needs to be fitted for multiple curves at the same time. Each of these discharge curves is at a different current. For this reason, the battery current I_b changes for each of these curves. It is therefore a multiple regression analysis in which the equation changes slightly for each data set. It was decided to perform the regression analysis for 0.2C (0.6A), 1C (3A), 5C (15A), 20A and 25A as these show a clear capacity reduction in Figure 12.2. This means that the peukert coefficient will most likely be estimated in the best possible way as it models the capacity reduction as a function of discharge rate.

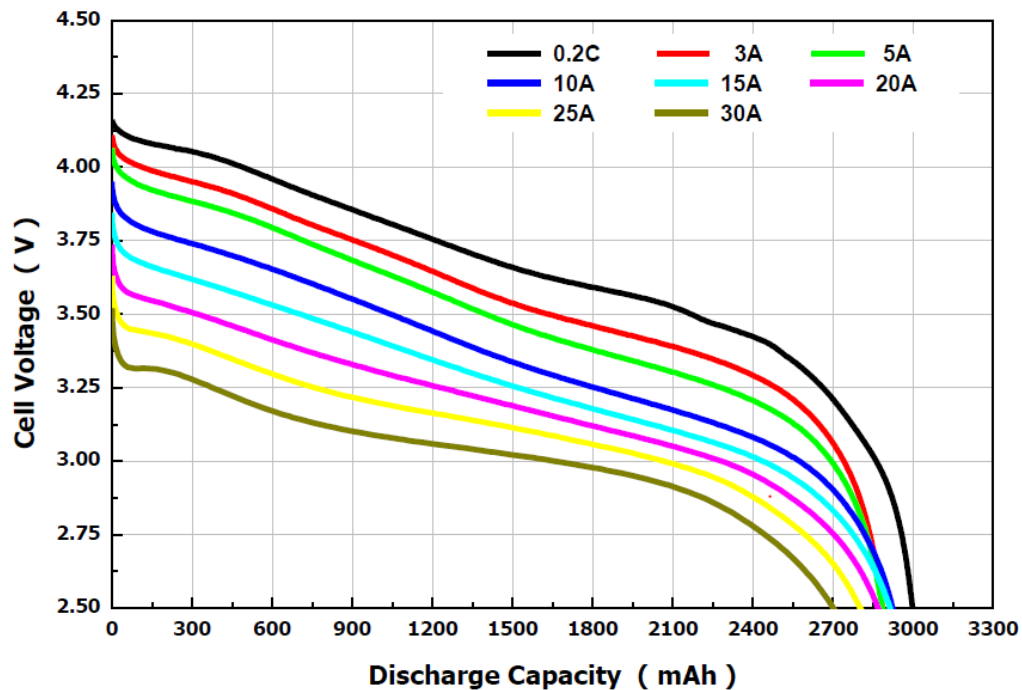


Figure 12.2: LG-HG2 Discharge Curves [6]

12.3.1. Data Extraction

The data was extracted from the LG-HG2 data sheet [6] using *ScanIt* by AmsterChem. This allows to define axes, trace the curves and obtain data points for each of the curves. It is important to recognize that because the multiple regression is performed, each of the data sets needs to have approximately and preferably the same number of points. Otherwise more weight is put on discharge curves that have more data points, as

Specification	Value / Description	Unit
Name	LG-HG2	-
Type	Cylindrical: 18650	-
Diameter (D_B)	18	[mm]
Length (L_B)	65	[mm]
Nom. Energy Density	240	[Wh/kg]
Nom. Vol. Energy Density	Ca. 670	[Wh/L]
Rated Capacity	3000	[mAh]
Cell Mass	44.5	[g]
$I_{max,cont}$	20	[A]
$V_{cut-off}$	2.5	[V]
V_{nom}	3.6	[V]

Table 12.2: LG-HG2 18650 cylindrical cell specifications

the sum of the error determines the goodness of the fit. AmsterChem's *ScanIt* allows to trace the curve and resample to a user-defined number of points. Each data set consists of ≈ 132 points.

12.3.2. Multiple Regression: MatLab

This section discusses the multiple regression analysis performed in MatLab. The *fminsearch* algorithm was used in *MatLab* to perform the regression. This algorithm uses the simplex search method of Lagarias et al. [29], as it allows for a reasonable straightforward set-up in which the battery current I_b changes for each of these data sets and therefore also the analyzed Equation 12.2. The main disadvantage of this is that it does not necessarily converge to a local minimum and therefore the result should be critically reviewed.

12.3.3. Data Preparation

The data of each of the data sets was prepared for the multiple regression analysis. Each data point gets three values as seen by the columns in Matrix 12.9. The first column is the current value for the data set, the second the time it has discharged and the third column the voltage at that point in the discharge curve. Note that all discharge curves are constant current discharge curves.

$$M = \begin{bmatrix} I_{0.6A} & t_1 & V_{0.6A}(t_1) \\ I_{0.6A} & t_i & V_{0.6A}(t_i) \\ \dots & \dots & \dots \\ I_{0.6A} & t_n & V_{0.6A}(t_n) \\ I_{3A} & t_1 & V_{3A}(t_1) \\ I_{3A} & t_i & V_{3A}(t_i) \\ \dots & \dots & \dots \\ I_{3A} & t_n & V_{3A}(t_n) \\ I_{15A} & t_1 & V_{15A}(t_1) \\ I_{15A} & t_i & V_{15A}(t_i) \\ \dots & \dots & \dots \\ \dots & \dots & \dots \\ I_{25A} & t_n & V_{15A}(t_n) \end{bmatrix} \quad (12.9)$$

This first two columns from this matrix form the x -vector (where current is $x(:,1)$ and time $x(:,2)$) and the last the y -vector. A third vector was introduced to contain all the fitting parameters, as seen in vector 12.10. An alternative was used that also kept the nominal voltage V_0 as a variable (vector 12.11), which yielded negative values (but an even better fit). Because this would not be physical, it was decided to opt for the former variable definition even though the fit was slightly worse for high depth of discharge. It was also attempted to pre-define the peukert coefficient pc , which would result in very bad fits. It is also important to define Q_{rat} and I_{rat} very well, because otherwise the algorithm will not perform the fit.

$$b = [K \ A \ R \ p_3 \ p_2 \ p_1 \ p_0 \ pc] \quad (12.10)$$

$$b_{alt} = [K \ A \ R \ p_3 \ p_2 \ p_1 \ p_0 \ pc \ V_0] \quad (12.11)$$

12.3.4. Objective Function and Tolerances

This section discusses the objective function. For this objective function a vector norm is applied in *MatLab*. This considers the L^2 -norm, or vector norm. Equation 12.12 shows the objective that is minimized.

$$J = |\bar{y} - \bar{y}_{data}| = \sqrt{\sum (y(i) - y_{data}(i))^2} \quad (12.12)$$

The calculated norm of this minimum square of residuals equals 1.67351 after 1674 iterations and 2492 function evaluations. This was done for a total of 662 data point evaluations. The optimization in Equation 12.12 had the following optimization settings as seen in Table 12.3. *fminsearch* stops when it satisfies both TolFun and TolX. The simulation ends when the solver attempts a step that is smaller than defined by TolX. The same is valid for TolFun. It stops when there are changes with two subsequent iterations smaller than the defined TolFun.

Setting	Value	Explanation
MaxIter	10000	Maximum Number of Iterations
MaxFunEvals	10000	Maximum Number of Function Evaluations
TolX	1.00E-06	Lower bound on step size for subsequent iterations
TolFun	1.00E-07	Lower bound on function evaluation changes for subsequent iterations

Table 12.3: Optimization options for battery fitting with *fminsearch*

12.3.5. Initial Values

The initial values and resulting outcome of the fitting parameters are shown in this section. It is very sensitive to initial values and therefore these have to be considered closely. As a starting point, the values in the analysis by Verstraete et al. [70] were used and adjusted. For example, fitting parameter A was severely lowered because the exponential component at the start of the discharge curve is not as clearly present in the data sheet. Also the initial resistance was lowered to 0.015 as provided on the data sheet. The result of the fit shows that this is increased to a higher value. The fixed value of V_0 (nominal voltage) was set at 3.29. This is approximately the average nominal voltage for the different discharge curves and should be carefully chosen for improved fits. It is considered not necessary to specify R^2 in the case of non-linear curve fitting. The fit does very well for DoD until 0.8 (or SoC of $\approx 20\%$) for low discharge rates and very well for higher discharge rates. Table 12.4 shows the parameters initially chosen for the design vector b , as well as the resulting b after the analysis.

Battery	K [V]	A [V]	R [Ω]	p_3 [Ah^2]	p_2 [Ah]	p_1 [A]	p_0 [Ah^{-1}]	pc [-]	R^2
Verstraete Nominal	0.08726	2.451	0.07712	$9.331e^{-5}$	0.1273	-0.6613	3.057	1.02	0.968
Initial b	0.08	0.3	0.015	0.02	-0.3	2.0	0.5	1.005	N/A
Resulting b	0.0165	0.91	0.026	0.003	-0.048	0.176	0.524	1.0085	N/A

Table 12.4: Initial values and outcome of the algorithm

12.4. Modelling Results: Discharge Curves

The first battery discharge curves are fitted based on the LG-HG2 battery at 240 Wh/kg. Although this value could be used for conceptual sizing, the capacity reduces for higher discharge rates. For this reason, it is important to simulate the battery discharge so this can be analyzed and implemented in further models.

The resulting fit has very good quality from 0.2C (600mA) to 8.33C (25A). When compared to the SimScape fit (shown in the following section), this model is therefore valid for a much larger range of discharge currents. The reduction in capacity is modelled quite well too due to the addition of the peukert coefficient. At high depth of discharge, it can be seen that the voltage drops a bit slower at first but eventually goes to the right battery capacity at the cut-off voltage of 2.5V. The obtained curve fit for the LG-HG2 of the discharge curve in Figure 12.2 is shown in Figure 12.3.

12.5. Modelling in SimScape

One of the questions to be answered is whether the generic battery model in SimScape is suitable enough for modelling using Shepherd's modified model for charging and discharging. The previous model uses an

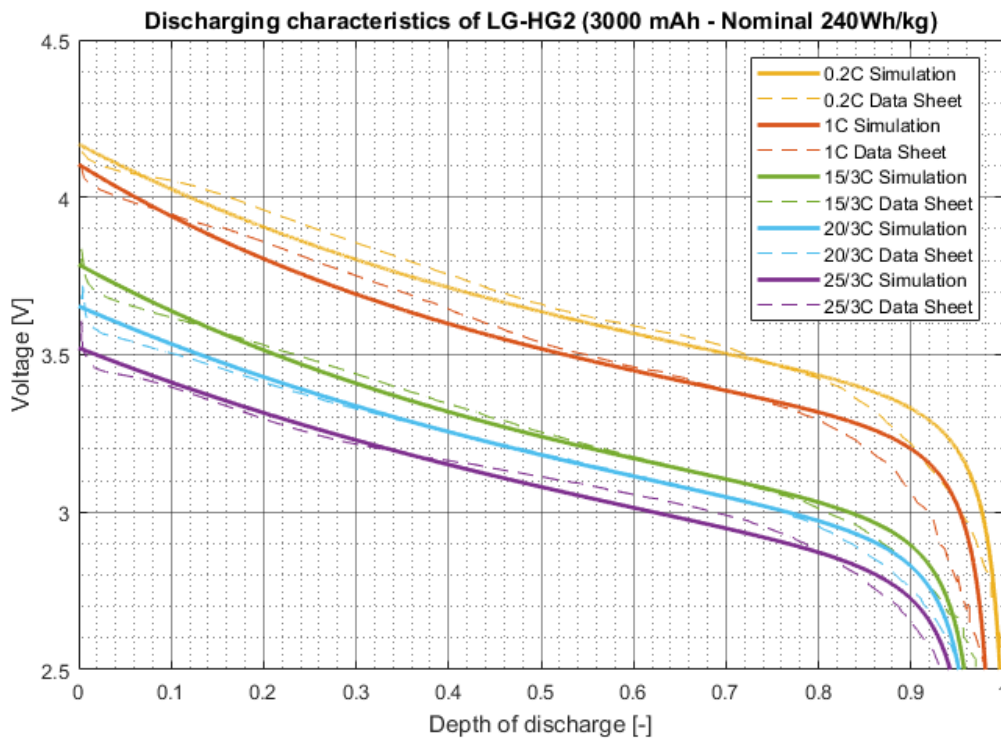


Figure 12.3: Fit of 5 curves simultaneously using the method of Section 12.3 for the LG-HG2 [6]

adjusted version of Shepherd’s original model - which has no consideration of charging - which is however seen in Shepherd’s modified model.

The model in SimScape Power Systems uses Shepherd’s modified model. Peukert’s law is not included for the capacity effect. Although Novak [41] specifies this is low for Li-Ion batteries - which is true as it is in the order of 1.005 to 1.4 [70]- it showed to make a difference in the curve fitting method previously explained. The SimScape/Simulink model used is shown in Figure 12.4 for ease of replication.

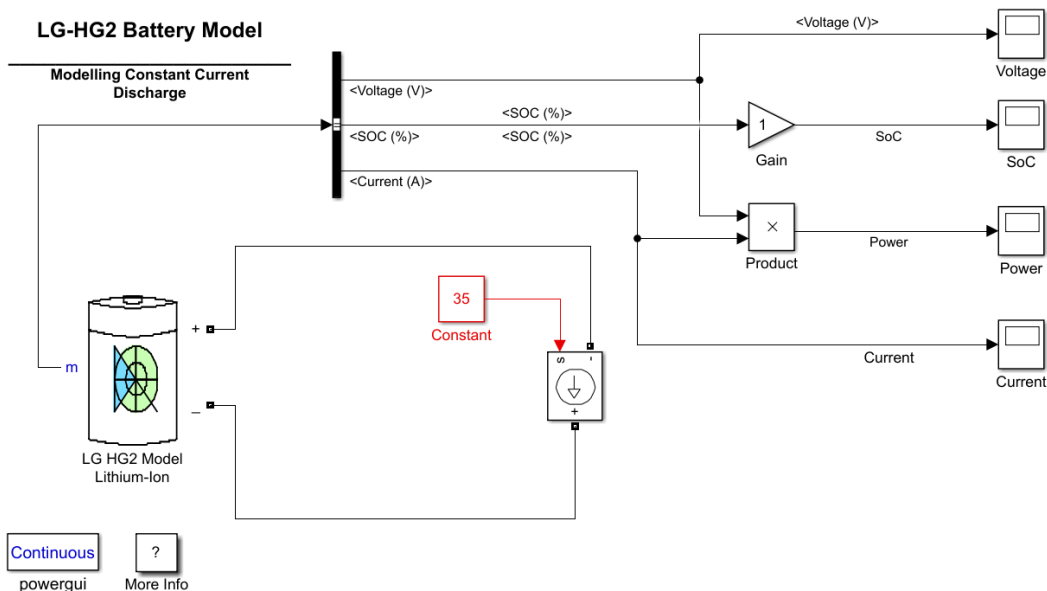


Figure 12.4: SimScape Discharge model with controlled current source for Simulink-SimScape interaction included for reproducibility

Model 1: Standard Method

The standard SimScape fitting method was first applied, which requires certain values from the data sheet. Also, it requires a number of values from the discharge curve at the rated current. The SimScape model then

performs its own fit to Shepherd's modified model. This, however, yields very poor results and the input values have to be tweaked to obtain a better fit at the rated condition. However, because this is a single regression it performs poorly at discharge rates other than the rated current. Because the Peukert coefficient is not included in this method, the effect of the discharge rate on the cell capacity also shows a high discrepancy.

Model 2: High Discharge Rate

For the reason of these large discrepancies, an attempt was made to model specifically for high discharge currents as these are likely to be used when the battery is used in combination with the fuel cell.

The high discharge battery was modelled for the high discharge rate of 35 A in Simscape because it was already expected that the battery would only be necessary for a relatively short time. Also, the discharge curves shows the closest correlation with the standard shape of Shepherd's modified model within SimScape. A bigger discrepancy can be seen for when the discharge rate is 20 A, but approximately follows the original curve. Larger discrepancies will be seen if this current is further reduced. It shows that it is difficult to model the battery well for all discharge rates, especially when the batteries show a more linear voltage reduction as the battery is discharged. Therefore, this model will not work well for lower discharge rates of the LG-HG2. It should also be noted that 35 A can only be used for short periods of time, the maximum continuous current is at 20-25 A.

It was therefore decided not to use the generic battery model in SimScape [64]. The next section will elaborate further on how the multiple regression fit based on Shepherd's original model was simulated.

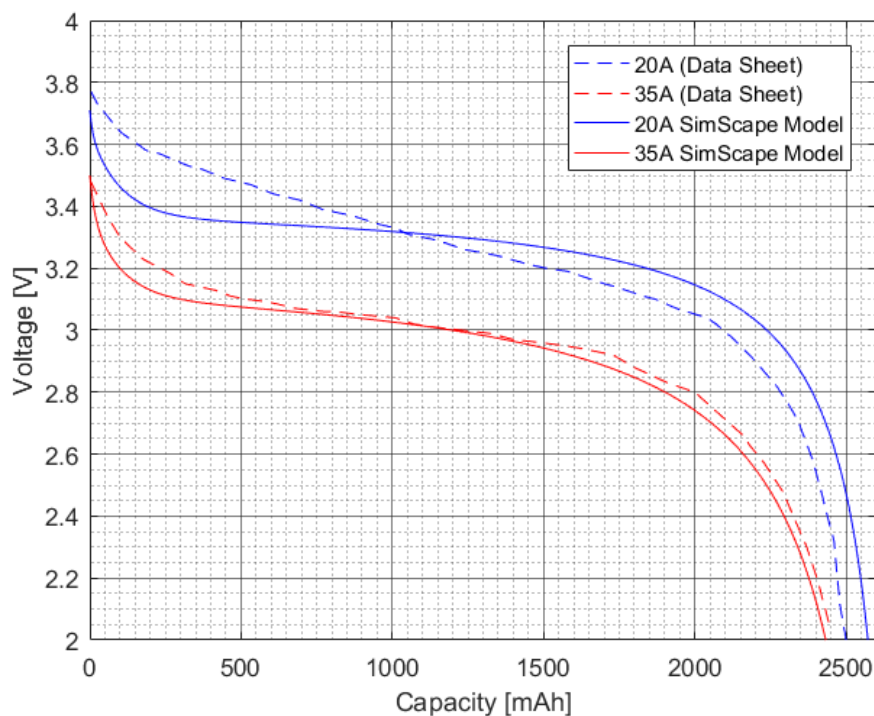


Figure 12.5: Data Sheet LG-HE2 High Discharge Battery vs. SimScape Model. Modelled for 35A and adjusted for decent behaviour between currents of 20A and 35A

12.6. Simulation of LG-HG2 According to Curve Fit Results

This section explains the simulation method and results for the curve fitted LG-HG2 battery which showed good correlation with the data. The equation with fitted parameters is directly used for this analysis.

12.6.1. Methodology

The simulation starts by using Shepherd's original model with the cubic polynomial extension to calculate the required current to reach the initial power requirement. An initial low assumption of I_b is made and set at 0.6 A or 0.2 C. With this, the voltage V_b is calculated using the model, followed by the power as in Equation 12.13

$$P_b = V_b \cdot I_b \quad (12.13)$$

This is used to check whether P_b is higher or lower than the power requirement as set in the profile. I_b is then increased or decreased accordingly in a *while*-loop, as long as the power is lower or higher and outside a margin of 1E-4 W.

When the initial current is set, the time is increased by a timestep dt , set at 1/3600 hours - or 1 second. For each of these time steps, the power requirement is checked and the current of the previous timestep used to calculate the power through Equation 12.13. If this is too high or too low, the current is increased or reduced until it falls into the power margin of 1E-4.

Surrogate Time

The most important parameter in this analysis is the capacity (Ah), also indicated by SoC and DoD. For each time step, the used capacity (Ah) needs to be determined by the current and time step dt as seen in Equation 12.14. This can also be written as Equation 12.15 or 12.16

$$Ah_{used}(t + dt) = Ah_{used}(t) + I_b \cdot dt \quad (12.14)$$

$$DoD(t + dt) = DoD(t) + \frac{I_b \cdot dt}{Q_{rat}} \quad (12.15)$$

$$SoC(t + dt) = SoC(t) + \left(\frac{I_b \cdot dt}{Q_{rat}} - 1 \right) \quad (12.16)$$

At each time step, Shepherd's model needs to be evaluated at a new current I_b because of reducing voltage and changing power requirements. This cannot be done at the runtime t but has to be done for the particular SoC / DoD / Ah_{used} . These therefore need to be evaluated at a surrogate time t^* . Here the I_b is acquired from an iteration procedure and V_b is analyzed as in Equation 12.18.

$$t^* = \frac{Ah_{used}}{I_b(t)} \quad (12.17)$$

$$V_b = V_0 - K \frac{Q_b}{Q_b - I_b \cdot t^*} + A \cdot e^{-B \cdot I_b \cdot t^*} - R \cdot I_b \quad (12.18)$$

12.6.2. Conditions

Condition in Equation 12.19 is used to make sure the discharge stops. Technically, this means the maximum capacity at that power level is reached. Generally, if this is a high power setting, some power can still be extracted at a lower current, as will be shown in Section 12.6.3.

$$V < V_{cut-off} \quad (12.19)$$

Another condition that can be set is that the DoD is only allowed to be used up to a certain value to ensure no full discharge. An example can be found in Equation 12.20 in which 15% SoC is always available. This can be adjusted according to safety standards, to increase cycle life or battery limitations. This was not done in this analysis. Instead, the maximum continuous current of 20 A is only allowed to be exceeded by a maximum of 10 seconds, which occurs in the FC-B configuration.

$$DoD \leq 0.85 \quad (12.20)$$

12.6.3. Simulation Test

Figure 12.7 shows the simulation test results for the power settings as shown in Equation 12.21 according to the arbitrary power profile in that same equation. The simulation was compared with the discharge behaviour for constant power in the generic power model in Simulink/SimScape, showing very similar results. This simulation, however, unlike SimScape, does not take into account a transient. It should be noted that the transient is very small for Li-Ion.

Figure 12.8 shows the comparison between the SimScape model and the model based on the curve fitting result. It shows that both models perform the same analysis, but because the fit of the SimScape model is not as good at high DoD, the battery can only be discharged for 90%. The reason is that the discharge curve of 3C drops much sooner in the SimScape model. This SimScape model can be improved with extra effort, as it requires a lot of trial and error. Data can only be given to SimScape for the rated discharge curve and direct comparison to the data sheet is difficult. Even though the fit is not perfect, it still shows reasonable results for low discharge rates as the rated capacity is better matched. The discharge curves from the curve fit can actually continue until the cut-off voltage is reached, whereas SimScape struggles to deliver the required

power at this point due to the diverging discharge curves at high discharge rates. For this verification of the model, the SimScape model was created and is shown in Figure 12.6. As shown, this comparison verifies the simulation method and mainly shows differences due to the respective curve fits.

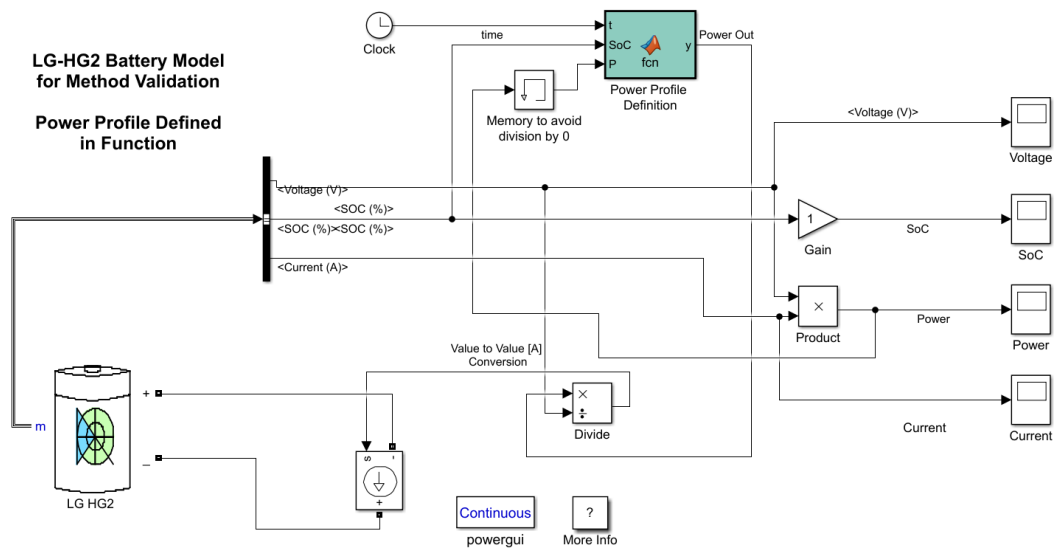


Figure 12.6: SimScape power profile model for verification of the custom discharge model. Included for reproducibility.

$$P_b(t) = \begin{cases} 15 & 0 \leq t \leq 0.1 \\ 45 & 0.1 < t \leq 0.15 \\ 30 & 0.15 < t \leq 0.25 \\ 15 & 0.25 < t \leq 0.35 \\ 30 & 0.35 < t \leq 0.4 \\ 15 & t > 0.4 \end{cases} \quad (12.21)$$

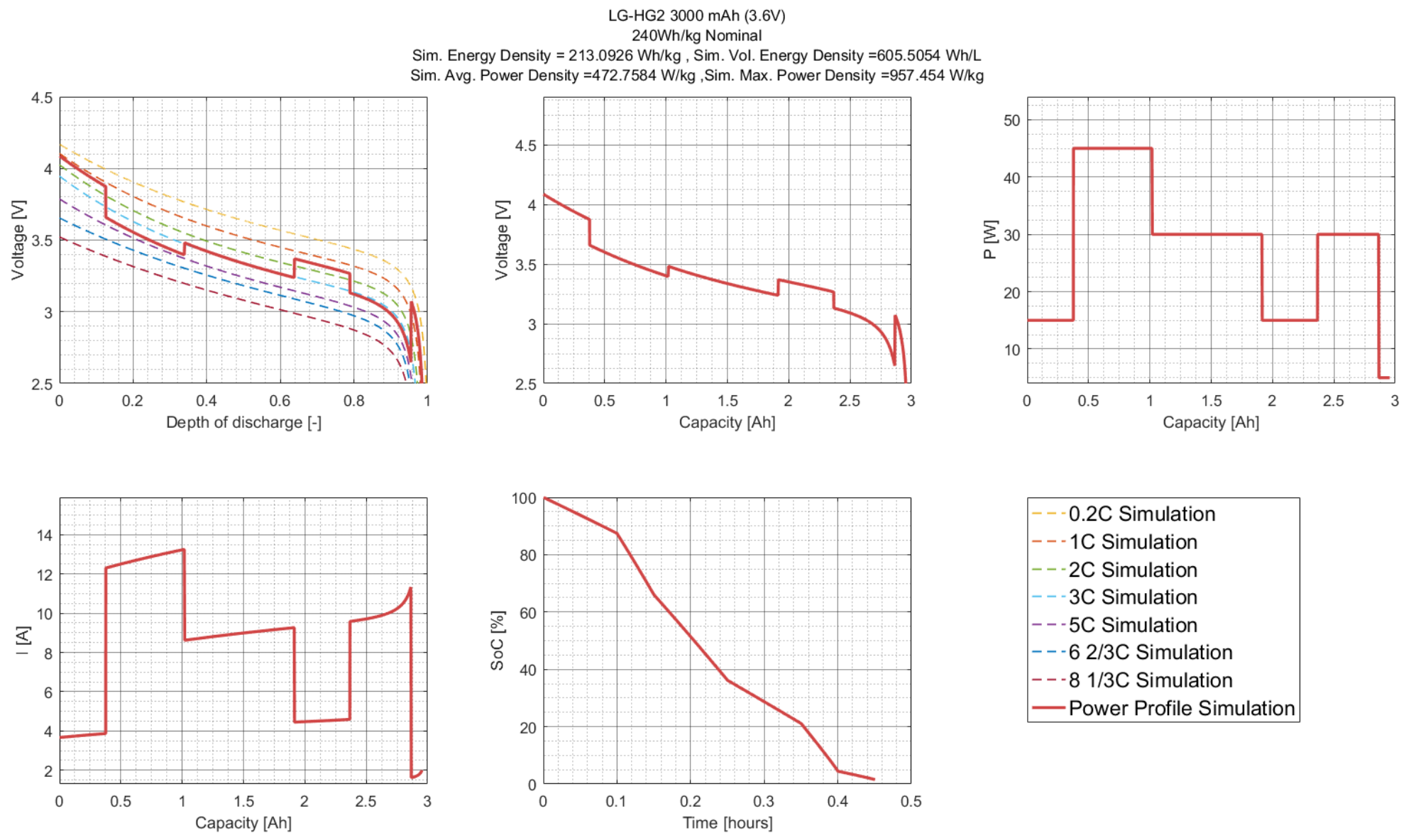


Figure 12.7: Simulation test of the LG-HG2 based on the curve fit

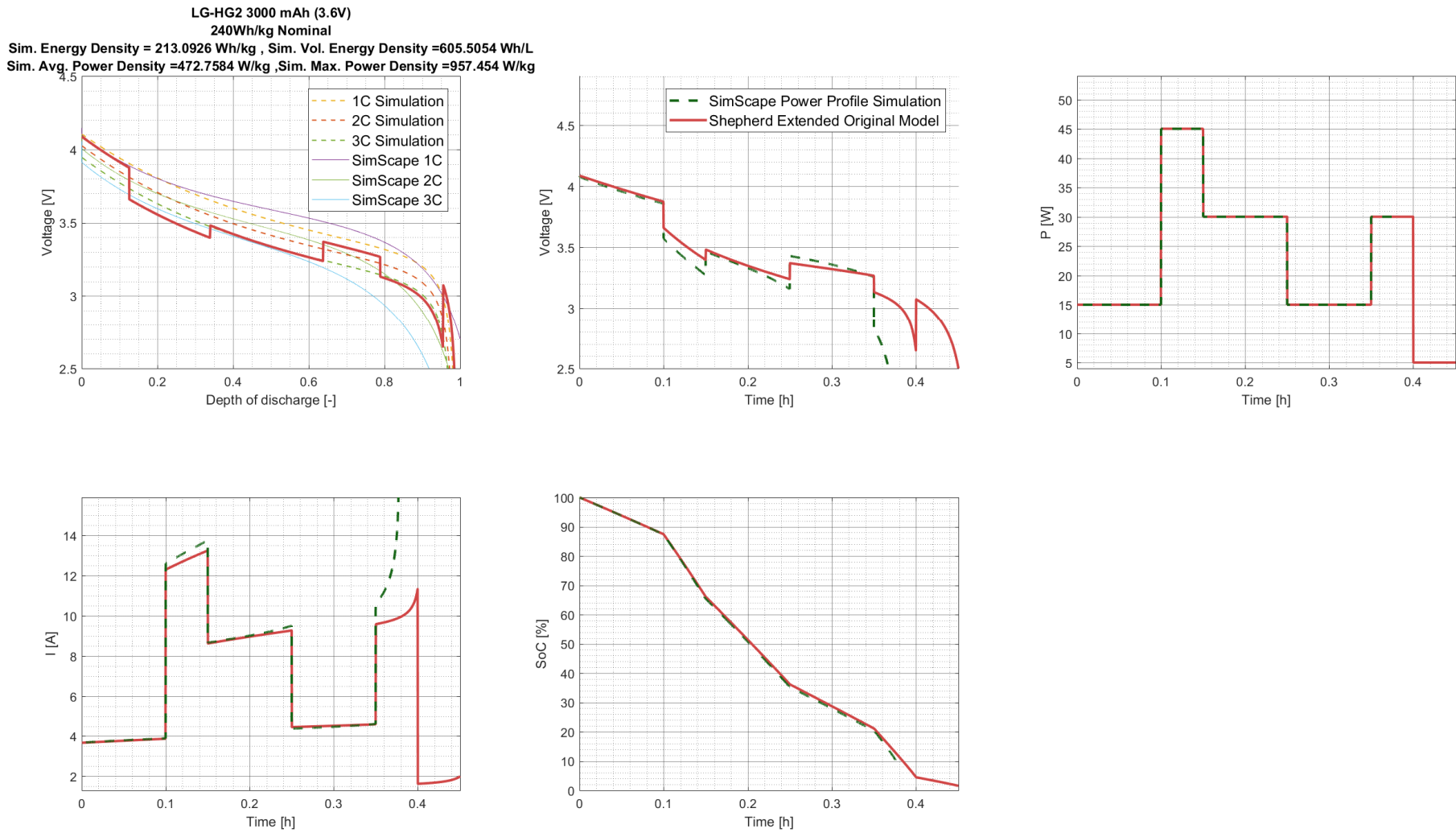


Figure 12.8: Simulation comparison of Shepherd's extended original model and SimScape

12.6.4. Charging Modelling: Future Improvement Consideration

The charging modelling option could be simplified for sizing purposes, but is not considered altogether in this thesis. Normally, Li-Ion batteries use a standard CC-CV (constant current, constant voltage) charging method. This could be done at the maximum charging current according to the specification sheets. At constant current charging, SoC goes up linearly up to a certain point. After this point, the current drops as voltage remains constant, meaning charging will be slower. It could be assumed that the entire battery can be charged using constant current charging, or split up into a fast and slow section. Otherwise, more elaborate charging modelling needs to be researched.

12.7. Voltage Range and Aviation Standards

Voltage standards were analyzed (Table 12.5) to understand what the existing and emerging standards are. This will give a better understanding of the voltage standards that could be used in this study. High voltage systems are beneficial in terms of cable weight as a result of reduced losses and overall current. It should be noted, however, that cables are taken as an overhead and not as a variable based on voltage choice. A bigger effect that is seen in realistic battery pack sizing, is that the maximum voltage determines the number of cells in series. The available weight and/or volume then determine how many parallel rows can be implemented. This discrete sizing could mean that a slight deviation from the standard voltage allows for a more efficient use of available weight.

For standard cases, it was decided to specify a voltage of 270 Vdc. Table 12.5 shows common values in aviation. For the battery only study, it was decided to introduce the maximum voltage V_{max} as a variable. 270 Vdc is one of the current standards that the table specifies. It needs to be taken into account that power electronics need to be able to work with a voltage range between 160-270 Vdc with typical Li-Ion batteries that generally have a cut-off voltage at approximately 2.5 a voltage of around 4 V when fully charged. It is assumed that the power electronics in this study will deal with this variation and only have a specified maximum voltage.

Case	Voltage	Range	Use case	Industry	Status
Source [73]	28 Vdc	-	Low Power LPA and small A/C	Aerospace	Existing
	270 Vdc	± 135	LPA subsystems	Aerospace	Existing
	115 Vac (at 400Hz)	-	Larger loads on LPA	Aerospace	Existing
	540 Vdc	-		Aerospace	Emerging
	230 Vac (400Hz)	-		Aerospace	Emerging
	230 Vac (320-800Hz)	-		Aerospace	Existing

Table 12.5: Voltage standards seen in the Aerospace industry

12.8. Battery Sizing for Battery-Only Configuration

The battery sizing follows directly from the available volume and weight, as well as the maximum power requirement. Table 12.6 shows the used power densities and efficiencies in the analysis. It should be noted that the mechanical efficiency η_{mech} was unchanged from the conventional gas turbine case at 97%. These values were previously elaborated on in Chapter 11.

Component	Power Density	Unit	Power Density	Unit	Efficiency	Unit
Electric Motor	7	[kW/kg]	6.7	[kW/L]	95	[%]
Inverter	7	[kW/kg]	7	[kW/L]	94	[%]

Table 12.6: Power density and efficiency of power electronics

Table 12.7 shows the weight breakdown before the battery sizing, taking into account that power electronics are sized for the maximum power requirement of 16 kW. Given the higher volumetric energy density of the battery cells, the volume should be no limit for battery only configurations. Instead, the payload volume can be restricted.

Equation 12.22 shows the calculation of the number of cells in series depending on the maximum specified design voltage and the maximum voltage of each cell. For the battery-only case, the number of cells in parallel can be easily determined from this, taking the floor integer value as seen in Equation 12.24. In this case the OEW includes the motor and inverter weight. It could be that some of the weight is not used because of the fact the number of cells is not continuous but increases step-wise by the number of cells in series N_s .

Weight Breakdown	Value	Unit	Comments
MTOW	100	[kg]	
Payload	0	[kg]	
Empty Weight + Blades	39.7	[kg]	
Electric Motor	2.3	[kg]	$P_m = 16$ [kW]
Motor Peripherals	1.3	[kg]	
Inverter	2.66	[kg]	$P_{inv} = 1/(\eta_m \cdot \eta_{inv})$
Total / OEW	46	[kg]	
Available for Battery Sizing	54	[kg]	
Available Volume	86.3	[L]	

Table 12.7: Voltage standards in the aviation sector, where 270 and 540Vdc are especially important for electric powertrains

$$N_s = \left\lceil \frac{V_{max}}{V_{cell,max}} \right\rceil \quad (12.22)$$

Parameter	Value	Unit	Description
$\eta_{overhead}$	0.6	[-]	Battery overhead factor

Table 12.8: Overhead factor used in all analyses

The overhead efficiency was set at 0.6 as seen in Table 12.8. This is similar to the overhead seen in battery packs in the automotive industry, which was already further elaborated on. This overhead is a result of the casing, cooling system, control, sensory equipment and miscellaneous components. Although batteries are very efficient, they operate in a very narrow temperature range. The maximum temperature of the LG-HG2 cells - and most Li-Ion cells - is 70 degrees Celsius. The optimum operating temperature is lower and therefore cooling has to be done with a very small temperature difference.

The overhead factor will be consistently used for both the battery-only and FC-B cases. The available weight for the cells can be determined using Equation 12.23, in which the total available weight for pack and overhead is W_{av} .

$$W_{av,pack} = W_{av} \cdot \eta_{overhead} \quad (12.23)$$

$$N_p = \left\lceil \frac{(MTOW - OEW) - W_{PL}}{m_{cell} \cdot N_s} \right\rceil = \left\lceil \frac{[(MTOW - OEW) - W_{PL}] \cdot \eta_{overhead}}{m_{cell} \cdot N_s} \right\rceil \quad (12.24)$$

12.8.1. Volume: Cylinder Packing

The volume was estimated as follows, based on the fact that the chosen cells are of the cylindrical type. A volume loss needs to be accounted for when packing cylindrical cells. This extra volume does help with battery cooling, however. Equation 12.25 shows the hexagonal packing density. For further analysis, square packing is used in volume estimates as seen in Equation 12.26. A comparison of the two packing options is shown in Figure 12.9. The volume is subsequently calculated with Equation 12.27. A quick comparison of battery weight and volume can be made through the gravimetric and volumetric energy densities and the available volume and mass. Given there is more volume available than there is mass, and the volumetric energy density is almost 3 times higher, volume is generally not an issue at all for battery-only configurations. The overhead that is applied to the weight is also applied to the volume of the battery pack. This overhead factor is 0.6, considering 40% of the pack consists of overhead components.

$$\eta_{hex} = \frac{1}{6} \pi \sqrt{3} \approx 0.907.. \quad (12.25)$$

$$\eta_{square} = \frac{\pi \cdot R^2}{4R^2} = 0.785.. \quad (12.26)$$

$$V_{B,pack} = \frac{\pi D_B^2}{4 \cdot \eta} \cdot L_B \cdot (N_s \cdot N_p) \cdot \frac{1}{\eta_{overhead}} \quad (12.27)$$

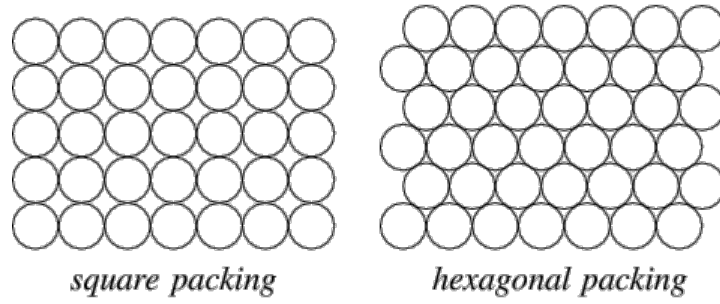


Figure 12.9: Circle packing options for improved battery pack volume estimates [72]

12.8.2. Battery Limits

Two limits are imposed on the battery cells. First of all, the battery cells need to stay under the maximum continuous current of 20 A as seen in Equation 12.28. It is allowed to exceed this for a maximum of 10 seconds. Secondly, the cell voltage need to stay above the cut-off voltage of 2.5 V according to Equation 12.29.

$$I_{cell} \leq 20 \quad (12.28)$$

$$V_{cell} \geq 2.5 \quad (12.29)$$

12.8.3. Range and Endurance Calculations through Simulation

The battery was sized by determining the average power in each flight section through helicopter power curves and power requirements for the rate of climb / descent. This consists of an initial hover of 30 s, a vertical climb to 100 m at 4 m/s, a climb at best range forward speed V_{br} to cruise altitude at a given RoC, a cruise phase, descent phase with V_{br} , vertical descent at -1 m/s and final hover for 30 s.

The current limit and cut-off limit are both imposed on the battery. The method chosen here is to find the maximum range for which the final battery voltage stays just above the cut-off voltage. The mission profile parameters directly determine the mission profile, but the cruise time remains an unknown as this is not a linear calculation but results from simulations. Two options were considered for determining the cruise time:

- **Option 1:** 'Trial and Error', in which the cruise time is increased by a standard amount until the simulation breaches the condition in Equation 12.29.
- **Option 2:** Binary Search for a quicker search of the maximum cruise time at the best range velocity and therefore cruise range

Eventually a third option was chosen due to instability of the simulation when it goes too far beyond the cut-off voltage. It is an improved version of the first option as the cruise time step reduces as it approaches the cut-off voltage. This means that initially it does not have to run many simulations. This method is summarized by Equations 12.30 and 12.31, showing that initially the step size of the cruise phase increases by 20 seconds (equals approximately 600 m at V_{br}) and reduces towards 1 second when the voltage drop becomes more significant. For quicker calculations, especially the first two values can be increased. For this method, the initial cruise time needs to be underestimated.

$$t_{cr}(i+1) = t_{cr}(i) + \Delta t_{cr} \quad (12.30)$$

$$\Delta t_{cr}[s] = \begin{cases} 20 & 3.3 \leq V_{cell} \leq V_{cell,max} \\ 10 & 2.9 \leq V_{cell} < 3.3 \\ 1 & 2.5 \leq V_{cell} < 2.9 \end{cases} \quad (12.31)$$

12.9. Battery Sizing for the FC-B Configuration

The second battery sizing method is different from the battery-only case. The fuel cell is sized for the cruise phase and therefore has approximately the same available power for the entire flight. The peak power requirements depend on the power requirement, efficiencies of inverter and motor, and the available fuel cell power in each section. Equation 12.32 is valid for each section in the flight and shows the battery power requirement. It should be noted that the fuel cell available power $P_{FC,a}$ is the power that goes into the inverter. The fuel cell also needs to power the compressor in this study. Some of The peak power sections are the initial

hover, vertical climb, forward speed climb, vertical descent and final hover phase. Therefore, the battery is required for a total of 5 sections.

$$P_{batt,a} = \frac{P_r}{\eta_{mech} \cdot \eta_{motor} \cdot \eta_{inv}} - P_{FC,a} \quad (12.32)$$

For the sizing, the same current and cut-off limits apply as in Equations 12.28 and 12.29. Two different methods in the sizing were tested:

- **Analysis Method 1:** Full discrete analysis, meaning that when a bigger battery is required, a full string of cells has to be added in accordance to the voltage requirement
- **Analysis Method 2:** Semi-continuous method where only a fraction of a string is added, allowing the battery sizing to be more continuous. This is not realistic, but may aid the optimization procedure because the function becomes more continuous.

It is clear that the aim is to use a battery of minimal size, as it deals with a peak power for a relatively short amount of time. Because of the small size, there is a high likelihood that the current limit is reached sooner and sizing is limited by the current, not necessarily by energy content. For this reason, there will also be an analysis with an extra vertical climb variable. This was initially implemented to ensure that 16 kW maximum is approximately reached. However, when this 16 kW requirement is removed, the battery could potentially be sized smaller, as well as the motor and inverter, leaving more space for hydrogen storage and increasing the vehicle range. Therefore, the following variable sets could be used. The vertical rate of climb will instead be used in a sensitivity study, rather than introduced as a variable.

- **Variable Set 1:** $h, RoC, RoD, i_{des}, p_{des}$
- **Variable Set 2:** $h, RoC, RoD, i_{des}, p_{des}, RoC_{vert}$

Equations 12.33 and 12.34 show the sizing of the battery within the FC+B configuration. The number of cells in series depends directly on the maximum voltage V_{max} , but the number of cells added in parallel is either 1 (most realistic, discrete) or 1/20 in order to test the effect on the optimizer and results. The sizing continues until both the cut-off voltage and current limit requirements are satisfied. The initial value for the number in parallel is application specific, but chosen to be 1 based on preliminary analysis.

$$N_p(i+1) = N_p(i) + \Delta N_p \quad (12.33)$$

$$\Delta N_p = \begin{cases} 1 & \text{Discrete} \\ 1/20 & \text{Semi-Continuous} \end{cases} \quad (12.34)$$

As a result of the small battery size, it is very likely that the current limit is reached instead of the cut-off voltage in most - if not all - cases for the FC-B configuration.

Chapter Conclusion

This chapter was dedicated to the sizing of the battery. Shepherd's original model was chosen to represent the discharge curves of the LG-HG2 Li-Ion battery. This original model as well as the modified model used in the generic battery model in SimScape Power Systems do not work well for a wide range of discharge rates. For this reason, an extended version of Shepherd's original model was fitted with good results. This required multiple regression as multiple discharge curves were fitted simultaneously. The peukert coefficient was introduced for better modelling of the capacity loss as a result of larger discharge rates.

The generic model in SimScape was still used to verify the custom simulation that was applied to the improved curve fits. This showed very similar behaviour between the different simulations. The battery is sized based on both voltage and power requirements and different methods are used for the battery-only and FC-B configurations.

This concludes the component sizing chapters. The next chapter will show the sizing procedure and optimization that was used to yield the results. This therefore also summarizes the modelling chapters.

Sizing Procedure and Optimization

This chapter discusses the sizing and optimization structure for the different mission profiles of the helicopter. This is shown both for the battery-only configuration, as well as the FC-B configuration. It combines the sizing procedures of the fuel cell, battery and additional components with the helicopter performance results and mission profile definitions. These sizing steps for the different configurations will be elaborated on.

13.1. Sizing Steps

The next sections will show the sizing steps performed for the different configurations:

- Sizing Flow Diagram Battery-Only Configuration
- Sizing Flow Diagram FC-B Configuration

The main difference between these two configurations is that the complexity of the battery-only sizing procedure is much lower for the B-Only case. This is because the battery weight is directly derived from the available weight when including the battery overhead, inverter and electric motor. In the case of the FC-B configuration, the battery sizing is based on power, current limits and energy content requirements. Also, the FC-B has additional sizing of components on top of the fuel cell stack. The compressor requires a power input from the fuel cell stack. Cooling and humidification are part of the reference stack weight.

13.1.1. Battery-Only Configuration

Figure 13.1 gives a global overview of the battery-only configuration and its sizing procedure. The dotted lines are part of the optimizer input and output, indicating which variables are sent to the objective function by the optimizer. The objective function calls all the other parts of the analysis and compares the range (or endurance) to the reference value. Most of what is performed inside the objective function is in the steps seen in the grey background in Figure 13.1.

The optimizer calls the objective function which includes the entire sizing procedure. Since the battery-only configuration depends on available weight for the battery pack and its overhead, the inputs have the biggest effect on the battery sizing. Of course, inverter and motor sizing needs to be done first based on the maximum power to ensure the available weight is known. The maximum power is determined through the analysis of the mission profile, consisting of two 30 s hover phases, a vertical climb to 100 m, a forward speed climb to the specified altitude, a forward speed descent to 100 m and a vertical descent. The power is determined through helicopter P-V curves and power averaging for each flight section.

Given the chosen payload, the weight budget for the battery and its overhead is now known and based on this, a battery simulation can be performed for the mission profile. The input for this simulation is the constant, averaged power for each flight section.

The battery simulation is run multiple times with an initial underestimated guess for the cruise time. Determining the cruise time is determined through running multiple simulations within a while-loop. The cruise time is increased in steps - which are large initial steps and small final steps - until the battery is discharged to the cut-off voltage. The payload limit can be observed when the current limit is reached.

When the cut-off voltage is reached for a given cruise time, the simulation-loop is stopped and the range determined. This range depends on all forward speed phases, which are the forward climb, cruise and forward descent sections. The optimizer then chooses a new set of variables, which are the altitude, rate of climb, rate of descent and the maximum voltage.

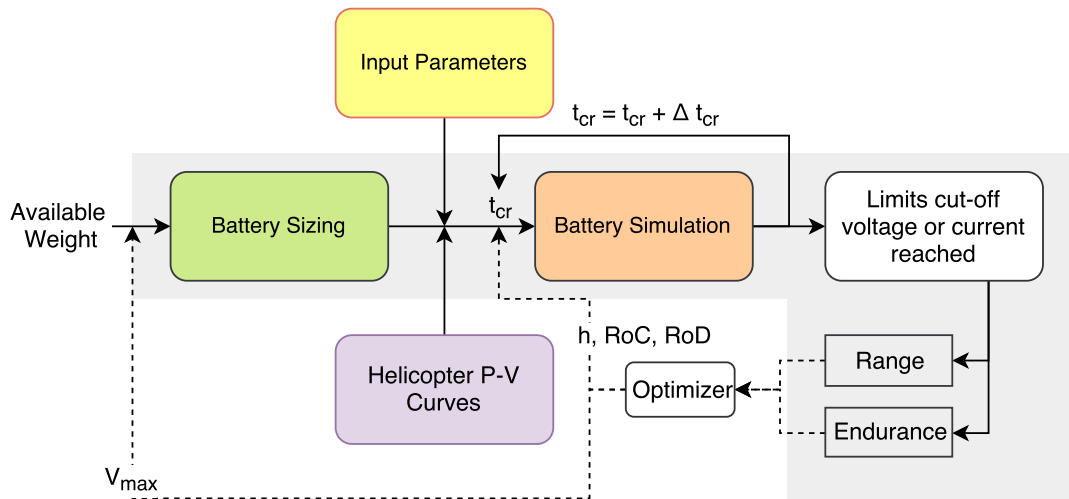


Figure 13.1: Sizing procedure for the battery-only configuration

13.1.2. FC-B Configuration

Figure 13.2 shows the global sizing procedure of the FC-B configuration. Again, the grey area indicates what is inside the objective function and the figure is structured in the same way. The sizing procedure is more elaborate than the battery-only scenario, which was mainly weight-driven. This configuration is mainly sized based on voltage and power requirements for the power sources. After the power systems are sized, which include the fuel cell system and the battery system, the remainder of the available weight is used towards a hydrogen storage tank. The volume is also considered for these scenarios, but showed no clear limitation.

The optimizer starts with an initial design vector specified by the user. The objective function uses this set as well as the input parameters (yellow) and helicopter P-V curves for the sizing to determine the cruise power level at first. The fuel cell is designed according to the cruise power and compressor power requirements (function of current density and stack pressure). The design power by the fuel cell stack therefore depends on the helicopter power requirement, the inverter and motor efficiency, as well as the compressor power needed. Because the compressor power also further increases the fuel cell power requirement, this is an iterative process as shown in the figure. Besides the fuel cell and compressor, other balance of plant components are sized at this point.

Before the battery can be sized, the fuel cell power needs to be determined for all other phases in the mission profile. The power requirement for each section is determined by averaging the power based on the helicopter P-V curves and climb/descent rates. The compressor power is kept constant in all these phases, allowing slightly higher performance from the fuel cell stack at lower altitudes. The combination of helicopter power requirements and fuel cell available power, determine the power requirements in each phase for the battery. This can be used directly in the battery sizing, which again uses simulation.

The battery in the FC-B configuration is sized based on the two limits: current and discharge (content) limit. In most cases, it will be shown that the current limit is leading as the battery is made as small as possible. The effect this will have is that the battery is oversized in terms of energy content. These limits are determined through battery simulation and the battery is enlarged when one of the limits is reached too soon. When the battery size meets both the discharge limit and the current limit, the next step can be performed. This next step is using the available weight for the hydrogen storage system to run the entire flight profile. For this, mass flows need to be calculated for each individual mission profile section. Part of this available weight for the storage method goes to the pressure regulators.

Based on this, the range or endurance can be determined directly as a result of hydrogen content and mass flows. This range/endurance is fed back into the optimizer, which decides on a new set of variables. These variables are the fuel cell stack current density and stack pressure, as well as altitude, rate of climb and rate of descent in forward speed phases.

13.2. Definition of Optimization

The definition of the optimization is shown here. It will elaborate on the design objective, normalization of variables and optimizer settings used for the battery-only and FC-B cases. For this, the function *fmincon* was used in MatLab, which finds the minimum of constrained nonlinear multi-variable functions. It is a gradient-based method that is designed for problems where the objective and constraints are both continuous with continuous first derivatives. For this reason, it was also decided to test a more continuous battery sizing

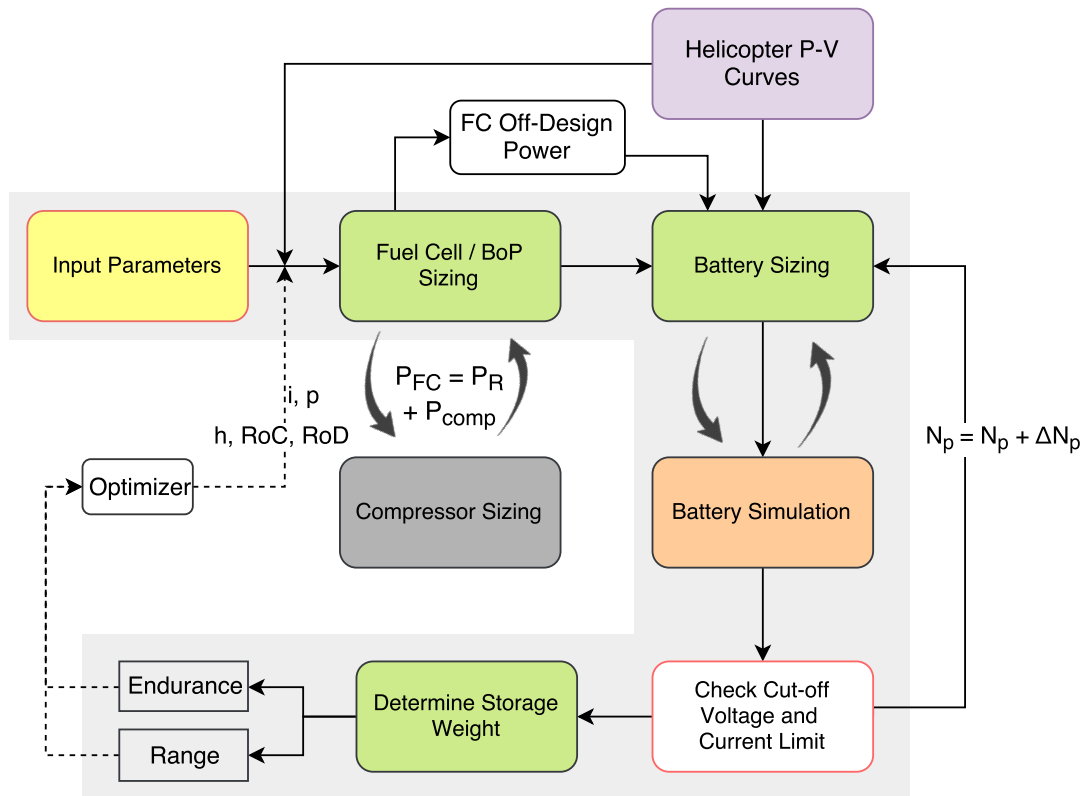


Figure 13.2: Sizing procedure for the FC-B configuration

($\Delta N_p = 0.05$) to ensure the battery weight and therefore also the range, does not show a significant step in the sizing procedure. It can already be noted that the fully discrete procedure ($\Delta N_p = 1$) also worked without any issues and showed very similar variable outputs compared to the semi-discrete case. The main effect of the semi-discrete battery modelling is a reduced battery size and increased range.

The advantage of the *fmincon* function is that it can be extended with constraints when necessary, such as volume constraints. For this analysis, it proved to be of little importance to impose any constraints. However, it is recognized that a more extensive analysis may require a number of constraints, especially when the effect of variables or variable combinations is no longer clear.

Also, when the helicopter (or fixed wing aircraft) design is integrated with the power system design, a function that allows constraints is beneficial. For now, the inputs into this function are the objective function, initial design vector and upper and lower bounds. Also, optimizer settings have to be entered and will be elaborated on. It should be noted that the optimizer aims for the minimum value while the aim is maximum range or endurance.

13.2.1. Design Objective

The design objective needs to be normalized with a reference value to ensure an order of magnitude of 1, such as the initial/reference range or endurance. A non-optimized result can be used for this, at specific payloads. The objective J needs to be clearly defined in the minimization problem. Although the majority of the problems are to either maximize airtime or distance, a minimum is determined by the *fmincon* optimizer in MatLab, using the standard *interior-point* algorithm. No big difference in results was observed when using different algorithms.

This section describes the optimization problems for the given mission profile. Objective functions need to be written as a minimum because *fmincon* aims for the set of design variables that yields the minimum objective. In all of the cases either range or endurance is maximized, meaning the objective has to be rewritten into a minimization form. The best endurance and best range optimization can be defined according to Equation 13.1 and 13.2. For the endurance, altitude plays no difference and therefore no optimization is considered but rather single analyses. The best range problems will go through the optimizer to yield payload-range diagrams based on optimized results.

$$\min \left(\frac{t_{BE,ref}}{t_{BE}} \right) \quad (13.1)$$

$$\min \left(\frac{R_{BR,ref}}{R_{BR}} \right) \quad (13.2)$$

13.2.2. Normalizing Variables

The design vector is normalized using reference values. This means that the initial design vector and objective J are of the order 1. This is to ensure the optimizer works as expected due to step sizes being in the right order of magnitude and similar for the different variables.

13.2.3. Optimizer Settings

This section discusses the settings used in *fmincon*. One choice to be made is the algorithm used by this optimizer. The default within *fmincon* is the 'interior-point' algorithm. A second option is sequential quadratic programming 'sqp'. Furthermore, there is the 'active-set' and the 'trust-region-reflective' algorithm. Running the optimization with the different algorithms did not have a large effect on the results. Also, the trust-region-reflective algorithm requires the gradient to be specified as an input to the optimizer.

The sequential quadratic programming algorithm can attempt to take a step and is allowed to fail during that step. This means the objective returns a value that is either infinite, not a number or complex. This situation does not occur and therefore the default interior-point algorithm was used for the optimization, especially since the choice of optimizer had close to no effect. The settings used in *fmincon* are shown by Table 13.1. The settings *DiffMinChange* and *DiffMaxChange* show the minimum and maximum change in variables by the optimizer. *TolFun* and *TolX* are stopping criteria for the optimizer. Either the objective function needs to change by less than the tolerance, or the step size of the design vector needs to be smaller than *TolX*. Due to normalization of variables and the objective, each variable is treated similarly. Lower and upper bounds will be treated further in the results chapter. The display option in the optimizer allows to show iteration information such as function evaluations and tolerances.

Setting	FC-B	Battery-Only	Explanation
Optimizer in MatLab Algorithm	fmincon Interior Point	fmincon Interior Point	Allows for constrained minimization Solves a sequence of approximate minimization problems
DiffMinChange	0.005	0.01	Minimum change in variables for finite-difference gradients
DiffMaxChange	0.1	0.1	Maximum change in variables for finite-difference gradients
TolFun	1E-04	1E-03	fmincon stops when function tolerance is reached
TolX	1E-04	1E-03	fmincon stops when step tolerance is reached
Display	iter	iter	Iteration display during optimization

Table 13.1: fmincon optimizer settings used to obtain the optimized results

Chapter and Part Conclusion

This chapter mainly provided an overview of the sizing procedure for the two configurations. This basically summarized Part II of this thesis, which consisted of the modelling of the different components and helicopter performance. Part III will elaborate on the results, mainly in the form of payload-range diagrams. Comparisons between B-only and FC-B configurations will be made and application areas identified. For the battery-only case, altitude, RoC, RoD and the maximum voltage will be the variables in the optimization. For the FC-B configuration, the voltage variable is replaced by semi-discrete sizing of the battery in some instances. Variables are the altitude, RoC, RoD, the current density of the fuel cell stack and its stack pressure. Unoptimized results will also be shown and compared.

III

Results, Conclusions and Recommendations

Results: Battery-Only and FC-B Configurations

This chapter is dedicated to all the results obtained through non-optimized and optimized analyses. The first section (14.1) is aimed at providing more insight in the helicopter power curves and the marginal gains that are possibly obtained here. Section 14.2 is dedicated to results of the battery-only scenario, showing the payload-range diagrams of the performed studies. Section 14.3 shows more elaborate results for the FC-B (Fuel Cell - Battery) configuration, in which the results are also compared to the battery-only scenario.

14.1. P-V Curves Helicopter

Table 14.1 shows the marginal gains that can be obtained by flying at a certain altitude. It can be seen that there is not a large difference in the best range velocity (V_{BR}) and their corresponding power. Note that the best range conditions were determined by minimizing P/V. Based on these parameters, it is expected that the best altitude will be around 1000-1200 meters, as the fuel cell power loss is limited. The lower bound of fuel cell stack pressure will be set at 1 atm. Therefore, only compressor weight slightly changes at increased altitude as pressure ratio is slightly higher. This will only be the case if for two instances, the same stack pressure is chosen. It will be shown that the pressure always goes to the minimum of 1 atm and small changes in altitude have a small effect. Although these results seem to indicate that for minimum P/V, the altitude should be beyond 1000 meters, the sizing of the fuel cell stack and compressor still have an altitude dependency.

Because of these small differences, it will also be possible to design the fuel cell for the required maximum cruise altitude specified by the user, as it will not impact range significantly. The minimum altitude set in all the analyses is 500 m. Figure 14.1 shows the improvement in minimum P/V at different altitudes, which becomes much less apparent after 1200 meters and reaches a minimum at 2000 m.

Altitude	V_{BE} [m/s]	P_{BE} [kW]	V_{BR} [m/s]	P_{BR} [kW]	P/V_{BR}
0	20	7.43	30.1	8.75	290.7
200	20.2	7.43	30.8	8.88	288.3
400	20.4	7.43	31	8.87	286.1
600	20.8	7.43	30.8	8.75	284.1
800	20.7	7.44	31.4	8.86	282.2
1000	21.3	7.44	31.1	8.72	280.4
1200	21.4	7.45	30.9	8.61	278.6
1400	21.6	7.46	31.2	8.65	277.2
1600	22	7.47	31.3	8.64	276.0
1800	21.8	7.49	31.4	8.64	275.2
2000	22.4	7.5	31.3	8.6	274.8
2200	22.5	7.52	31	8.52	274.8
2400	22.4	7.55	31.1	8.57	275.6
2600	22.7	7.58	31.2	8.65	277.2
2800	22.6	7.63	30.5	8.54	280.0
3000	23	7.69	30.3	8.64	285.1

Table 14.1: Important Performance parameters from the P-V Curves

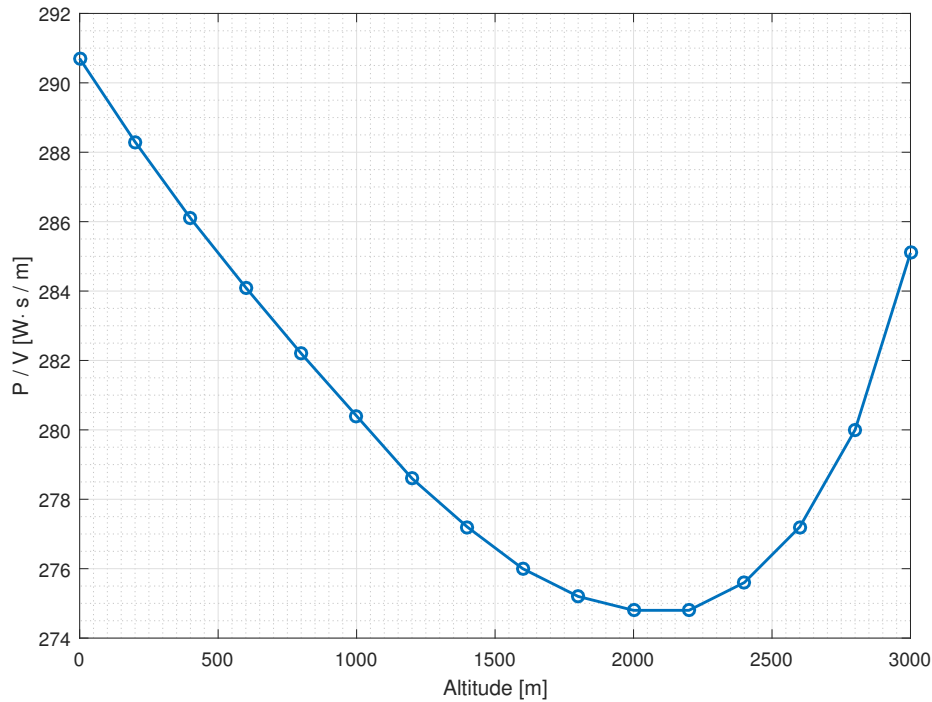


Figure 14.1: Indication of P/V reduction with altitude, showing a quick improvement up to ~1200 meters, after which the improvement quickly reduces.

14.2. Battery-Only Configuration

This section contains the battery-only results. The main results will be discussed, taking into account the limiting factors in the payload-range diagrams. It will be shown that the main limits for the battery-only configuration are either energy content (low payload) or current limits in a high payload configuration which automatically has a small battery pack.

14.2.1. Fixed Parameters

The fixed parameters in the sizing are the start and end hover times of 30 seconds (OGE, out of ground effect), a vertical climb of 4 m/s to reach the maximum power P_{max} of around 16 kW and the vertical descent of -1 m/s. Vertical phases are between 0 and 100 meters altitude.

For the 500 m and 1500 m non-optimized analyses, the forward speed RoC was set to a maximum of 6.8 m/s reaching approximately 16 kW. The RoD in the forward speed descent phase was set at a moderate -2 m/s.

An important consideration is that the maximum payload cases are determined by the maximum payload at which the cruise altitude is barely reached, with enough hydrogen left to still perform the descent and landing sections.

14.2.2. Variables for Optimization: Battery-Only

In case of the battery, there is not much variation possible due to both a lower number of variables and also a lower number of components. Therefore the optimization is not as elaborate as the FC-B case. It is, however, important to see what can be achieved with the battery-only configuration.

A number of mission profile variables can be specified on top of a variable maximum voltage - which is the core of the battery pack sizing due to discretization of cells in series and parallel. Other than these variables, the reference battery could be changed by another battery in future studies. The variables considered in the Battery-Only analysis are shown in Table 14.2. The vertical climb rate is not considered as it gives a maximum available power of 16 kW (same as conventional) near sea level and was set at a fixed 4 m/s. Also, for the battery-only design this is not a limiting factor.

A recommendation could be to investigate the vertical rate of climb (RoC_{0-100m}) and its effect on the payload-range diagram, which will be done for the FC-B scenario. A performance reduction could result in a lighter battery in that case and therefore also an increased range. In the battery-only case, it will barely affect battery size, but rather the power electronics sizing, amongst which the inverter and motor.

Variable Number	Variable
1	V_{max} (Voltage)
2	h_{cruise}
3	$RoC_{100m-h_{cruise}}$
4	RoD

Table 14.2: Variables for Battery-Only Optimization

14.2.3. Initial Points

Table 14.3 shows the initial points considered for each optimization run to avoid poor local minimum solutions. It was, however, observed that different solutions only deviated slightly when the final \bar{x} has some differences in RoC and RoD. Altitude has a small but relatively insignificant impact as expected. The design vector is $\bar{x} = [h, RoC, RoD, V_{max}]$ with the reference values (normalized to 1) chosen as $\bar{x}_{ref} = [1500, 4, -3, 270]$. The variable lower and upper bounds can be found in Table 14.4.

Run	Chosen x0	Strategy
Run 1	[1, 1, 1, 1]	Standard
Run 2	[0.33, 1.7, 1.5, 0.95]	Low Altitude, high RoC/RoD
Run 3	[1,1,1,0.95]	Standard, low voltage
Run 4	[1.5,1,1,1]	High altitude
Run 5	[0.33, 1,1,1]	Low Altitude

Table 14.3: Initial points considered in the optimization

Variable	Unit	LB and UB	Elaboration
h	[m]	$500 \leq h \leq 3000$	Altitude
RoC	[m/s]	$2.8 \leq RoC \leq 6.8$	Forward speed climb rate
RoD	[m/s]	$-4.5 \leq RoD \leq -2$	Forward speed descent rate
V_{max}	[V]	$254 \leq V_{max} \leq 286$	Battery maximum voltage

Table 14.4: Variables in the battery-only configuration

The following sections will show the unoptimized 500 m and 1500 m results for the battery-only configuration, but also the improvements in range that are achieved through optimization. It will be shown that these are small improvements, mostly achieved by choosing a voltage at which the unused weight (Equation 14.1) is close to zero. Otherwise, small improvements with altitude can be observed. The unused weight is the weight available for the battery pack, subtracted by the pack weight and overhead. Due to discretization - when choosing a fixed voltage of e.g. 270 V - some unused weight was added to the payload to yield those unoptimized results.

$$W_{unused} = W_{av,pack} - W_{pack} - W_{overhead} \quad (14.1)$$

14.2.4. Payload-Range: 500m, 1500m (Unoptimized)

This section discusses the payload-range for the mission at 500 m and 1500 m altitude. For the purpose of showing a bit more data on the battery pack configuration, the 500 m and 1500 m mission profiles were run from 0 kg to maximum payload in steps of 5 kg. Table 14.5 shows the result for 0 kg payload to 29.6 kg maximum payload for a cruise phase at 1500 m.

For this unoptimized result, the battery was sized at 270 Vdc, resulting in 66 cylindrical LG-HG2 cells in series. After reducing the available weight with the electric motor, inverter and payload weight, the battery could be sized in accordance with the overhead parameter. This results in a 32.3 kg battery pack (21.7 kg overhead) when there is no payload and 14.7 kg of batteries at the maximum payload. The overhead in the latter case is 11.7 kg. The volume is not an issue with battery packs given that 91.25 L is available for the battery pack, inverter (DC/AC), motor and overhead and that maximum volume is reached when battery size is largest. This yields a volume of only 15.29 L for pack only. This needs to be divided by the overhead factor of 0.6 to acquire the volume of both pack and overhead. Therefore, the maximum volume of the battery pack is approximately 25.5 L, 30 L when including the inverter and motor. This means that over 60 L is still available for the payload.

Parameters	Unit	Payload [kg]						
		0	5	10	15	20	25 (RoD -3)	29.6 (RoD -3)
Peak Current	[A]	8.29	9.1	10.13	12.97	15.16	18.17	18.17
Energy Density	[Wh/kg]	228.98	227.62	226.06	221.75	218.9	215.2	215.2
Actual Energy Density	[Wh/kg]	137.1	136.4	135.5	125.85	123.3	120	120
N_s	[-]	66	66	66	66	66	66	66
N_p	[-]	11	10	9	7	6	5	5
Battery Pack	[kg]	32.3	29.37	26.43	20.55	17.62	14.69	14.68
Overhead	[kg]	21.66	19.66	17.66	15.66	13.66	11.66	11.66
Unused mass	[kg]	0.1858	0.12	0.0598	2.93	2.87	2.8	0.05
Volume	[L]	15.29	13.9	12.5	9.7	8.34	6.95	6.95
Vmax	[V]	270	270	270	270	270	270	270
Range	[km]	75.8	67.8	59.8	43.8	35.9	28.5	28.5
Flight time	[min]	43.69	39.4	35.14	26.6	22.4	18.4	18.4
Cruise Time	[min]	25.28	21	16.7	8.21	4	3.9	3.9

Table 14.5: Overview of Parameters for the 1500 meter analysis. Note that for large payloads, the RoD

This battery size reduction with increasing payload means that the number of parallel rows reduces from 11 to 5, meaning fewer cells have to deliver the same peak power. The peak current allowed is 20 A as this is the LG-HG2 maximum continuous current. A further reduction in parallel rows (below 5) would immediately result in exceeding the maximum current. A maximum payload of 29.6 kg can be reached when increasing the rate of descent from -2 to -3 m/s. This means the vehicle can make it up to the defined altitude, descent and land.

Furthermore, an energy density reduction is observed as a result of a shift downward in the battery discharge curve at higher currents. The actual energy density, when considering the overhead too, is not even close to the nominal 240 Wh/kg of the cells, but rather in the order of 120-140 Wh/kg. In the battery-only configuration, the battery can be discharged to about 5% SoC and therefore these real energy densities are at the high end of what the state-of-the-art batteries are capable of in real applications. For a FC-B configuration where peak powers have to be delivered, it will be shown that in many cases the battery is oversized in terms of energy content, with size restrictions mainly based on the peak current.

Figure 14.6 shows that the result changes for the 500 m analysis. No massive changes can be observed in terms of range, which is overall only slightly lower. This is expected due to the helicopter (GC-201) power curves being very close together at the best range velocity V_{br} for different altitudes.

Parameters	Unit	Payload [kg]						
		0	5	10	15	20	25	29.6
Peak Current	[A]	8.3	9.13	10.12	13	15.11	18.12	18.12
Energy Density	[Wh/kg]	228.89	227.59	226	221.9	219.1	215.5	215.5
Range	[km]	73.54	65.83	58.11	42.78	35.16	27.6	27.6
Flight time	[min]	42.52	38.39	34.26	26.04	21.96	17.9	17.9
Cruise Time	[min]	34.9	30.77	26.6	18.4	14.3	10.28	10.28

Table 14.6: Changing results for the mission with 500 m altitude, RoD is -2 for all cases

Battery Characteristics in Low and High Payload Configurations

The sizing method of the battery-only configuration allows 60% of the remainder of the weight to be used by battery cells, as 40% goes to battery overhead in accordance to state-of-the-art automotive applications.

For this exact reason, when the payload is increased, the battery size gets smaller and the load per cell is increased, resulting in a payload limit. The range limit is mostly a function of the energy density, but it can be shown that the energy density of the cells is reduced as the current is increased. Therefore, smaller packs have a disadvantage in terms of range. The current limit is taken into account directly for the FC+B sizing as will be shown in later results.

Figure 14.2 to 14.4 show the discharge curve and the current diagrams of an unoptimized configuration, but with all forward speed flight sections at the best range velocity V_{br} . It can be shown that for a large pay-

load, the discharge curve moves downwards from being around 4 A (Figure 14.4) to 9 A (Figure 14.5) because of a smaller battery. Because the size of the battery is relatively large, there is no current limit at the vertical climb section of 4 m/s. Another observation in the discharge curve is that the low payload version (big battery) is able to discharge for 96%, whereas the smaller battery is only able to discharge for about 94%, because the cut-off voltage is reached sooner.

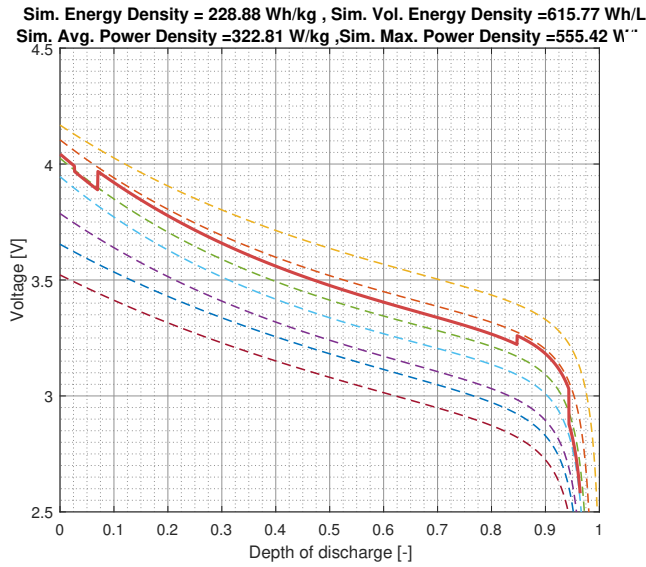


Figure 14.2: Discharge curve with 0 kg payload. The dashed lines indicate discharge curves (top to bottom) of 0.6, 3, 6, 15, 20 and 30 Amperes

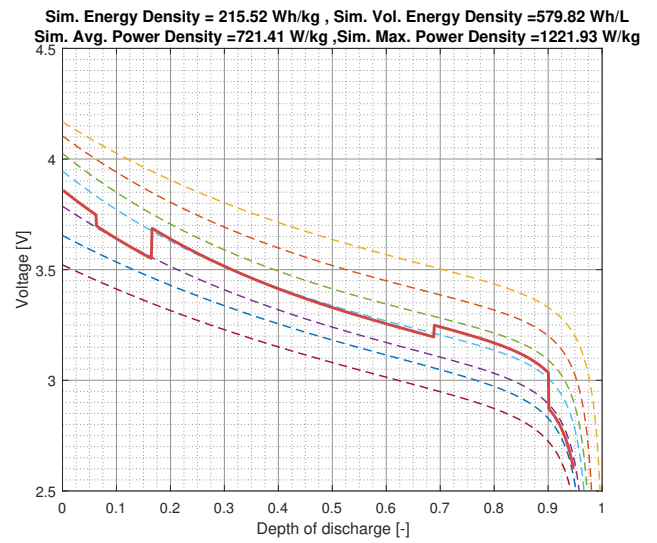


Figure 14.3: Discharge with 29.6 kg payload. The dashed lines indicate discharge curves (top to bottom) of 0.6, 3, 6, 15, 20 and 30 Amperes

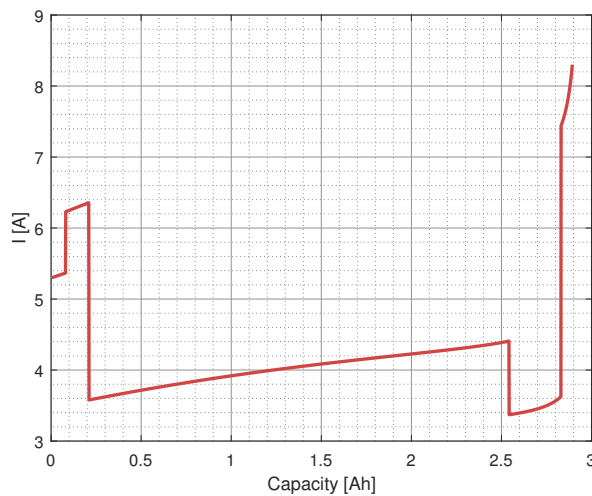


Figure 14.4: Current at 0 kg payload

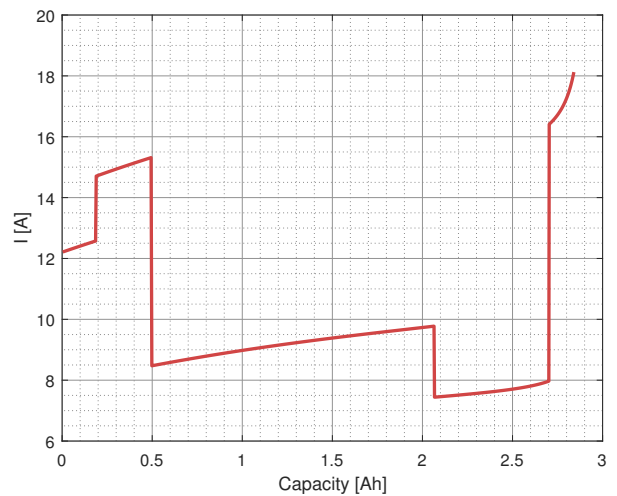


Figure 14.5: Current at 29.6 kg payload

14.2.5. Payload-Range: Optimized Battery

This section shows the payload-range diagram of the 500 m and 1500 m unoptimized analyses compared to the optimized analysis. Table 14.7 shows a number (but not all) of the runs that were performed in the optimization. Figure 14.6 shows the comparison between the 500 m, 1500 m and optimized runs. The reason why the 1500 m version may perform better can be observed in Figures A.1 and A.2 in Appendix A, showing the simulation results of the batteries. Although the peak power during climb needs to be delivered for a longer time, this is done when the battery voltage (see discharge curve) is highest, with relatively low currents, barely affecting energy density. Due to the larger altitude, the descent time is increased, allowing a current drop when voltage drops towards a lower State of Charge (1-DoD). This is the phase in which a lower current benefits the average energy density slightly. However, it should be noted that the V_{BR} at 500 m is approximately 30.9 m/s and 31.25 m/s at 1500 m, with no power reduction of the battery with altitude, so this is

another explanation that can be provided. The P/V is smaller at 1500 m, meaning this should be better for a best range analysis.

Payload	x0	x	h	RoC	RoD	V_{max}	Range
0	[0.33, 1.7, 1.5, 0.95]	[0.97, 1.26, 1.06, 0.99]	1450	5	-3.2	268	76.29
0	[1, 1, 1, 1]	[1, 1, 1, 1]	1500	4	-3	270	76.24
5	[1, 1, 1, 1]	[0.997, 1.01, 0.998, 0.992]	1494	4.04	-3	268.9	68.25
5	[1,1,1,0.95]	[0.94, 1.12, 0.99, 0.995]	1417	4.47	-2.97	268.6	68.17
10	[1, 1, 1, 1]	[0.996, 1.01, 0.9925]	1494	4.04	-3	267.99	60.21
10	[0.33, 1.7, 1.5, 0.95]	[0.64, 0.995, 0.6147, 0.99]	969	4	-1.84	266.8	59.57
10	[1,1,1,0.95]	[0.9645, 1.15, 1.01, 0.99]	1447	4.58	-3.04	268.2	60.25
15	[1,1,1,1]	[0.35, 0.89, 0.85, 1.05]	526	3.56	-2.54	284.4	46.28
15	[1,1,1,0.95]	[0.9, 1.13, 0.99,0.99]	1349	4.54	-2.96	266.44	51.2 (+17%)
15	[0.33, 1.7, 1.5, 0.95]	[0.96, 1.29, 1.01, 0.95]	1446	5.15	-3.03	264.8	51.28
20	[1,1,1,0.95]	[0.85, 1.2, 1.04, 0.98]	1270	4.8	-3.12	265.3	43.47
20	[0.33, 1.7, 1.5, 0.95]	[0.61, 1.0, 0.61, 0.98]	921	4.03	-1.84	263.75	42.87
20	[1.5,1,1,0.95]	[0.899, 1.21, 1.024, 0.98]	1349	4.82	-3.07	264.39	43.46
25	[1,1,1,0.95]	[0.86, 1.06, 0.94, 0.984]	1291	4.24	-2.8	265.7	35.56
25	[1.5,1,1,0.95]	[0.5345,1.25,0.81,0.977]	802	4.99	-2.44	263.8	35.34

Table 14.7: Best results obtained

The clearest difference between the 500 m and 1500 m cases is the improvement from 73.51 km maximum range to 75.8 km (3.1% improvement). This is marginal as expected from the P-V curves. Also, the optimized results show that no larger altitude than 1500 m is beneficial. This would put a larger load on the battery in the climb phase.

The main benefit in the optimization is through the variable V_{max} , the maximum voltage. This is due to discretization, further explained in the following section. The optimized result shows a further improvement from 75.8 to 76.29 km as a result of a changing V_{max} , but mainly showing improvements in results obtained for payloads between 15 and 25 kg as seen in Figure 14.6. This is because the optimization through V_{max} gets rid of the unused weight as a result of discretization.

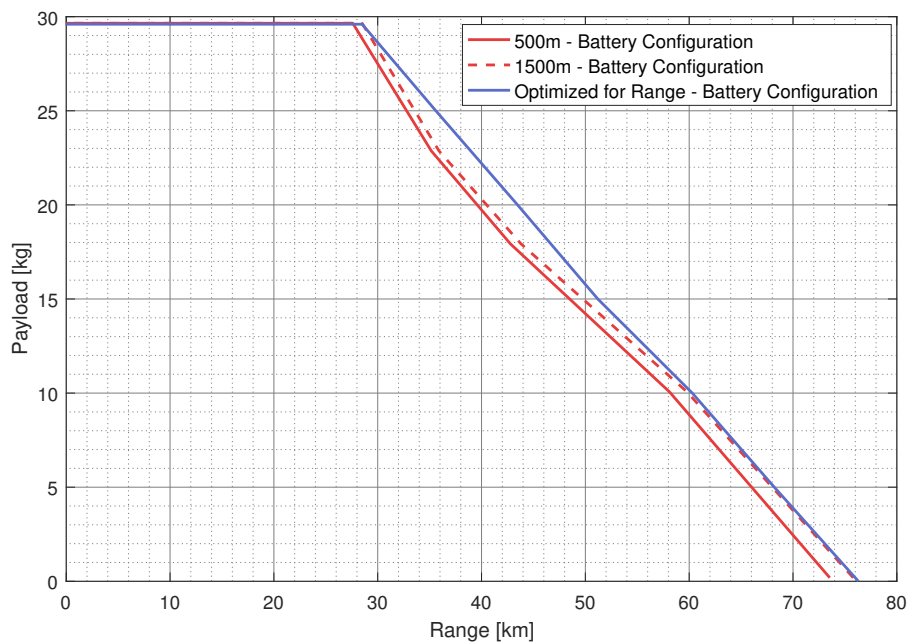


Figure 14.6: Payload-Range diagram of the battery-only configuration for the LG-HG2 18650 battery at a nominal energy density of 240Wh/kg

Elaboration on Discretization

The discretization effect is the clearest effect seen in the optimization. The unused weight as a result of having to round the number of cells in series N_s to the upper integer and the cells in parallel to the lowest integer (to stay within the weight limit), does have an impact on the range if the voltage is not optimized to maximize the battery size. By changing the voltage, the range can be improved significantly because the unused weight is minimized. The battery benefits from a slightly larger size, meaning lower average currents and a higher average energy density.

Variable Analysis: Optimized Overview

This section discusses the general tendency within the optimization for a certain set of variables. It can be seen that there is a tendency for the optimizer to go to 1200-1500 m altitude. This was expected based on P-V curve analysis of the helicopter. This showed that P/V improvements are low beyond 1000-1200 meters. The battery is not altitude dependent (although the cooling would be) and therefore is expected in the minimum P/V section. However, a longer peak power phase will impact battery energy density and it is therefore not odd that the optimum altitude is slightly lower. Altitude changes will yield marginal gains based on the P-V curves.

The effect of RoC and RoD is low. RoC is a peak power phase, but the 500 m and 1500 m analyses showed that even a maximum RoC (for the 16 kW peak power limit) in the highest payload case, is not touching the current limit in the climb phases. Hence, it can be said that this is barely influencing the result. The rate of descent varies in the optimized results, but was not the main factor in obtaining improved or reduced range. Small changes after performing the optimization runs also had minimal effects.

14.2.6. Sensitivity of Nominal Energy Density

This section studies the effect of increasing the nominal energy density of the battery. This is based on Li-S and Solid-state Li-Ion values towards 2030, going towards 400 Wh/kg. Volume is further improved for these batteries and therefore not further considered. For state-of-the-art Li-Ion battery technology, volume is already no issue in this application. The assumptions for this sensitivity and forecast are explained through the following points:

- **Cell weight reduction:** The assumption is that 400 Wh/kg is achieved by reducing the weight of the current LG-HG2 battery from ~44.5 to 26.7 grams.
- **Equal battery characteristics:** In reality the battery chemistry will most likely be different (such as Lithium-Sulfur) due to the materials used. The effect this may have on maximum discharge rate or the exact discharge characteristics can be significant. If the maximum discharge rate is reduced, this will severely impact the maximum allowable payload and shift the payload-range diagram downwards as the current limit is reached sooner.
- **Overhead unchanged:** The overhead is still 40% of the total pack weight, meaning 60% is used by the battery cells. Therefore, overhead weight also reduces to the same extent as the battery cells.

Figure 14.7 shows the payload-range diagram comparison between a nominal cell of 240Wh/kg and 400Wh/kg under the previous assumptions. The first observation that can be made is that the maximum range at 0 kg payload reaches 135 km, almost 78% up from the current state-of-the-art. This maximum range is energy density limited.

The maximum payload, as was seen before, is mostly limited by the current of the cells. Because for the same weight budget, more cells can be put in parallel, there is a smaller discretization effect and more cells can deliver the same power level. This means overall current is reduced, also meaning that overall energy density is improved. The maximum payload therefore shifts up based on the assumption of equal battery characteristics. Because these characteristics are unknown, the low payload range estimates are of higher confidence than the high payload range estimates.

14.2.7. Maximum Endurance: 500 m

The maximum endurance will be considered for the 500 m case. Note that the P_{BE} as was seen in Table 14.1 is constant and the speed at which the helicopter power requirement is about 15% lower than at the best range speed. The velocity is approximately 20.6 m/s at 500 m altitude with a power of 7.43 kW.

Table 14.8 shows the flight time data for the 500 m best range (BR) and best endurance (BE) analyses. The flight time for 0 kg payload at the best range speed is only 42.5 minutes, whereas this goes up to 51.1 minutes at the best endurance velocity. For the maximum payload of 29.6 kg, the current limit is reached at the hover phase at the end of the flight. The result is a best endurance of 21.4 minutes, compared to 17.9 minutes when

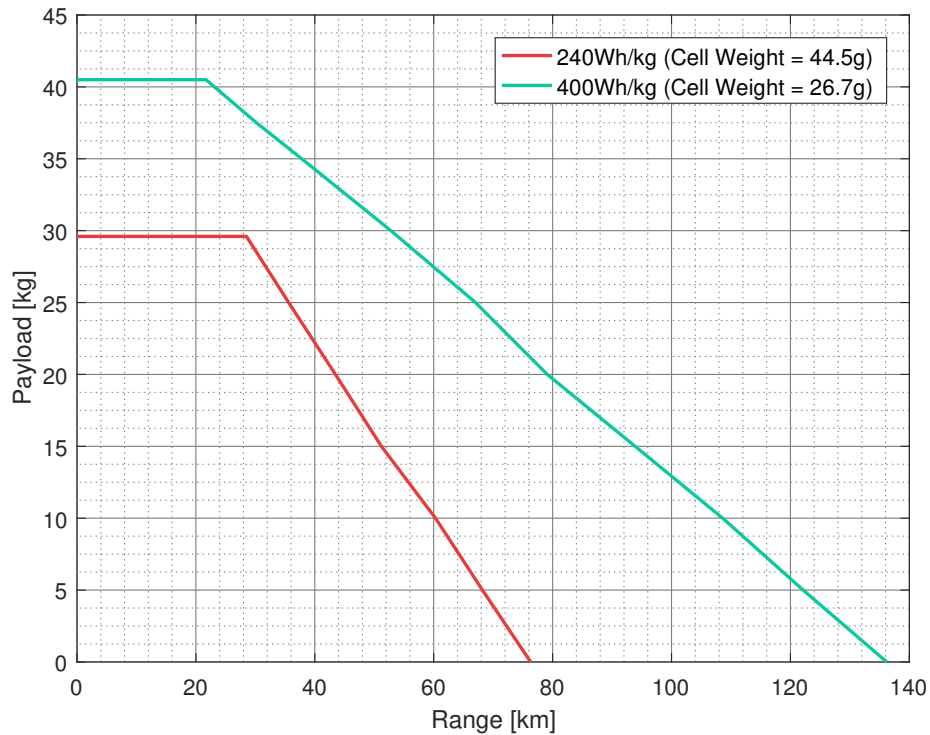


Figure 14.7: Payload-Range diagram of the battery-only configuration in which the LG-HG2 battery weight has been reduced to 26.7 grams to emulate a 400 Wh/kg battery

flying at a best range velocity. This does, however, show that the current battery technology already offers a range of options.

Case	Payload [kg]	Cruise Time [min]	Total Time [min]	Range [km]
BR	0	34.9	42.5	73.5
BR	29.6	10.3	17.9	27.6
BE	0	43.5	51.1	58.2
BE	29.6	13.8	21.40	22.2

Table 14.8: Endurance / flight time data for the 500 m best range and best endurance analysis

14.3. Fuel Cell + Battery Configuration

This section elaborates further on the results acquired from the fuel cell and battery configuration. First, the storage options, the battery discretization, fixed parameters, variables and initial points will be discussed.

14.3.1. Storage Options

Different storage options are considered in the analyses with varying gravimetric and volumetric storage efficiencies. The 300 bar case has the worst properties, with liquid hydrogen having a high storage efficiency in terms of both weight and volume. All these three options are considered and will be a good reference for other storage options for which the storage efficiencies are known. It will be shown what payload conditions these different options excel or do not excel in compared to the battery-only configuration.

- 300 bar
- 700 bar
- LH2

14.3.2. Discrete and Semi-Discrete Battery Sizing and Notation

The battery sizing within the FC-B configuration is slightly different. Instead of filling the available space with the cells and their overhead, the battery is solely sized for the peak power requirement and the energy content needed for the 5 flight sections where peak powers are needed. These sections are the initial hover, vertical climb, normal climb, vertical descent and the final hover phase.

Because the fuel cell is sized for the cruise phase, the maximum power that can be achieved with the fuel cell in the other lower altitude sections is determined next. This power then determines the battery power requirement for each individual section. For this reason, the battery pack is very small as each string of 66 cells (to reach 270 V) in series can already deliver approximately 3.35-5.4 kW given the voltage drop during the discharge. The battery pack is sized based on both the current limit and the cut-off voltage, which basically represents the capacity limit at a given discharge rate. The FC voltage and battery maximum voltage are the same.

Two analyses were made for a number of configurations. One in which a full parallel row is added when either of the battery limits is breached, indicated by $\Delta N_p = 1$. The other one is a semi-discrete approach in the battery sizing, in which $1/20^{th}$ parallel row (equivalent to 3.3 cells) is added. This is done to ensure battery sizing shows more continuous behaviour for the optimizer. Results obtained with this method will be marked with $\Delta N_p = 0.05$. It was found that it does not significantly affect the variables, but only the battery sizing.

One other reason for using both a discrete and semi-discrete approach is that other battery cells - other than the LG-HG2 cells - may be better suited for a specific power and energy requirement. In the $\Delta N_p = 1$ analysis the likelihood of over-sizing the battery pack is high. Another way of doing this could be by introducing the variable V_{max} again, but that also has a more narrow lower and upper bound. For the given LG-HG2 batteries, however, it should be clear that the $\Delta N_p = 1$ analysis represents a real battery pack sizing for the given LG-HG2 18650 battery cells.

14.3.3. Fixed Parameters

This section gives an overview of the fixed parameters used in the different analyses. For the unoptimized cases, the fixed mission profile parameters are shown in Table 14.9. Table 14.10 shows some of the parameters used for the fuel cell. The current density is set at its maximum and the stack pressure (and therefore air pressure) is set at 2 atm for cruise. Table 14.11 shows some of the battery parameters for which more info is found in the dedicated chapter about the battery modelling.

Parameter	Value	Unit	Elaboration
h_{cr}	500/1500	[m]	Cruise altitude
t_{hover}	30	[s]	Hover time at start and finish (OGE)
RoC_{vert}	4	[m/s]	Vertical climb rate
RoC	6.8	[m/s]	Forward speed climb rate
RoD	-2	[m/s]	Forward speed descent rate
RoD_{vert}	-1	[m/s]	Vertical descent rate
h_{vert}	100	[m]	Begin and end of vertical climb phases

Table 14.9: Fixed mission profile parameters for the 500 m and 1500 m unoptimized analyses

Parameter	Value	Unit	Elaboration
i_{des}	0.73	[A/cm ²]	Cell current density at its maximum
p_{des}	2	[atm]	Cruise stack pressure at the set maximum
$W_{stack,ref}$	0.5	[kg]	Reference stack (A200) weight
$V_{stack,ref}$	0.55	[L]	Reference stack (A200) volume
$f_{overhead}$	0.15	[kg/kg]	Fuel cell system overhead

Table 14.10: Fuel cell fixed parameters for the un-optimized analyses

14.3.4. Variable Choice and Initial Points

This section provides an overview of variables used for the optimized results. Table 14.12 provides the lower and upper bounds for the variables considered in this analysis method. The battery has no variables but is sized based on the current and cut-off voltage limit using the simulations. The current density lower bound was set based on preliminary calculations showing that fuel cell weight would become a problem at lower

Parameter	Value	Unit	Elaboration
V_{max}	270	[V]	Maximum voltage for battery and FC
$\eta_{overhead}$	0.6	[-]	Overhead efficiency
Cell	LG-HG2	[-]	Cell specifications used
ΔN_p	0.05/1	[-]	Discretization options

Table 14.11: Fixed battery parameters. Note that the fuel cell stack is also sized for the maximum voltage

current density. The pressure was chosen between the nominal operating pressure of the reference stack - which is 1 atm - and 2 atm. The other variables are the same as in the battery-only case, except that the discretization approach is slightly different for the battery sizing.

Variable	Unit	LB and UB	Elaboration
h	[m]	$500 \leq h \leq 3000$	Altitude
RoC	[m/s]	$2.8 \leq \text{RoC} \leq 6.8$	Forward speed climb rate
RoD	[m/s]	$-4.5 \leq \text{RoD} \leq -2$	Forward speed descent rate
i_{des}	[A/cm ²]	$0.55 \leq i_{des} \leq 0.7358$	FC cell current density
p_{des}	[atm]	$1 \leq p_{des} \leq 2$	FC stack pressure

Table 14.12: Variables in the FC-B configuration

Different initial points were used to increase the chance that no local minimum is obtained. The most important variables in this analysis will be the fuel cell design point in terms of current density and design pressure, as they directly affect the sizing.

Initial Points

The initial points for the optimized results are summarized in Table 14.13. It should be noted that the design vector follows the structure of $\bar{x} = [h, \text{RoC}, \text{RoD}, i_{des}, p_{des}]$. Also, the reference values normalized to 1 are $\bar{x}_{ref} = [1500, 4, -3, 0.64, 1.5]$. Initial points were chosen according to a standard strategy, maximizing current density and stack pressure, a minimum altitude and a maximum current density/minimum pressure combination.

Run	Chosen x0	Strategy
Run 1	[1, 1, 1, 1, 1]	Standard
Run 2	[1,1,1,1.15,1.33]	Maximum i_{des} and p_{des}
Run 3	[0.33,1,1,1,1]	Minimum altitude (500 m)
Run 4	[2,1,1,1]	Maximum Altitude
Run 5	[1,1,1,1.15,0.67]	Maximum i_{des} and minimum p_{des} for high payloads

Table 14.13: Initial points considered in the optimization

14.3.5. Payload-Range: 500m and 1500m (Unoptimized)

For this analysis the fixed parameters were used, based on the modelling parameters of the components, Table 14.9 and Table 14.10. The result with a fully discrete battery sizing is shown in Figure 14.8. A small difference can be observed when the battery pack is sized with a semi-discrete approach ($\Delta N_p = 0.05$) in Figure 14.9. The main reason is that the battery size is slightly reduced. Because of the maximum current, 2 parallel rows are necessary as a result of discretization. In the semi-discrete analysis, this is between 1 and 2.

The 300 bar case shows a maximum range of about 100 km and a maximum payload of approximately 15 kg. The maximum payload increases slightly as a result of a slightly smaller battery for the semi-discrete analysis to about 16.5 kg. The maximum range in the semi-discrete approach has a 10% improvement due to the smaller battery, to 110 km.

The 700 bar configuration has a higher power system weight as a result of requiring a heavier pressure regulator for the high pressure tank. This is 2.0 kg compared to 0.6 kg for the 300 bar tank. This shows in the maximum payload of this configuration. However, the storage efficiency is better for the 700 bar tank, creating a larger maximum no payload range of 120 km (discrete battery) or 130 km (semi-discrete) compared to the 300 bar configuration. Further slope reductions are seen when using a liquid hydrogen storage method,

which again has a lower power system weight as the storage efficiency is considered to take into account the hydrogen heating elements and any form of pressure regulation.

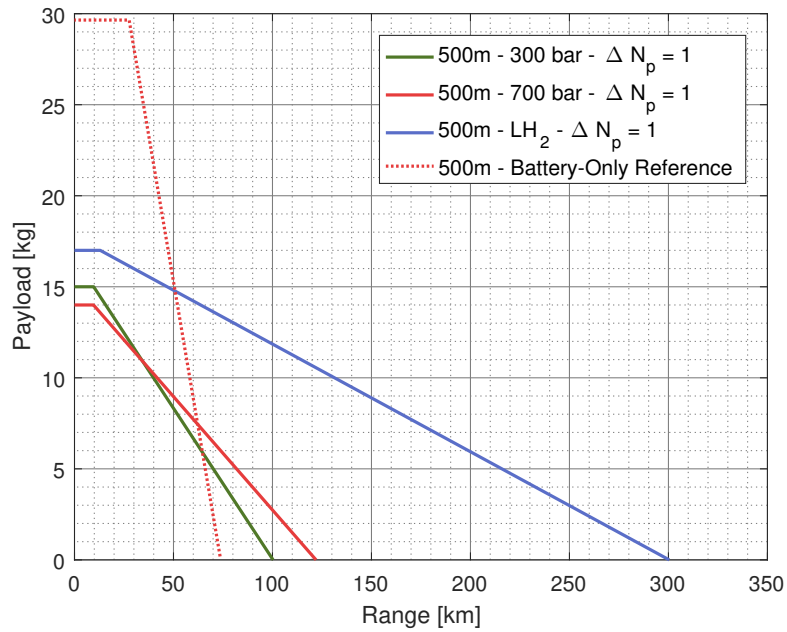


Figure 14.8: Payload-Range diagram for 500m $\Delta N_p = 1$, $i=i_{max}$ and $p = p_{max} = 2$ atm. RoC = 6.8 m/s, RoD = -2 m/s

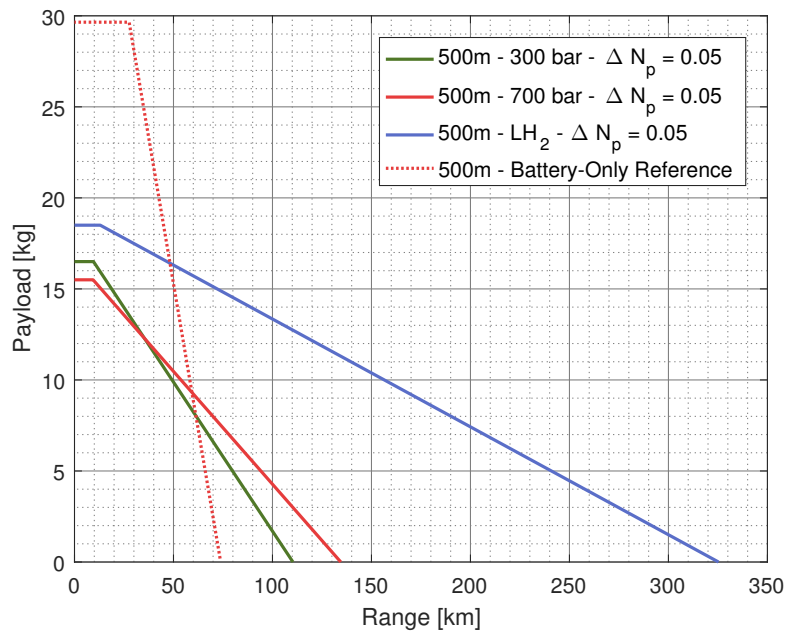


Figure 14.9: Payload-Range diagram for 500m $\Delta N_p = 0.05$, $i=i_{max}$ and $p = p_{max} = 2$ atm. RoC = 6.8 m/s, RoD = -2 m/s

Weight and Volume Overview for 500 m Mission Profile

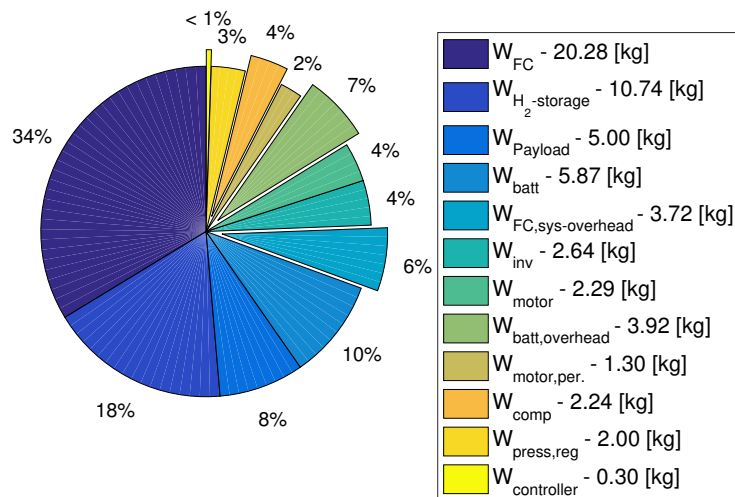
This section gives a weight and volume overview of the unoptimized analyses for the FC-B configuration. The results shown are for a 5 kg payload and a 700 bar storage option, with ΔN_p equal to 1. The first pie diagram as seen in Figure 14.10 shows the weight overview for this configuration. It can be seen that the majority of the power system weight goes to the fuel cell stack. The battery design shows that a minimum of 2 parallel rows are required to deal with the current limit. This is the same for the 1500 m case. When the semi-discrete approach is used, this is 1.7 parallel rows (500 m) compared to 1.85 rows for 1500 m. For the 500 m case, this is shown in Table 14.14.

Battery Configuration	$\Delta N_p = 1$	$\Delta N_p = 0.05$
N_s	66	66
N_p	2	1.7

Table 14.14: Battery sizing for 500 m at $\Delta N_p = 1$ and $\Delta N_p = 0.05$

The simulation of the batteries is shown in Appendix B as Figure B.1 ($\Delta N_p = 1$) and Figure B.2 ($\Delta N_p = 0.05$). It clearly shows in both cases that sizing is limited by the current limit. For the $\Delta N_p = 1$ case, the large climb rates have no effect. However, if the climb rate is reduced for the semi-discrete analysis, the battery can be made smaller and can be discharged to a much lower state of charge (SoC). If a lighter battery cell is available, with smaller capacity but the same discharge rates, the battery pack weight could be further reduced. Otherwise, a lower peak power and poorer helicopter performance has to be accepted to increase helicopter range.

Getting back to the weight overview in Figure 14.10, the overhead of the FC and battery system both form a large weight component. Due to the low certainty on the fuel cell system overhead factor, this will be further investigated at a later point. The compressor weight does not go much higher than the current value of 2.24 kg, only at higher altitudes. The reason is that in the unoptimized analyses, the upper bound of stack pressure was considered at 2 atm. The turbo-compressor used comes in at 1.5 kg per kW input power and is therefore relatively lightweight, unlike other scroll compressor systems for example used in the analysis by Guida and Minutillo [18]. The remainder of the weight is used for hydrogen storage, in this case a 700 bar tank. A tank of 10.74 kg equals a mere 558 g of H_2 stored, however, a range of 120 km can still be reached with this.

Figure 14.10: Weight overview for the unoptimized case at 500 m, with ΔN_p at 1, $i=i_{max}$ and $p = p_{max}$ and a 700 bar storage tank

The volume overview, seen in Figure 14.11, shows that a large part of the volume goes to the fuel cell stack. For low payload such as in this scenario (5 kg), the volume of the hydrogen storage tank is also relatively high. Other components are relatively low on volume, leaving 35.6 L for the payload or extra volume requirements that were not accounted for. At 0 kg payload, the available volume for the payload is lowest, as the storage is rather voluminous. It should be noted that in all analyses, the available volume for the payload never went under ~20 L, even for the 300 bar case which has the lowest volumetric storage efficiency of the considered storage options. This still leaves some excess volume in case the volume was underestimated for any of the parts. Double the volume for the fuel cell stack would clearly result in a significantly reduced available volume for the payload.

Each section in the mission profile requires a certain hydrogen mass, which is shown in Figure 14.12. The mass shown is the hydrogen in combination with the tank weight, therefore the mass divided by the storage efficiency of the storage method. In this case, that is 0.052 for the 700 bar tank. Due to the low altitude, the cruise phase occupies a large portion of total hydrogen usage.

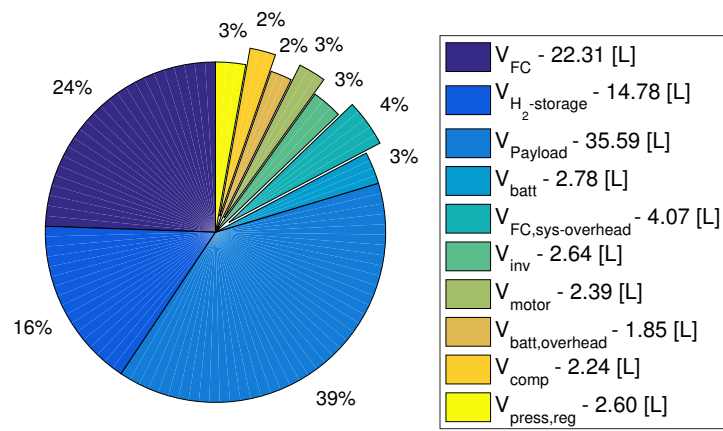


Figure 14.11: Volume overview for the unoptimized case at 500 m, with ΔN_p at 1, $i=i_{max}$ and $p = p_{max}$ and a 700 bar storage tank

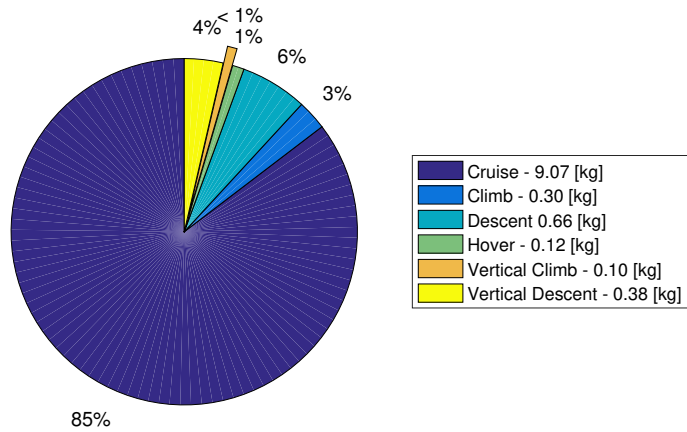


Figure 14.12: H₂ Storage weight overview for the unoptimized case at 500 m, with ΔN_p at 1, $i=i_{max}$ and $p = p_{max}$ and a 700 bar storage tank

Discretization Effect on Payload-Range

Figure 14.13 shows the effect of a different ΔN_p on the payload-range of the unoptimized case with a cruise altitude of 500 m. This shows no clear effect other than that the semi-discrete (or semi-continuous) approach shows a displaced payload-range diagram. This is because in the discretization, the battery is slightly oversized as two parallel rows are necessary, each row containing 66 LG-HG2 cells in series. Due to the high rate of climb (vertical fixed at 4 m/s and the forward speed climb at 6.8 m/s), the battery limit is found as a result of the maximum allowable current. This results in 1.7 parallel rows (instead of a realistic 2 rows) for 500 m and 1.85 rows for 1500 m, because of the longer climb phase in the latter flight profile. These are marginal changes for high rate of climb, but will be larger when the rate of climb is limited and power requirements go down. The effect on range for the current configuration is approximately 10% for the 500 m analysis, in favour of the semi-discrete battery analysis.

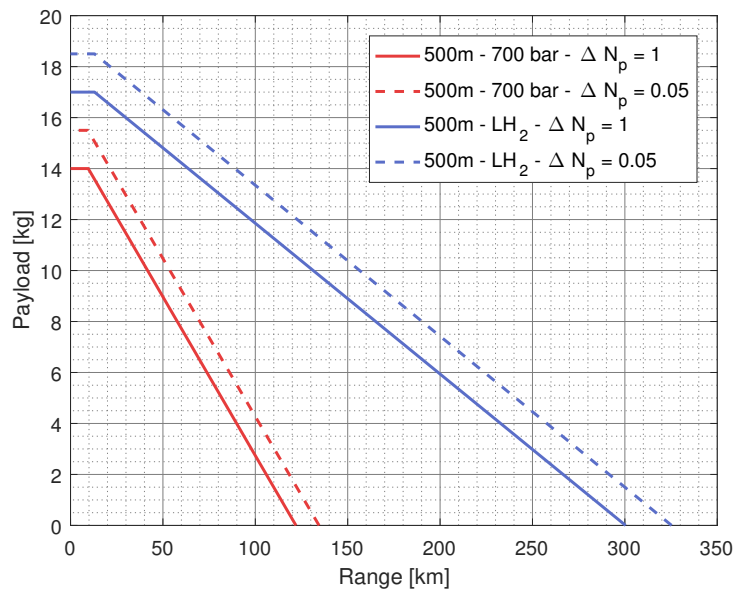


Figure 14.13: Payload-Range diagram for 500m, $i=i_{max}$ and $p=p_{max}$. RoC = 6.8 m/s, RoD = -2 m/s. This shows the effect of different ΔN_p

Differences 500m and 1500m

This section discusses differences for two different altitudes: 500 m and 1500 m. This was done for the 700 bar and liquid hydrogen configurations for clarity. The performance of the 300 bar tank is very similar and slightly worse than the 700 bar configuration at low payload. Note that for high payload, the analysis specifies that it should still be possible to reach 1500 m. This mission is not sensible in reality, as there is then only hydrogen left to immediately descent and land. Hence, there are big payload gaps between 500 and 1500 meters. Apart from this low range (high payload) section, Figure 14.14 shows very minor differences between flying at 500 or 1500 meters. The main reason is that for a discrete battery sizing, the peak power levels during the climb are delivered entirely by the battery. Due to an excess in battery energy content, the size of the battery is the same in both scenarios. The climb phase is also at the best range velocity, meaning that the fuel cell operation is very similar to that of the cruise phase during this climb. This, in combination with a small improvement in P/V at 1500 m and a slightly larger compressor for the 1500 m scenario, results in almost equal range.

Figure 14.15, which shows the same for a semi-discrete battery sizing, displays a bigger difference in the large range area as a result of a smaller battery size for the climb to 500 m, as the current limit is not reached as quickly. This battery weight reduction immediately translates into a larger storage tank budget. However, the effect is minor and it shows that for large payloads, a mission to 1500 m is still not sensible due to the hydrogen requirement needed to reach the altitude and immediately descent.

14.3.6. Payload-Range: Optimized with i, p, h, RoC, RoD

This section is dedicated to the optimized results for five variables. This section will show some selected tabulated optimization results, as well as visual reference and comparisons to earlier results. Table 14.15 shows the tabulated results for the 300 bar optimized results. It shows mainly that altitude, as expected according to the P-V analysis and slightly reduced FC performance with altitude, goes to approximately 1000 m. RoD

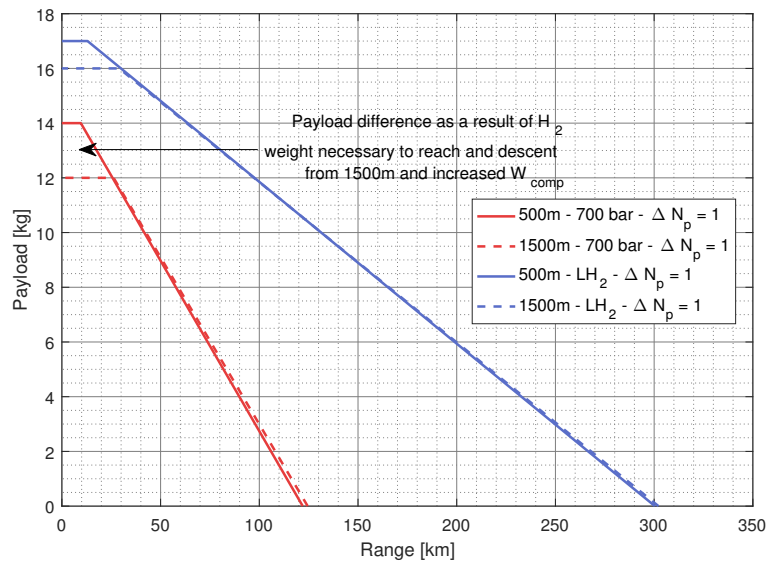


Figure 14.14: Difference between 500 and 1500 meters. It shows minimal differences due to battery size not changing (both equal size). The payload difference is mostly explained as the hydrogen weight for non-cruise phases is larger to reach 1500m, and compressor weight)

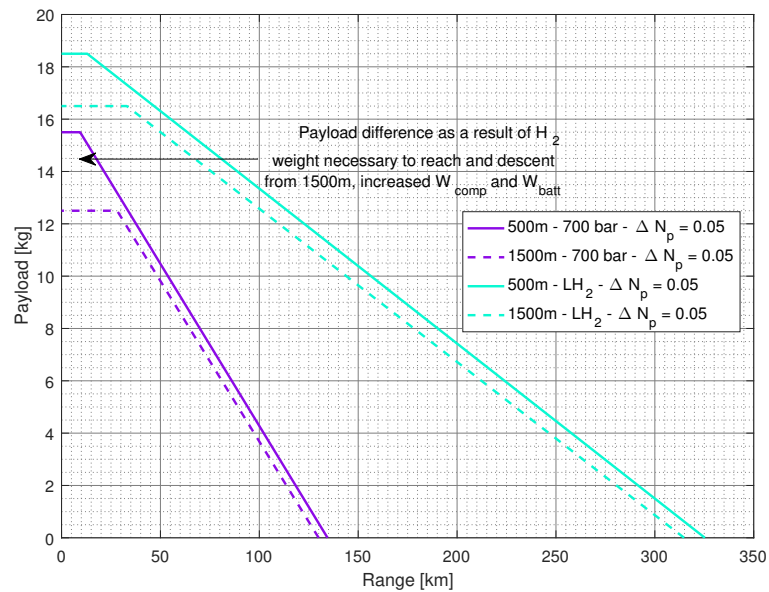


Figure 14.15: Difference between 500 and 1500 meters. It shows a bigger difference due to different battery sizes (semi-discrete approach) and the payload gap can be explained due to compressor weight, battery size and larger hydrogen storage for reaching 1500m

has a really small effect as it does not influence battery sizing at all. FC hydrogen usage is affected somewhat as a result of the reduced power levels during descent. The RoC only affects the battery sizing, but because the current limit is reached during the maximum vertical climb rate, the RoC at the optimized values do not result in an even larger battery.

This forward speed RoC could become limiting when the helicopter performance is reduced through lowering the fixed vertical climb rate. The current density and pressure always tend to go towards the maximum and minimum value respectively, meaning the compressor is made as small as possible and the fuel cell stack is always used at the cell maximum power level. This is due to the low power density of the fuel cell stacks. Adding more weight to the compressor due to increased power requirements, also immediately means increased fuel cell power requirements.

In the majority of cases the current density is around 0.71-0.72, slightly below the 0.736 maximum. Only for the maximum payload, the current density goes to the upper bound because possible efficiency improvements are of no benefit for short flight times. The current density of 0.71-0.72 as compared to the maximum has a marginal effect on the range.

Payload	x0	h	RoC	RoD	i_{des}	p_{des}	Range	V_{PL}
0	[1,1,1,1,1]	993	4.07	-3.12	0.71	1	141.67	17.98
0	[1,1,1,1.15,1.33]	989	4.83	-3.37	0.68	1.07	139.02	18.47
0	[0.33,1,1,1,1]	993	4.85	-3.45	0.68	1.06	139.33	18.46
0	[2,1,1,1,1]	997	4.81	-2.91	0.7	1.025	140.9	18.2
5	[1,1,1,1,1]	996	4.5	-3.4	0.72	1	108.1	26.9
5	[1,1,1,1.15,1.33]	1199	4.8	-3.3	0.7	1.04	104.84	27.4
5	[0.33,1,1,1,1]	998	4.72	-3.3	0.7	1.04	106.4	27.2
5	[2,1,1,1,1]	993	4.78	-3.4	0.7	1.04	106.4	27.2
10	[1,1,1,1,1]	1200	4.8	-3.44	0.72	1.03	72.2	36
10	[1,1,1,1.15,1.33]	1200	4.83	-3.32	0.72	1.02	72.2	36
10	[0.33,1,1,1,1]	600	4.74	-3.35	0.71	1.02	68.04	36.3
10	[2,1,1,1,1]	1000	5.13	-2.98	0.72	1.02	73.9	35.8
15	[1,1,1,1,1]	1000	4.85	-3.2	0.72	1.03	39.91	44.9
15	[1,1,1,1.15,1.33]	1200	4.68	-3.2	0.72	1.03	38.84	45.1
18	[1,1,1,1.15,0.67]	1000	4.08	-3.1	0.736	1	21.75	50

Table 14.15: 300 bar optimization results show a tendency for 1000 m altitude, maximum current density and low stack pressure

It should be noted that similar results in terms of variables were obtained for 700 bar and liquid hydrogen. It was expected that possibly the current density would come down or pressure would go up with longer flight times, but this was not the case. The efficiency advantage is still not large enough at these power densities of the fuel cell stacks. It will be shown in the 2030 forecast, that an increased power density provides a better range when current density is lowered slightly to values between 0.65-0.68, except when payload is high and therefore range low.

The next sections show the optimized results for the 300 and 700 bar compressed gas tanks compared to the unoptimized results at 500 m altitude. This will show a clear difference due to the fact that the stack pressure goes to the lower bound instead of the upper bound which was considered for the unoptimized scenarios.

Optimized: 300 bar

Figure 14.16 shows the optimized results for the 300 bar storage method. The result obtained in the reference payload-range shows much worse results, which in the graph is seen by the 500 m line. The main reason is that the optimization prefers no compression beyond 1 atm, which was considered in the unoptimized scenarios. The dotted line indicates the optimized result with the semi-discrete battery sizing, yielding a further improvement of about 10% at low payload.

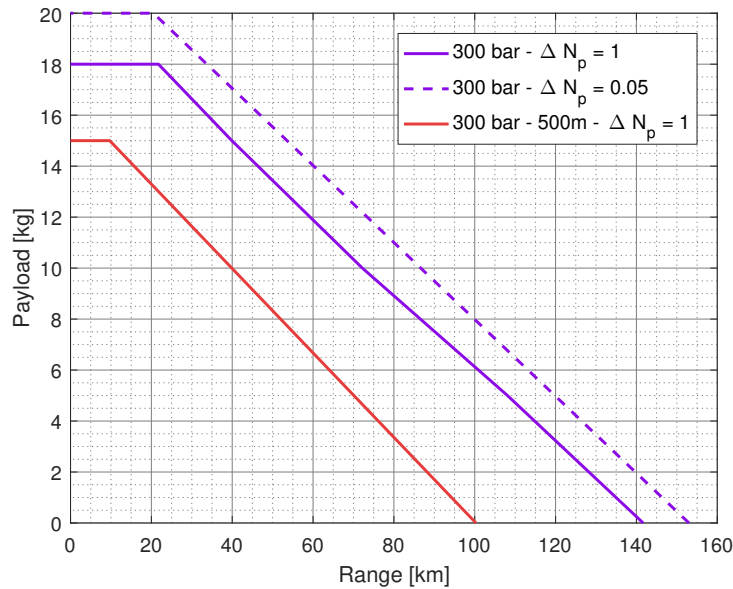


Figure 14.16: Optimized results for 300 bar

Optimized: 700 bar

Figure 14.17 shows the same results for the 700 bar case. The expected improved efficiency from a lower i_{des} or a higher stack pressure is not seen, as the optimizer chooses the lower bound for stack pressure and the upper bound - or very close to - for the current density. The main reason is the snowball effect as a result of higher compressor power. The fuel cell is designed to deliver the compressor power at the cruise altitude. This means the fuel cell becomes bigger iteratively. The improvement in efficiency through the pressure increase does not offset the increase in weight due to the larger compressor and therefore also fuel cell stack, increasing the mass flow again. However, for continuous and smooth operation of the fuel cell, the mass flow should still be guaranteed using a compressor or pumps. The weight required for this may now be underestimated as a result of a very small pressure ratio.

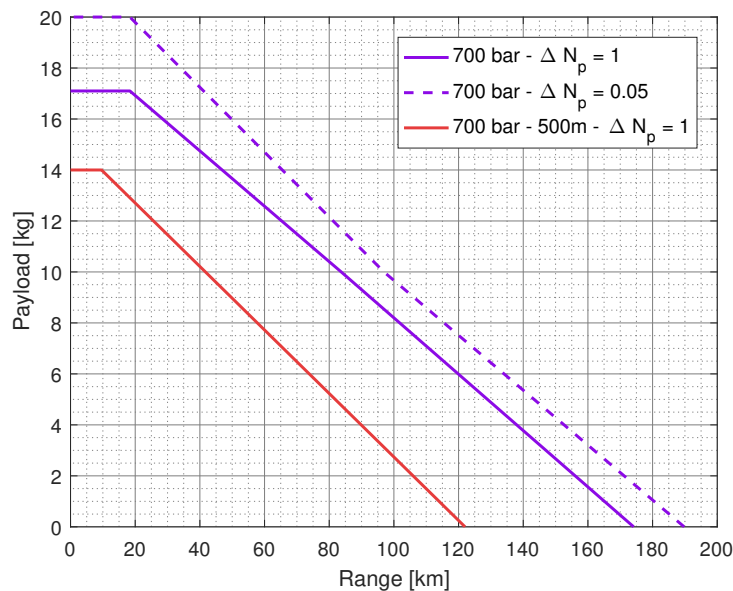


Figure 14.17: Optimized results for 700 bar

Overall, quite a massive increase in range can be observed in the optimized case and the range increases over 40% as a result of the lighter fuel cell stack and very small compressor. This weight overview is seen in Figure 14.18. Due to the smaller size of those components, the remainder of the weight can be used for storage. More hydrogen is needed due to the low efficiency, but also less power from the FC stack is needed as the compressor does not need to be powered.

One option that could be studied is to run the compressor using the remainder of the energy content in the oversized battery pack. This could allow for a combination of the efficiency improvement of a higher stack pressure, a lower fuel cell stack size (due to more power per cell), but a larger compressor. Note that this strategy can be considered when the battery pack is oversized in terms of energy content and it can be guaranteed that the current limit of 20 A will not be reached.

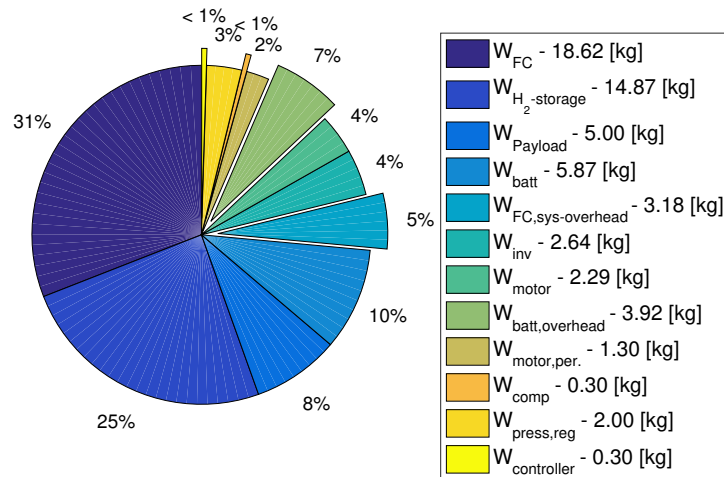


Figure 14.18: Weight overview for the optimized case with ΔN_p at 1, a 700 bar storage tank and a payload of 5 kg

Figure 14.19 shows a slight volume reduction for the payload as a result of being able to bring a larger tank. This payload volume is the volume that is still available and therefore a limit for the payload that can be taken on board. Otherwise, this volume can be used by other subsystems that prove to be of larger volume than expected.

Regarding the tank, it should also be noted that the maximum payload might be limited by the minimum tank size that can be found. Most tanks with a larger storage efficiency are over 30 L in size. The DoE 2022 goal of 5.7wt% is reached only with a tank size of 64 L as was shown in the storage tank sizing. Here, it is shown that the tank size is only 20 L, meaning that it may be difficult to find a 700 bar tank, even at 5.2wt%. For larger payloads than 5 kg, the storage volume reduces and even smaller storage options have to be considered. It might be necessary to opt for 300 bar storage tanks with worse properties than considered in this analysis.

Finally, Figure 14.20 shows the hydrogen usage per section. The hover phases at the beginning and end are combined.

Optimized: Liquid Hydrogen

Figure 14.21 shows the same payload-range comparisons for liquid hydrogen. It is clear that the maximum range at 0 kg payload is much better than any other option. Higher payloads can be taken on board and using a realistic battery sizing method, a range of approximately 410 km is reached. A comparison to the conventional reference helicopter - which is micro gas turbine powered - will be shown later, as the liquid hydrogen case shows very similar results in terms of range (for 0 kg payload).

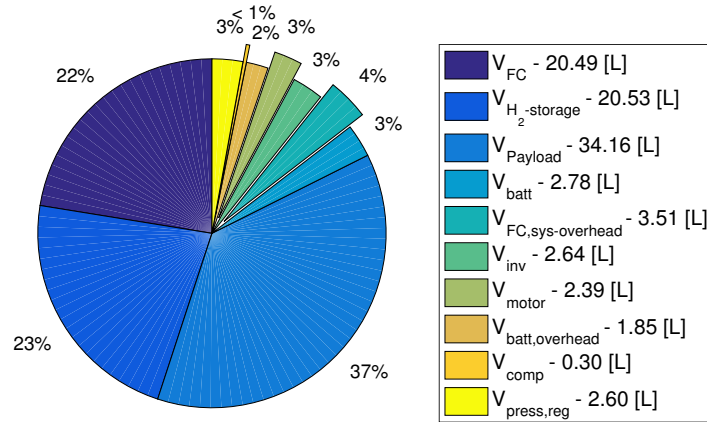


Figure 14.19: Volume overview for the optimized case with ΔN_p at 1, a 700 bar storage tank and a payload of 5 kg

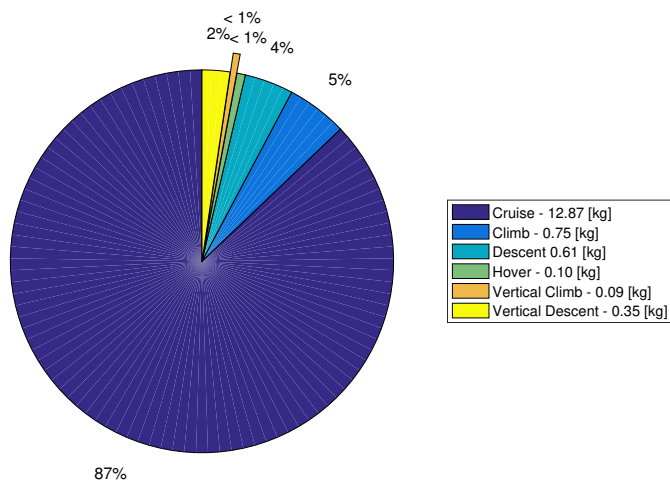


Figure 14.20: H_2 Storage weight overview for the optimized case with ΔN_p at 1, a 700 bar storage tank and a payload of 5 kg

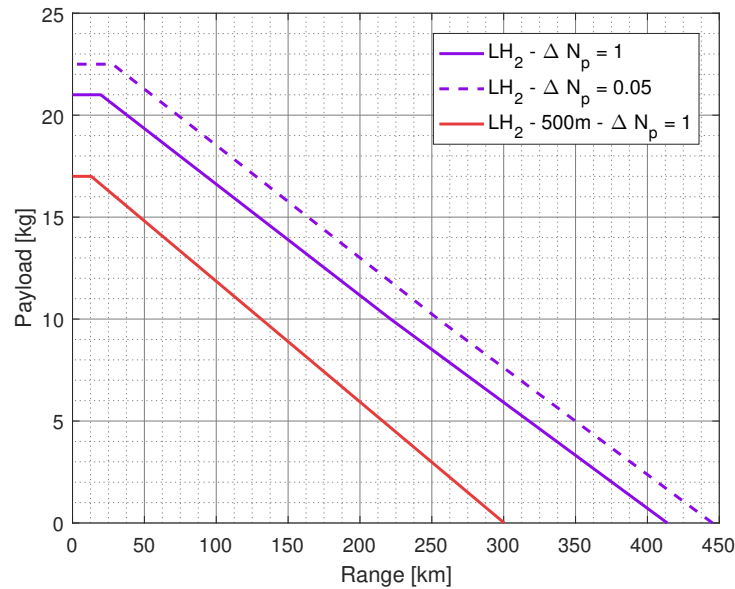
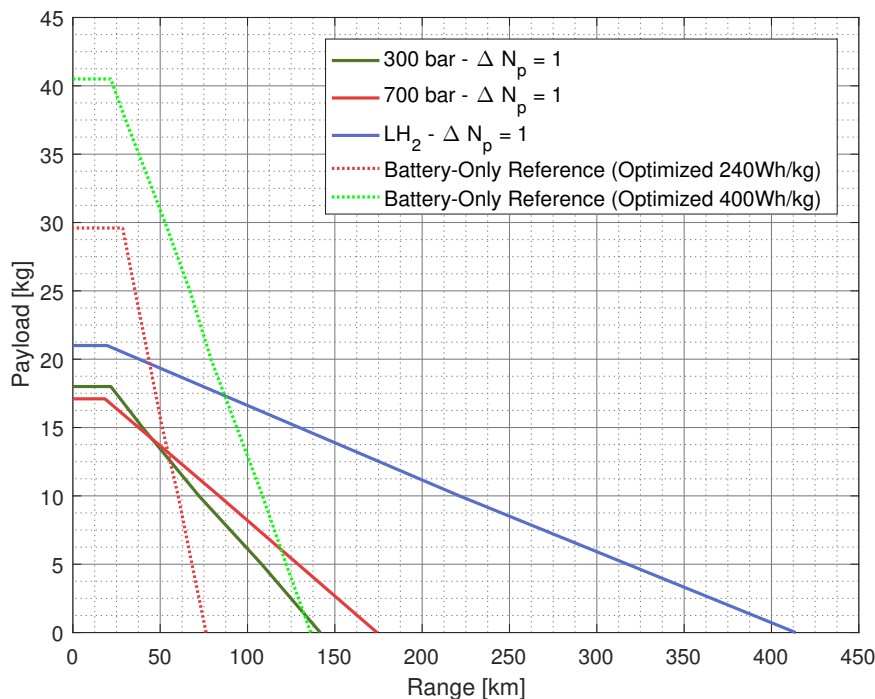


Figure 14.21: Optimized results for liquid hydrogen

Full Comparison

The full comparison of optimized results is shown in Figure 14.22. A few observations can be made. First of all, the 300 bar and 700 bar cases do not differ a lot. With the parameters used for these analyses, the range of these two configurations is already (over) twice the range of the battery-only configuration. This latter configuration, however, performs much better in extremely high payload configurations. Up to 29.6 kg of payload can be taken on board before the current limit of the battery pack is reached (as the battery gets smaller with increasing payload).

Figure 14.22: Comparison of all optimized results, battery sizing with $\Delta N_p = 1$

However, it can be seen that if the energy density of the current batteries goes up to 400 Wh/kg, which is expected towards 2030, the range of the battery-only configuration reaches that of the 300 bar and 700 bar FC-B options. Note that this is no fair comparison, because this does not include the same forecast for the

FC-B configuration. This will be discussed in the section on the 2030 forecast.

Current fuel cell power densities are already demonstrated higher than the power density in this analysis. Therefore, the maximum payload and range automatically become higher and the FC-B will still show significant benefits over future battery configurations. The battery pack weight in the FC-B configuration will also go down with these battery advancements.

The liquid hydrogen configuration shows the best range as expected. For the same H_2 storage tank weight budget, it can have significantly more hydrogen content. Hence, the slope of the payload-range diagram is much smaller. This yields very good results in terms of range and small power system weight savings will have a big impact on the range.

14.3.7. Sensitivity of FC,sys Overhead and Stack Weight

This section elaborates on the sensitivity of the fuel cell system overhead, which was previously set at 15%. In the optimized 700 bar configuration this resulted in a fuel cell system overhead of 3.18 kg. The result of doubling the overhead to 30% is shown in Figure 14.23 for the 700 bar and liquid hydrogen configurations. The payload-range diagram shifts downwards as the power system weight increases, leaving a lower budget for the storage system.

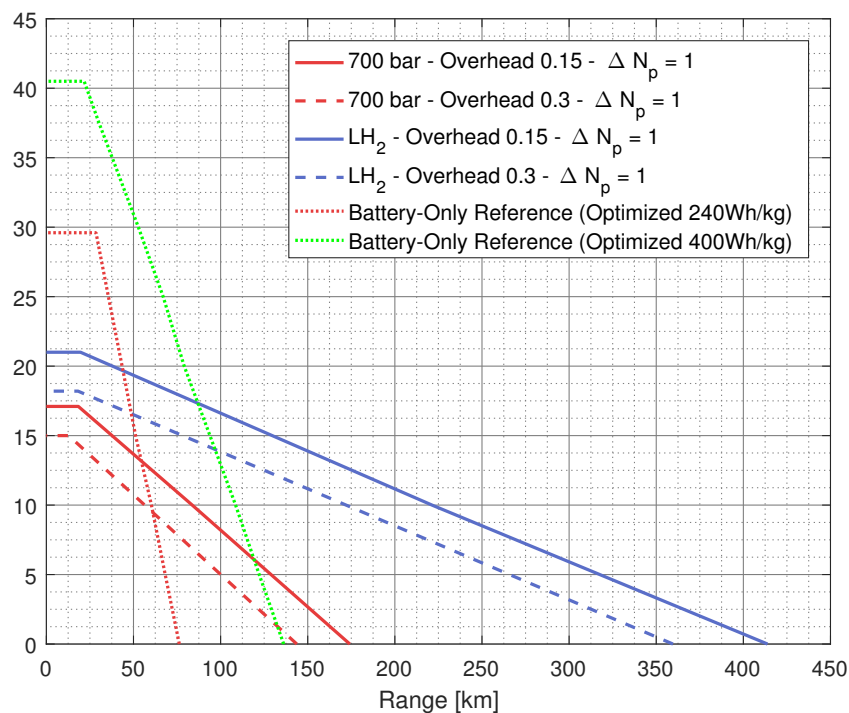


Figure 14.23: Sensitivity of the overhead from 15% to 30% of the fuel cell system weight

Assuming that nothing else changes and the fuel cell is still used at its maximum power, the following can be said. In the optimized range case, the FC weight is approximately 18.62 kg, corresponding to a power delivery of 10.2 kW (550W/kg at 1 atm). A 3.18 kg increase in FC stack would result in a power density of ~ 470 W/kg for FC stack and cooling system combined. A reduction to this power density would yield similar results as the overhead changing from 15 to 30% as seen in the figure. For this change, the liquid hydrogen range at 0 kg payload reduces with approximately 13%. The 700 bar configuration has a range reduction at 0 kg payload of approximately 17%. It shows that even at 30% fuel cell system overhead, the 700 bar tank still has a large increase in range over the battery-only reference at 240 Wh/kg, which are both the current state-of-the-art. Even when overhead goes up more, the FC-B configuration will show benefits when the payload is less than 5 kg.

14.3.8. Comparison B-Only an FC-B Configurations to Conventional MGT Powered GC-201

Figure 14.24 shows the comparison of the studied configuration to the conventional micro gas turbine powered GC-201 helicopter. This shows that only the liquid hydrogen configuration gets close. If the gravimetric storage efficiency is slightly improved, as well as FC stack + cooling power density, the same range as the

conventional MGT configuration can be reached. Currently, the range of the FC-B with the liquid hydrogen storage method is about 20% lower. It should also be noted that the conventional power system can operate at payloads comparable to that of the battery-only configuration as long as the fuel tank size is reduced. This makes the conventional powertrain the most flexible powertrain, mainly due to the high energy content of hydrocarbon fuels and the power system weight.

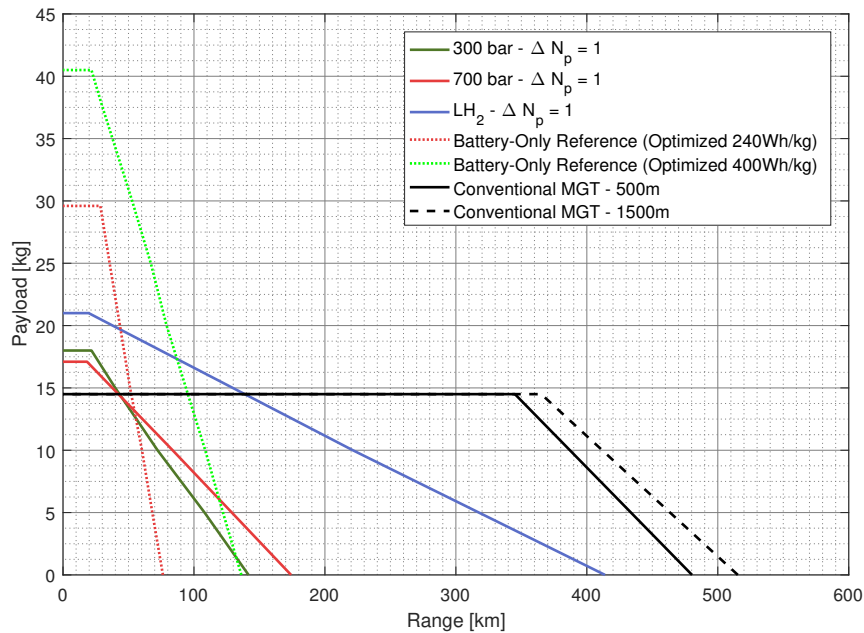


Figure 14.24: Comparison to the conventional MGT configuration with current state-of-the-art parameters showing that only liquid hydrogen can get close to the range of the conventional MGT, but does not compete in terms of payload

14.3.9. Sensitivity to Vertical RoC

This section discusses the sensitivity of the results towards a change in vertical rate of climb and therefore power requirements. When the vertical rate of climb is reduced, the rate of climb during the forward speed phase can become the limiting element. It is therefore expected that when this climb rate is reduced, the range improves as a result of lower maximum power and worse sea level performance.

In all previous analyses, the vertical rate of climb was kept constant and therefore the maximum power of ~16 kW was reached during this vertical phase. Because of this lower maximum power, the electric motor and inverter can be made smaller.

Table 14.16 shows the obtained results when lowering the vertical climb rate from 4 m/s, back to 1 and 0.5 m/s. This was done for ΔN_p of 0.05 and 1. Appendix C also shows the battery simulations for all cases. These will be used in the elaboration of the results as some significant changes can be seen.

For the discrete cases (battery simulations in Figures C.1 to C.3), it can be seen that battery size does not reduce as a result of the reduction in maximum power. This is explained by the fact that a size reduction would mean the battery pack loses 50% of its size as it only had 2 parallel rows to start with. However, range still increases from 173.7 km to 175.6 km when reducing the vertical rate of climb from 4 to 1 m/s. A further reduction to 0.5 m/s actually shows no further improvement. This makes sense because now a lot of energy is spent by the fuel cell during this longer peak power phase, leaving less energy for the forward flight phases. For the fuel cell, the power level stays the same during this phase and does not depend on the peak power.

The fact that the vertical climb phase is longer can be seen through the battery SoC reduction at the end of battery usage in Figures C.1 to C.3. The SoC actually reduces from 52 to 37% when reducing the vertical rate of climb, because battery peak power is only changed slightly with reducing vertical rate of climb, however the duration of peak power is more significant. Because of lower peak power, motor and inverter size are slightly reduced which yielded an advantage when reducing to 1 m/s.

For semi-discrete cases, the current limit is reached for 1.65 parallel cells when the rate of climb is 4 m/s. This current limit is reached in the vertical climb phase (see Figure C.4) and thus requires a bigger battery. When reducing the climb rate to 1 or 0.5 m/s, almost the entire battery energy content is used (discharge curves and SoC in Figures C.5 and C.6) and peak currents shift to the final hover phase due to dropping voltage. This allows for a battery size reduction to 1.4 parallel for 1 m/s climb rate. When the climb rate

is further reduced to 0.5 m/s, the battery size increases again to 1.45 parallel. Because of longer peak power usage during the vertical climb phase, the battery is discharged a bit sooner. This is because the battery power requirement is not much different as it increases by less than 0.5 kW when climbing with 1 m/s compared to 0.5 m/s, but only for half the time. This 0.5 kW is only about a tenth of the entire battery power needed in that section. Therefore, range also reduces slightly again for this vertical rate as seen in Table 14.16.

Inputs/Outputs	Run 1	Run 2	Run 3	Run 4	Run 5	Run 6
Storage option	700 bar	700 bar	700 bar	700 bar	700 bar	700 bar
Initial	[1,1,1,1,1]	[1,1,1,1,1]	[1,1,1,1,1]	[1,1,1,1,1]	[1,1,1,1,1]	[1,1,1,1,1]
ΔN_p [-]	1	1	1	0.05	0.05	0.05
Vert. RoC [m/s]	4	1	0.5	4	1	0.5
$W_{payload}$ [kg]	0	0	0	0	0	0
h [m]	1198	1199	1000	1200	993	933.3
RoC [m/s]	4.5	4.7	4.81	4.06	4.12	4.11
RoD [m/s]	-3.1	-3.6	-3.4	-3.1	-3.2	-3.13
i [A/cm²]	0.71	0.704	0.703	0.7	0.6925	0.69
p [atm]	1	1	1	1	1	1
Range [km]	173.7	175.56	175.4	188.96	204.1	198.47
P_{max} [kW]	15.5	13.98	13.73	15.5	13.98	13.73
W_{inv} [kg]	2.55	2.31	2.26	2.55	2.31	2.26
W_m [kg]	2.21	2	1.96	2.21	2	1.96
$W_{m,per}$ [kg]	1.3	1.3	1.3	1.3	1.3	1.3
W_{FC} [kg]	18.87	18.94	18.8	18.98	18.96	19.07
$W_{FC,sys-over}$ [kg]	3.23	3.24	3.21	3.24	3.23	3.25
W_{batt} [kg]	5.87	5.87	5.87	4.85	4.11	4.26
$W_{batt,over}$ [kg]	3.92	3.92	3.92	3.23	2.74	2.84
W_{comp} [kg]	0.35	0.35	0.28	0.35	0.28	0.26
$W_{press,reg}$ [kg]	2	2	2	2	2	2
$W_{H2-storage}$ [kg]	19.71	20.09	20.4	21.3	23.1	22.79
V_{left} [L]	27.24	27.78	27	25.7	24.4	24.6
N_p [-]	2	2	2	1.65	1.4	1.45
N_s [-]	66	66	66	66	66	66

Table 14.16: Results overview in the vertical RoC investigation

14.4. Forecast 2030

This section gives a forecast towards 2030. For batteries, estimates show that new technologies such as Li-S and Solid-State batteries are likely to become more widely available around 2030. Li-S currently reaches 370-400 Wh/kg on an experimental level and solid-state batteries can reach up to two to three times the level of 2015, which should be around 400-750 Wh/kg when taking a 200-250 Wh/kg 2015 reference. The forecast value was therefore chosen to be 400 Wh/kg for batteries, assuming the same characteristics. This was done for both the battery-only and the FC-B configuration.

For the fuel cells the market forecast up to 2025 shows a steady growth in PEMFC revenue up to 2025 and therefore continuing R&D is expected. Due to the number of variables from one fuel cell stack to the other, it is hard to give an exact prediction. Current state-of-the-art FC stacks give approximately 300-600 W/kg for relatively small stacks up to 10-15 kW seen in HES Aerostacks and the PowerCell S2. The PowerCell S2 shows up to 724 W/kg for larger stacks (15-35 kW), but still require a radiator for cooling.

Prototypes without cooling show values between 2-3 kW/kg for smaller and bigger systems, but 1 kW/kg for larger systems around 100 kW with cooling can be found. A 2030 prediction is assumed to be up 20% from the value used in all previous analyses (ca. 550 W/kg) to a reference stack weight of 0.4 kg instead of 0.5 kg, getting closer to the high end of the current PowerCell systems at 700 W/kg that are larger systems than needed for this helicopter. However, with a growth in PEMFC revenue and the potential for HT-PEMFC and hence reduced cooling requirements, this seems to be a reasonably conservative estimate for 2030. To conclude, the following changes are made to the input parameters:

- Fuel cell stack power density goes up 20% to approximately 700 W/kg. This is the result of reference

stack weight going down 20%. Directly, overhead weight will also reduce. Other parts in the FC system are assumed to remain the same. Some of this improvement might come from high temperature PEMFC (HT-PEMFC) which make cooling a bit less critical due to their higher operating temperature.

- Lighter battery with a 400 Wh/kg energy density and therefore a reduced cell weight from 44.5 g to 26.7 g.
- Because the characteristics of the battery stay the same, the power density also improves. Li-Ion power density was at approximately 800 W/kg including battery overhead and is higher than the 2030 FC stack power density at 700 W/kg. Because of reduced cell weight, this power density will improve to approximately 1300 W/kg. A FC-B system is therefore still expected to make sense in the future, instead of a fuel cell only configuration.
- It is assumed that the MGT powered helicopter shows very minimal improvements, so estimates were not made.

When running the 700 bar case with these input parameters, the result shows that the range is 250 km when the current density is reduced to 0.66 A/cm^2 . If the current density is set at the maximum of approximately 0.73 - with all else equal - the range actually reduces to 245 km. This is a result of the increased power density, allowing a slightly higher weight budget for the power system while increasing fuel cell efficiency. For high payloads, the flight time is too short to benefit from the increased efficiency. For the state-of-the-art parameters (2018), the current density was always around 0.7 or higher. The main reason is the power density that was lower. Also the other storage options show that current density is slightly lower, all between 0.66 and 0.68. The stack pressure tends to still go to the lower bound. Minimal to benefits can be obtained with increased stack pressure for the cells used in this study.

Figure 14.25 shows the 2030 estimates, showing that the liquid hydrogen case may be able to compete with the conventional helicopter. The battery size is still 66 in series and 2 in parallel. However, lower FC stack weight and also lower battery weight helps improve the performance of the helicopter with FC-B configuration. The 300 and 700 bar cases also show a clear advantage over the 400 Wh/kg battery for payloads below 10 kg. Previously it was shown that if FC-B is stagnant but battery weight reduces, there is no advantage for the FC-B case, only at 0 kg payload.

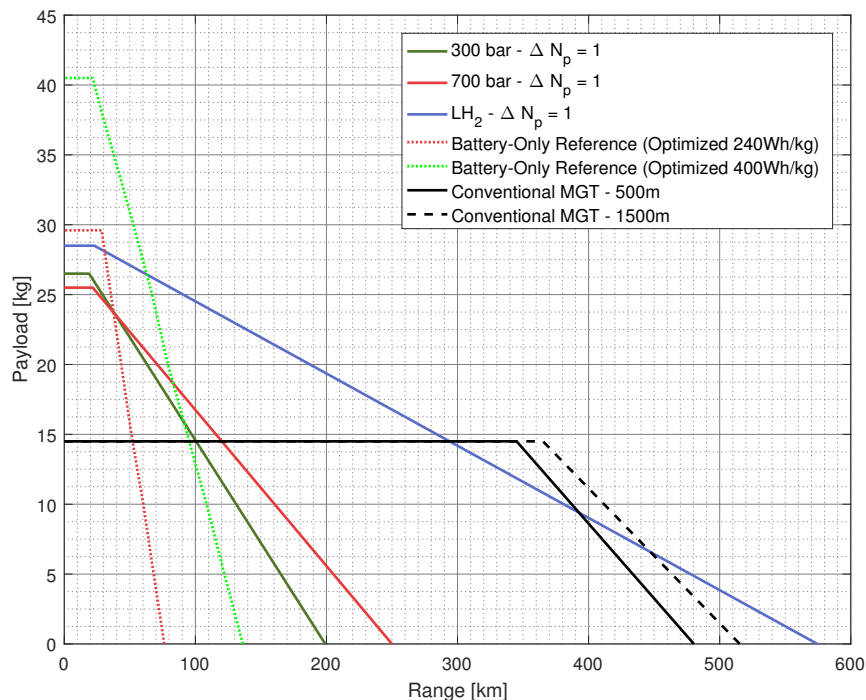


Figure 14.25: 2030 comparison: 300 bar, 700 bar and LH₂ are 2030 estimates, as well as the 400 Wh/kg battery case.

14.5. Piloted/Manned Helicopter

If it is assumed that the power levels scale directly for larger systems, the influence of a manned helicopter can be estimated based on the results as obtained previously. The MTOW of a Robinson R22-like helicopter including passenger is approximately 809kg, with a hover power of 110 kW and best range power estimate of 75 kW [8]. This is a similar power density compared to the current UAV. Considering that about 80 kg would be needed for a pilot, the payload-range diagram shifts downward by approximately 10 kg in the results seen in previous chapters. It should be noted, however, that higher fuel cell stack (+cooling) power densities can be found for larger FC systems. Power densities including some cooling components can come near 1 kW/kg for 100 kW systems, for example found in the PowerCell MS-100. This reduces the weight of the power system significantly as well, making the FC-B configuration feasible for manned helicopters.

If the power density and all other components remain equal to the parameters used in this study, the pilot forms a mandatory payload and the battery-only configuration becomes more competitive. For liquid hydrogen, this would mean a range reduction from ~400 km to approximately 220 km (liquid hydrogen) when shifting the lines in Figure 14.24 downwards by 10 kg. The battery, 300 bar and 700 bar cases are then almost equal, with 60, 70 and 80 km respectively. The reason is that pilot, payload and storage are interchangeable weights. For manned helicopters, volume is also more likely to form a problem as a result of sheer cabin size. It is expected that this may be more limiting due to the fact that larger FC systems show higher power densities.

14.6. Energy Density and Power Density

This section elaborates on the resulting optimized energy densities and power densities in the system. This concerns the battery energy density in a battery-only system, but also the battery energy and power density in a fuel cell system. The battery-only case can be compared to FC-B energy and power densities. The following comparisons will be made, providing four different results for each power source.

- Energy- and Power density
- Gravimetric and Volumetric
- Results obtained for a 5 kg payload

Battery-Only

The battery-only configuration is energy density focused, because the battery needs to be larger in order to be able to increase range or endurance. Therefore power densities are of lower importance in this case. The gravimetric power density (GPD) of battery cells is estimated through Equation 14.2. For this value, the maximum continuous current (20 A) is combined with the nominal voltage of 3.6 V. The voltage when fully charged is 4.1 V and 2.5 V when fully discharged. This means the cell reaches 82 W fully charged, 72 W nominally and 50 W near 0% SoC. For a cell weight of 44.5 g, this is 1840, 1620 and 1120 W/kg respectively. It is therefore advantageous to have the highest power at the start of the discharge and therefore at the start of the mission profile. With helicopters, a peak power vertical descent and hover is still required at the end of the flight.

$$GPD_{Cell} = \frac{P_{max,cell}}{W_{cell}} \quad (14.2)$$

In the battery-only case, the actual battery pack consists for 60% out of battery cells and 40% overhead. The power density can be determined using Equation 14.3. For the scenario with 5 kg payload as seen in Table 14.5 (note the unoptimized cases are very close to the optimized scenarios), the battery pack weight is 29.37 kg. With the additional overhead, this totals approximately 49 kg. Maximum power delivered by the battery during the flight is approximately 18 kW due to motor and inverter efficiency. This means that the maximum power density is 367 W/kg. This low power density is expected in this case, because the battery is mainly sized for energy content. Technically, higher power densities can be reached because at this battery pack size, the maximum continuous current is not reached.

$$GPD_{Batt} = \frac{P_{max}}{W_{batt} + W_{batt,overhead}} \quad (14.3)$$

The simulated energy density is approximately 227.6 Wh/kg, which is under the rated cell energy density (nominal) of 240 Wh/kg. The main reason is that only about 95% of the capacity can be used. The full capacity of 3000 mAh can only be reached for discharge rates at or under the rated current of 3 A. However, the peak current in the final second of the battery simulation is 9.1 A. This results in a capacity change as a result of the peukert coefficient in the battery model. Also, the cruise phase power level is approximately 10 kW

after taking into account powertrain efficiencies, meaning current is higher than the rated capacity during the cruise phase as well beyond 4 A. This causes a downward shift in the discharge curve, meaning lower energy content can be obtained from the battery cells. The simulated energy density of 227.6 Wh/kg is further reduced by the overhead to 136.4 Wh/kg. For high payloads and therefore smaller batteries, currents are increased, resulting in a further reduction of capacity and a larger downward shift in the discharge curves. Therefore, at high payloads, the actual energy including overhead is reduced to 120 Wh/kg, half of the rated cell energy density. This occurs when the current is close to reaching the maximum continuous current with a battery pack approximately half the size, see Table 14.5. This energy density was determined from the area under the battery discharge curve during the simulation.

The volumetric power density and energy density are a slightly different story. Battery cells have a nominal battery energy density of 670 Wh/L. A single cell has a volume of 0.01654 L. For a 5 kg payload, Table 14.5 showed a total of 660 cells, equal to 10.91 L, but after considering the packing efficiency of 0.785 as a result of square packing, this becomes 13.9 L as seen in the table. When the same overhead is added, this comes down to 23.2 L. The 6.68 kWh battery then has a reduced volumetric energy density of approximately 288 Wh/L.

The power density (volumetric) is calculated according to Equation 14.4 for the cell and 14.5 for the entire battery pack. Remember that the cell can reach 82 W when fully charged, 72 W nominally and 50 W near 0% SoC. For the cell volume of 0.01654 L (1.8 cm diameter and 6.5 cm length), this comes down to 4.96 kW/L, 4.35 kW/L and 3 kW/L respectively. The maximum power that is delivered by the battery pack is approximately 18 kW. When taking into account battery and overhead volume (23.2 L), the maximum power density in this mission is 776 W/L. However, the battery would be capable of reaching higher power densities as the maximum continuous current is not reached for low payloads.

$$VPD_{Cell} = \frac{P_{max,cell}}{V_{cell}} \quad (14.4)$$

$$VPD_{Batt} = \frac{P_{max}}{V_{batt} + V_{batt,overhead}} \quad (14.5)$$

Battery in FC-B

It was shown in the results section that the battery in the FC-B configuration is mainly current limited and generally does not use the full capacity. Therefore, power density is high when considering the maximum power it reaches. However, the energy density is low when only considering the used energy. When ΔN_p is equal to 1, all battery packs had 66 cells in series and 2 parallel, making the battery pack 5.87 kg. Adding the overhead, this comes down to 9.78 kg. The volume equals 4.63 L with overhead, 2.78 L without. It should be noted that maximum battery power in the FC-B configuration reaches approximately 7.6 kW as seen in the simulations such as Figures B.1 and B.2. The power density reached equals 780 W/kg (gravimetric) and the volumetric power density is 1.64 kW/L.

Due to the fact that only a part of the energy content is used, Figure B.2 shows a simulated energy density of 84.9 Wh/kg (cell only), which results in a mere 51 Wh/kg when dividing the used energy by the weight of the battery pack and overhead. However, it should be noted that this remaining energy content could still be used during additional maneuvers in the flight profile. An additional landing and take-off would most likely be possible as less than half the capacity is used by the current hover, take-off and vertical descent phases. Figure 14.26 shows an overview of gravimetric energy densities in both B-Only and FC-B configurations. In this figure, 1 to 4 are battery energy density specifications in the B-only configuration. Bars 5 and 6 are the battery inside the FC-B configuration. Bar 1 shows the rated cell nominal energy density, which is in reality lower in the cell simulation (2). The same simulation, but then at pack level (includes overhead) is shown in bar 3. When the payload is at its maximum, the battery is small and the energy density is even lower, see bar 4. For the FC-B scenario, the cell simulated energy density is low, because not the full energy content is used in the best range mission profile. Bar 6 shows this energy density when including the overhead.

The volumetric energy density at cell level is 180 Wh/L and when including the overhead this comes down to 108 Wh/L. Again, note that this energy is not lost, but the battery is oversized in terms of energy content due to the current limits. The more advanced best range mission profile with an additional landing phase as seen in Figure 7.6 is possible with the current setup, especially when the vertical rate of climb is slightly reduced (in case of $\Delta N_p = 1$) so that current limits are not reached with a 66x2 battery pack size. Figure 14.27 shows the overview of battery volumetric energy densities.

Fuel Cell System in FC-B

Equation 14.6 gives the power density for the fuel cell system without the tank. The design power in the optimized scenarios coming from the fuel cell is approximately 10.25 kW. Where the stack power density is approximately 550 W/kg in all analyses, the power density is reduced to 420 W/kg when evaluating Equation

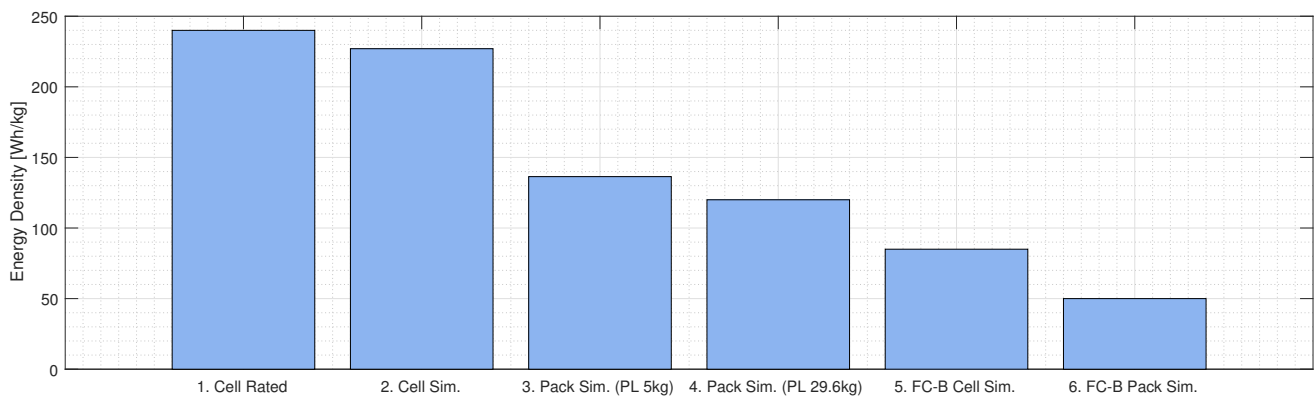


Figure 14.26: Overview of energy density of batteries. 1 to 4 are results for the B-only case and 5 and 6 are results for the battery inside the FC-B configuration

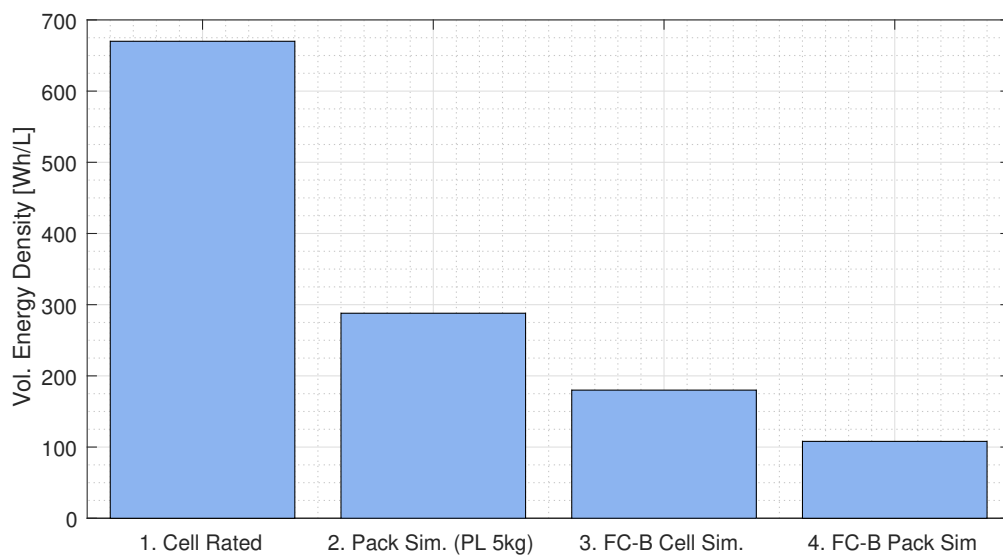


Figure 14.27: Overview of energy density. 1 and 2 are results for the B-only case, 3 and 4 are results for the battery inside the FC-B configuration

14.6. The battery itself provides both the power and the energy needed, therefore it would be a fair comparison to add the hydrogen storage tank weight to create an even more fair comparison. For a payload of 5 kg, 14.87 kg of storage is possible, leading to a power density of only 260 W/kg. This follows Equation 14.7. Note that this value gets closer to the 420 W/kg value when payload is increased and only a small storage tank can be placed in the helicopter.

$$GPD_{FC,sys-notank} = \frac{P_{des,FC}}{W_{FC} + W_{FC,overhead}W_{cont} + W_{press,reg} + W_{comp}} \quad (14.6)$$

$$GPD_{FC,sys+tank} = \frac{P_{des,FC}}{W_{FC} + W_{FC,overhead}W_{cont} + W_{press,reg} + W_{comp} + W_{H_2-tank}} \quad (14.7)$$

In terms of energy density, the hydrogen storage tank contains the entire energy content for the fuel cell system. When the payload is 5 kg, the storage tank in case of the 700 bar optimized analysis weighs 14.87 kg. At 5.2wt% H_2 (storage efficiency), this means a hydrogen content of 0.77 kg. Hydrogen has an energy density of 33.3 kWh/kg, however, the efficiency at maximum power and 1 atm stack pressure is approximately 43%, resulting in an effective energy of 11 kWh. The weight of the fuel cell system including the tank, but excluding the battery components, motor and inverter, is then 39.3 kg. This results in a mere 280Wh/kg, however, this is much better than the actual energy density of 136.4 Wh/kg in the battery only system. When this 14.87 kg storage tank is replaced by LH_2 at 12 wt%, the energy content after fuel cell efficiency is 25.6 kWh, making the energy density 650 Wh/kg.

The volume of the fuel cell system without the tank is 27 L and 47.5 L with the tank. Given the 11 kWh effective energy content for 700 bar configuration, this yields 400 Wh/L and 230 Wh/L respectively.

Overall Power Density and Energy Density

The overall energy density and power density of the full FC-B system are lower. This analysis does not include the inverter and motor weights, because the comparison is to power densities and energy densities previously evaluated for the battery-only case without the motor and inverter. Also, these components weigh the same in both systems. This means that in reality, the overall power and energy density are slightly lower. This section still uses the configuration with 5 kg payload in the evaluation.

The total power delivered by the system is approximately 18 kW, going into the inverter. For the energy content of the batteries, the FC-B analysis in this section uses the low end of the actual battery energy density at 120 Wh/kg. This means that effectively, for high power phases, the battery pack of 9.79 kg stores close to 1.2 kWh of energy. The 700 bar tank stores 11 kWh, meaning a combined 12.2 kWh. The FC system plus battery weight is approximately 49.3 kg. The result is an overall energy density of 250 Wh/kg with a 700 bar storage method and 540 Wh/kg with liquid hydrogen. This is significantly more than the energy density of the battery-only case at 136.4 Wh/kg, as can be seen in Figure 14.28. This mainly explains the additional range with the FC-B configuration.

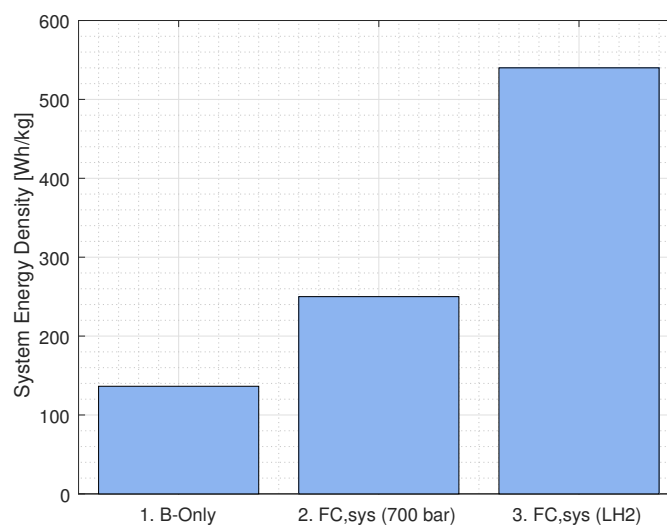


Figure 14.28: Overview of energy density at system level. 1 is the battery-only case at 136.4 Wh/kg, 2 is the fuel cell system (700 bar) including battery weight and 3 is the fuel cell system (LH_2) including battery weight.

The volume of the fuel cell system with the tank was evaluated as 47.5 L. When including the batteries, this adds 4.63 L up to 52.1 L. Volumetric energy density is then found to be 234 Wh/L for the 700 bar FC-B configuration. The tank volume is reduced for liquid hydrogen from 20.5 L to 11.7 L. Hence, for the energy content in a liquid hydrogen configuration the volumetric energy density becomes approximately 620 Wh/L. This overview is shown in Figure 14.29. The battery-only configuration is actually beneficial in terms of volume when compared to a high pressure 700 bar tank. When compared to liquid hydrogen, this benefit disappears.

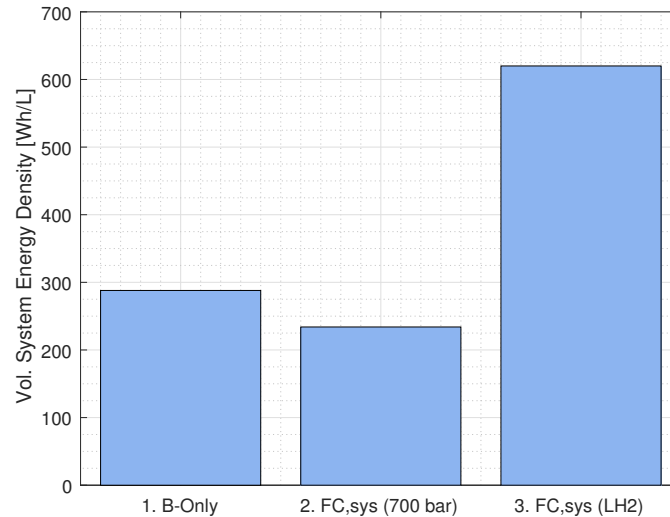


Figure 14.29: Overview of volumetric energy density at system level. 1 is the battery-only case at 288 Wh/L, 2 is the fuel cell system (700 bar) including battery weight and 3 is the fuel cell system (LH₂) including battery weight

The overall power density can also be determined. For the battery-only case this was found to be 367 W/kg and 776 W/L for the 5 kg payload mission, but capable of reaching higher power densities. For the FC-B at the same maximum power level, this power density is approximately 365 W/kg. This is 38% higher than the fuel cell system alone (at 260 W/kg) without the batteries but including the storage tank. This is approximately 345 W/L when considering the FC-B system is 52.1 L total. The B-only configuration shows no major improvement in gravimetric power density. In reality, however, the batteries are capable of a much higher power density when used at higher discharge rates. Therefore, Figures 14.28 and 14.29 representing the system energy densities are more important and show why the FC-B system has increased range. The gravimetric energy density of the FC-B system shows a significant improvement.

Conclusions

This study carried out a preliminary sizing and optimization of battery-only (B-only) and fuel cell - battery (FC-B) powertrain configuration towards improved endurance and especially range. Previous fuel cell applications were shown to be mainly fixed wing UAV and small demonstrator aircraft with higher aerodynamic efficiency and a larger difference between nominal cruise and peak power than for rotorcraft. Battery only technology is generally used for smaller UAVs or 2-seater aircraft such as the Pipistrel Alpha Electro with a maximum endurance of approximately 1 hour. For this study, the approach was to convert the power system of the GeoCopter GC-201 helicopter UAV with a MTOW of 100 kg and maximum power output of 16 kW into an all-electric powertrain, due to lower aerodynamic efficiency compared to fixed wing aerial vehicles.

The main objective in the study was to understand focus areas for further powertrain development and application areas of B-only and FC-B configurations. The chosen method for the comparisons of these systems was by payload-range diagrams, immediately showing application limits of the individual configurations.

This was done through a literature review of aspects related to this study (Part I), performance modelling of the GeoCopter GC-201 helicopter, defining best range and best endurance mission profiles and strategy, semi-empirical fuel cell modelling, modelling of Balance of Plant, battery modelling and combining these components into a full sizing and optimization procedure. Crucial Balance of Plant (additional) components are considered in the study: battery overhead, the air compressor, fuel cell system overhead, pressure regulators, a double inverter and an electric motor. The research question was stated as follows:

How can the range and/or endurance of an electrically powered helicopter UAV be optimized by using a hybrid fuel cell-battery powertrain?

One important part was to find suitable battery and fuel cell technology for the UAV. Suitable battery technologies currently available are Lithium-Ion cells, with the LG-HG2 cell used in this study at an energy density of 240 Wh/kg. However, it was found that at higher discharge rates this energy density and cell capacity reduce and that when including overhead, the pack energy density is much lower. The advantage of the Lithium-Ion cells is that the maximum power density of these cells is around 1.5 kW/kg. A forecast of upcoming battery technology was found to be Li-S or Solid-State Li-Ion, with Li-S energy density estimates around 400 Wh/kg. In the case for battery-only technology, cells with high energy density are more important than maximum power density, while in a FC-B configuration the current (and thus power) limit is more important due to short duration peak power phases. This became clear from the battery simulations of the mission profiles.

It was found that low temperature PEMFCs are the most suitable fuel cells for this helicopter application due to its wide usage in vehicular applications and short start-up times. For larger systems, SOFCs can reach much higher system efficiency levels when its exhaust heat is used effectively. Power densities of PEMFC that include cooling and humidification were found to reach up to approximately 550 W/kg for power systems of the size in this thesis, which was used in all analyses. For this reason, the fuel cell stacks and the hydrogen storage tank are two of the largest weight and volume contributors. Although hydrogen contains 33.3 kWh/kg, this reduces to 1.7 kWh/kg or 4 kWh/kg when including 700 bar and liquid hydrogen storage tanks. Taking operating efficiency into account, only 700 Wh/kg or 1.7 kWh/kg can be effectively reached. When including the other fuel cell system components, this reduces to 350 Wh/kg and 750 Wh/kg for applications with a 5 kg payload. Also including battery components in the FC-B system, this was evaluated to be 250 and 540 Wh/kg. This was found to be higher than the energy density of a low payload, longer range battery-only mission, showing 136 Wh/kg.

For the modelling of the fuel cell, a semi-empirical method was used for static modelling and two variables were introduced: cell current density and stack pressure. It was found that the current density goes

to its maximum (maximum power and hydrogen mass flow) for shorter flight times and reduces slightly (increased efficiency) when flight times are longer or when fuel cell power density is reduced. The stack pressure always went to the lower bound, indicating that a larger compressor has no benefits for this fuel cell and its application. Other variables that were introduced in the mission profiles were forward speed rate of climb and descent, as well as altitude. The forward speed rate of climb and descent had a small effect on the results. However, reducing the vertical rate of climb from 4 to 1 m/s and thus reducing the sea level performance compared to the conventional configuration, showed an increase in range. Optimized altitudes for battery-only showed to be around 1500 m for battery-only and 1200 m for FC-B configurations. However, differences in range are relatively small and it is recommended to size the powertrain based on application needs in terms of altitude.

The modelling of the battery used a custom simulation and curve fit based on an extension to Shepherd's model. The generic battery model in SimScape Power systems showed bad fitting behaviour, but was still used for the verification of the simulation method. The effect of capacity loss with discharge rates was modelled through the Peukert coefficient. The good results of this method make it a recommended approach for battery simulation. For the battery, it is important to understand that not the full capacity can be used at high discharge rates. However, if current is reduced to the rated current, the last bit of capacity can still be discharged.

Volume is no issue for battery-only configurations. For 300 bar and 0 kg payload configurations, a large part of the volume budget was used due to a relatively large storage tank. The other main volume contributor is the fuel cell stack. At low payloads, it was found that at least 20-30 L of the 91.25 L volume budget was still available. When increasing the fuel cell system overhead from 15 to 30%, this reduced slightly but a volume for the payload was still available. The main point is that for this unmanned rotorcraft system, the weight budget is more limiting than the volume budget. For piloted rotorcraft, the cabin size may limit the volume for the power system. Fixed wing aircraft are more slender, but also have severely reduced cruise power levels. Because the majority of the volume is in the fuel cell stack (sized for power), this may not be as limiting.

The payload-range diagrams indicated large differences between the conventional powertrain, the battery-only configuration and FC-B configuration. The original micro gas turbine powered rotorcraft has an estimated range of 500 km. The battery configuration reaches about 75-80 km with state-of-the-art batteries. A 300 bar configuration reaches around 140 km, 700 bar goes up to 180 km and liquid hydrogen to 410 km. Battery maximum payload is limited by current, where FC-B is limited by the weight budget for hydrogen storage tanks. Batteries go up to 30 kg payload up to 30 km range, where FC-B configurations can reach 15-20 kg payload. The break-even point for FC-B with batteries is at approximately 60 km range. In application areas below or near this range, or for higher payloads, it is therefore beneficial to go for the simpler battery-only configuration. When considering a 2030 forecast - with a 20% fuel cell power density increase and a battery cell energy density of 400 Wh/kg - the liquid hydrogen configuration shows a higher maximum range than the conventional rotorcraft. The battery-only configuration can fly up to 135 km, whereas 300 bar and 700 bar configurations reach 200 and 250 km. Break-even for 300 bar and 700 bar is around 100 km and 15 kg payload, which is 60 km and 25 kg payload for liquid hydrogen. Improvements in fuel cell stack power density have a significant effect. Also, slight improvements in storage efficiency will result in a less steep payload-range diagram and improvements in range.

Bibliography

- [1] Frano Barbir. *PEM fuel cells: theory and practice*. Academic Press, 2012.
- [2] Jérôme Bernard, Marcel Hofer, Uwe Hannesen, Antoine Toth, Akinori Tsukada, Félix N Büchi, and Philipp Dietrich. Fuel cell/battery passive hybrid power source for electric powertrains. *Journal of Power Sources*, 196(14):5867–5872, 2011.
- [3] Celeroton. Ct-17-1000.gb data sheet. https://www.celeroton.com/fileadmin/user_upload/produkte/kompressor/datasheets/Datasheet-CT-17-1000.GB.pdf, . Retrieved 02-2018.
- [4] Celeroton. Ct-17-700.gb data sheet. https://www.celeroton.com/fileadmin/user_upload/produkte/kompressor/datasheets/Datasheet-CT-17-700.GB.pdf, . Retrieved 02-2018.
- [5] Celeroton. Energy saving potential with oil-free turbo compressors in fuel cell systems. <https://www.celeroton.com/en/technology/tech-blog/detail/energy-saving-potential-with-turbo-compressors-in-fuel-cell-systems.html>, . Retrieved 01-2018.
- [6] LG Chem. Technical information of lg 18650hg2. URL <https://www.nkon.nl/sk/k/hg2.pdf>. Retrieved 06-2017.
- [7] Satishkumar B Chikkannanavar, Dawn M Bernardi, and Lingyun Liu. A review of blended cathode materials for use in li-ion batteries. *Journal of Power Sources*, 248:91–100, 2014.
- [8] Anubhav Datta and Wayne Johnson. Requirements for a hydrogen powered all-electric manned helicopter. In *12th AIAA Aviation Technology, Integration, and Operations (ATIO) Conference and 14th AIAA/ISSMO Multidisciplinary Analysis and Optimization Conference*, page 5405, 2012.
- [9] Baptiste Delhomme, Patricia De Rango, Philippe Marty, Maria Bacia, Bartosz Zawilski, Cécile Raufast, Salvatore Miraglia, and Daniel Fruchart. Large scale magnesium hydride tank coupled with an external heat source. *International Journal of Hydrogen Energy*, 37(11):9103–9111, 2012.
- [10] Renault Battery Development Department. Zoe battery durability, field experience and future vision. http://cii-resource.com/cet/AABE-03-17/Presentations/BMGT/Delobel_Bruno.pdf. Retrieved 02-2018.
- [11] A Dinger, R Martin, X Mosquet, M Rabl, D Rizoulis, M Russo, and G Sticher. Batteries for electric cars: Challenges, opportunities, and the outlook to 2020, the boston consulting group, 2010, 2010.
- [12] Stephan Eelman, I Pozo del Poza, and T Kreig. Fuel cell apu's in commercial aircraft-an assessment of sofc and pemfc concepts. In *24th International Congress of Aeronautical Sciences (ICAS)*, 2004.
- [13] Emerson. Temson 20-1200 series pressure regulator data sheet. <http://www.emerson.com/documents/automation/20-1200-series-data-sheet-en-135996.pdf>. Retrieved 02-2018.
- [14] Oxis Energy. Lithium sulfur ultralight pouch cell, 2017. URL <https://oxisenergy.com/products/>.
- [15] Liping Fan, Dong Huang, and Minxiu Yan. Fuzzy sliding mode control for a fuel cell system. 11, 05 2013.
- [16] Antonio Filippone. *Flight performance of fixed and rotary wing aircraft*. Elsevier, 2006.
- [17] G Girishkumar, B McCloskey, AC Luntz, Sally Swanson, and W Wilcke. Lithium- air battery: promise and challenges. *The Journal of Physical Chemistry Letters*, 1(14):2193–2203, 2010.
- [18] D Guida and M Minutillo. Design methodology for a PEM fuel cell power system in a more electrical aircraft. *Applied Energy*, 192:446–456, 2017.
- [19] Shaker Haji. Analytical modeling of pem fuel cell i-v curve. *Renewable Energy*, 36(2):451–458, 2011.
- [20] Fuel Cell Handbook. Eg&g technical services, inc. under contract no. DEAM26-99FT40575, US Depart-

- ment of Energy, Office of Fossil Energy, National Energy Technology Laboratory, Morgantown, West Virginia, USA, 2004.
- [21] Troy R Hawkins, Bhawna Singh, Guillaume Majeau-Bettez, and Anders Hammer Strømman. Comparative environmental life cycle assessment of conventional and electric vehicles. *Journal of Industrial Ecology*, 17(1):53–64, 2013.
- [22] P Jackson, K Munson, and L Peacock. *Ihs jane's all the world's aircraft: Development & production*, 2014.
- [23] JetCat. Jetcat sph5 instruction manual. <http://www.jetcat.de/jetcat/Bedienungsanleitung/SPH5-german-13062017.pdf>. Retrieved 02-2018.
- [24] Lonnie Johnson. The viability of high specific energy lithium air batteries. In *Symposium on Research Opportunities in Electrochemical Energy Storage-Beyond Lithium Ion: Materials Perspectives*, 2010.
- [25] Wayne Johnson. *Helicopter theory*. Courier Corporation, 2012.
- [26] Josef Kallo, Gwénaëlle Renouard-Vallet, Martin Saballus, Gerrit Schmithals, Johannes Schirmer, K Andreas Friedrich, et al. Fuel cell system development and testing for aircraft applications. In *18th World Hydrogen Energy Conference 2010–WHEC 2010*, pages 16–21, 2010.
- [27] P Kurzweil and J Garche. Overview of batteries for future automobiles. In *Lead-Acid Batteries for Future Automobiles*, pages 27–96. Elsevier, 2017.
- [28] Oak Ridge National Laboratory. Electric drive inverter research and development. https://energy.gov/sites/prod/files/2015/06/f24/edt053_chinthavali_2015_o.pdf. Retrieved 02-2018.
- [29] Jeffrey C Lagarias, James A Reeds, Margaret H Wright, and Paul E Wright. Convergence properties of the nelder–mead simplex method in low dimensions. *SIAM Journal on optimization*, 9(1):112–147, 1998.
- [30] N. Lapena-Rey, E. Troncoso-Munoz, A.C. Abad, P.P. Martin-Alonso, and J. Qing. Lightweight gas pressure regulator, June 13 2017. URL <http://www.google.ch/patents/US9678515>. US Patent 9,678,515.
- [31] Nieves Lapeña-Rey, Jonay Mosquera, Elena Bataller, and Fortunato Ortí. First fuel-cell manned aircraft. *Journal of aircraft*, 47(6):1825–1835, 2010.
- [32] James Larminie, Andrew Dicks, and Maurice S McDonald. *Fuel cell systems explained*, volume 2. J. Wiley Chichester, UK, 2003.
- [33] Cosmin Laslau, Lilia Xie, and Christopher Robinson. The next-generation battery roadmap: Quantifying how solid-state, lithium-sulfur, and other batteries will emerge after 2020, October 2015. URL <http://web.luxresearchinc.com/hs-fs/hub/86611/file-442189130-pdf/outlook>.
- [34] Gordon J Leishman. *Principles of helicopter aerodynamics with CD extra*. Cambridge university press, 2006.
- [35] Mykhaylo V Lototsky, Ivan Tolj, Lydia Pickering, Cordellia Sita, Frano Barbir, and Volodymyr Yartys. The use of metal hydrides in fuel cell applications. *Progress in Natural Science: Materials International*, 2017.
- [36] General Motors. 2016 chevrolet volt battery system. https://media.gm.com/content/dam/Media/microsites/product/Volt_2016/doc/VOLT_BATTERY.pdf. Retrieved 02-2018.
- [37] Arie Nawawi, Chin Foong Tong, Shan Yin, Assel Sakanova, Yitao Liu, Yong Liu, Men Kai, Kye Yak See, King-Jet Tseng, Rejeki Simanjorang, et al. Design and demonstration of high power density inverter for aircraft applications. *IEEE Transactions on Industry Applications*, 53(2):1168–1176, 2017.
- [38] Nedstack. Fuel cell types, 2017. URL <http://www.nedstack.com/technology/fuel-cell-types>.
- [39] Akira Nishizawa, Josef Kallo, Olivier Garrot, and Jörg Weiss-Ungethüm. Fuel cell and li-ion battery direct hybridization system for aircraft applications. *Journal of Power Sources*, 222:294–300, 2013.
- [40] Naoki Nitta, Feixiang Wu, Jung Tae Lee, and Gleb Yushin. Li-ion battery materials: present and future. *Materials today*, 18(5):252–264, 2015.
- [41] David Novák. Design of a li-ion battery pack emulator. 2015.
- [42] Department of Energy. Technical system targets: Onboard hydrogen storage for light-duty fuel cell vehicles. https://energy.gov/sites/prod/files/2015/01/f19/fcto_myrrdd_table_onboard_h2_storage_systems_doe_targets_ldv.pdf, 2015.
- [43] United States Department of Energy. Targets for fuel cell system humidifiers and air compression systems. <https://energy.gov/eere/fuelcells/doe-technical-targets-fuel-cell-system-humidifiers-and-air-compression-systems>, . Retrieved 04-2017.

- [44] U.S. Department of Energy. Overview of the doe advanced power electronics and electric motor research and development program. https://energy.gov/sites/prod/files/2014/09/f18/fy_2014_vto_amr_apeem_overview-final_version.pdf, . Retrieved 02-2018.
- [45] Isaac Pilatowsky, Rosenberg J Romero, CA Isaza, SA Gamboa, PJ Sebastian, and W Rivera. *Cogeneration fuel cell-sorption air conditioning systems*. Springer Science & Business Media, 2011.
- [46] Sion Power. Lithium sulfur licerion, 2017. URL <http://www.sionpower.com/technology-licerion.php>.
- [47] Md Arafat Rahman, Xiaojian Wang, and Cuie Wen. A review of high energy density lithium–air battery technology. *Journal of Applied Electrochemistry*, 44(1):5–22, 2014.
- [48] Kaushik Rajashekara, James Grieve, and David Daggett. Hybrid fuel cell power in aircraft. *IEEE Industry Applications Magazine*, 14(4), 2008.
- [49] Grand View Research. Fuel cell market analysis by product (pemfc, pafc, sofc, mfc), by application (stationary, transportation, portable) and segment forecast, 2014 - 2025. URL <http://www.grandviewresearch.com/industry-analysis/fuel-cell-market>. Retrieved 07-2017.
- [50] Giulio Romeo and Fabio Borello. Design and realisation of a two-seater aircraft powered by fuel cell electric propulsion. *The Aeronautical Journal*, 114(1155):281–297, 2010.
- [51] RE Rosli, AB Sulong, WRW Daud, MA Zulkifley, T Husaini, MI Rosli, EH Majlan, and MA Haque. A review of high-temperature proton exchange membrane fuel cell (ht-pemfc) system. *International Journal of Hydrogen Energy*, 42(14):9293–9314, 2017.
- [52] NAA Rusman and M Dahari. A review on the current progress of metal hydrides material for solid-state hydrogen storage applications. *International Journal of Hydrogen Energy*, 41(28):12108–12126, 2016.
- [53] John M Seddon and Simon Newman. *Basic helicopter aerodynamics*, volume 40. John Wiley & Sons, 2011.
- [54] Siemens. Electric propulsion components with high power densities for aviation. <https://nari.arc.nasa.gov/sites/default/files/attachments/Korbinian-TVFW-Aug2015.pdf>. Retrieved 02-2018.
- [55] KM Spencer and CA Martin. Investigation of potential fuel cell use in aircraft. *Institute For defense analyses*, 2013.
- [56] Air Squared. Scroll compressor and scroll vacuum pump efficiency explained. <https://airsquared.com/scroll-technology/articles/scroll-compressor-and-scroll-vacuum-pump-efficiency-explained/>, . Retrieved 02-2018.
- [57] Air Squared. P24h056a-blcd scroll air compressor data sheet. <https://airsquared.com/wp-content/uploads/2015/12/p24h056a-blcd.pdf>, . Retrieved 02-2018.
- [58] Richard O Stroman, Michael W Schuette, and JR Southwick. Design challenges and modeling for an efficient liquid hydrogen storage tank for autonomous systems. In *Proceedings of 2011 AIChE Annual Meeting*, 2011.
- [59] Stefan Stückl, Jan van Toor, and Hans Lobentanzer. Voltair—the all electric propulsion concept platform—a vision for atmospheric friendly flight. In *28th International Congress of the Aeronautical Sciences (ICAS)*, 2012.
- [60] Jing Su. Development of a novel compact reformer for pemfc. 2009.
- [61] Karen Swider-Lyons, Richard Stroman, Joseph Rodgers, Daniel Edwards, Joseph Mackrell, Michael Schuette, and Gregory Page. Liquid hydrogen fuel system for small unmanned air vehicles. In *51st AIAA Aerospace Sciences Meeting including the New Horizons Forum and Aerospace Exposition. American Institute of Aeronautics and Astronautics*, pages 1–6, 2013.
- [62] Karen Swider-Lyons, Richard O’Neil Stroman, Benjamin D Gould, Joseph A Rodgers, Joseph Mackrell, Michael Schuette, and Gregory Page. Hydrogen fuel cells for small unmanned air vehicles. *ECS Transactions*, 64(3):963–972, 2014.
- [63] Horizon Energy Systems. Specifications of horizon h1000 pemfc, . URL <https://www.hes.sg/>. Retrieved 07-2017.
- [64] MatLab SimScape Power Systems. Generic battery model, . URL <https://mathworks.com/help/physmod/sps/powersys/ref/battery.html>. Retrieved 07-2017.
- [65] MatLab SimScape Power Systems. Generic fuel cell model, . URL <https://>

- mathworks.com/help/physmod/sps/powersys/ref/fuelcellstack.html;jsessionid=17676145ee135615eebf9f847c50. Retrieved 07-2017.
- [66] Michael M Thackeray, Christopher Wolverton, and Eric D Isaacs. Electrical energy storage for transportation—approaching the limits of, and going beyond, lithium-ion batteries. *Energy & Environmental Science*, 5(7):7854–7863, 2012.
- [67] Olivier Tremblay, Louis-A Dessaint, and Abdel-illah Dekkiche. A generic battery model for the dynamic simulation of hybrid electric vehicles. In *Vehicle Power and Propulsion Conference, 2007. VPPC 2007. IEEE*, pages 284–289. Ieee, 2007.
- [68] Julius M Vegh, Juan J Alonso, Tarik H Orta, and Carlos Ilario da Silva. Flight path and wing optimization of lithium-air battery powered passenger aircraft. In *53rd AIAA Aerospace Sciences Meeting*, page 1674, 2015.
- [69] Dries Verstraete, Kai Lehmkuehler, Andrew Gong, James R Harvey, Geoff Brian, and Jennifer L Palmer. Characterisation of a hybrid, fuel-cell-based propulsion system for small unmanned aircraft. *Journal of Power Sources*, 250:204–211, 2014.
- [70] Dries Verstraete, Andrew Gong, Dylan D-C Lu, and Jennifer L Palmer. Experimental investigation of the role of the battery in the aerostack hybrid, fuel-cell-based propulsion system for small unmanned aircraft systems. *International Journal of Hydrogen Energy*, 40(3):1598–1606, 2015.
- [71] Lin Wang, Attila Husar, Tianhong Zhou, and Hongtan Liu. A parametric study of pem fuel cell performances. *International Journal of Hydrogen Energy*, 28(11):1263–1272, 2003.
- [72] Eric W Weisstein. Circle packing. 2002.
- [73] Pat Wheeler and Sergei Bozhko. The more electric aircraft: Technology and challenges. *IEEE Electrification Magazine*, 2(4):6–12, 2014.
- [74] Nicholas Williard, Wei He, Christopher Hendricks, and Michael Pecht. Lessons learned from the 787 dreamliner issue on lithium-ion battery reliability. *Energies*, 6(9):4682–4695, 2013.
- [75] David Wright. Epa request for issuance of a new certificate of conformity tesla model 3. https://www3.epa.gov/otaq/datafiles/FOI_HTSLV00.0L13_APPIPT1.PDF. Retrieved 02-2018.
- [76] S. Yin, K. J. Tseng, R. Simanjorang, Y. Liu, and J. Pou. A 50-kw high-frequency and high-efficiency sic voltage source inverter for more electric aircraft. *IEEE Transactions on Industrial Electronics*, 64(11):9124–9134, Nov 2017. ISSN 0278-0046. doi: 10.1109/TIE.2017.2696490.
- [77] Xingwen Yu and Peter G Pickup. Recent advances in direct formic acid fuel cells (dfa-fc). *Journal of Power Sources*, 182(1):124–132, 2008.

A

Appendix A: Battery-Only 500 and 1500m Simulations

This appendix shows battery simulations for the battery-only simulations. This means no fuel cell was present in the configuration. The corresponding results section is found in Section 14.2. The comparison in this appendix is between Figures A.1 and A.2 for 0 kg payload. It shows that currents are relatively low, small changes in the discharge curve due to a longer high power phase, but almost equal energy density and range.

Sim. Energy Density = 228.88 Wh/kg , Sim. Vol. Energy Density =615.77 Wh/L
Sim. Avg. Power Density =322.81 W/kg ,Sim. Max. Power Density =555.42 W/kg

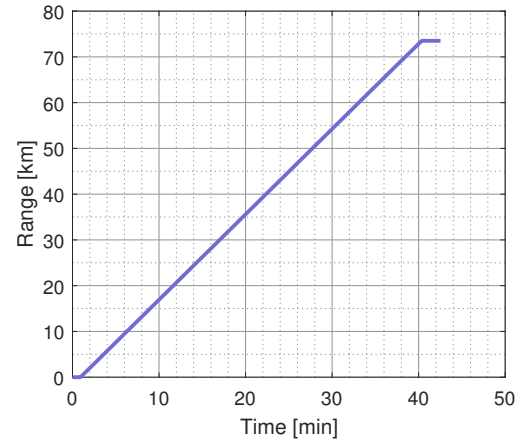
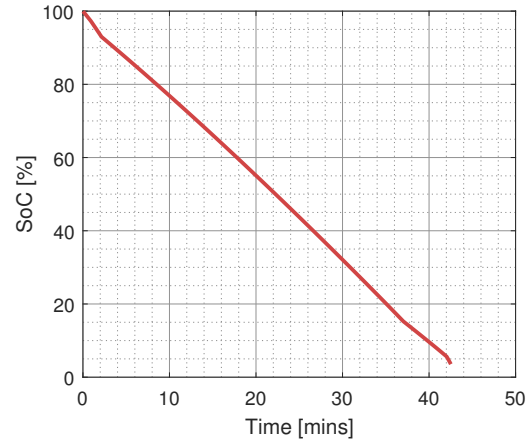
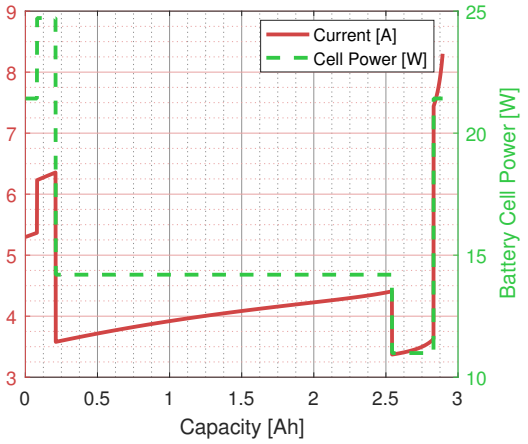
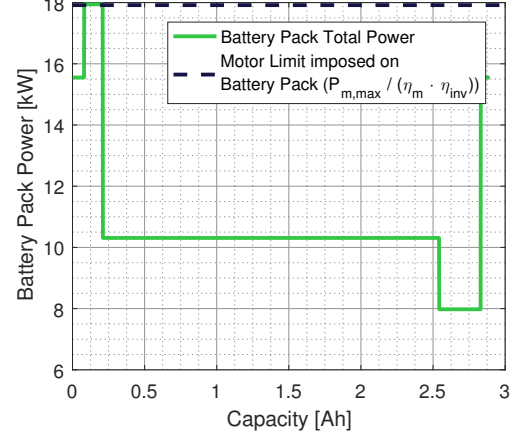
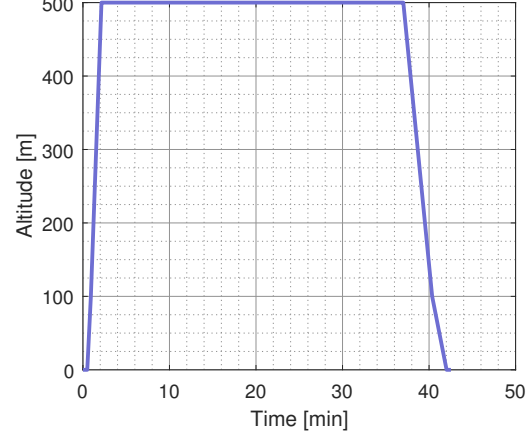
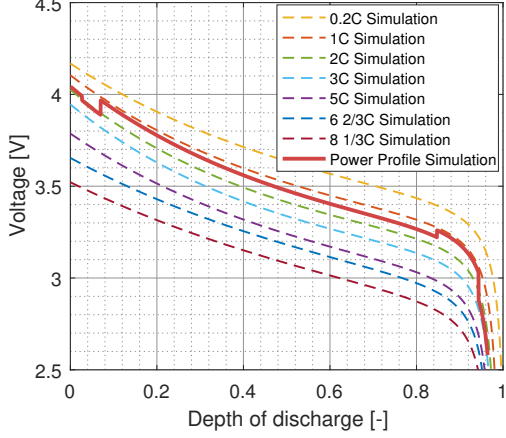


Figure A.1: Simulation of Battery for maximum range at 500 m cruise altitude

Sim. Energy Density = 228.98 Wh/kg , Sim. Vol. Energy Density =616.04 Wh/L
Sim. Avg. Power Density =314.32 W/kg ,Sim. Max. Power Density =550.33 W/kg

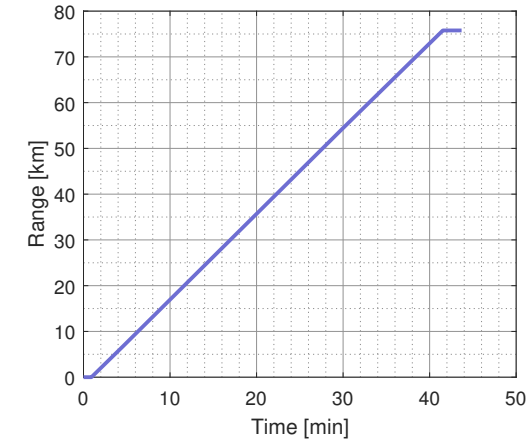
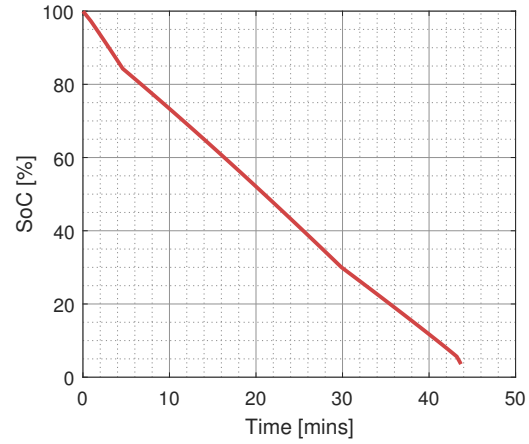
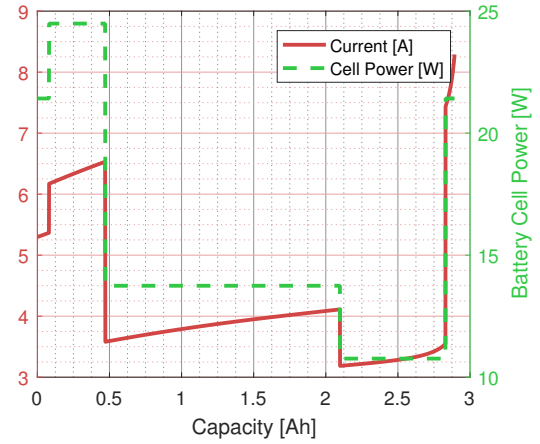
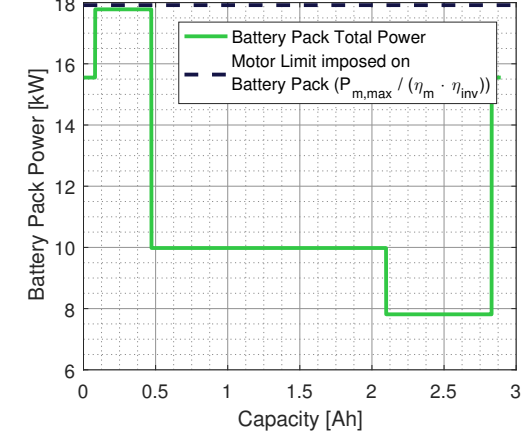
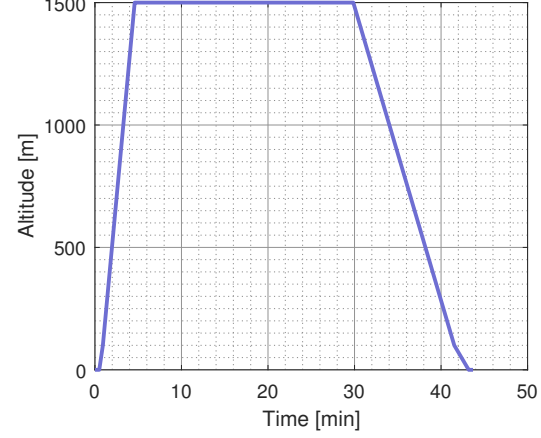
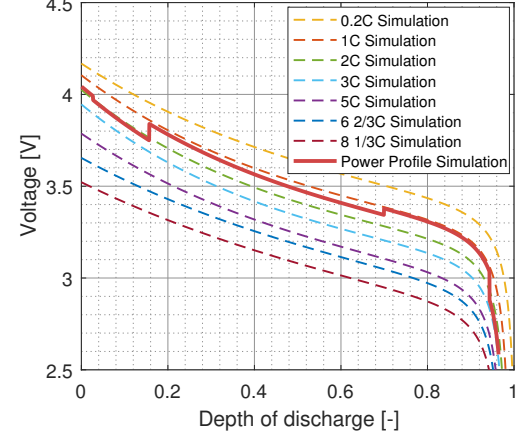


Figure A.2: Simulation of Battery for maximum range at 1500 m cruise altitude

Appendix B: FC-B Configuration Battery Simulations

This Appendix shows battery simulations within the FC-B configuration. Here, the battery is sized based on the energy content and the current limit and made as small as possible while staying within these limits. The FC-B configurations were discussed in the results Section 14.3. Figure B.1 shows the simulation for 500 m (unoptimized) with a discrete battery sizing (66 series, 2 parallel) and Figure B.2 shows the same simulation for 500 m and a semi-discrete battery sizing. It can be seen that in the latter case a larger part of the battery capacity is used as a result of a smaller battery which approaches the current limit in the climb phases. The discrete case is further below the current limit as expected. Because of the proximity to the current limit, not the full energy content can be used. However, this energy/capacity could potentially be used for other maneuvers where peak power is required.

LG-HG2 3000 mAh (3.6V)
240Wh/kg Nominal
Sim. Energy Density = 72.4032 Wh/kg , Sim. Vol. Energy Density =194.7912 Wh/L
Sim. Avg. Power Density =1001.7805 W/kg ,Sim. Max. Power Density =1288.2234 W/kg

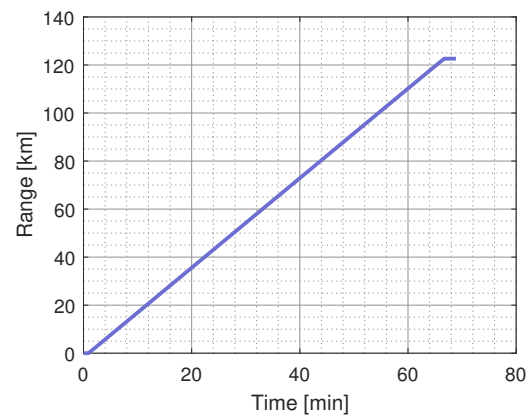
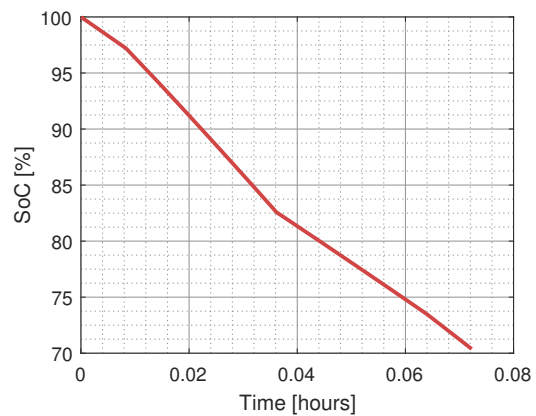
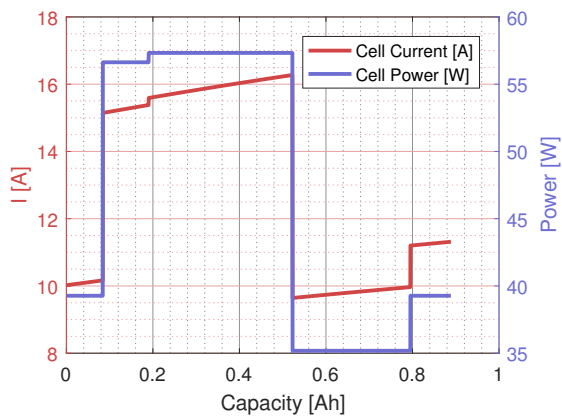
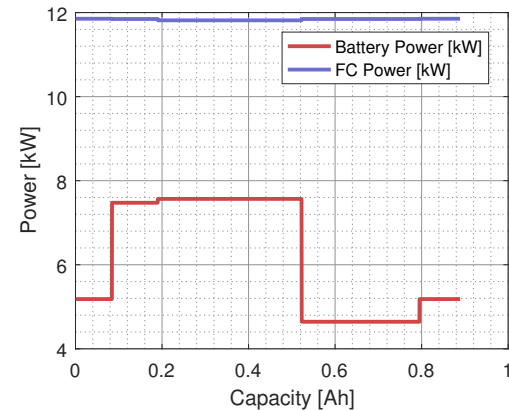
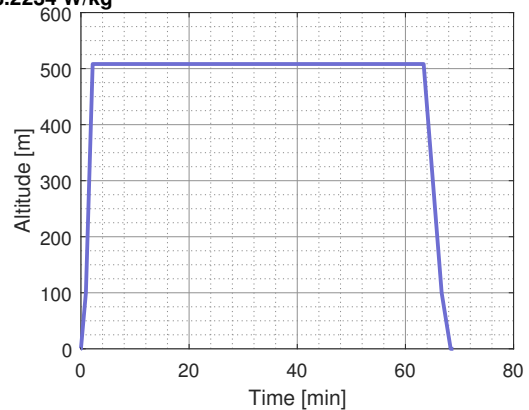
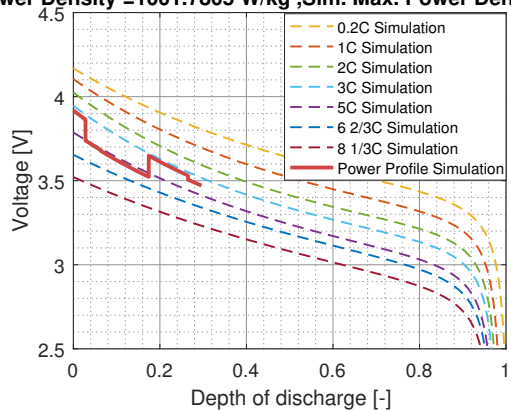


Figure B.1: Simulation of battery for the 500 m unoptimized range case with $\Delta N_p = 1$

LG-HG2 3000 mAh (3.6V)
240Wh/kg Nominal
Sim. Energy Density = 84.9426 Wh/kg , Sim. Vol. Energy Density =228.5269 Wh/L
Sim. Avg. Power Density =1177.5405 W/kg ,Sim. Max. Power Density =1515.3114 W/kg

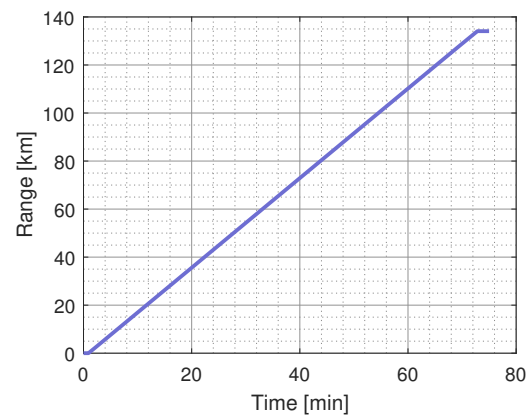
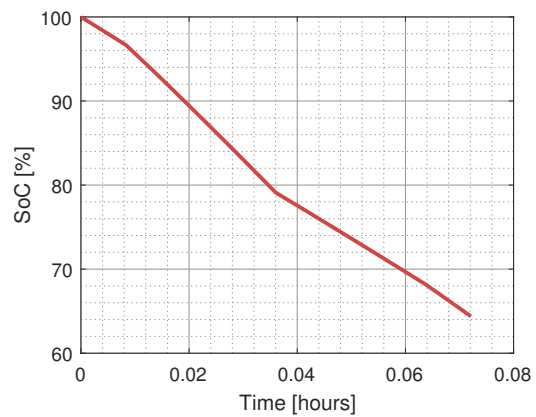
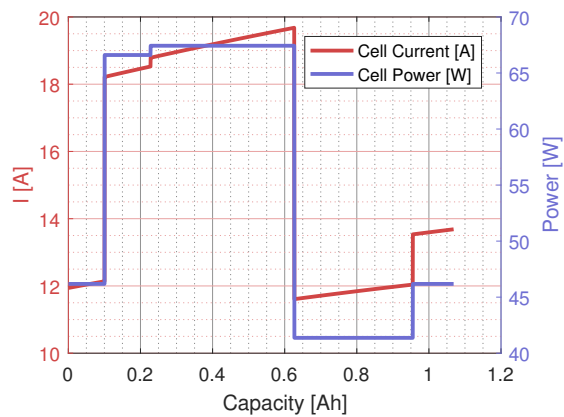
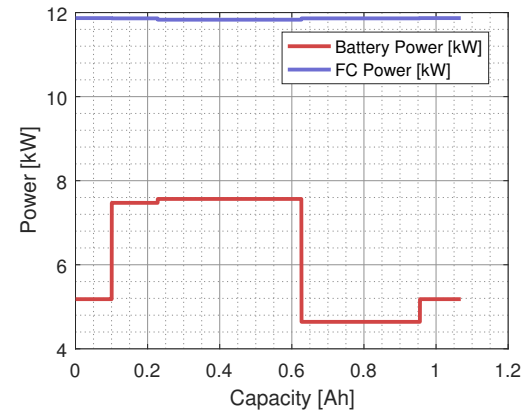
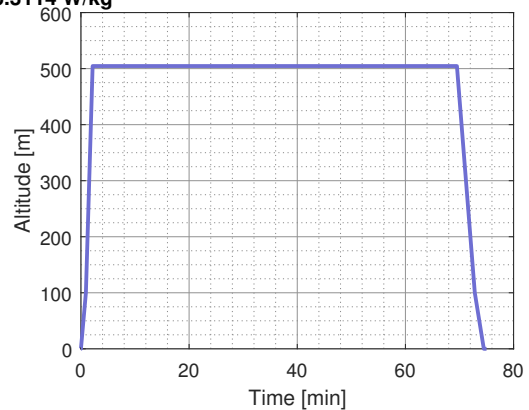
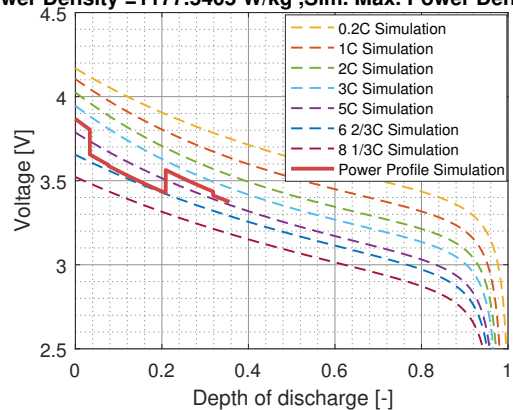


Figure B.2: Simulation of battery for the 500 m unoptimized range case with $\Delta N_p = 0.05$

Appendix C: FC-B Configuration Vertical RoC Investigation

This appendix shows an overview of battery simulations for the Vertical RoC investigation. The Vertical RoC can define the maximum power level the helicopter experiences. This investigation was performed in Section 14.3.9.

Figures C.1 to C.3 show the simulations for discrete battery sizing. Each of the battery packs have 66 cells in series and 2 cells parallel. Figures C.4 to C.6 show the simulations for the semi-discrete battery sizing and have 66 series and 1.65, 1.4 and 1.45 parallel respectively.

LG-HG2 3000 mAh (3.6V)
240Wh/kg Nominal

Sim. Energy Density = 112.9627 Wh/kg , Sim. Vol. Energy Density =303.9112 Wh/L
Sim. Avg. Power Density =901.491 W/kg ,Sim. Max. Power Density =1321.9432 W/kg

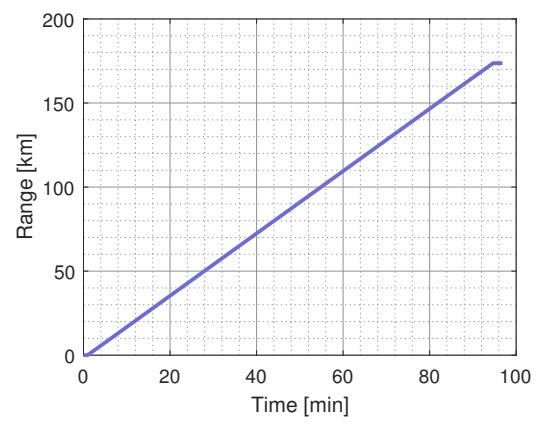
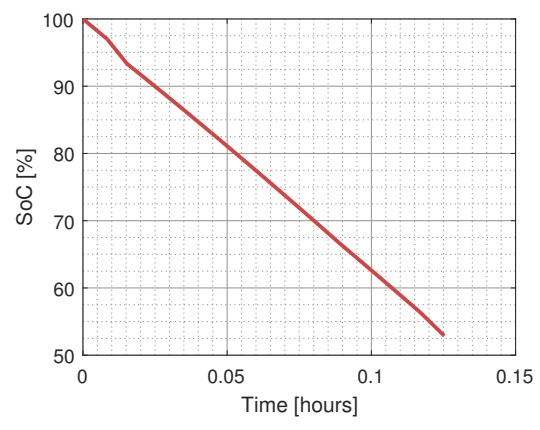
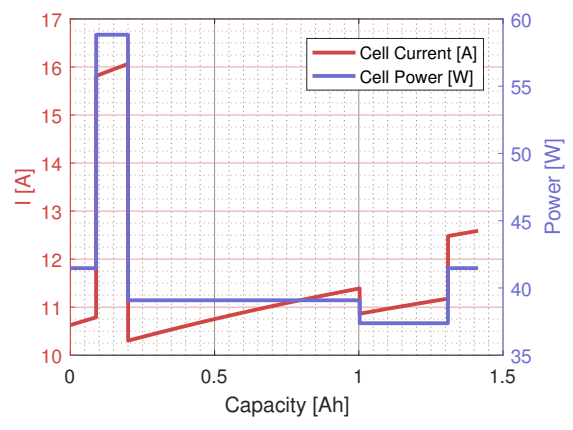
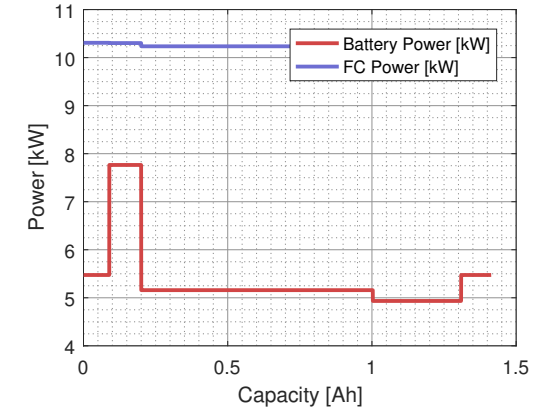
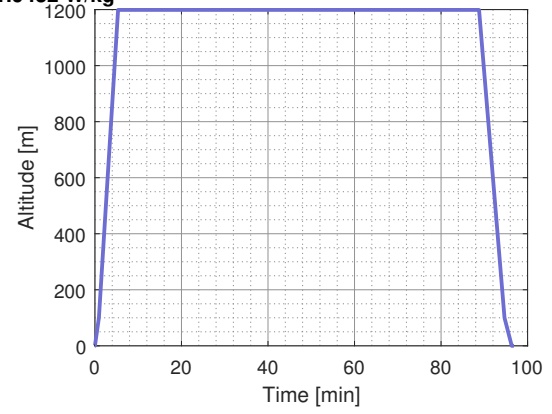
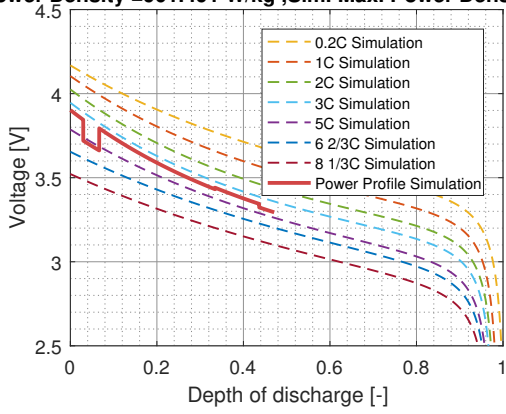


Figure C.1: 4 m/s and $\Delta N_p = 1$

LG-HG2 3000 mAh (3.6V)
240Wh/kg Nominal

Sim. Energy Density = 132.4419 Wh/kg , Sim. Vol. Energy Density =356.3176 Wh/L
Sim. Avg. Power Density =925.8066 W/kg , Sim. Max. Power Density =1032.8424 W/kg

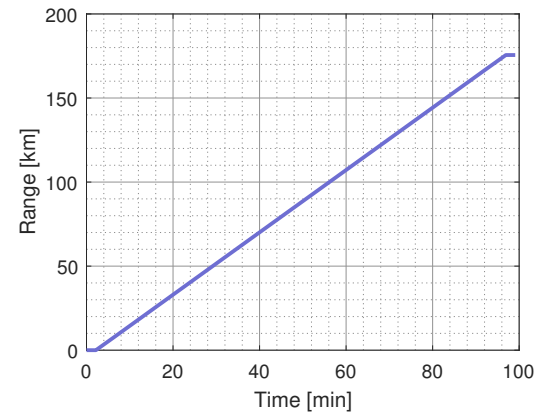
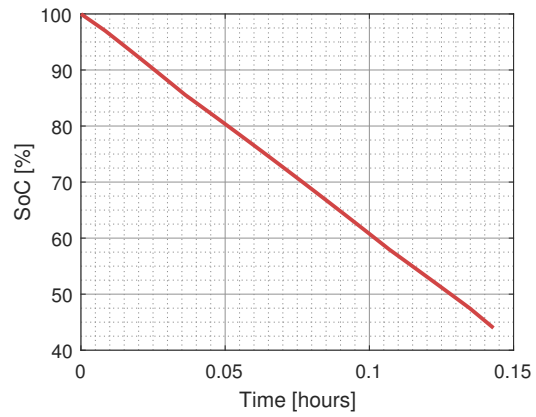
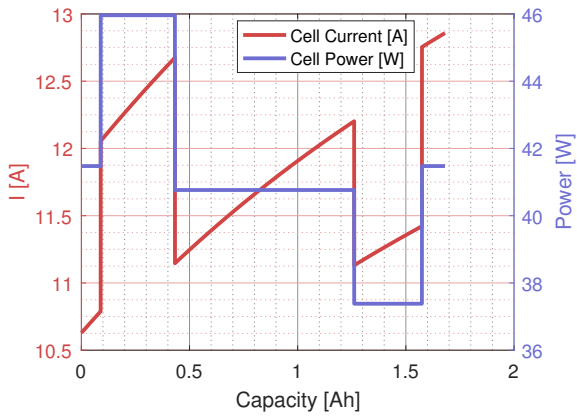
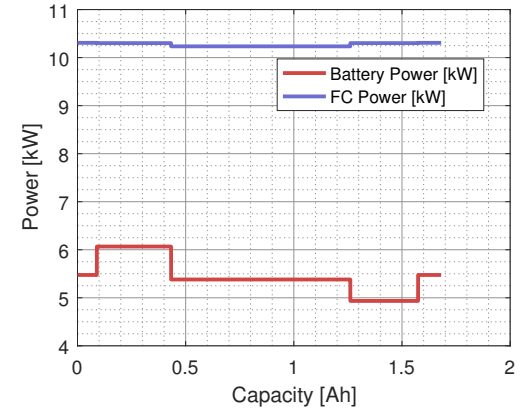
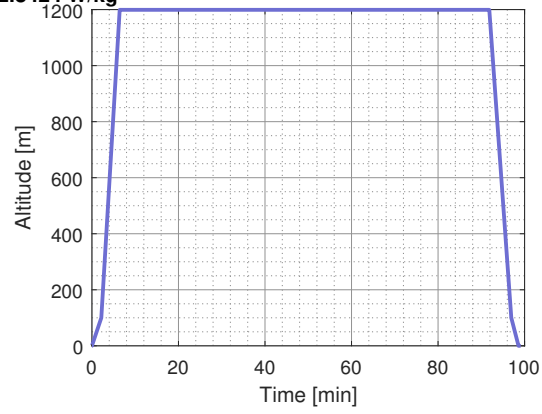
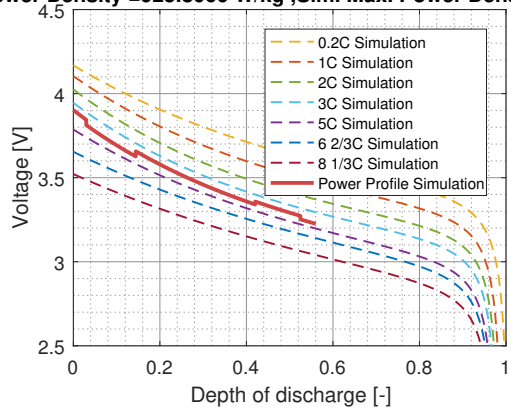


Figure C.2: 1 m/s and $\Delta N_p = 1$

LG-HG2 3000 mAh (3.6V)
240Wh/kg Nominal
Sim. Energy Density = 148.93 Wh/kg , Sim. Vol. Energy Density =400.6766 Wh/L
Sim. Avg. Power Density =943.9229 W/kg ,Sim. Max. Power Density =994.5716 W/kg

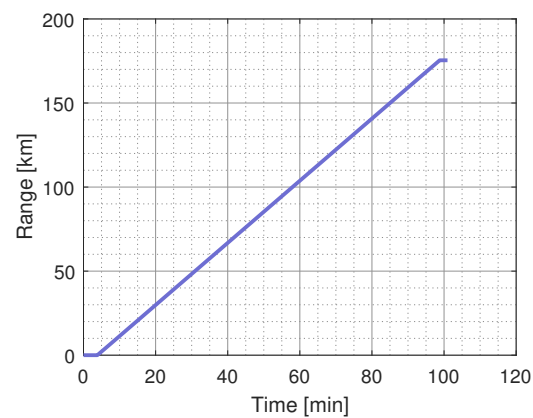
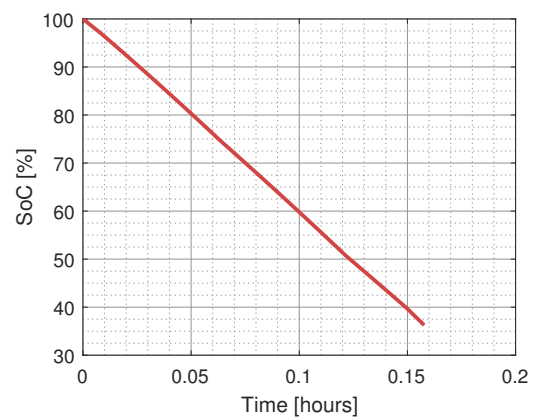
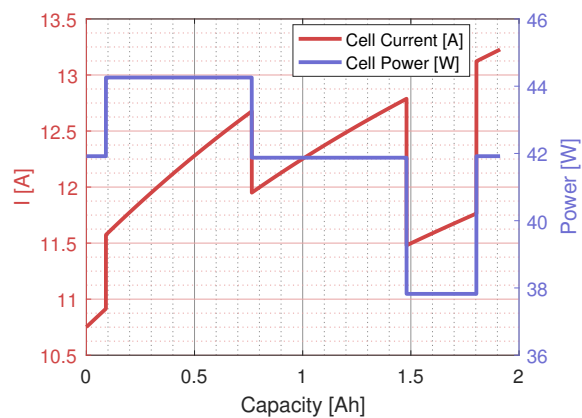
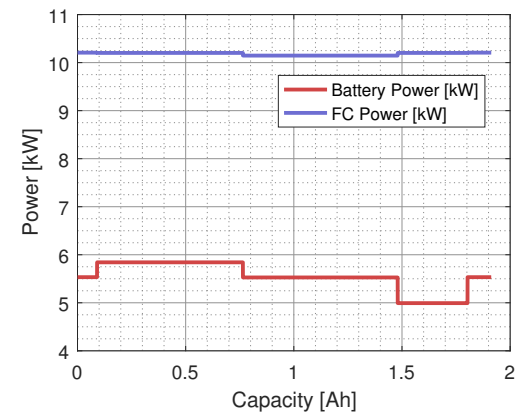
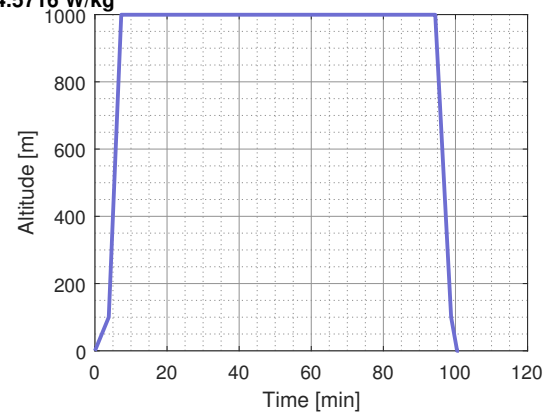
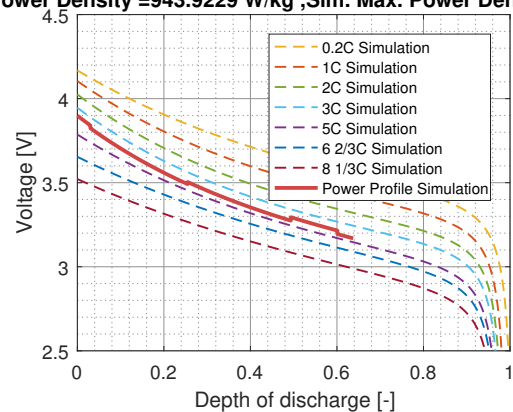


Figure C.3: 0.5 m/s and $\Delta N_p = 1$

LG-HG2 3000 mAh (3.6V)
240Wh/kg Nominal

Sim. Energy Density = 137.0714 Wh/kg , Sim. Vol. Energy Density =368.7724 Wh/L
Sim. Avg. Power Density =1026.944 W/kg , Sim. Max. Power Density =1602.5752 W/kg

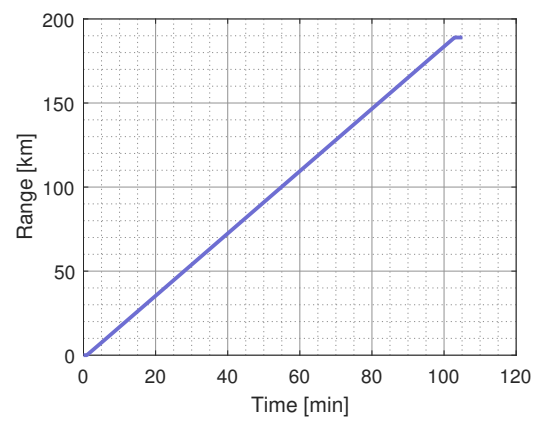
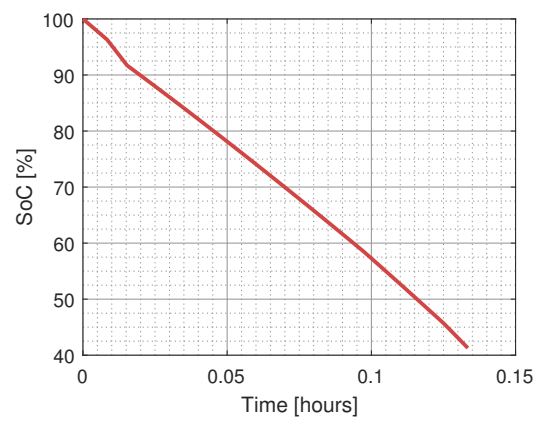
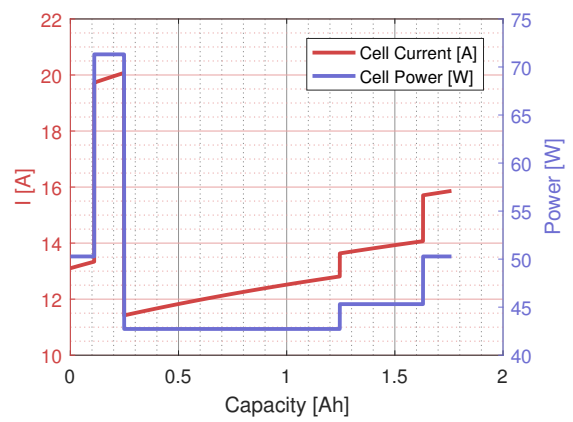
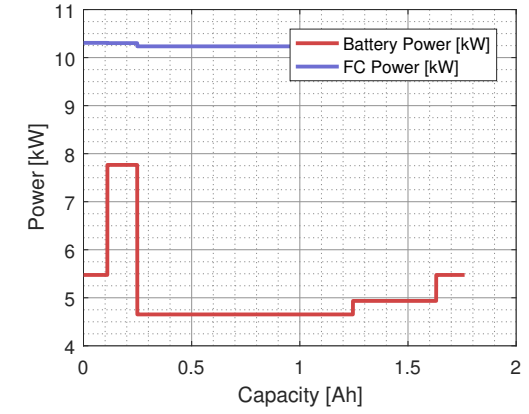
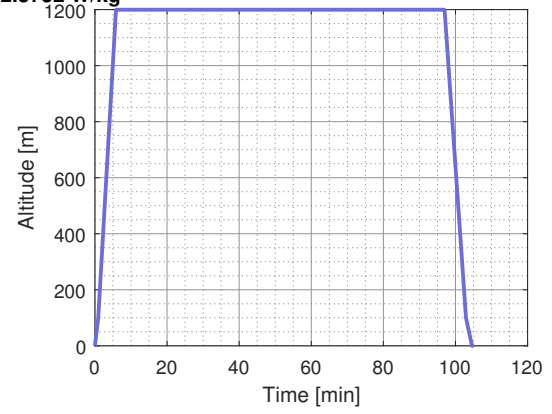
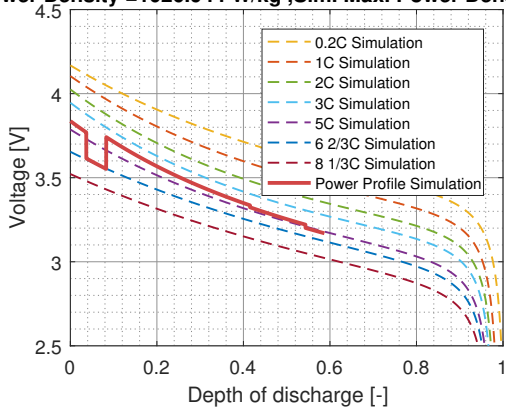


Figure C.4: 4 m/s and $\Delta N_p = 0.05$

**LG-HG2 3000 mAh (3.6V)
240Wh/kg Nominal**

**Sim. Energy Density = 174.7819 Wh/kg , Sim. Vol. Energy Density =470.2277 Wh/L
Sim. Avg. Power Density =1255.3989 W/kg , Sim. Max. Power Density =1488.7032 W/kg**

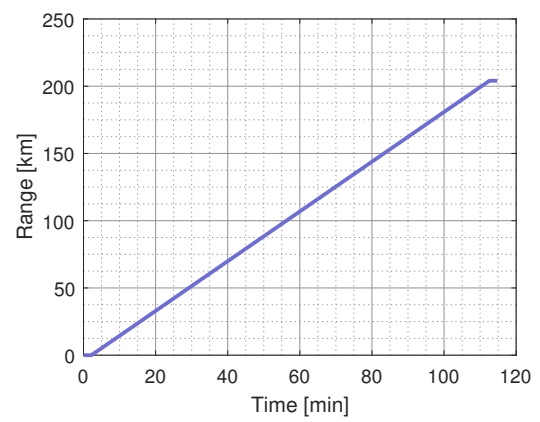
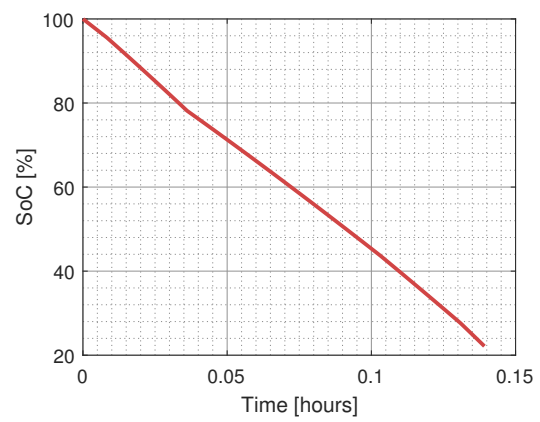
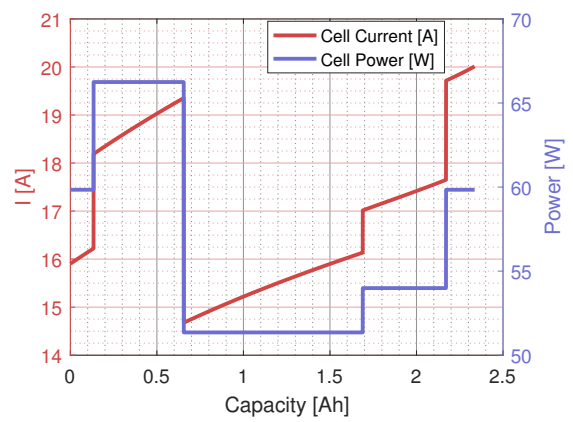
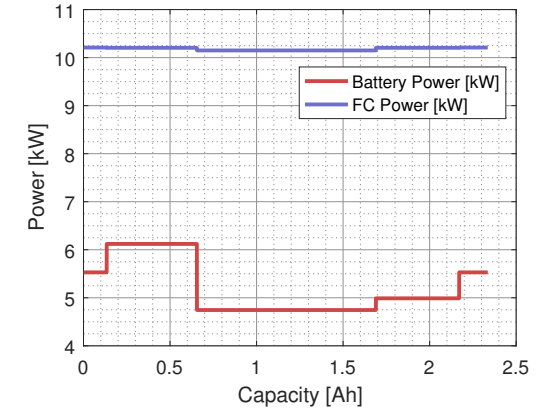
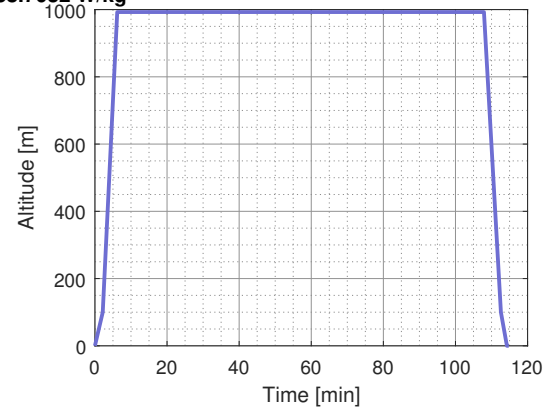
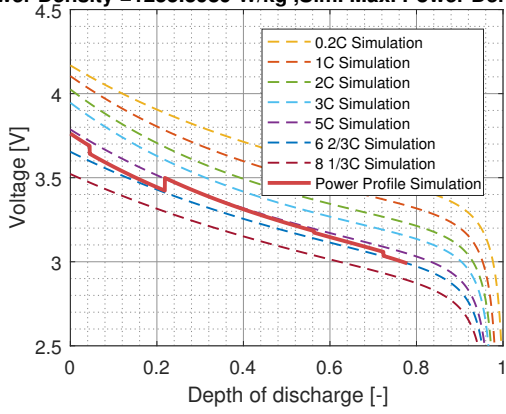


Figure C.5: 1 m/s and $\Delta N_p = 0.05$

**LG-HG2 3000 mAh (3.6V)
240Wh/kg Nominal**

**Sim. Energy Density = 199.2354 Wh/kg , Sim. Vol. Energy Density =536.0166 Wh/L
Sim. Avg. Power Density =1221.6669 W/kg ,Sim. Max. Power Density =1361.1448 W/kg**

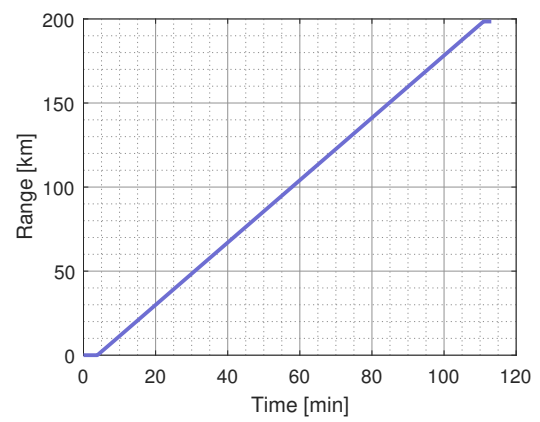
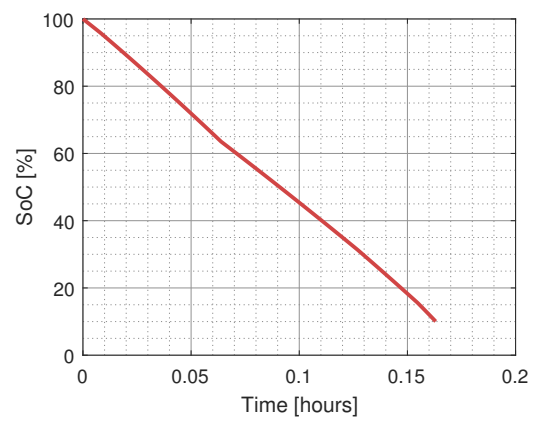
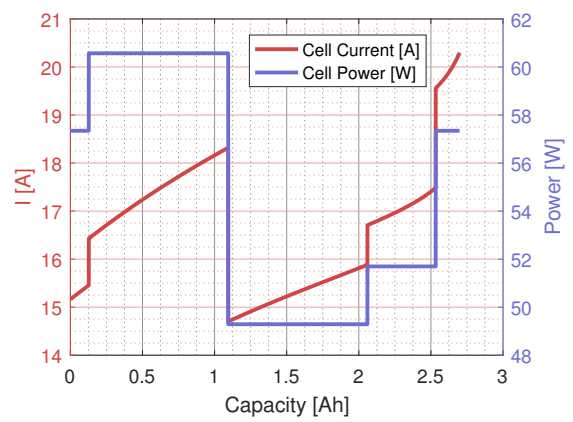
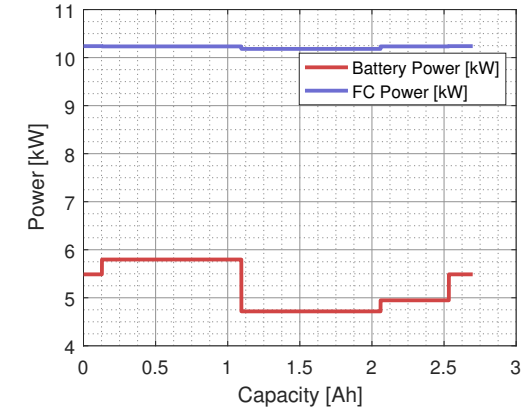
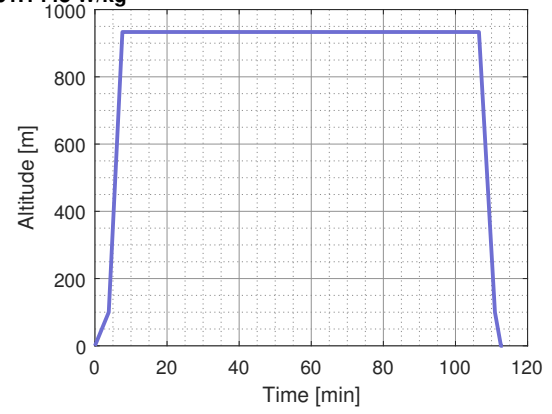
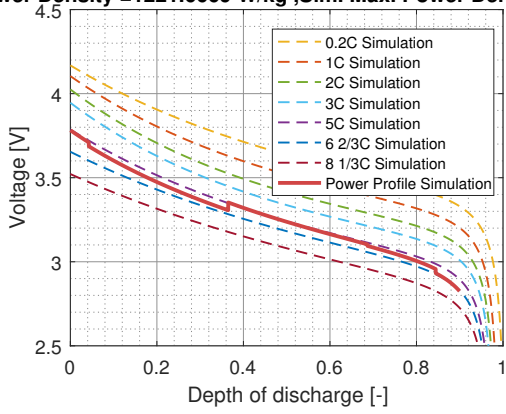


Figure C.6: 0.5 m/s and $\Delta N_p = 0.05$

Appendix D: FC Fitting Parameters

This appendix shows the effect of the fitting parameters on the polarization curve. Figure D.1 shows the effect of a changing V_0 parameter, which is expectedly a vertical shift as a result of the open circuit voltage change. Figure D.2, shows the effect of the coefficient in the activation loss term. The larger this term, the more the open circuit voltage shifts up and the larger the initial losses are. The ohmic resistance is a term that can be approximated given the fuel cell experimental points as R can be directly derived from the linear part in the I-V or i-V diagram. This effect can be seen in Figure D.3. The final term of the polarization model consists of two parameter, where a larger m can increase the concentration loss, but n in the exponential both determines this deflection in the polarization curve and at what current (density) this occurs.

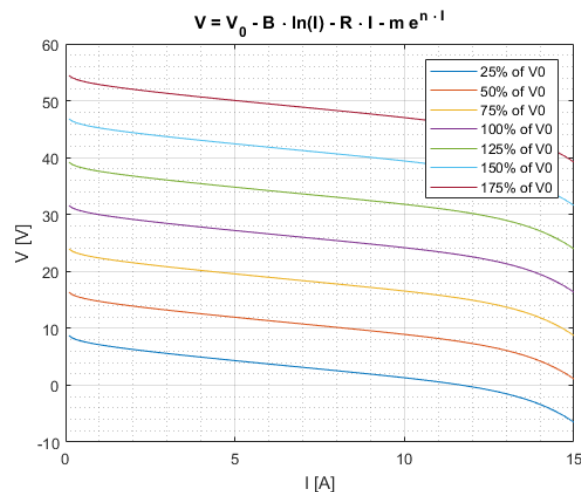


Figure D.1: The effect of parameter V_0 on the curve fit $V = V_0 - B \cdot \ln(I) - R \cdot I - m \cdot e^{(n \cdot I)}$

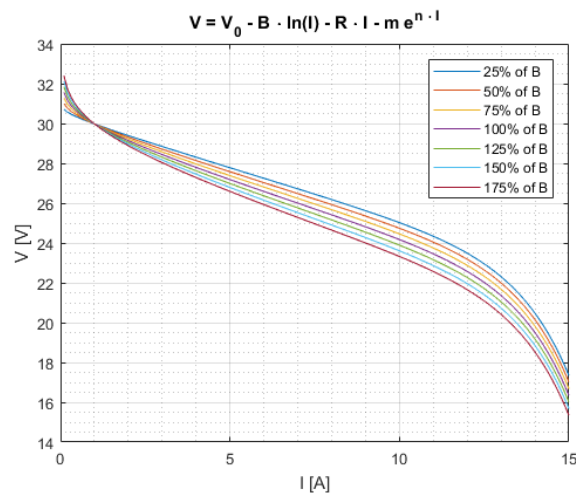


Figure D.2: The effect of parameter B on the curve fit $V = V_0 - B \cdot \ln(I) - R \cdot I - m \cdot e^{(n \cdot I)}$

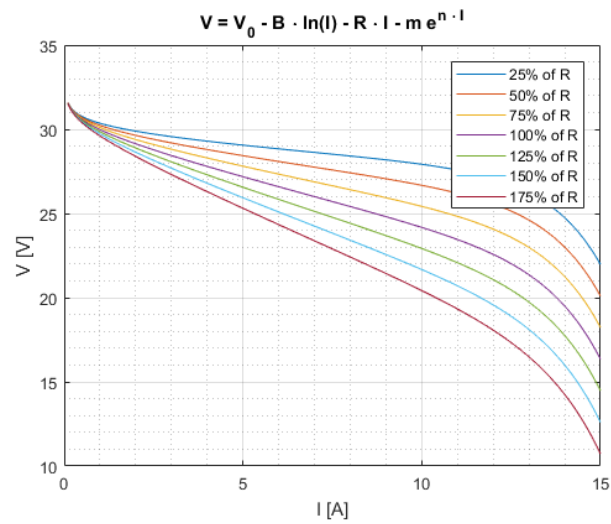


Figure D.3: The effect of parameter R on the curve fit $V = V_0 - B \cdot \ln(I) - R \cdot I - m \cdot e^{(n \cdot I)}$

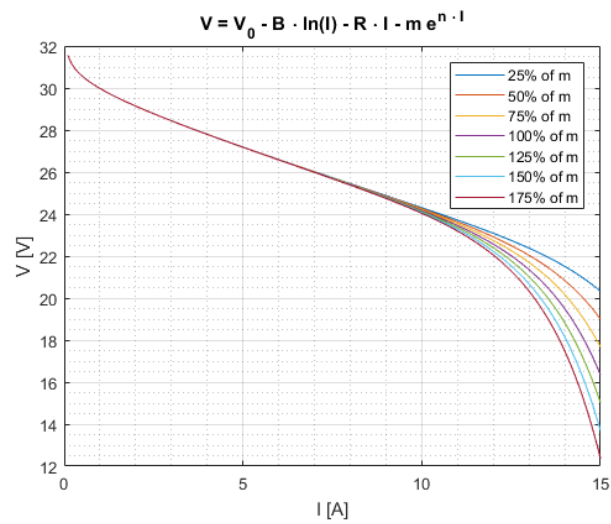


Figure D.4: The effect of parameter m on the curve fit $V = V_0 - B \cdot \ln(I) - R \cdot I - m \cdot e^{(n \cdot I)}$

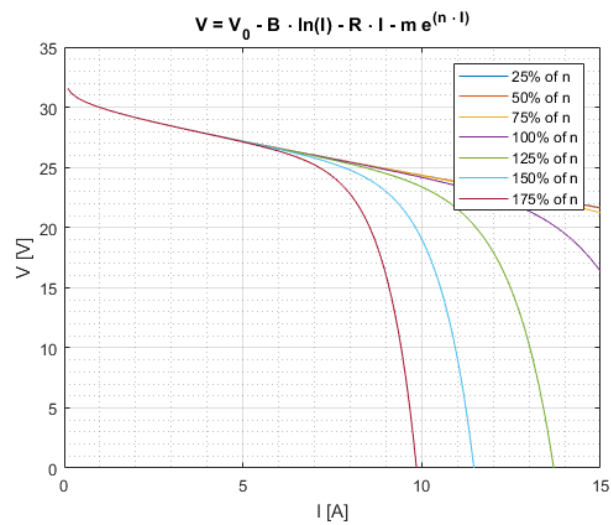


Figure D.5: The effect of parameter n on the curve fit $V = V_0 - B \cdot \ln(I) - R \cdot I - m \cdot e^{(n \cdot I)}$

